8

Signature Splitting and Non-Axiality in the Nuclei ^{164}Ta and ^{165}Ta

Thesis submitted in accordance with the
requirements of the University of Cape Town
for the degree of Doctor of Philosophy

by

David Gerhardus Roux

ysics Department
iversity of Cape Town

September 4, 2001

Dedicated to my parents.

Abstract

High-spin states in two deformed nuclei (^{164}Ta and ^{165}Ta) have been studied in two separate experiments with the AFRODITE escape suppressed spectrometer array at the National Accelerator Centre, near Cape Town. For both of these nuclei, definitive rotational band structures up to high spins have been established for the first time.

Excited states in ^{165}Ta ($Z = 73$, $N = 92$) were populated in both the first experiment, ^{142}Nd(^{27}Al,4n)^{165}Ta, and the second experiment, ^{141}Pr(^{28}Si,4n)^{165}Ta. The yrast rotational decay sequence, identified up to spin $53/2^-$, has been assigned the $\pi[514]9/2^-$ configuration. A comparison of the experimental results with predictions of Cranking Shell Model (CSM) calculations reveal an unexpectedly large signature splitting, for a high-Ω configuration, for the yrast band. Further discrepancies between theory and experiment are observed for the bandcrossing frequency and the signature splitting of the $B(M1)/B(E2)$ ratios. The possibility that these discrepancies are associated with a substantial deviation from an axially symmetric shape is explored. In addition a weaker excited band, possibly associated with the $\pi[402]5/2^+$ configuration, has also been identified.

High-spin states in ^{164}Ta ($Z = 73$, $N = 91$) were populated in the first experiment. The yrast band, identified up to spin 21^-, has been assigned the configuration $\pi[514]9/2^- \otimes \nu[660]1/2^+$. Anomalous signature splitting of the yrast band is observed at low spins. The splitting is discussed in relation to the systematic trends and its implications for the nuclear shape are considered. Previous attempts to explain the phenomenon are reviewed. The 11^- level was found to be isomeric, both in this nucleus and in its $N = 91$ isotone ^{162}Lu, a by-product of the first experiment. This is the first time that a nanosecond-range isomer has been found in the light tantalum or lutetium nuclei. A less intense excited band was also identified, and was tentatively associated with a four-quasiparticle configuration.

Acknowledgements

All the work towards this dissertation was done at the National Accelerator Centre, South Africa, during the period April 1997 to March 2001. Many people have contributed to the project, and to them I wish to express my gratitude.

I would like to specially thank my supervisors:

- Prof. D. G. Aschman, for his readiness to listen to my questions, a good relationship, and giving physics a human face;
- Prof. B. R. S. Babu, for getting me started, and inspiring me with his adventurous ideas;
- Dr. E. Gueorguieva-Lawrie, for thinking especially deeply about the problems that arose, helping to solve many of them, and for a great deal of moral support;
- Dr. J. J. Lawrie, for sharing his electronics expertise, ultimately getting the experiments to *work*, and his willingness to help with almost everything.

My NAC colleagues and fellow students provided invaluable humour and support. In particular I would like to express my appreciation to Marco Benatar, Roger Fearick, Mirela Fetea, Siegfried Förtsch, Given Mabala, Simon Mullins, Sean Murray, Judith Ncapayi, Richard Newman, John Pilcher, Ricky Smit, Deon Steyn, Charlie Wikner and William Whittaker. I would also like to thank the NAC staff in general, who were consistently helpful.

I owe thanks to the tenacious cyclotron operators who provided stable beams: Deon de Villiers, Ben Greyling, Lowrie Conradie and Willem van Heerden.

I am grateful to my friends and family - particularly Gillian, Kenney and Nicola - for just being there, and providing much-needed encouragement and support.

Finally I wish to acknowledge the financial support I received from both the University of Cape Town and the National Accelerator Centre.

Contents

List of Figures

List of Tables

Chapter 0

Introduction

This work presents a spectroscopic investigation of the high-spin structure of two little-known isotopes of tantalum, ${}^{164}_{73}\mathrm{Ta}_{91}$ and ${}^{165}_{73}\mathrm{Ta}_{92}$. To date these are the most neutron-deficient tantalum isotopes to have been studied at high spin.

The first identification of the ^{164,165}Ta nuclei was reported in 1982 by Liang and Paris [1]. Subsequent investigations [2, 3, 4] however were restricted to a study of the $\beta-$decay and $\alpha-$branching ratio of ^{164}Ta. Perhaps the most complete study was that of Hild *et al.* [3], in which $I^{\pi} = 3^{+}$ was deduced for the ground state of ^{164}Ta, based on *log ft* values for the $\beta-$feeding of the 4^{+} and 2^{+} states of ^{164}Hf. In the same work the half-life of the ^{164}Ta ground state was reported as 14.9(2) seconds.

Prior to the present investigation, high-spin states in ^{164,165}Ta had been populated by bombarding a ^{106}Pd target with a ^{63}Cu beam at 290 MeV [5]. While several $\gamma-$rays had been associated with ^{164}Ta on the basis of mass recoils, no high spin band structure was proposed for this nucleus, and although Clark *et al.* [6] placed some of the $\gamma-$rays associated with ^{165}Ta in a tentative level scheme, their proposed band structure is not supported by the present work.

The light rare-earth nuclei in the $A \sim 160$ mass region are known to have medium prolate deformation $\beta_2 \sim 0.1 - 0.3$ [7]. The ground-state equilibrium shape results from the competition between opposing shape-driving effects of the high$-j$ intruder orbitals occupied by the neutrons and protons, respectively. The nuclei with $N \sim 90$ correspond to the onset of filling the $i_{13/2}$ shell. Consequently the valence neutrons occupy high$-j$, low$-\Omega$ orbitals which drive the nucleus towards a prolate shape. For tantalum ($Z =$

73) isotopes the proton Fermi level is situated high in the $h_{11/2}$ shell. In this shell the lower proton states occupied are therefore also prolate-driving low$-\Omega$ orbitals. Only the last proton states occupied have high Ω and would therefore tend to favour an oblate shape. The lightest members of the tantalum isotopic chain have the smallest quadrupole deformation, and are therefore more likely to be $\gamma-$soft.

The $A \sim 160$ nuclei are known to exhibit rotational bands which often decouple into two signature-partner sequences linked via $M1$ cascade transitions. These bands frequently exhibit phenomena which challenge our understanding of nuclear structure, such as

(i) the behaviour of the signature splitting in bands built on the $\Omega = 9/2\ \pi h_{11/2}$ orbital. In the odd$-Z$ even$-N$ isotopes these bands show unexpectedly large signature splitting, whose amplitude increases with decreasing N down to $N \sim 90$ [8]. However after the first backbending (known to be due to the rotational alignment of a pair of $i_{13/2}$ neutrons) the signature splitting becomes small and signature inversion is observed in several cases.

(ii) In doubly-odd isotopes the bands built on the $\pi h_{11/2} \otimes \nu i_{13/2}$ configuration exhibit small anomalous signature splitting at low spins. The staggering amplitude increases with decreasing N, and the signature inversion point moves to higher spins [8].

Attempts to reproduce these phenomena have been made by taking into account a possible deviation from an axially symmetric nuclear shape. Potential energy surface (PES) calculations [9] have shown that a $\pi h_{11/2}$ orbital in the upper half of the shell drives the prolate deformed nucleus towards negative γ deformations ($\gamma \sim -20°$), where the two signatures of the orbital show considerable splitting even at low rotational frequency. On the other hand, the low-Ω components of the $\nu i_{13/2}$ shell strongly favour shapes with $\gamma \geq 0°$. Therefore, if the nucleus is sufficiently $\gamma-$soft to respond to the deformation-driving effect of the odd quasiparticle, the experimentally observed features of signature splitting in odd$-A$ nuclei and signature inversion on doubly-odd nuclei can be qualitatively explained [9].

In the rare-earth region Bengtsson et al. [10] considered the $N \sim 90$ and $62 < Z < 70$ nuclei as sufficiently $\gamma-$soft for the odd $h_{11/2}$ quasiproton to induce a negative γ deformation for which signature inversion can take place. However, the phenomenon has been observed up to the $Z = 73$ tantalum isotopes. Although several alternative attempts have been made (section 5.4.2) to explain signature inversion, none has been entirely satisfactory, and the question of the underlying mechanism remains open.

This work thus aims to extend the systematic investigation of signature splitting in the $A \sim 160$ region by performing a γ−ray spectroscopic analysis of ^{164,165}Ta. The experimental data were obtained in two experiments using the AFRODITE spectrometer array at the National Accelerator Centre, near Cape Town. The yrast band of ^{164}Ta (^{165}Ta) is established up to $I^{\pi} = 21^{-}$ ($53/2^{-}$), and in each nucleus a less intense, excited band is identified. The assignment of intrinsic configurations to the respective bands is discussed. The nuclear shape is studied for each structure using Total Routhian Surface (TRS) calculations. The experimental observables - alignments, bandcrossing frequencies, signature splitting and B(M1)/B(E2) ratios are compared with the results from Cranking Shell Model (CSM) calculations, and their implications for the nuclear deformation are considered. The results of Tilted Axis Cranking (TAC) calculations are discussed in relation to the experimental data. The Recoil Shadow Anisotropy Method (RSAM) [11], allowing nanosecond-range half-life measurements, is used to search for isomeric states in ^{164}Ta, ^{165}Ta and ^{162}Lu, and the identification of two new isomers, in ^{164}Ta and ^{162}Lu, is discussed.

The analysis of the ^{165}Ta yrast band presented in Chapters 4 and 5, with the exception of the sections on TAC calculations, has recently been published [12].

This thesis is organised as follows:

- Chapter 1 discusses the theoretical models describing the rotational bahaviour of the nucleus.
- Chapter 2 gives an overview of the experimental techniques currently used for studying high spin states in nuclei. The development of multi-detector γ−ray spectrometers is reviewed. A description is given of the NAC facility, the AFRODITE array and the associated electronics.
- Chapter 3 describes in detail the experiments performed in this work.
- Chapter 4 details the data reduction, presents the experimental results including the level schemes, and discusses the assignment of an intrinsic configuration to each rotational band.

- Chapter 5 contains the discussion on the experimental quantities deduced from the level schemes, and compares these to the predictions of theoretical models (CSM and TAC). Proposed mechanisms for the signature inversion phenomenon are reviewed.
- Chapter 6 contains some concluding remarks.

Chapter 1

Theoretical models

1.1 Single-particle and collective degrees of freedom

In general, nuclear excitation may exhibit two extreme types of behaviour: (i) single-particle excitations of the individual valence nucleons to different single-particle levels, and (ii) collective modes of excitation involving a coherent motion of the nucleus as a whole. Excitations of the first type imply a change of the intrinsic configuration. Those of the second type generally mean that a particular nucleon configuration collectively vibrates or rotates. The interplay between the single-particle and collective excitation modes underlies an astounding diversity of experimental level schemes.

The coupling of individual nucleon spins is the main mechanism for generating angular momentum in spherical or weakly deformed systems. Transitions in such nuclei are non-collective. Their decay schemes consequently exhibit an irregular sequence of states connected by $\gamma-$ray transitions of different multipolarities. The nucleus of ^{147}Gd provides a good example of such behaviour, as shown in Figure 1.1.

On the other hand well-deformed systems (those characterised by a non-spherical mass distribution) often exhibit extremely regular sequences of states with consecutively increasing angular momentum. These are known as rotational bands. The possibility of rotational motion is a direct consequence of deformation. It involves the coherent contributions of many nucleons and is thus considered to be a collective motion. Rotation takes place about an axis perpendicular to the symmetry axis. The relation between the excitation energy E and angular momentum I for a rotational band usually follows the

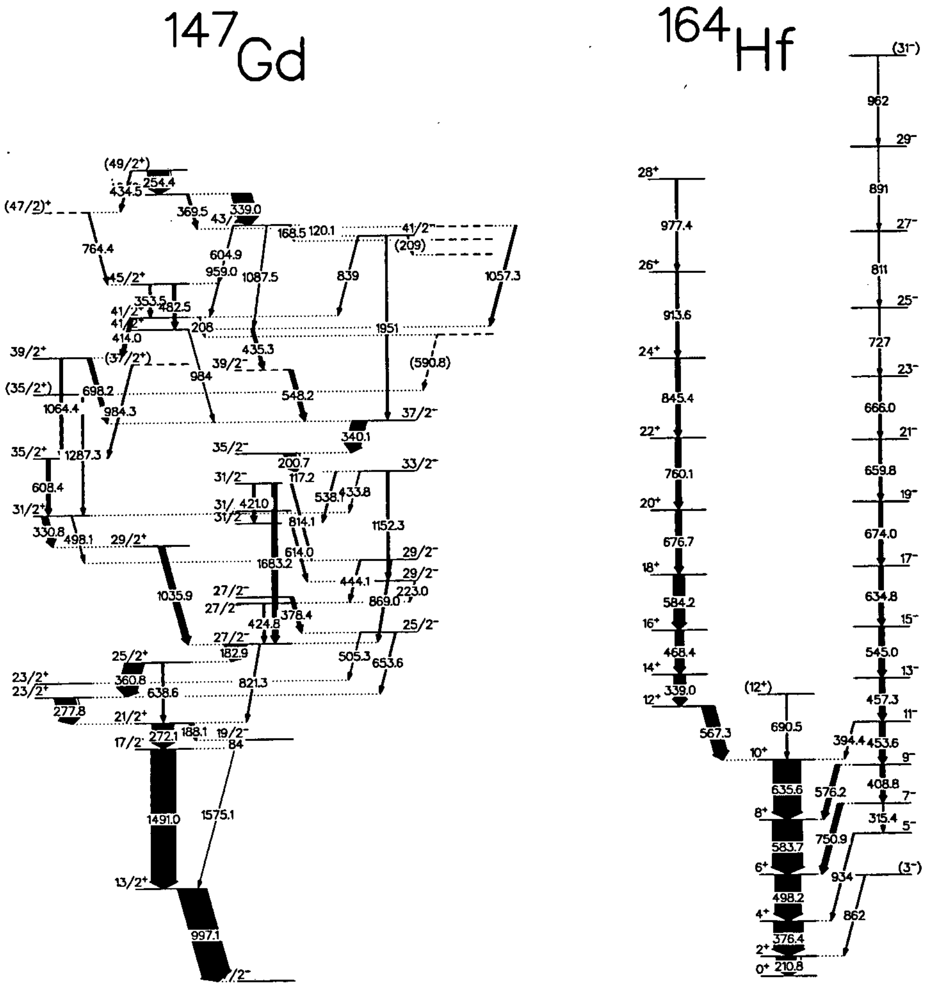

Figure 1.1: Partial decay schemes of ^{147}Gd and ^{164}Hf.

well-known $E \sim I(I+1)$ rule. The lowest state of the band is referred to as the bandhead. For example the nucleus ^{164}Hf, one of the residuals produced in the present work, exhibits collective behaviour. It may be seen in Figure 1.1 that its decay sequence is extremely regular and contrasts sharply with the haphazard level structure of ^{147}Gd. Nuclei with a strong prolate deformation show the best examples of rotational bands.

1.2 Parametrization of the nuclear shape

The surface of a deformed nucleus can be expressed as a superposition of spherical harmonics Y_λ^μ:

$$R(\theta,\phi) = R_0[1+\sum_{\lambda=0}^{\infty}\sum_{\mu=-\lambda}^{\lambda}\alpha_{\lambda\mu}Y_\lambda^\mu(\theta,\phi)] \tag{1.1}$$

where $R(\theta,\phi)$ is the length of a radius vector from origin to the surface, and R_0 is the radius of a sphere of equal volume to the deformed nucleus [13]. For the case of pure, static quadrupole deformation ($\lambda = 2$) the five coefficients $\alpha_{2\mu}$ reduce to only two real independent variables, α_{20} and α_{22}, since $\alpha_{21} = \alpha_{2-1} = 0$ and $\alpha_{22} = \alpha_{2-2}$ (due to reflection symmetry). They are related to the β_2 and γ parameters as follows:

$$\alpha_{20} = \beta_2 \cos\gamma \tag{1.2}$$

and

$$\alpha_{22} = \frac{1}{\sqrt{2}}\beta_2 \sin\gamma \tag{1.3}$$

The nuclear shape is then described only in terms of β_2 and γ. β_2 is referred to as the Woods-Saxon deformation parameter and represents the extent of quadrupole deformation. The triaxiality parameter γ represents the extent of deviation from axial symmetry. The parametrization of nuclear shapes in terms of β_2 and γ is particularly convenient if the Woods-Saxon potential is used in the calculation of single particle energies.

The inclusion of additional harmonics beyond the quadrupole term extends this description of the nuclear surface to higher order axially symmetric shapes ($\mu = 0$). For example, octupole (hexadecapole) deformations are described by including the Y_3^μ (Y_4^μ) terms in equation 1.1, and defining a deformation parameter β_3 (β_4) in an analogous manner to β_2.

Nuclear shapes may be represented on the (β_2, γ) plane as defined by the Lund sign convention [14] shown in Figure 1.2. Figure 1.2 shows the three sectors in the (β_2, γ) plane which are needed to describe nuclei up to states of high spin. The γ values range from -120° to +60°, with axial shapes corresponding to values which are integral multiples of 60°. Other values of γ correspond to triaxial shapes. At $\gamma = 0°(-60°)$ the nuclei are axially symmetric, prolate (oblate), and rotation is collective. On the other hand at $\gamma = -120°(+60°)$ they are prolate (oblate), but rotation is non-collective, about the symmetry axis. This parametrization is used by the Total Routhian Surface (TRS) and Cranking Shell Model (CSM) calculations, Sections 5.2.1 and 5.2.2. The relation between these parameters and the nuclear radius is:

$$\delta R_k = R_k - R_0 = \sqrt{\frac{5}{4\pi}} R_0 \beta_2 \cos(\gamma - \frac{2k\pi}{3}) \tag{1.4}$$

with $k = 1, 2, 3$.

It is important to note that β_2 is just one of many quadrupole deformation parameters. There exists another parametrization in terms of the Nilsson quadrupole deformation parameter ϵ_2. The so-called Nilsson parametrization (ϵ_2, γ) is used when the Anisotropic Harmonic Oscillator (AHO) potential, for which equipotential surfaces are ellipsoids, is included in the Hamiltonian. In this case the deformation parameters occur in the expression of the three harmonic oscillator frequencies, which correspond to nucleon motion along each of the three principal axes (labelled 1, 2 and 3):

$$\omega_1(\epsilon_2, \gamma) = \omega_2(\epsilon_2, \gamma) = \omega_0 \left\{ 1 + \frac{1}{3}\epsilon_2 \cos\gamma + \frac{1}{\sqrt{3}}\epsilon_2 \sin\gamma \right\} \tag{1.5}$$

$$\omega_3(\epsilon_2, \gamma) = \omega_0 \left\{ 1 - \frac{2}{3}\epsilon_2 \cos\gamma \right\} \tag{1.6}$$

Both (ϵ_2, γ) and (β_2, γ) parametrizations are equivalent and their use is a matter of convenience. The triaxiality parameter γ has the same value in both cases, but clearly the quadrupole parameters are different, $\epsilon_2 \simeq 0.944\beta_2 - 0.122\beta_2^2$. It is therefore obvious that ϵ_2 expresses the elongation of the nuclear potential. The (ϵ_2, γ) parametrization is used in the Tilted Axis Cranking (TAC) calculations, Section 1.7.

One method to obtain information about the nuclear shape is by measuring the nuclear transition probabilities.

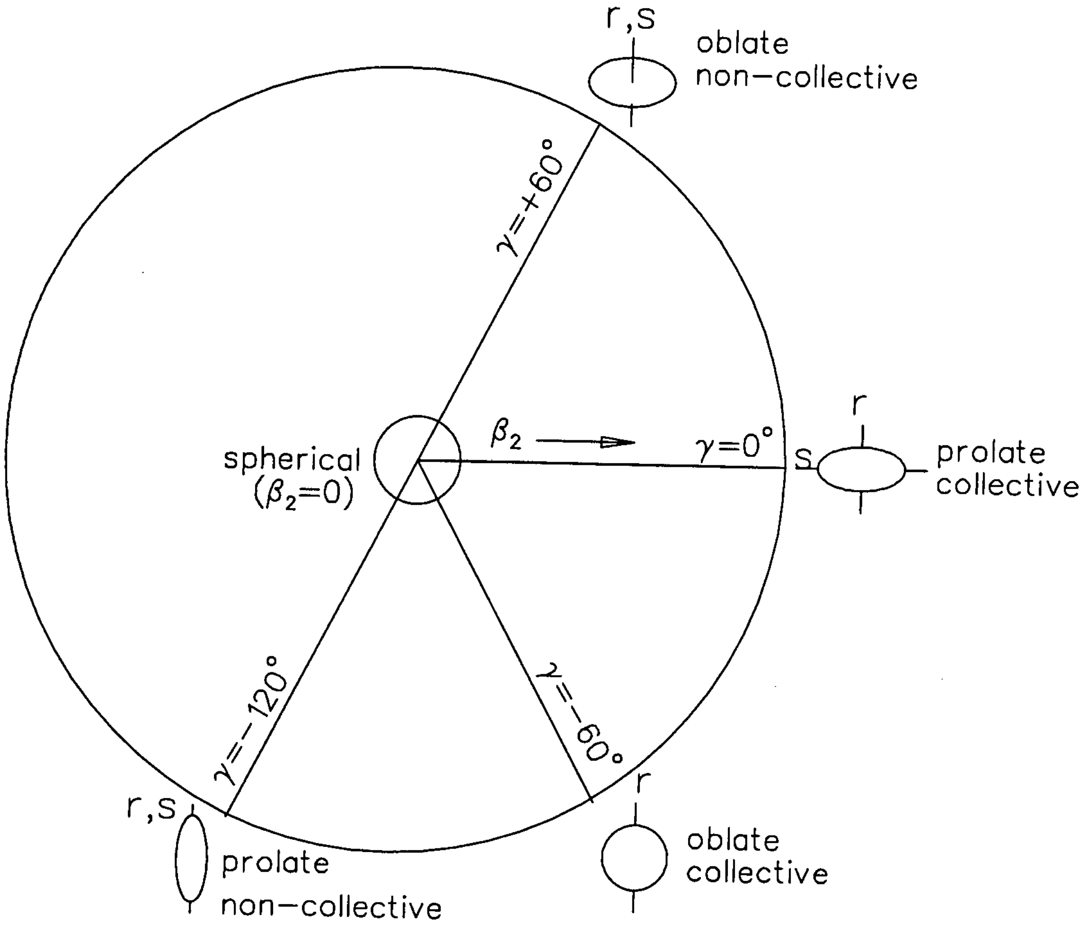

Figure 1.2: Lund sign convention for parametrizing nuclear shape. All axially symmetric shapes are shown. The letters s (r) denote the symmetry (rotation) axis. For the oblate collective case, s is perpendicular to the page.

1.3 Electromagnetic moments and transition probabilities

In order for the nucleus to de-excite from an initial state $|\psi_i\rangle$ to a final state $|\psi_f\rangle$ it is necessary that the two states interact. Quantum mechanically this requires that the matrix element of the interaction between the two states be non-vanishing, i.e.

$$\langle\psi_f|H'|\psi_i\rangle \neq 0 \tag{1.7}$$

where H' represents a time-dependent perturbation of the mean field. If the perturbation is small, first order time-dependent perturbation theory may be used to derive the well-known Fermi Golden Rule

$$T_{fi} = \frac{2\pi}{\hbar}\left|\langle\psi_f|H'|\psi_i\rangle\right|^2 \rho(E_f) \tag{1.8}$$

where $\rho(E_f)$ is the density of final states. T_{fi} expresses the probability per unit time for a transition between the initial and final states via single photon emission.

H' can be expanded in terms of the electric ($Q_{\lambda\mu}$) and magnetic ($M_{\lambda\mu}$) transition multipole operators as follows:

$$H' = \sum_{\lambda\mu} a_{\lambda\mu}Q_{\lambda\mu} + b_{\lambda\mu}M_{\lambda\mu} \tag{1.9}$$

where

$$Q_{\lambda\mu} = \int \rho(\mathbf{r})\, r^\lambda Y_{\lambda\mu}(\theta,\phi)\, d\tau \tag{1.10}$$

and

$$M_{\lambda\mu} = \int \mu(\mathbf{r})\, \nabla(r^\lambda Y_{\lambda\mu}(\theta,\phi))\, d\tau \tag{1.11}$$

The parities of the above operators together with the parity-conserving property of the electromagnetic interaction place constraints on the parities of the wavefunctions of the initial and final states if there is to be any transition between them. This together with angular momentum conservation imposes well-known parity and angular momentum selection rules on electric and magnetic transitions of different multipolarities. These are summarized in Table 1.3 for the lowest order electric and magnetic operators.

A useful quantity, which contains information about the magnetic or electric multipole moments of states $|\psi_i\rangle$ and $|\psi_f\rangle$, is the reduced transition strength $B(\hat{O}\lambda)$, where $\hat{O}$

	E1	E2	E3	M1	M2	M3
$\Delta\pi$	-1	+1	-1	+1	-1	+1
ΔI	≤ 1	≤ 2	≤ 3	≤ 1	≤ 2	≤ 3

Table 1.1: Parity and spin selection rules for lowest order electromagnetic transitions, where the parity change is $\Delta\pi = \pi_i\pi_f$.

represents the electric or magnetic multipole operator of multipolarity λ. A relationship (Section 1.3.1) exists between $B(\hat{O}\lambda)$ and the transition rate $T_{fi}\left(\hat{O}\lambda\right)$, which can be deduced from experimentally determined lifetimes , τ, of nuclear states:

$$T_{fi}\left(\hat{O}\lambda\right) = \frac{1}{\tau} \tag{1.12}$$

Lifetime measurements thus allow information on the multipole moments present in the nucleus to be extracted. The power series expansion of the multipole moments converges rapidly so that only the lower orders are important. Two special cases are of interest here:

1.3.1 Electric quadrupole moments

The electric quadrupole operator is defined in terms of the nuclear charge density distribution $\rho(r)$:

$$eQ(\mathbf{r}) = \int \rho(\mathbf{r})\, r\,(3\cos^2\theta - 1)\, d\tau \tag{1.13}$$

where $\mathbf{r}$ is the radius vector and θ is the angle it subtends. The integral vanishes for spherically symmetric charge distributions and thus only a deformed nucleus will have a static quadrupole moment. The intrinsic quadrupole moment is defined [15] in terms of the deformation parameter β_2 (Section 1.2):

$$Q_0 = \frac{3}{\sqrt{5\pi}} Z R^2 \beta_2 \tag{1.14}$$

where R is approximated by $R \simeq 1.23A^{1/3}$ fm. For a nucleus with prolate (oblate) deformation, Q_0 is positive (negative). The reduced transition strength B(E2) for a quadrupole transition linking states of spins I and $I-2$ is given by the expression

$$B(E2) = \frac{5}{16\pi} Q_0^2 \langle I\, K\, 2\, 0 | I-2\, K\rangle^2 \qquad (eb)^2. \tag{1.15}$$

This in turn is related to the transition probability by

$$T_{fi} = \frac{12\pi}{225\hbar}\left(\frac{E_\gamma}{\hbar c}\right)^5 B(E2) \tag{1.16}$$

The measurement of reduced E2 transition strengths thus leads to information about the overall deformation of the nucleus.

1.3.2 Magnetic dipole moments

Classically, the nuclear magnetic field is the product of two phenomena: the orbital motion of the protons which constitutes a current, and the intrinsic spin of the nucleons. Even for the neutron, there is an intrinsic magnetic dipole moment associated with its internal quark structure. Measured M1 strengths thus provide a probe into nuclear currents and hence the single-particle structure.

The reduced transition strength $B(M1)$ for stretched magnetic dipole (M1) transitions linking states with spins I and $I-1$ is defined in terms of the nuclear g-factors:

$$B(M1) = \frac{3}{4\pi}\left(g_K - g_R\right)^2 K^2 \left\langle I\,K\,1\,0|I-1\,K\right\rangle^2 \qquad \mu_N^2 \tag{1.17}$$

where $\mu_N = e\hbar/2mc$ is the nuclear magneton. The rotational g-factor g_R describes the current arising from the collective rotation of the core:

$$\mu = g_R\,R\,\mu_N \tag{1.18}$$

and can be approximated by $g_R \simeq Z/A$ although in practice this represents an upper limit for g_R. On the other hand the intrinsic g-factor g_K describes the currents which arise from the orbital motion of the valence nucleons:

$$g_K = g_l + \frac{1}{\Omega}(g_s - g_l)\,\left\langle\Omega\,|s_z|\,\Omega\right\rangle. \tag{1.19}$$

The Nilsson quantum numbers K and Ω used in the above expressions are defined in Section 1.4.2. The total magnetic dipole moment μ for total angular momentum $\mathbf{I} = \mathbf{R}+\mathbf{j}$ is given by

$$\mu = \left(g_R\,I + (g_K - g_R)\,\frac{K^2}{K+1}\right) \quad \mu_N \tag{1.20}$$

The reduced transition strength $B(M1)$ is related to the transition probability T_{fi} as follows:

$$T_{fi} = \frac{16\pi}{9\hbar}\left(\frac{E_\gamma}{\hbar c}\right)^3 B(M1). \tag{1.21}$$

1.4 Collective rotation in the laboratory frame

1.4.1 Collective rotation of even-even nuclei

The collective rotational behaviour of well-deformed nuclear systems is directly analogous with that of a classical rigid rotor. For a classical object the energy E and angular momentum R are related by

$$E = \frac{1}{2J}R^2 \tag{1.22}$$

where J is the classical moment of inertia. An equivalent relation holds for nuclear rotational states, characterised by their excitation energy $E(I)$ and their total angular momentum or spin I:

$$E(I) = \frac{\hbar^2}{2J}I(I+1) \tag{1.23}$$

This equation defines the nuclear moment of inertia J, which should be constant and equal to the rigid body value for an ideal rotor. However deformed nuclei deviate from this simple picture. Their moments of inertia generally change with increasing spin and are smaller than the rigid body values on account of pairing.

The deviations from the ideal rotational spectrum may be described by using the following expansion:

$$E(I) = AI(I+1) + B\left[I(I+1)\right]^2 + C\left[I(I+1)\right]^3 + ... \tag{1.24}$$

In practice this equation converges rather slowly for higher values of angular momentum I, and so it can only be employed for $I \leq 10$. Not only do the moments of inertia vary, but the adiabatic approximation (which requires that the collective rotation should be slow compared with the intrinsic motion) breaks down at higher angular momentum. It turns out that an expansion in terms of the angular frequency ω, instead of $I(I+1)$, will improve the convergence across a wider range of angular momentum. However ω is not directly measurable. It is defined semi-classically as

$$\omega = \frac{dE}{d(\hbar I)} = \frac{1}{\hbar}\frac{dE}{dI} \tag{1.25}$$

where it is understood that I is the expectation value of the total angular momentum i.e. $I = \sqrt{I(I+1)}$. Since neither E nor I are continuous quantities, it is necessary to make an approximation using the discrete values of the excitation energy and spin. For a K=0

(Section 1.4.2) rotational band of stretched electric quadrupole ($E2$) transitions, as found in the yrast systems of even-even nuclei,

$$\hbar\omega = \frac{E_I - E_{I-2}}{[I(I+1)]^{1/2} - [(I-2)(I-1)]^{1/2}} \quad . \tag{1.26}$$

For spin values larger than $I \sim 8$ this simply approximates to

$$\hbar\omega = \frac{E_\gamma}{2} \quad . \tag{1.27}$$

At sufficiently high spins, therefore, this simple relation allows the rotational frequency to be obtained directly from the measured γ-ray energies.

The energy E of the rotating nucleus may now be expanded in ω as first proposed by Harris [16]:

$$E(\omega) = \alpha\,\omega^2 + \beta\,\omega^4 + \gamma\,\omega^6 + ... \tag{1.28}$$

Odd powers in ω do not occur on account of the time reversal invariance (E cannot change by reversing the angular velocity). As mentioned above this expansion produces much faster convergence to rotational spectra and also holds for higher spins. In fact the series is often truncated after the second term.

The moment of inertia J can be parametrized in a similar fashion. There are two different moment of inertia parameters defined for a rotating nucleus: the kinematic moment of inertia $J^{(1)}$ and the dynamic moment of inertia $J^{(2)}$. These inertia parameters reflect different aspects of nuclear dynamics. The kinematical moment of inertia derives from equation 1.23 and is defined as follows:

$$J^{(1)} = \frac{\hbar^2}{2}\left[\frac{dE}{dI(I+1)}\right]^{-1} \simeq \frac{\hbar I}{\omega} \tag{1.29}$$

The last approximation employs the definition for the angular velocity ω in equation 1.25 and is valid for large values of I where $I \sim \sqrt{I(I+1)}$. The dynamic moment of inertia is related to the curvature of the E vs $I(I+1)$ curve and expresses the response of the nucleus to a force:

$$J^{(2)} = \left(\frac{d^2E}{d(I(I+1))^2}\right)^{-1} = \hbar\frac{dI}{d\omega} \tag{1.30}$$

which can also be approximated by

$$J^{(2)} \simeq \frac{4\hbar^2}{\Delta E_\gamma} \tag{1.31}$$

Since this quantity is independent of the nuclear spin it is extremely useful for extracting information about rotational bands where the spin assignments may be unknown. For rigid rotation the moment of inertia is a constant. It follows from equations 1.29 and 1.30 that

$$J^{(2)} = J^{(1)} + \omega \frac{dJ^{(1)}}{d\omega} \tag{1.32}$$

from which it can be seen that for a rigid rotor

$$J^{(1)} = J^{(2)} = J_{rigid} \tag{1.33}$$

Further, the definition of the angular velocity given in equation 1.25 can be used to derive the relation

$$\frac{dE}{d\omega} = \hbar\omega \frac{dI}{d\omega} \tag{1.34}$$

The $J^{(2)}$ moment of inertia may be parametrized in ω by substituting this last relation, and the expansion $E(\omega)$ (equation 1.28), into the expression 1.30. This ultimately gives the relation

$$J^{(2)} = 2\,\alpha + 4\,\beta\,\omega^2 + 6\,\gamma\,\omega^4 + ... \tag{1.35}$$

which may then be integrated to yield a similar expression for$J^{(1)}$:

$$J^{(1)} = 2\,\alpha + \frac{4}{3}\beta\,\omega^2 + \frac{6}{5}\gamma\,\omega^4 + ... \tag{1.36}$$

However it is customary to use the so-called Harris parameters J_0, J_1, J_2 (where $J_0 = 2\alpha$, $J_1 = 4/3\beta$, $J_2 = 6/5\gamma$) instead of α, β, γ. Thus the well-known Harris expansions of the moments of inertia are finally given as follows:

$$J^{(1)} = J_0 + J_1\,\omega^2 + J_2\,\omega^4 + ... \tag{1.37}$$

$$J^{(2)} = J_0 + 3J_1\,\omega^2 + 5J_2\,\omega^4 + ... \tag{1.38}$$

It turns out that the above expansions, even if they are truncated to the first two terms, give very good agreement with the experimental data in the low spin regime of deformed even-even nuclei. In practice the truncated expansions are therefore used to fit the moments of inertia of a band structure (or part thereof) which can act as a reference rotor for odd-odd or odd-A nuclei. Typically the ground-state band or the first excited band of a neighbouring doubly-even deformed nucleus is used for this purpose. The subtraction of a reference core serves to expose effects that arise from the alignment or excitation of the valence nucleons.

1.4.2 Collective rotation of odd-A nuclei

Axially symmetric rotor + one quasiparticle

At low rotational frequencies the interplay between single-particle and collective degrees of freedom in axially symmetric odd-A nuclei may be described by assuming that the unpaired nucleon moves more or less independently is the deformed potential of the core, and coupling its angular momentum $\mathbf{j}$ to that $\mathbf{R}$ of the collective rotor which represents the rest of the particles. This picture is valid when the collective rotation is slow relative to the single-particle motion (adiabatic approximation). The total angular momentum $\mathbf{I}$ is then given by:

$$\mathbf{I} = \mathbf{R} + \mathbf{j} \tag{1.39}$$

The three principal body-fixed axes are labelled 1, 2 and 3. The 3-axis is considered as the symmetry axis and the 1-axis the axis of rotation.

The Particle-plus-Rotor Model (PRM) splits the Hamiltonian into two parts:

$$H = H_{intr} + H_{coll} \tag{1.40}$$

where H_{intr} (also known as the single-particle Hamiltonian) describes the single-particle motion of the odd nucleon in the intrinsic frame and H_{coll} reflects the collective rotational kinetic energy of the core, $\frac{\hbar^2}{2J}\mathbf{R}^2$. Equation 1.40 may be recast as

$$H = H_{intr} + \frac{\hbar^2}{2J}(\mathbf{I} - \mathbf{j})^2 = H_{intr} + \frac{\hbar^2}{2J}\left[\mathbf{I}^2 + \mathbf{j}^2 - 2(\mathbf{I} \cdot \mathbf{j})\right] \tag{1.41}$$

Because the 3-component of $\mathbf{R}$ has to vanish (no rotation about the symmetry axis) it follows that the 3-component of $\mathbf{I}$, $I_3 = K$, derives entirely from the the 3-component of $\mathbf{j}$, $j_3 = \Omega$. It is then convenient to rewrite equation 1.41 as

$$H = H_0 + H_{Cor} \tag{1.42}$$

where

$$H_0 = \frac{\hbar^2}{2J}\left[\mathbf{I}^2 - I_3^2 + (j_1^2 + j_2^2)\right] + H_{intr} \tag{1.43}$$

and

$$H_{Cor} = -\frac{\hbar^2}{J}(\mathbf{I} \cdot \mathbf{j}) = -\frac{\hbar^2}{2J}(I_+ j_- + I_- j_+) \tag{1.44}$$

with $j_+ = j_1 + i j_2$, $j_- = j_1 - i j_2$. The term H_{Cor} is called the Coriolis interaction in analogy with its classical counterpart. It is the only term which couples the single-particle motion with that of the rotating core. It is obvious from equation 1.44 that its contribution is maximally negative when **j** and **I** are both large, and parallel. The Coriolis force therefore tries to align these two vectors with each other, and with the rotation. The presence of this coupling disturbs the simple rotational-band spectrum, admixing different K values. This has the effect of introducing small amounts of triaxiality since K is a good quantum number only for axially symmetric potentials.

It turns out that it is useful to consider two limits in which the Coriolis interaction plays either an insignificant or dominant role, respectively. These limits correspond to deformation alignment (DAL) and rotational alignment (RAL). They are discussed in the following two subsections, where the Nilsson asymptotic quantum numbers $[N, n_3, \Lambda]\Omega^{\pi}$ of the deformed shell model are used to label the odd particle. In this model N denotes the corresponding harmonic oscillator shell, n_3 the number of nodes along the intrinsic 3-axis, Λ the projection of the orbital angular momentum ℓ on the 3-axis, and Ω the projection of the total angular momentum **I** along the same axis. Depending on whether the spin is aligned or anti-aligned with the orbital angular momentum, $\Omega = \Lambda \pm 1/2$. In general the total angular momentum j of the single-particle orbital is not a good quantum number on account of the configuration mixing. However, j is approximately good for small deformations where the mixing is minimal. It is also approximately good for high-j "intruder" orbitals. The energy of these orbitals has been sufficiently lowered by the inverted spin-orbit coupling such that they "intrude" into the next lower harmonic oscillator shell. The intruder orbitals remain relatively pure since they have opposite parity to the normal states, and therefore no mixing can occur.

Deformation Alignment (DAL) DAL is realised when the Coriolis matrix elements are small compared with the energy splitting of single-particle energies with different values of Ω. The Coriolis force is then not strong enough to align the spin of the odd particle with the rotation axis. It remains strongly coupled to the deformation, and adiabatically follows the rotations of the even core. This is illustrated in Figure 1.3.

In the DAL case the Coriolis matrix elements are $\sim \frac{\hbar^2}{2J}\left[(I(I+1) - K^2)(j(j+1) - \Omega^2)\right]^{1/2}$. One therefore expects DAL to occur: (i) for large deformation β_2, since the level splitting in the Nilsson Hamiltonian is proportional to β_2^2 whereas the rotational constant $\frac{\hbar^2}{2J}$ scales as β_2^{-2}; and (ii) for low spins I, or for nucleons with small particle angular momenta j;

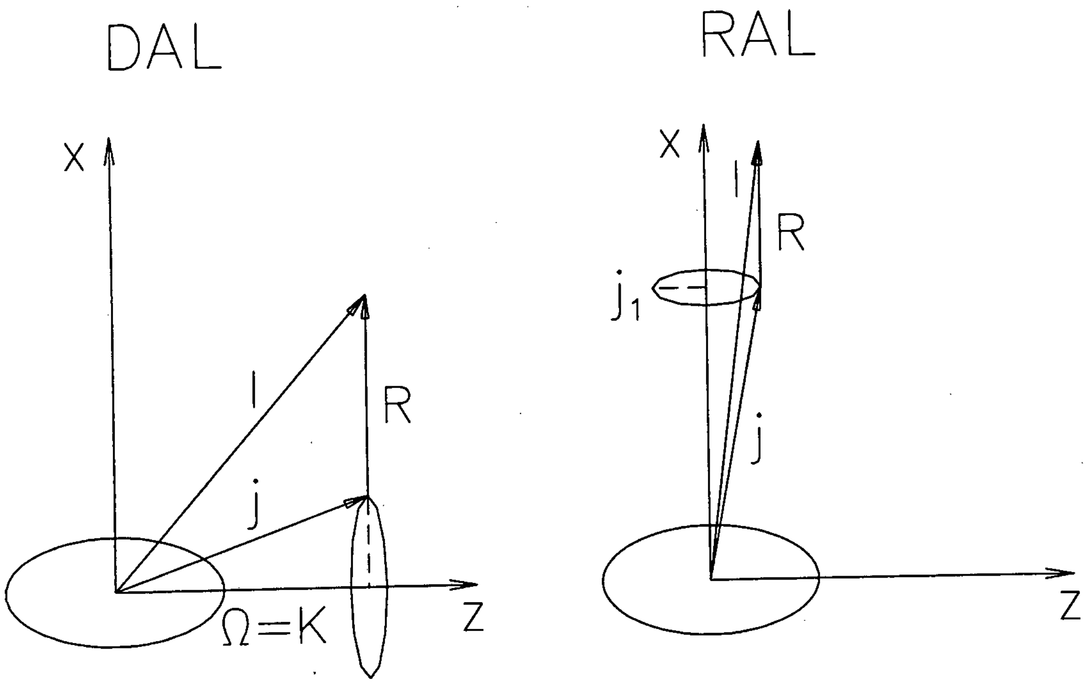

Figure 1.3: Deformation aligned (DAL, left) and rotation aligned (RAL, right) coupling schemes.

(iii) for large j values DAL can only occur for high Ω orbitals. The projection K along the symmetry axis is equal to Ω and is a good quantum number. The corresponding rotational band spectrum is given by

$$E_I^K = \frac{\hbar^2}{2J}\left[I(I+1) - K^2\right] \tag{1.45}$$

and has a spin sequence with $\Delta I = 1$:

$$I = K,\ K+1,\ K+2, ... \tag{1.46}$$

for $K \neq 1/2$ [17]. This sequence normally decouples into two $\Delta I = 2$ bands, denoted "favoured" and "unfavoured" respectively, and characterised by different signatures α (Section 1.9). For $K = 1/2$ bands an additional term appears on account of the Coriolis interaction.

Rotational Alignment (RAL) The other extreme case (RAL) occurs when the quadrupole deformation is small (small splitting in H_{intr}) and the rotational frequency is sufficiently large to align the single-particle angular momentum with the rotation axis. This situation as also shown in Figure 1.3. Particles in high-j orbitals, and those with low K-values in particluar, are the most sensitive to the Coriolis force. They are aligned most easily. For a prolate nucleus, this is consistent with the requirement of maximal overlap of the single-particle density distribution (concentrated in a plane perpendicular to $\mathbf{j}$) with the core. The vector $\mathbf{j}$ precesses about the rotation axis. Consequently K is no longer a good quantum number, although the projection of $\mathbf{j}$ onto the rotation axis, j_1, is now a good quantum number. The spin values and the level energies of the states in the corresponding rotational band are thus completely determined by j_1:

$$I = j_1,\ j_1 + 2,\ j_1 + 4, ... \tag{1.47}$$

and

$$E = \frac{\hbar^2}{2J}(I - j_1)(I - j_1 + 1) \tag{1.48}$$

The last equation expresses that states with maximal alignment ($j_1 = j$) have the lowest energy. This band is therefore the favoured one. Conversely the lesser aligned band ($j_1 = j - 1$) is unfavoured. It has the following spin sequence:

$$I = j - 1,\ j + 1,\ j + 3, ... \tag{1.49}$$

The unfavoured band often lies much higher in energy and is then not populated in heavy-ion reactions.

1.4.3 Collective rotation of odd-odd nuclei

Axial case

In doubly-odd nuclei, the RAL and DAL coupling features of high-spin states in the odd mass transitional nuclei ($\beta_2 \sim 0.13 - 0.15$) are found to persist. Theoretical calculations by Toki *et al.* [18, 19] for two odd particles occupying high-spin orbitals (e.g. $\pi h_{11/2}$ and $\nu i_{13/2}$) coupled with a deformed rotor have successfully predicted trends in the electromagnetic properties and the level systematics for these nuclei.

The above authors distinguish between two different particle behaviours. In the first case, the so-called "peaceful case", both quasiparticles act as either particles or holes and have similar dynamical tendencies. Both try to remain strongly coupled to the core, or alternatively to align with the rotation. This would occur, for example, when both the proton and neutron occupy either high- or low-Ω states. In a sense the two particles act in unison as a "super odd particle". It turns out that the resultant spin j_{tot} of the two quasiparticles can be treated approximately as a good quantum number. This allows states with the same j_{tot} value to be grouped into bands. A consequence of this is that the rotational spectra for the doubly-odd nuclei with the $\pi h_{11/2} \otimes \nu i_{13/2}$ configuration bear a remarkably close resemblance with the spectra observed in the odd-mass transitional region [19].

In the second situation, the so-called "conflicting case" [18, 19], the two quasiparticles have opposite interests. One of them prefers to remain strongly coupled, whereas the other tries to decouple from the core. This situation could arise, for example, when the odd particles occupy Nilsson levels at contrary ends of their respective shells. With increasing rotational frequency, the strongly coupled particle and the core both compete to share the total spin of the system, which may result in the gradual alignment of the strongly coupled particle. This tendency gives rise to a sequential band with $\Delta I = 1$, which has neither the strongly coupled nor the decoupled features. When the strongly coupled particle manages to remain coupled to the deformation the so-called semidecoupled bands arise.

A third situation arises in which only the neutron in the $i_{13/2}$ shell aligns, whereas the proton remains oriented along the symmetry axis. This also gives rise to semidecoupled band structures.

1.5 Pairing correlations and quasiparticles

Many nuclear properties can be described in terms of a model of independent particles constrained by the nuclear mean field and the spin-orbit force. However there exists in addition an attractive residual pairing interaction acting only on two identical particles in total angular momentum 0^+ states. It thus strongly favours the anti-alignment of the single-particle angular momenta $\mathbf{j}$ of pairs of protons (neutrons) in time-reversed states.

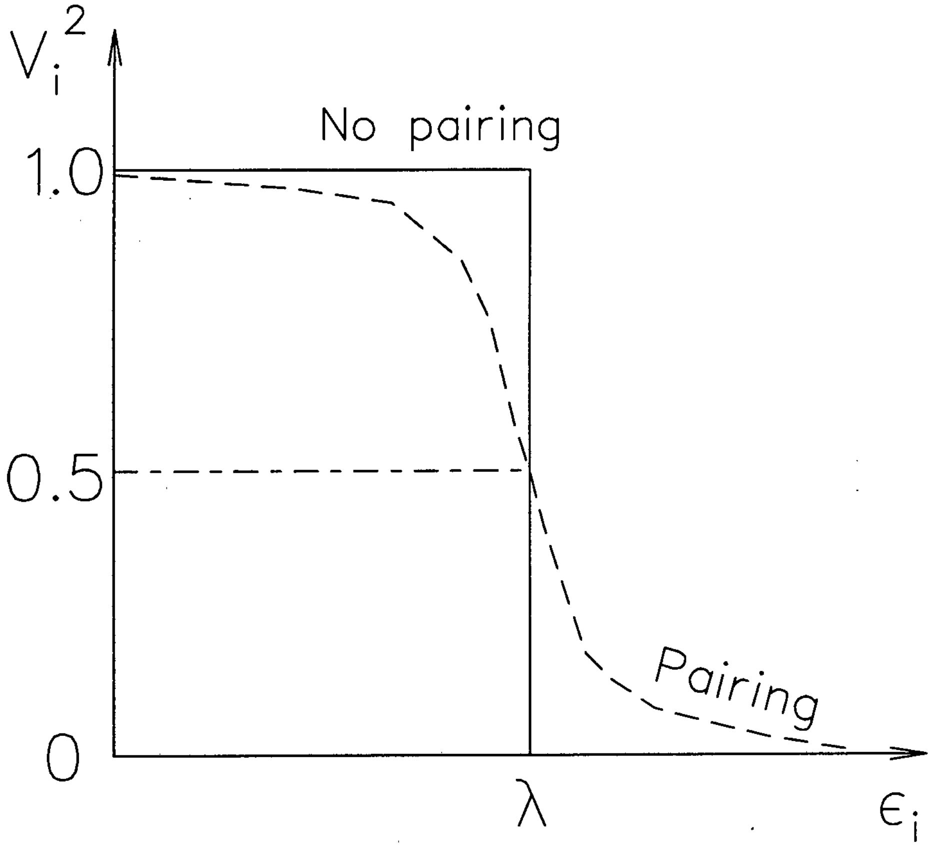

Figure 1.4: Smearing of the Fermi surface due to pairing. The solid (dashed) lines show the occupancy probability in the absence (presence) of pairing correlations. The Fermi level is denoted by λ.

The existence of the pairing force is supported, *inter alia*, by the well-known fact that the ground-state of all even-even nuclei is 0^+. A related point is that this 0^+ state is located well below other noncollective intrinsic states, the so-called pairing gap Δ. The odd-even mass difference provides further evidence for the existence of an attractive pairing force. This refers to the fact that when nucleons are added to a nucleus, the gain in binding energy is greater when an even-even nucleus is formed than when an odd-odd nucleus with the same mass number is formed. Separation energy data suggest a strength of $\sim 1 - 2$ MeV for the pairing interaction. Its matrix element may be written

$$\langle j_1 j_2 J \,|V_{pair}|\, j_3 j_4 J' \rangle = -G \left(j_1 + \frac{1}{2}\right)\left(j_3 + \frac{1}{2}\right)\delta_{j_1 j_2}\delta_{j_3 j_4}\delta_{J0}\delta_{J'0} \tag{1.50}$$

where G is the strength of the pairing force. It is obvious from the above expression that the pairing interaction is short-range, being effective only when the nucleons have the "same" spatial coordinates, or, alternatively, when they collide. An important consequence of this force, therefore, is that it scatters identical nucleons in time-reversed states $|j_1, \pm\Omega_1\rangle$ near the Fermi level into empty states $|j_2, \pm\Omega_2\rangle$ just above the Fermi surface. The scattering of particles from one j-orbit into another creates partial occupancies and effectively smears out the Fermi surface (see Figure 1.4). It should be noted here that particles deep within the Fermi sea cannot scatter on account of the Pauli principle.

The pairing correlations are taken into account by adding a two-body operator H_{pair} to the single-particle Hamiltonian. It may be written in the formalism of second quantisation:

$$H_{pair} = -G \sum_{i,j>0} a_j^\dagger a_{\bar{j}}^\dagger a_{\bar{i}} a_i \tag{1.51}$$

where a and $a^\dagger$ are the annihilation and creation operators operating on state i (and time reversed state $\bar{i}$). The sum must be restricted to states around the Fermi surface where the residual interactions are important. The annihilation and creation operators destroy a pair of nucleons in one orbital and recreate them in another. This models the scattering discussed above.

The simplest way to solve the new Hamiltonian including H_{pair} involves the introduction of BCS-type wavefunctions. These wavefunctions derive from a model known as the BCS model, devised by Bardeen, Cooper and Schrieffer [20] to describe the behaviour of Cooper electron pairs in a superconductor. In direct analogy with the ground state of a superconductor, the ground state of even-even nuclei and the core of odd-A and odd-odd

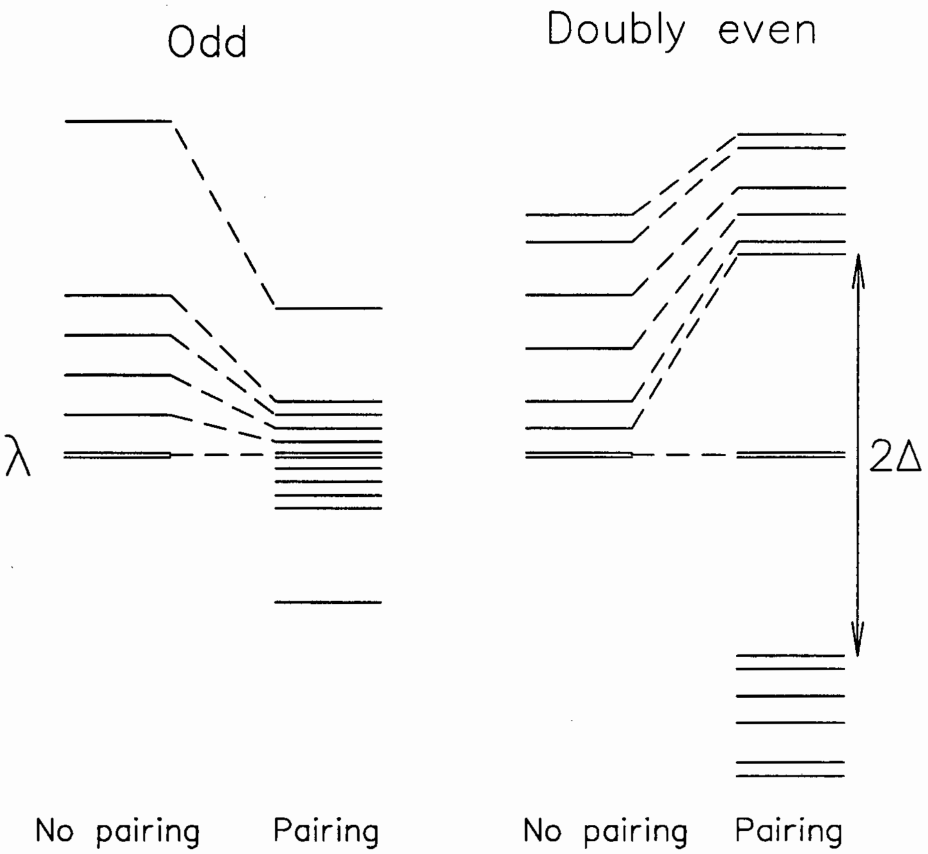

Figure 1.5: Effects of pairing in odd and even nuclei. (Left) Level compression near the ground state for odd-mass nuclei. (Right) The energy gap in even-even nuclei.

nuclei can be considered as a boson condensate. The ground-state wavefunction in the BCS model is given as

$$|BCS\rangle = \prod_{i>0} \left(u_i + v_i a_i^\dagger a_{\bar{i}}^\dagger\right) |0\rangle \tag{1.52}$$

where $|0\rangle$ is the single-particle vacuum state and u_i (v_i) are the hole (occupation) probability amplitudes for a pair state $(i, \bar{i})$. The constraint that $u_i^2 + v_i^2 = 1$ applies. The occupation of the states is determined according to the principle of minimization of energy. An implication of the BCS-type wavefunctions is the non-conservation of particle number. However the expectation value of particle number $(\hat{N})$ can be made equal to the actual number of particles by adding the term -$\lambda\hat{N}$ to the Hamiltonian where λ is a Lagrange multiplier whose physical meaning is the Fermi energy.

The BCS-type wavefunctions are further generalised with the help of a variable transformation proposed by Bogolyubov. The original wavefunctions are projected onto a new basis representing each (particle or hole) basis state as a linear superposition of both hole and particle states, or quasiparticles. Quasiparticles are *fictitous* entities introduced to simplify the calculations. The advantage of this representation lies in the transformation from a complicated sum of pairwise interacting particles to a set of non-interacting quasiparticles.

The quasiparticle operators are defined in terms of the creation and annihilation operators:

$$\alpha_k^\dagger = u_k a_k + v_k a_{\bar{k}}^\dagger \tag{1.53}$$

and

$$\alpha_{\bar{k}} = u_k a_{\bar{k}} + v_k a_k^\dagger \tag{1.54}$$

The quasiparticle vacuum is then produced by operating on the BCS ground-state wavefunction with the quasiparticle annihilation operator. The ground state of doubly even nuclei corresponds to the quasiparticle vacuum. The first excited state corresponds to a two-quasiparticle excitation, and the minimum excitation energy will be $\sim 2\Delta$ (fig. 1.5). On the other hand the ground state of odd nuclei corresponds to a one-quasiparticle excitation, and the ground-state of doubly-odd nuclei to a two-quasiparticle excitation.

In the absence of pairing, the Fermi surface λ would coincide with the filling of the last orbital. Thus $(\epsilon_k - \lambda)$ would be the excitation energy required to excite one of the nucleons in this orbit to a higher level ϵ_k. However in the presence of pairing this single-particle excitation energy $(\epsilon_k - \lambda)$ is replaced by the quasiparticle energy spectrum E_k:

$$E_k = \pm\sqrt{(\epsilon_k - \lambda)^2 + \Delta^2} \tag{1.55}$$

where typical values for the pairing gap Δ are $\gtrsim$ 1 MeV. It is defined in terms of the pairing interaction strength and the particle and hole amplitudes:

$$\Delta = G\sum_i u_i v_i. \tag{1.56}$$

Equation 1.55 above implies that there are positive and negative quasiparticle states above and below the Fermi surface, which are reflections of each other (see fig. 1.5). The decreased level density around the Fermi surface provided by the pairing gap enhances nuclear stability in the case of even nuclei. In the case of odd nuclei however, pairing leads to a bunching of levels near the Fermi surface, and a lowering of those levels further from the Fermi surface by $\sim \Delta$. Both effects are illustrated in Figure 1.5.

1.6 Cranking Shell Model (CSM)

At very high spins, when the Coriolis and centrifugal forces strongly perturb the wavefunctions of many nucleons, a better description of the single-particle energies is provided by the Cranked Shell Model. CSM is a fully microscopic description of the rotating nucleus and was first proposed by Inglis [21, 22]. The principal assumptions of CSM are that the nuclear mean field in the intrinsic frame is static and unchanged by any rotation, and that the rotation affects only the energies of the single-particle (and quasiparticle) orbits. The nucleons are thought of as independent particles moving in a deformed potential well which is rotating with the intrinsic coordinate frame at fixed rotational frequency ω.

1.6.1 The Cranking Hamiltonian

The single-particle cranking Hamiltonian was originally derived by transforming the time-dependent Schrödinger equation from the space-fixed coordinate system to an intrinsic body-fixed system in which the deformed nuclear potential is static. It is shown ([21, 23] and in many textbooks, for instance [17, 24]) that the Schrödinger equation in the rotating system can be solved in the standard way as an eigenvalue problem. Consider a system of independently moving particles (i.e. neglecting residual interactions) in an intrinsic frame rotating with frequency ω about the 1-axis. The single-particle Hamiltonian h_i in the space-fixed frame for a given state i is transformed by adding the cranking term $-\hbar\omega j_{i\cdot 1}$, giving the single-particle cranking Hamiltonian in the body-fixed frame

$$h_i^\omega = (h_i - \hbar\omega j_{i\cdot 1})\psi_i^\omega = e_i^\omega \psi_i^\omega \tag{1.57}$$

where $j_{i\cdot 1}$ is the expectation value of the single-particle angular momentum along the rotation axis, and e_i^ω is the eigenvalue of the single-particle cranking Hamiltonian for fixed rotational frequency ω. The eigenvalues are referred to as single-particle energies in the rotating basis, or single-particle routhians. They can be found by taking the expectation value of the single-particle Hamiltonian h_i as follows

$$e_i^\omega = e_i - \hbar\omega j_{i\cdot 1} \tag{1.58}$$

The total cranking Hamiltonian H^ω of the nucleus can be obtained by summing the single-particle cranking Hamiltonians h_i^ω. Thus

$$H^\omega = \sum_{i_{occ}} h_i^\omega = H - \hbar\omega I_1 \tag{1.59}$$

where I_1 is the alignment i.e. the sum of the expectation values of individual angular momenta projected onto the rotation axis :

$$I_1 = \sum_{i_{occ}} j_{i\cdot 1} \tag{1.60}$$

The eigenvalues E^ω of the total cranking Hamiltonian H^ωcan correspondingly be written in terms of independent single-particle contributions:

$$E^\omega = \sum_{i_{occ}} e_i^\omega \tag{1.61}$$

The total energy of the nucleus E^ω in the body-fixed frame is called the total routhian and can be written as

$$E^\omega = E - \hbar\omega I_1 \tag{1.62}$$

The sequence of the lowest eigenstates E^ω in the rotating (body-fixed) frame corresponds to the yrast line.

It should be noted that the operators H and I_1 do not have simultaneous eigenfunctions, implying mixing of the single-particle wavefunctions for $\omega \neq 0$. Further, the total spin I is not a good quantum number in these calculations. However an important advantage of CSM is that it provides a microscopic treatment of both single-particle and collective phenomena and hence is very useful in the interpretation of experimental data.

1.6.2 Symmetries of the cranking Hamiltonian

It is important to discover the constants of the motion in the rotating system. This is done by noting which of the system observables commute with the cranking Hamiltonian H^ω.

It is apparent that the *static* Hamiltonian H, describing the non-rotating nuclear system, is invariant with respect to space and time inversion. By implication therefore, the parity π and the projection of nuclear spin Ω onto the symmetry axis are good quantum numbers in the absence of rotation. A two-fold degeneracy in Ω follows from the time-reversal invariance. However the onset of rotation is, like deformation, a symmetry-breaking act. Time-reversal symmetry is thereby lost, and thus an additional quantum number (the signature α defined below) is required to label single-particle states.

An important class of potentials[1] is invariant with respect to rotation of 180° about the three principal axes of the system. The rotation operators are

$$R_k = e^{-i\pi j_k} \tag{1.63}$$

where k denotes the 1-, 2- or 3-axis and j_k the projection of the single-particle angular momentum onto the k-axis. It turns out that, due to the rotation of the coordinate basis, only a rotation about the 1-axis is a symmetry of the cranking Hamiltonian i.e.

$$[R_1, H^\omega] = 0 \tag{1.64}$$

The signature quantum number α is defined by allowing R_1 to operate on a state ψ_i, as follows:

$$R_1\psi_i = e^{-i\pi\alpha}\psi_i \tag{1.65}$$

Allowing R_1 to operate twice is equivalent to rotating the system through the angle 2π. For an odd-mass system the total wavefunction is antisymmetric, and $R_1^2\psi = -\psi$ therefore implies that $r_1 = \pm i$, corresponding to $\alpha = \mp 1/2$. On the other hand for an even-mass system the total wavefunction is symmetric and similarly $r_1 = \pm 1$, corresponding to $\alpha = 0$ and $\alpha = 1$.

More correctly the eigenvalue $r_1 = e^{-i\pi\alpha}$ is referred to as signature although in practice the related quantum number α is often used since it is additive. A simple relation exists between I and α :

$$I = 0,\ 2,\ 4...,\qquad r = +1,\ \alpha = 0 \tag{1.66}$$

$$I = 1,\ 3,\ 5...,\qquad r = -1,\ \alpha = 1 \tag{1.67}$$

$$I = 1/2,\ 5/2,\ 9/2...,\qquad r = -i,\ \alpha = +1/2 \tag{1.68}$$

---

[1] This arises when only even-λ components appear in the multipole expansion of the nuclear surface.

$$I = 3/2,\ 7/2,\ 11/2...,\qquad r = +i,\ \alpha = -1/2 \tag{1.69}$$

In summary, the only remaining good quantum numbers after the introduction of the cranking Hamiltonian are parity and signature (π, α). At non-zero rotational frequencies, a single-particle level degenerate in Ω (and hence a rotational band characterised by a particular K) generally splits into two levels (bands) corresponding to both signatures. While the Nilsson quantum numbers $[Nn_3\Lambda]\ \Omega$ are convenient for labelling states in a rotating nucleus, they are constants of the motion only in the asymptotic limit of zero rotational frequency and large deformation.

1.6.3 CSM diagrams

The results of CSM calculations are usually presented in diagrams which show the quasiparticle routhians as a function of the rotational frequency ω and are extremely useful for comparing experimental data with theoretical predictions. The quasiparticle routhians are calculated for fixed values of deformation parameters $(\beta_2,\ \beta_4,\ \gamma)$, particle numbers Z and N, pairing gap Δ and Fermi level energy. Each routhian is characterised by its parity and signature $(\pi, \alpha) = (\pm 1, \pm 1/2)$.

All the quantities in the CSM are calculated relative to a reference configuration called the vacuum state. The vacuum is defined for even particle number as the state in which all negative-energy quaisparticle routhians are occupied. It has total parity and signature $(\pi, \alpha) = (+1, 0)$. The calculated quasineutron routhians for $N = 92$ are shown in Figure 5.22 as a function of rotational frequency. At zero rotational frequency Nilsson quantum numbers are used to label the quasiparticle routhians, but at non-zero frequencies A, B, C... are used instead for levels with positive energy (A', B', C'... denote levels with negative energy). Upper (lower)-case letters denote quasineutron (-proton) routhians according to the following convention (shown for neutrons):

Lowest routhian	Second routhian	(π, α)
A	C	$(+, +1/2)$
B	D	$(+, -1/2)$
E	G	$(-, -1/2)$
F	H	$(-, +1/2)$

Figures 5.21 and 5.22 show that the positive- and negative- energy routhians approach and apparently deflect one another at higher frequencies. The no-crossing rule applies for levels of identical parity and signature, but such states interact and become increasingly mixed as they approach one another. For example, Figures 5.21 and 5.22 show that the positive-energy routhians labelled A and B interact with negative-energy routhians B' and A' respectively. Deflection occurs at $\hbar\omega = 0.21$ MeV. Around the point of closest approach the levels exchange their wavefunctions. The excitation of two quasiparticles is thus predicted at this frequency, known as the bandcrossing frequency. The two-quasiparticle configuration is labelled AB. The interaction strength V is taken to be equal to half the separation at the inflection point. The excitation of quasiparticles always requires that two initially empty routhians (having the same parity but opposite signature) exchange their wavefunctions with two corresponding initially occupied routhians. When the nuclear ground-state configuration corresponds to a one-quasiparticle excitation (i.e. for odd particle number) this situation cannot occur and the crossing is said to be blocked by the odd particle.

The slope of each routhian corresponds to the expectation value of its aligned angular momentum j_1 at that frequency. A gain in the alignment is therefore expected near the backbending frequency where the routhians change their slopes.

As mentioned in Section 1.6.2, the breaking of time-reversal symmetry causes the splitting between the two signatures of states having the same set of Nilsson labels. Classically the splitting is a consequence of the Coriolis force which is velocity-dependent. Quantum mechanically however it arises as a result of perturbations induced by mixing of single-particle wavefunctions. It is worth noting that the splitting of levels with low-Ω values occurs practically at zero frequency. Such highly aligned orbitals are particularly sensitive to Coriolis mixing. Conversely the splitting of high-Ω levels is delayed.

1.6.4 CSM and experimental observables

The theoretical quantities which are predicted by the CSM (e.g. the routhians, bandcrossing frequency and aligned angular momenta) are defined in the rotating basis with reference to the vacuum. On the other hand the experimentally measured quantities are valid only in the laboratory frame. Obviously any comparison with experiment can only be effected in a common coordinate frame and after determining an appropriate vacuum state. It is most convenient to transform the experimental data into the rotating basis.

Experimental quantities in the rotating basis

A rotational band sequence corresponds to a particular quasiparticle configuration and thus to a particular CSM routhian. The total signature α of each state is related to its total spin I by the equations 1.66 - 1.69. For a nucleus decaying from a state with spin $I+1$ to a state with spin $I-1$, the aligned angular momentum I_x along the rotational axis is defined as:

$$I_x = \sqrt{I(I+1) - K^2} \sim \sqrt{(I+1/2)^2 - K^2} \tag{1.70}$$

The projection K of the total spin onto the symmetry axis is set to be equal to the bandhead spin, if K is sufficiently well conserved. At the discrete intermediate spin values I the experimental rotational frequency is defined as:

$$\hbar\omega(I) = \frac{dE}{dI_x} = \frac{E(I+1) - E(I-1)}{I_x(I+1) - I_x(I-1)} \tag{1.71}$$

Thus by interpolation the sequence of discrete values $I_x(I)$ may be approximated by the continuous function $I_x(\omega)$.

The energy in the rotating frame E^ω, called the total routhian, is defined for the transition $I+1 \longrightarrow I-1$ as:

$$E^\omega = \frac{1}{2}\left[E(I+1) + E(I-1)\right] - \hbar\omega(I)I_x(I) \tag{1.72}$$

To compare the experimental energies E^ω and aligned angular momenta I_x with the CSM quantities, it is necessary to define them relative to a reference rotational band which represents the collective motion of the core.

$$i_x^\omega = I_x^\omega - I_{x\,ref}^\omega \tag{1.73}$$

$$e^\omega = E^\omega - E_{ref}^\omega \tag{1.74}$$

Usually the ground-state rotational band or the first excited band are used as the reference. However a band belonging to an adjacent even-even nucleus may also be used.

Calculation of the reference parameters

The reference functions are parametrized by the Harris expansions 1.37, 1.38 truncated to the first two terms:

$$I^{\omega}_{x\ ref} = \hbar^{-1}\omega J^{(1)}_{ref} = \hbar^{-1}(J_0\omega + J_1\omega^3) + i_x \tag{1.75}$$

where $i_x = 0$ if the ground band is used as a reference. If the first excited band is used then i_x is its initial aligned angular momentum. The Harris parameters J_0 and J_1 are obtained by plotting the quantity $\hbar I^{\omega}_{x\ ref}/\omega$ against ω^2 and fitting a linear function.

The reference energy is evaluated using the expression

$$E^{\omega}_{ref} = -\frac{1}{2}J_0\omega^2 - \frac{1}{4}J_1\omega^4 + \frac{\hbar^2}{8J_0} \tag{1.76}$$

The backbending phenomenon

The alignment process is associated with changes in the collective properties by its influence on the mean field. Firstly, the aligned particles have an oblate density distribution symmetrical about the rotational axis, thereby introducing triaxial admixtures to the prolate density distribution of the core. Secondly, broken pairs no longer contribute to pairing correlations.

The first pair-breaking corresponds to the crossing of the ground state band with an excited band having different deformation parameters. This is manifested in several ways. Firstly, a change in the moment of inertia J usually accompanies the bandcrossing, reflecting a change in the nuclear shape (Fig. 5.4). Secondly, a rapid increase in the alignment i_x is generally observed at the backbending frequency ω_c (Fig. 5.1). This is consistent with the spins of the nucleon pair becoming aligned with the rotation. Thirdly, the dynamic moment of inertia $J^{(2)}$ increases above the backbend on account of diminished pairing correlations (fig. 5.5).

The excited band is not as superfluid as the ground state band. Backbending may thus be interpreted as a phase transition from a superfluid to a normal fluid state (Mottleson-Valatin effect [25]).

1.7 Tilted Axis Cranking (TAC) calculations

It is a well-known result of classical mechanics that a rigid ellipsoid rotates uniformly only about the long or the short principal axis. This has been a basic assumption of CSM, i.e. that the rotation axis is identical with one of the principal axes of the nuclear density distribution. However, a *non-rigid* classical body may also rotate about an axis other than a principal axis. For a nucleus, such "tilted rotation" is possible due to the quantized angular momenta $\mathbf{j}_i$ of the single particles, which may be thought of as "embedded gyroscopes" [26]. If the $\mathbf{j}_i$ have non-zero projections along the symmetry axis, then the axis of uniform rotation $\mathbf{R} + \sum \mathbf{j}_i$ will be different from one of the principal axes.

For a rotating nucleus the frequency ("cranking") vector ω fixes the rotational axis. The tilted axis cranking (TAC) model includes the possibility of a rotation axis with any orientation with respect to the density distribution. The TAC Hamiltonian H^ω for a cranking state $|\omega\rangle$ is related to the space-fixed Hamiltonian H by

$$H^\omega = H - \omega \cdot \mathbf{I_{op}} \tag{1.77}$$

where $\mathbf{I}_{op}$ is the operator of the total angular momentum. In general, the directions of the cranking vector ω and the total spin vector $\mathbf{I}$ are different. Their relative orientation enters into the expression for the total routhian E^ω :

$$E^\omega = \langle\omega|\mathrm{H}^\omega|\omega\rangle = \mathrm{E}(\omega) - \omega \cdot \mathbf{I}(\omega) \tag{1.78}$$

where

$$\mathbf{I}(\omega) = \langle\omega|\mathbf{I_{op}}|\omega\rangle \equiv (\mathrm{I}_1, \mathrm{I}_2, \mathrm{I}_3) \tag{1.79}$$

In order to find selfconsistent quasiparticle states, i.e. stable configurations corresponding to minima in the TRS, it is necesary to minimize the energy with respect to the angle degrees of freedom related to the cranking direction. The selfconsistent direction $\omega_{\mathrm{s.c.}}$ corresponding to a stable and uniformly rotating quasiparticle state $|\omega\rangle$ with minimal energy E^ω is achieved when the vectors ω and $\mathbf{I}$ become *parallel*, i.e.

$$\omega \times \mathbf{I} = \mathbf{0}. \tag{1.80}$$

The selfconsistent spin orientation also defines the laboratory spin axis which is space-fixed during rotation.

The selfconsistent spin orientation $\omega \| \mathbf{I}$ may occur in three different situations [27]:

(i) the direction of $\mathbf{I}$ is along a principal axis. This is the Principal Axis Cranking (PAC) discussed above under the heading CSM. The corresponding cranking term, $-\omega I_1$, is one-dimensional.

(ii) The vector $\mathbf{I}$ lies within one of the three principal planes (12), (13) or (23). This is Tilted Axis Cranking (TAC). A tilt angle θ defines the cranking axis. For example, if $\mathbf{I}$ lies in the (13) plane, θ is measured relative to the 3- (symmetry) axis, and the TAC cranking term, $-\omega(I_1 \sin\theta + I_3 \cos\theta)$, is two-dimensional.

(iii) The vector $\mathbf{I}$ lies outside any principal plane. This is known as Chiral Axis Cranking, and the corresponding cranking term is three-dimensional.

For the TAC case the selfconsistent tilt angle θ is determined by calculating the spin vector $\mathbf{I} = \langle \omega, \theta | \mathbf{I_{op}} | \omega, \theta \rangle$ at constant frequency ω for a sequence of $\theta-$values, while checking the parallel condition (eq. 1.80) Equivalently, the tilt angle may be found for which the perpendicular component

$$I_\perp \equiv I_1 \cos\theta - I_3 \sin\theta = 0. \tag{1.81}$$

This corresponds to the minimal routhian energy (eq. 1.78) and a *stable* tilt angle θ for the quasiparticle state $|\omega\rangle$.

When the rotational axis is tilted away from the principal axis the wavefunction is no longer invariant with respect to the rotation $R_1(\pi)$. This corresponds to a breaking of the signature symmetry and thus α is thus no longer a good quantum number. Consequently,

$$R_1(\pi)|\omega\rangle \neq e^{-i\pi\alpha}|\omega\rangle. \tag{1.82}$$

However, as ω increases along a band, so does the tilt angle (due to the increased contribution to $\mathbf{I}$ from the collective rotation) until it eventually reaches 90°, where $\mathbf{I}$ has the direction of the $1-$axis. Signature symmetry is thus restored. The transition from broken to restored $R_1(\pi)$ symmetry is quite a common feature of the well-deformed axial nuclei [26]. One consequence of signature symmetry breaking is enhanced $M1$ transition rates.

TAC has been used to describe the energies and transition probabilities of various well-deformed nuclei, e.g. ^{163}Er [28], ^{164}Tm [29], ^{168}Yb [30], ^{181}Re [31] and ^{180,182}Os [32, 33, 34]. Detailed descriptions of TAC have been given in many review articles, for example [26, 27, 35] and references therein.

1.8 Potential energy surface (PES) calculations

PES type calculations minimise the potential energy of the nucleus as a function of a given nucleon configuration, rotational frequency and the nuclear deformation parameters. The evolution of nuclear shape may thus be predicted within the framework of PES calculations which employ the CSM. However the CSM carries with it the main deficiency of phenomenological shell models, namely the inability to reproduce nuclear bulk properties. It is thus unable to accurately predict the binding energy, and hence the nuclear potential energy. On the other hand the liquid drop model (LDM) [36, 37] successfully predicts bulk nuclear properties that depend smoothly on nucleon number, but cannot account for contributions to the binding energy that arise from shell effects. Strutinsky [38, 39] developed a method to reconcile these extreme microscopic and macroscopic descriptions of the nucleus.

1.8.1 Strutinsky procedure for non-rotating nuclei

The sum $E_{s.p.}$ of the shell model single-particle energies e_ν can be expressed in terms of a smoothly varying part $\tilde{E}_{s.p.}$ reflecting nuclear bulk properties, and an oscillating part dE arising from shell effects:

$$E_{s.p.} = \sum_{\nu} e_\nu = \tilde{E}_{s.p.} + dE. \tag{1.83}$$

In the Strutinsky approach, only the fluctuating part dE of the total energy $E_{s.p.}$ is calculated within the shell model while the averaged part $\tilde{E}_{s.p.}$ is replaced with the liquid drop model total energy E_{LD}. First the level density function $g(\epsilon)$ is defined as the number of levels per unit energy interval:

$$g(\epsilon) = \sum_{\nu} \delta(\epsilon - \epsilon_\nu). \tag{1.84}$$

The total single-particle energy is then calculated as

$$E_{s.p.} = \int_{-\infty}^{\lambda} \epsilon\, g(\epsilon)\; d\epsilon \tag{1.85}$$

i.e. it is the integral of the density function over all available energy states up to the Fermi level λ. If a smoothed density function $\tilde{g}(\epsilon)$ is obtained by replacing the δ-function which describes the discrete energy levels in equation 1.84 by a Gaussian, the smooth energy contribution $\widetilde{E}_{s.p.}$ is described by a similar integral. The difference between the total energy and the smoothed energy gives the oscillatory part dE in equation 1.83. The final expression for the total energy is then

$$E_{tot} = E_{LD} + dE. \tag{1.86}$$

If equation 1.86 is calculated as a function of deformation for a particular nucleus, this provides a guide as to the most energetically favourable shapes.

It should be noted that dE should be calculated independently for protons and neutrons, and the contributions added:

$$dE = dE_n + dE_p. \tag{1.87}$$

In general a more realistic treatment of pairing forces than provided by the LDM is preferred. Therefore the contribution E_{LD} may exclude the LDM pairing term, and the pairing interaction in the BCS or Bogolyubov formalism is tacked onto equation 1.86 instead:

$$E_{tot} = E_{LD} + dE + E_{pair}. \tag{1.88}$$

The above equations are only valid for a non-rotating system and thus require modification after the onset of rotation. In particular, the averaged liquid drop energy should include a term describing the rotational energy of the nucleus, and the shell model terms should be expressed in terms of the CSM. These modifications are discussed in the following section.

1.8.2 Strutinsky procedure for rotating nuclei

Rotating LDM

The rotating liquid drop model describes the nucleus as a deformed homogeneous liquid drop which rotates about a non-symmetry axis. The total energy is expressed as

$$E_{LD}(Z,N,\hat{\beta};I) = E(Z,N,\hat{\beta}) + \frac{\hbar^2 I_1^2}{2J_{rig}(Z,N,\hat{\beta})} \tag{1.89}$$

where $\hat{\beta} = (\beta_2, \beta_4, \gamma)$, and $E(Z,N,\hat{\beta})$ is the LDM total energy at zero rotational frequency for the particular deformation. The rotational energy of the nucleus is represented by the second term where I_1 is the projection of the nuclear spin along the rotation axis. The moment of inertia J_{rig} is assumed to be equal to the corresponding rigid body value. Since this is invariant the left-hand side of equation 1.89 is also a function of rotational frequency and may be abbreviated as E^{ω}_{LD}.

Shell correction for $\omega \neq 0$

For rotating nuclei the wavefunctions are projected onto the body-fixed basis, and the single-particle energies e_ν are replaced by the single-particle routhians e^{ω}_{ν} defined at every value of ω, as already expressed in equation 1.58. The *total* single-particle routhian is thus given by

$$E^{\omega}_{s.p.} = \sum_{\nu} e^{\omega}_{\nu} \tag{1.90}$$

The averaged total routhian $\widetilde{E^{\omega}_{s.p.}}$ is then obtained by applying the Strutinsky smearing procedure to both the level and angular momentum densities, as follows. First the actual level density function is defined in analogy to equation 1.84:

$$g_1(e^{\omega}) = \sum_{\nu} \delta\,(e^{\omega} - e^{\omega}_{\nu})\,. \tag{1.91}$$

The level density function is defined as

$$g_2(e^{\omega}) = \sum_{\nu} j_1\,\delta\,(e^{\omega} - e^{\omega}_{\nu})\,. \tag{1.92}$$

Two corresponding smooth densities $\widetilde{g_1}(e^{\omega})$ and $\widetilde{g_2}(e^{\omega})$ may then be obtained as described in Section 1.8.1, which are then used to express the smoothed functions

$$\tilde{I}_1 = \int_{-\infty}^{\lambda} \widetilde{g_2}(e^{\omega})\,de \tag{1.93}$$

$$\widetilde{E^{\omega}_{s.p.}} = \int_{-\infty}^{\lambda} \widetilde{g_1}(e^{\omega})\,e^{\omega}\,de + (\hbar\omega)\,\langle I_1\rangle \tag{1.94}$$

Finally the shell correction $dE^{\omega}_{s.p.}$ is expressed as the difference

$$dE^{\omega}_{s.p.} = E^{\omega}_{s.p.} - \widetilde{E^{\omega}_{s.p.}} \tag{1.95}$$

As above the shell energy corrections for the protons and neutrons should be evaluated independently.

The total energy E^{ω}_{tot} of a rotating nucleus may thus be calculated at every value of ω, for a particular configuration, and spin projection on the rotation axis:

$$E^{\omega}_{tot} = E^{\omega}_{LD} + dE^{\omega}_{s.p.} + E^{\omega}_{pair} \tag{1.96}$$

The results of such calculations are presented as total energy surfaces called Total Routhian Surfaces (TRS), which show the total energy contours on the $\beta_2 - \gamma$ plane. Different contour plots are produced for different rotational frequencies, allowing the movement of minima in the energy surface to be studied as the rotational frequency changes.

Pairing correlations are known to decrease at higher rotational frequencies. Since the exact dependence is not known, different approximations are used in the literature.

1.8.3 Total Routhian Surface (TRS) calculations

In this work the TRS calculations performed by R. Wyss [40] were used. The total routhian $E^{\omega}_{tot}(Z, N, \hat{\beta})$ of a nucleus (Z, N) at a frequency ω and a deformation $\hat{\beta}$ is obtained within the Woods-Saxon Bogolyubov-Strutinsky approach. It is expressed (see eq. 1.96 above) as the sum of the macroscopic liquid-drop energy, the shell-correction energy and the pairing energy. For the liquid-drop term the standard liquid-drop mass formula [41] and rigid-body moment of inertia with $R = 1.23A^{1/3}$ fm are used.

The nuclear mean field is parametrized by a Woods-Saxon single-particle potential and a BCS pair field. The Woods-Saxon deformed shell-model potential [42] is used with the parameters of ref. [43], and includes a central potential, a spin-orbit term and the Coulomb potential. The nuclear shape is parametrized in terms of quadrupole, hexadecapole and triaxial degrees of freedom, $\hat{\beta}$. These, together with the BCS field parameters Δ_p and Δ_n for protons and neutrons, are treated as variational parmeters.

Cranking implies that the deformed nucleus rotates about a fixed axis with a given frequency ω. The routhian $\hat{H}^{\omega}$ is thus minimized at a fixed deformation and fixed ω by solving the cranked Hartree-Fock-Bogolyubov equations. The solutions provide the angular momentum and energy relative to the non-rotating state with $\omega = 0$. The deformation lattice is transformed into Cartesian coordinates, $X = \beta_2 \cos(\gamma + 30°)$ and $Y = \beta_2 \sin(\gamma + 30°)$, and covers 8×11 points in the (β_2, γ) plane, starting at $(X, Y) = (0.10, 0.00)$ with a step length of 0.05. Calculations were performed at three different β_4 values with a step of 0.04. For a fixed configuration the total routhian was first minimized at each (β_2, γ) grid point with respect to β_4, after which the equilibrium deformation was obtained by minimizing over the entire grid. The calculations were performed at 17 different frequencies starting at $\hbar\omega = 0.00$ MeV, with a step length of 0.05 MeV.

The pairing gap Δ_0 is calculated self-consistently at each grid point for $\omega = 0$ and is then allowed to decrease with ω in the following way

$$\Delta_\omega = \Delta_0 \left(1 - \frac{1}{2}\left(\omega/\omega_c\right)^2\right) \qquad (\omega < \omega_c) \tag{1.97}$$

and

$$\Delta_\omega = \Delta_0 \frac{1}{2}\left(\omega/\omega_c\right)^2 \qquad (\omega > \omega_c). \tag{1.98}$$

The critical frequency ω_c, defined as the frequency at which the pair gap is reduced to half its original value, was chosen to be ~ 0.7 MeV/$\hbar$ [40]. The chemical potentials λ_n and λ_p were adjusted separately at each frequency in order to give the correct expectation value of the number of nucleons. Examples of TR surfaces for ^{164,165}Ta are presented in Chapter 5.

1.9 Signature inversion

As already mentioned (Section 1.6.2), a rotational band built on a given intrinsic configuration generally decouples into two $\Delta I = 2$ rotational sequences with different signature (α) values, known as signature partner bands. Such bands differ in spin by $1\hbar$. In general the bands are not energetically equivalent - the level energies (and the routhians) of one band are expected to be energetically lowered with respect to those of the other. Accordingly, each band is said to be either "favoured" or "unfavoured". The energy difference $\Delta e'(\omega)$ is called signature splitting when measured in the rotating frame:

$$\Delta e'(\omega) = e'_{\alpha_u}(\omega) - e'_{\alpha_f}(\omega) \tag{1.99}$$

The energy splitting between the two signatures can be a sensitive indicator of the quasiparticles involved.

The origin of the splitting is essentially due to the Coriolis mixing of the $\Omega = 1/2$ state into the wavefunction. The contribution to the rotational energies from the Coriolis interaction alternates in sign with spin. For high-j one-quasiparticle configurations the favoured signature is given by the rule [44]

$$\alpha_f = 1/2(-1)^{j-1/2} \tag{1.100}$$

However, in some doubly-odd nuclei with a two-quasiparticle configuration the "favoured" band[2] is found to be unfavoured. This phenomenon is called signature inversion or anomalous signature splitting.

Well-known examples of anomalous splitting occur in doubly-odd nuclei with the $\pi h_{11/2} \otimes \nu h_{11/2}$ configuration in the $A \sim 130$ region, and the $\pi h_{11/2} \otimes \nu i_{13/2}$ configuration in the $A \sim 160$ region with $N \sim 90$ (see Section 5.4). In these nuclei the sign of the splitting is typically negative in the low-spin regime but reverts to positive values above the inversion frequency ω_i.

The underlying mechanism for this effect has been the arena for considerable debate for at least a decade, and several explanations have been proposed. A more detailed discussion is deferred until Section 5.4.2.

---

[2] $\alpha_f = 1/2(-1)^{j_p - 1/2} + 1/2(-1)^{j_n - 1/2}$

Chapter 2

Experimental techniques

The two nuclides investigated in this work are exotic and evanescent, differing by -16 and -17 neutrons from the most naturally abundant stable isotope of tantalum, ^{181}Ta. To investigate the behaviour of such neutron deficient nuclei - and high angular momentum structures in particular - requires special techniques for their continual production and the monitoring of their $\gamma-$decay. This may be realised by performing a heavy-ion fusion-evaporation (HI,xn) reaction in conjunction with an array of escape-suppressed high-purity germanium (HPGe) detectors. The present chapter presents the standard experimental techniques for populating high spin states, and reviews recent developments in the hardware used to measure the associated $\gamma-$radiation. The NAC facility and the AFRODITE array are also discussed.

2.1 Heavy-ion fusion-evaporation reactions

Heavy-ion fusion-evaporation reactions currently provide the best possible balance between large angular momentum transfer and appreciable production yields. If the incident beam energy exceeds the repulsive Coulomb barrier between beam and target nuclei, fusion will ensue, creating a hot compound system in a state of high spin (up to the fission limit). After equilibration, de-excitation occurs at first by neutron evaporation, the emission of charged particles being less likely on account of the Coulomb barrier[1]. The

---

[1] Charged particle emission from very neutron deficient nuclei may be favoured by Q-value and angular momentum considerations.

fusion-evaporation mechanism is thus able to produce highly neutron deficient residues, strongly peaked in a few reaction channels at a given bombarding energy.

The de-excitation process is depicted in Figure 2.1. A small fraction ($\sim 10^{-4}$) of the γ−rays are emitted in competition with neutrons at high excitation energies [45]. Since each neutron carries away $\sim$ 8 MeV excitation energy but only $1 - 2\hbar$ angular momentum, γ−ray emission is responsible for carrying away most of the initial angular momentum, and this occurs only after neutron emission has become energetically unlikely. The principal region of γ−ray emission is consequently between the yrast line and one neutron binding energy above it. In this region the nucleus de-excites mainly by stretched yrast-like[2] transitions in competition with statistical dipole transitions; the high level density results in a myriad different decay pathways, and so the γ−ray spectrum is a quasi-continuum of weak transitions. However, there are a number of preferred decay pathways relating to energetically favourable arrangements of protons and neutrons. These are often associated with specific nuclear shapes. If a sufficient fraction of the decay flows down a particular quantized pathway, the associated structure becomes visible. This typically occurs at lower excitation energies near the yrast line, where the diminished level density means that there are fewer available decay pathways. The flow of total γ−ray intensity in this region is thus funnelled through fewer, stronger channels and discrete γ-transitions may be resolved. In a sense the yrast line acts as a watershed for a "rain" of states populated in the deformed evaporation residue. No states are available below the yrast line. Typically the entire de-excitation process occurs within about 10^{-9} seconds.

A further advantage of HI reactions is the large forward linear momentum imparted to the reaction products, allowing them to be separated from the bulk target for further analysis or extracted as secondary projectiles. This is one important technique for producing radioactive ion beams (RIB). These beams, already neutron deficient, may be used to make isotopes even further from stability than is currently possible using stable beam-target combinations. With RIB reactions it is even possible to study nuclear matter beyond the proton drip line, where the Coulomb force becomes of comparable strength to the nuclear mean field.

---

[2] So-called because they are roughly parallel to the yrast line. Near-yrast states may correspond to a different intrinsic configuration than yrast states.

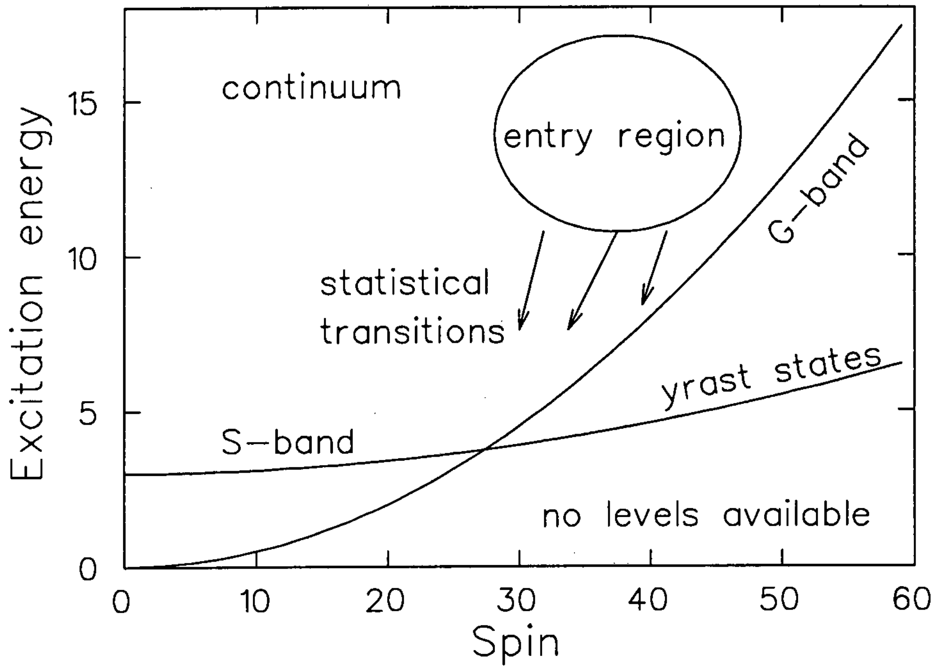

Figure 2.1: Schematic illustration of nuclear de-excitation following a (HI, xn) reaction, showing the crossing of the ground-state band (G-band) and the first excited band (S-band). Yrast states have the lowest energy at a given spin. The energy (MeV) spin ($\hbar$) values are only approximate.

These features of the HI reaction make it an excellent technique for investigating the evolution of nuclear structure with angular momentum.

2.2 Multi-detector gamma-ray spectrometers

The de-excitation burst of coincident $\gamma-$rays associated with a heavy-ion fusion-evaporation reaction residue contains crucial information on nuclear structure. A *single* detector used on its own would allow one to list the observed $\gamma-$ray energies from all manner of reaction products, but it would be impossible to infer anything at all about nuclear states from the data. However, a minimum of *two* detectors placed near to the target allow one to perform a *coincidence* experiment. Coincident $\gamma-$rays detected simultaneously in both detectors are associated with a particular decay pathway in one of the reaction products, and a level scheme may be constructed on the basis of the observed coincidence (and anti-coincidence) relationships. Clearly the chance of intercepting the maximum possible number of $\gamma-$rays from a given nuclear de-excitation improves as more detectors are used. This led to the development of large escape suppressed spectrometer arrays (ESSA's). Many reviews of the development of ESSA's have been published, e.g. [46, 47, 48, 49, 50, 51], and a brief resumé is given below.

ESSA's were first used in conjunction with modern heavy ion accelerators in late 1982. Prior to this high-spin $\gamma-$ray spectroscopy had employed a few unsuppressed Ge detectors in coincidence with multiplicity filters or sum spectrometers. While early experiments made important discoveries (e.g. backbending was discovered using just two unsuppressed Ge(Li) detectors [52]), the poor peak to total ratio ($P/T \sim 0.20$ at 1 MeV[51]) resulting from the Compton continuum remained a serious limitation. P/T could however be improved to ~ 0.65 [47] by surrounding the detector with an escape suppression shield (initially NaI(Tl), subsequently BGO) and rejecting events in coincidence with both detector and shield. This technique is referred to as *Compton* (or *BGO*, or simply *escape*) *suppression.*

An important design criterion for an ESSA is that of high granularity. An array consisting of a large number N of detectors, each subtending a small solid angle, will maximize both the isolated hit probability and the total solid angle subtended by all detectors. The optimum fold will be enhanced, since the probability of detecting an event of fold f varies approximately as N^f. Doppler broadening will be minimized, particularly important for detectors close to 90° to the beam axis, where the effect is most severe. By the mid 1980's about a dozen first generation ESSA's[3] with ~ 20 escape-suppressed spectrometers and total photopeak efficiencies ϵ_T of $0.5 - 1.0\%$ [47] had been constructed. Several important discoveries were made with these first generation arrays. For example, superdeformation was first observed [59] in ^{152}Dy using TESSA 3 at Daresbury (U.K.) . Superdeformed structures carry only around $1 - 2\%$ of the individual nucleus production cross-section and occur when shell effects help stabilise a prolate (2:1 axis ratio) shape.

The first generation arrays were based on large single-crystal Ge detectors. One disadvantage associated with the large half opening angle of these detectors was the sizeable Doppler broadening. The problem was addressed by developing the *Clover* detector, as a collaboration between CRN-Strasbourg and the company Eurysis Mesures. Each Clover comprises four n-type coaxial HPGe crystals housed in a common cryostat, arranged in the configuration of a four-leafed clover. Some of the advantages of Clovers over large single-crystal Ge detectors are discussed in Section 2.4.1. Clovers were included in the so-called second generation arrays such as EUROGAM II, which finally had a total of 126 detector elements covering a total solid angle of 40%.

The first and second generation arrays were developed within the framework of the EUROBALL III collaboration between six European countries. EUROBALL III, the third generation, was based on EUROGAM II and is currently located at the Centre de Recherches Nucléaires, Strasbourg. In addition to 30 large volume Ge detectors, it includes 26 Clovers and 15 Cluster detectors. With a total photopeak efficiency of 12.5% [46] and an observational limit of $\sim 5 \times 10^{-5}$ of the total production cross section, EUROBALL III is about 100 times more sensitive than the first generation arrays. Another third generation array of note is GAMMASPHERE, located at Argonne National Laboratory at the time of writing. In its present configuration GAMMASPHERE consists of 110 large volume escape suppressed germaniums used in conjunction with a suite of powerful auxiliary detectors.

The development of third generation arrays has made it possible to investigate a

---

[3] For example: TESSA 3 (UK)[53], Chateau de Cristal (unsuppressed) (France)[54], Osiris (Germany)[55], Nordball (Denmark)[56], Hera (Berleley, USA)[57], Spin spectrometer (unsuppressed) (Oak Ridge, USA) , Multispectrometer (Argonne, USA),8π Spectrometer (Canada) [58]

broader range of challenging nuclear phenomena than ever before, and several nuclear models could be confirmed for the first time. To provide a flavour of the physics that has been addressed, for example, experimental confirmation has been provided for the "Shears Mechanism". The Shears Mechanism was proposed explain the occurrence of regular "rotation like" $\Delta I = 1$ sequences in near-spherical nuclei, e.g. in lead nuclei ^{193}Pb [60] and ^{198,199}Pb [61]. The angular momentum generated by such "magnetic rotation" is associated with the anisotropic arrangement of nucleonic currents (due to valence protons and neutron holes, respectively) which break the rotational symmetry of the nucleus. In order to generate states of high spin, it was proposed that the spin vectors $\mathbf{j_p}$ and $\mathbf{j_n}$, associated with the protons and the neutron holes, align with the total angular momentum vector $\mathbf{J} = \mathbf{j_p} + \mathbf{j_n}$ (this may be visualised as the closing of a pair of shears). Because the magnetic dipole moment μ is aligned with $\mathbf{j_p}$, the component of the magnetic dipole moment $\mu_\perp$ perpendicular to $\mathbf{J}$ is expected to diminish with increasing spin. The reduced transition probabilities B(M1), being proportional to $\mu_\perp$, should thus decrease with increasing spin as the two vectors close. The expected decrease in B(M1) values was confirmed by using GAMMASPHERE to measure lifetimes of states in the M1 bands, providing the first direct evidence for magnetic rotation. As a further example, detailed lifetime measurements performed with GAMMASPHERE provided crucial confirmation of the "smooth band termination" model in nuclei near mass $A = 110$. This is observed when a rotational band loses its collectivity and is said to terminate, as the nuclear shape traces a path on the $\beta - \gamma$ plane from collective prolate ($\gamma = 0°$) to noncollective oblate ($\gamma = +60°$). Lifetime measurements showed for the first time convincing evidence for diminished quadrupole transition moments, or collectivity, with increasing spin in ^{109}Sb [62] and ^{108}Sn [63], confirming the model.

It is likely that recent developments in detector design will boost the performance of *fourth generation* arrays to an unprecedented level. The GRETA[4] project, for example, is expected to have a resolving power $\sim 10^3$ times that of GAMMASPHERE, and is expected to be able to sustain a count rate of ~ 10 times higher than GAMMASPHERE. The GRETA array will consist of a spherical shell of about 100 coaxial Ge detectors covering a solid angle of almost (allowing for entry and exit of the beam) 4π. Each detector will have

---

[4] Gamma Ray Energy Tracking Array

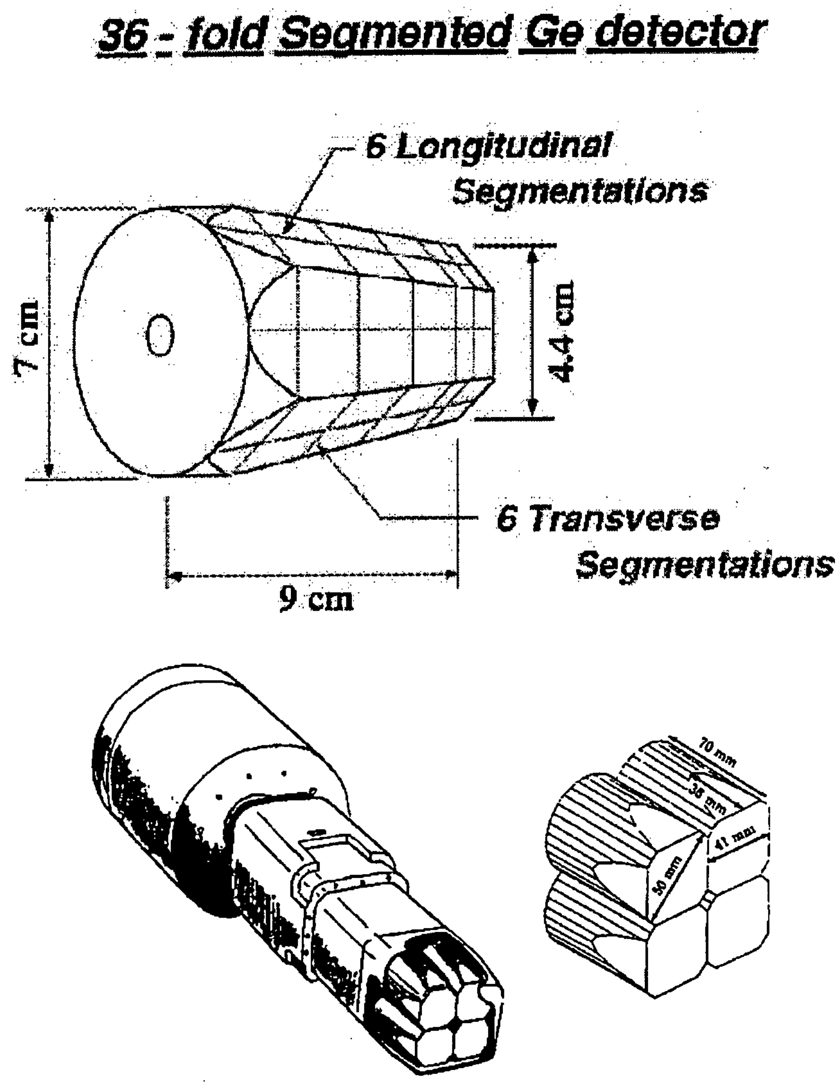

Figure 2.2: Above: the 36-fold segmented GRETA prototype detector with its tapered hexagonal shape [64]. Below: the 4-fold segmented Clover detector, showing the arrangement of the individual elements.

about 40 transverse and longitudinal segments similar to the prototype shown in Figure 2.2.

An important reason for the segmentation is to enable the tracking of $\gamma-$rays which undergo multiple scattering in the Ge crystal. The aim of $\gamma-$ray tracking is to identify and separate individual $\gamma-$rays, and to measure the energy and exact location of each interaction. One advantage of this is that the measured energies may then be summed together, improving the P/T ratio. Further advantages are the improvement in the polarisation sensitivity and reduction in the Doppler broadening. Although the size of a segment is of the order of centimetres, position sensitivity of the order of 1 mm can be achieved by analysing, in addition to the primary signal which arises as a consequence of an interaction, the charges induced in neighbouring detector elements. The time sequence of the interactions can be reconstructed by using tracking algorithms. The tracking algorithms and performance of the prototype detectors have been described in several review articles, e.g. [64, 65, 66, 67].

Performance features for some of the above-mentioned arrays are listed in Table 2.1.

2.2.1 Auxiliary detectors

Several auxiliary detector devices have been developed for use in conjunction with ESSA's. When operated in coincidence with $\gamma-$ray detectors these devices enhance the overall array sensitivity. They generally aim at improving reaction channel selectivity or allow lifetime measurements. For example the recoil fragments may be sent through a recoil mass spectrometer (RMS) which can separate ions of different masses with high selectivity. The reaction products are dispersed by their mass to charge ratios (A/q) at the focal plane. It is then relatively easy to select the products with a single mass A to eliminate contaminations from other residuals with different masses, enhancing the quality of the experimental data. Unfortunately the RMS is a sophisticated, costly device and none is available at NAC.

Another method to achieve reaction channel selectivity is by detecting evaporated charged particles. This is being implemented for the AFRODITE array by employing a mosaic of solar cells, mounted inside the target chamber as shown in Figure 2.7, for the detection of heavy ions and fission fragments. The particular detecting 'tile' of the mosaic

Table 2.1: Performance features of arrays for $E_\gamma = 1.33$ MeV, $M_{gamma} = 30$, $v/c = 0.025$ and $SE_\gamma = 70$ keV. The optimal fold is denoted by f_{opt}. Except for AFRODITE the data are from [49].

Array	N	ΔE_γ (keV)	P/T	ϵ_{T}	R	f_{opt}	α_0
NORDBALL	20	8.7	0.47	1.2%	3.8	3	2×10^{-3}
AFRODITE	15[a]		0.57	1.5%	3		
GASP (w. BGO ball)	40	6.9	0.61	2.8%	6.2	4	2×10^{-4}
EUROGAM I	45	8.7	0.56	4.6%	4.5	4	4×10^{-4}
EUROGAM II	54[b]	6.4	0.53	6.9%	5.8	5	1×10^{-4}
EUROBALL III	69[c]	6.0	0.55	8.8%	6.4	5	5×10^{-5}
GAMMASPHERE	110[d]	6.3	0.56	9.2%	6.2	5	5×10^{-5}

[a] 8 Clovers and 7 LEPS.

[b] 30 escape-suppressed HP-Ge detectors and 24 Clovers.

[c] 15 Cluster detectors, 24 Clovers and 30 escape-suppressed HP-Ge detectors.

[d] 80 segmented and 30 unsegmented escape-suppressed HP-Ge detectors.

gives directional information, which may be used to improve the Doppler shift corrections to the γ−ray energies detected in coincidence with the heavy ion. The solar cell mosaic was undergoing testing at the time of writing.

One type of auxiliary detector used extensively in this work for detecting characteristic K x−rays which accompany electron conversion is the Low Energy Photon Spectrometer (LEPS). LEPS are planar, four-fold segmented Ge detectors with enhanced sensitivity in the x−ray region. Their use is discussed in greater detail in Section 2.4.1.

Finally, lifetimes of the order of femtoseconds may be measured via the recoil distance method [68], using a plunger to stop the recoils. Various Doppler-shift methods are also used to determine the lifetimes of states in the hot recoiling residues [69, 70]. In this work however the recoil shadow anisotropy method (RSAM) [11], which requires no additional device, has been used to search for isomers in ^{164,165}Ta (Section 4.5).

2.3 The NAC facility

A floor-plan of the NAC facility is shown in Figure 2.3. The features relevant to this work are the electron cyclotron resonance (ECR) ion source (area Q), the two solid pole injector cyclotrons SPC1 and SPC2, the large $K = 200$ MeV separated sector cyclotron (SSC). The AFRODITE spectrometer array is located on beamline F.

A wide range of heavy ion beams is available at the NAC, including those listed in Table 2.2. It may be noted here that lithium and sodium beams are unavailable.

To produce a metal ion beam from non-volatile compounds, the metal vapour is extracted from a microfurnace and then stripped of several orbital electrons in the ECR ion source. The plasma is accelerated from the source using an electrostatic lens, and ions of the correct charge state are selected for injection into the $K = 10$ MeV SPC2[5]. The beam is extracted from the injector cyclotron and then further accelerated in the SSC until the beam particles attain the required kinetic energy. From the SSC the ions are guided to the experimental vault via the high-energy beamline using quadrupole magnets for focusing and dipoles for bending the beam. The SSC delivers a pulsed beam with repetition rate from 8 to 26 MHz.

---

[5] SPC1 is used to accelerate light-ion beams, while SPC2 is used to accelerate mainly heavy ions, polarized protons and deuterons.

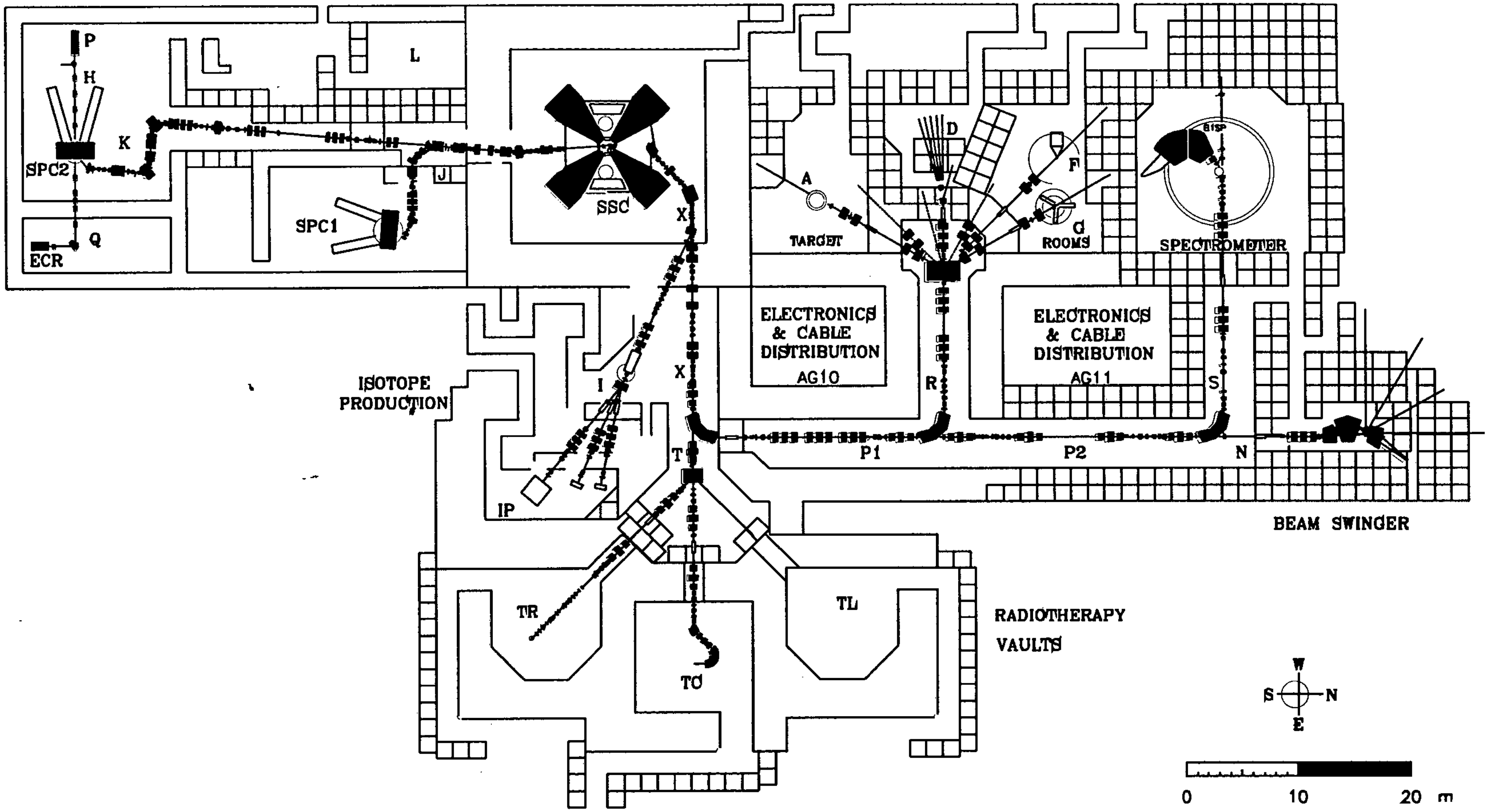

Figure 2.3: Floor-plan of the NAC cyclotron facility.

At NAC dedicated beam time for physics experiments is confined to scheduled weekends. Typically beam is available from 18h00 on Friday afternoon through to 06h00 Monday morning, i.e. for a maximum of 60 hours per weekend. In practice however the data acquisition period is less than this. Down-time is most commonly due to ion source depletion, or having to access the vault to replenish the liquid nitrogen supply.

Table 2.2: Heavy ion beams produced at NAC.

Ion	Charge state	Beam energy (MeV)
$^{1}_{1}\mathrm{H}$	1+	66, 200
$^{4}_{2}\mathrm{He}$	2+	160, 200
$^{12}_{6}\mathrm{C}$	3+	58, 150
	4+	100, 150, 180, 200, 230
	5+	300, 320, 380, 400
$^{14}_{7}\mathrm{N}$	4+	140
$^{16}_{8}\mathrm{O}$	5+	200, 250, 300
	6+	400
$^{18}_{8}\mathrm{O}$	4+	85, 90, 110
$^{20}_{10}\mathrm{Ne}$	4+	110, 115, 120, 125
$^{22}_{10}\mathrm{Ne}$	4+	125
$^{24}_{12}\mathrm{Mg}^{a}$	5+	
$^{27}_{13}\mathrm{Al}$	7+	150, 155
$^{28}_{14}\mathrm{Si}$	5+	141
$^{32}_{16}\mathrm{S}^{a}$	11+	
$^{35}_{17}\mathrm{Cl}$	8+	205
	9+	250
$^{40}_{18}\mathrm{Ar}$	8+	280, 380
$^{40}_{20}\mathrm{Ca}^{a}$	8+	
$^{56}_{26}\mathrm{Fe}^{a}$	11+	
$^{64}_{30}\mathrm{Zn}$	10+	165, 260
$^{79}_{35}\mathrm{Br}^{a}$	14+	
$^{84}_{36}\mathrm{Kr}$	13+	420
$^{84}_{36}\mathrm{Kr}$	14+	462
	15+	420, 450, 530

Ion	Charge state	Beam energy (MeV)
$^{121}_{51}Sb$	22+	700
$^{129}_{54}Xe$	17+	460
	22+	790
$^{131}_{54}Xe$	16+	350
$^{136}_{54}Xe$	22+	747, 750
$^{184}_{74}W$[a]	17+	
$^{202}_{80}Hg$[a]	21+	

[a] Not sent through the SSC.

2.4 The AFRODITE spectrometer array

Early plans for the implementation of the AFRODITE[6] [71, 72] γ-ray spectrometer elicited murmurs of scepticism. AFRODITE was to be based around an array of BGO-suppressed Clovers mounted on a support frame capable of holding up to 16 germanium detectors, and was intended to exploit the diverse heavy ion beams available at NAC in nuclear structure experiments. While it would be impossible for such a medium-sized array to match the sensitivity of contemporary third and fourth generation arrays, it was decided to construct a medium-cost device with enhanced sensitivity and energy resolution in the low energy regime ($\sim$ 100 keV). This was to be achieved by the inclusion of up to 8 LEPS in AFRODITE. Not only are LEPS less costly than the BGO-suppressed Clovers, they are ideal for detecting characteristic x−rays and this could afford the possibility of good Z-selectivity, particularly for heavy nuclei where conversion becomes important. M1 cascade transitions between pairs of signature partner bands, which are typically of low energy ($E_\gamma \leq 300$ keV), would also be accessible to detection by LEPS.

AFRODITE in its present configuration, as shown in Figure 2.4, was commissioned at NAC in January 1998. The photograph presents AFRODITE with its full complement of 8 BGO-suppressed Clovers and 7 LEPS. The results of measuring the total photopeak efficiencies of the Clovers and LEPS, obtained by placing ^{133}Ba and ^{152}Eu sources in the target position, are shown in Figure 2.6. It may be seen that, in terms of efficiency at 1332 keV, AFRODITE ($\epsilon_T \simeq 1.5\%$) matches first generation arrays such as TESSA 3 and NORDBALL. These arrays had total photopeak efficiencies of between 0.5 and 1.5%. It also shows that the combined total photopeak efficiency at 100 keV is about 11%.

2.4.1 Detectors

The Clovers[7] [46, 47, 49, 74, 75], comprising four n-type coaxial HPGe crystals housed in a common cryostat and BGO suppressor, are identical in design to those first used in the EUROGAM II array. Figure 2.2 illustrates this arrangement of the four Clover elements. Clover performance has been reported in detail elsewhere, e.g. [46, 75, 76] but some

---

[6] AFRican Omnipurpose Detector for Innovative Techniques and Experiments.

[7] Developed for the EUROBALL project in collaboration between CRN-Strasbourg and the company Eurysis Mesures [73].

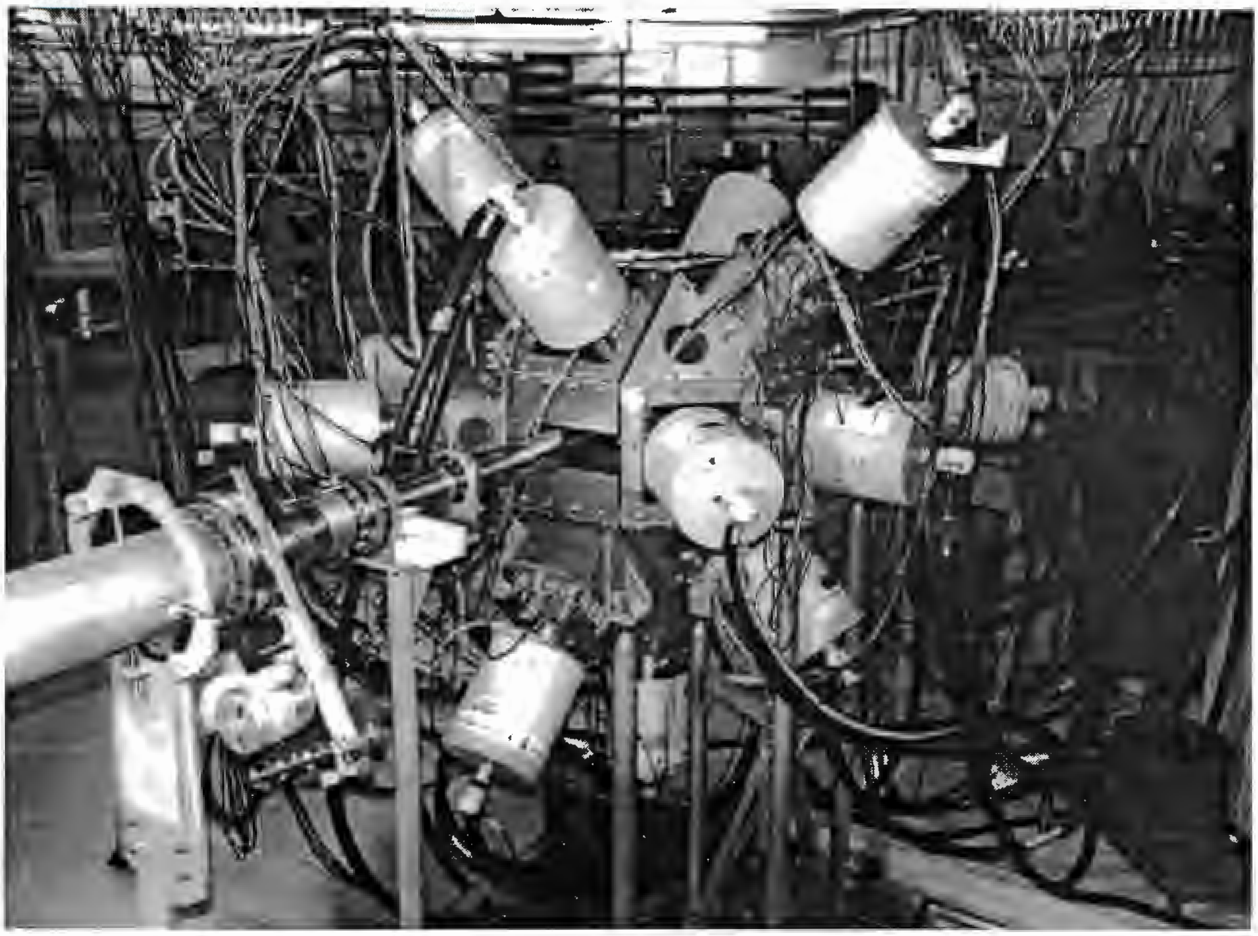

Figure 2.4: The AFRODITE array.

important features are discussed below.

Each crystal element has its own preamplifier, which allows energies deposited in more than one element of a detector due to Compton scattering, to be added. This *add-back* procedure has been shown to significantly enhance Clover photopeak efficiency, particularly in the high energy regime ($E_\gamma \geq 1000$ keV) as shown in Figure 2.6. An energy-dependent add-back factor of up to 1.5 has been reported [47, 76]. With scattered events included, the relative efficiency[8] for the Clover detectors is on average 140%, comparing favourably with a relative efficiency of ~80% for the large single-crystal Ge detectors [47] present in both EUROBALL III and GAMMASPHERE. The cost of this improvement however is a degradation of the energy resolution by about 0.3 keV at 1408 keV, compared with singles mode (i.e. complete energy deposition in a single crystal element)[76]. The energy dependence of FWHM for a typical single element (for Clovers and LEPS) of AFRODITE is shown in Figure 2.6, for in-beam and source data [72]. The FWHM of 2.5 keV for the ^{152}Eu 1408 keV line is comparable with the value 2.35 keV reported in [76] for singles mode.

Each BGO Compton suppression shield consists of 8 optically separated segments, each of which has in turn 2 PM tubes. All 16 PM tubes for a given shield are then connected in series. The BGO signal from a Compton-scattered event vetoes the associated Clover. The effects of suppression on the spectral peak to total ratio (P/T) were investigated for AFRODITE by placing a ^{137}Cs source (with a single photopeak at 662 keV) at the target position and acquiring singles data with and without the veto signals [72]. P/T was found to be 0.38 and 0.57 for suppressed and unsuppressed modes, respectively, for an energy threshold of 100 keV. Suppressed and unsuppressed spectra for the sum of all Clovers with full add-back are shown in the top panel of Figure 2.5. The lower panel shows the suppression factor spectrum, obtained by dividing the unsuppressed by the suppressed spectrum. It shows that a maximum suppression factor of ~ 3 at about 350 keV is currently achieved with AFRODITE.

Composite detectors have several further advantages over single crystals. The intrinsic Clover geometry makes it suitable for use in add-back mode as a Compton polarimeter

---

[8] Defined for 1332 keV radiation with respect to a 3 inch x 3 inch NaI(Tl) crystal located at the same distance (at 25 cm) from the source.

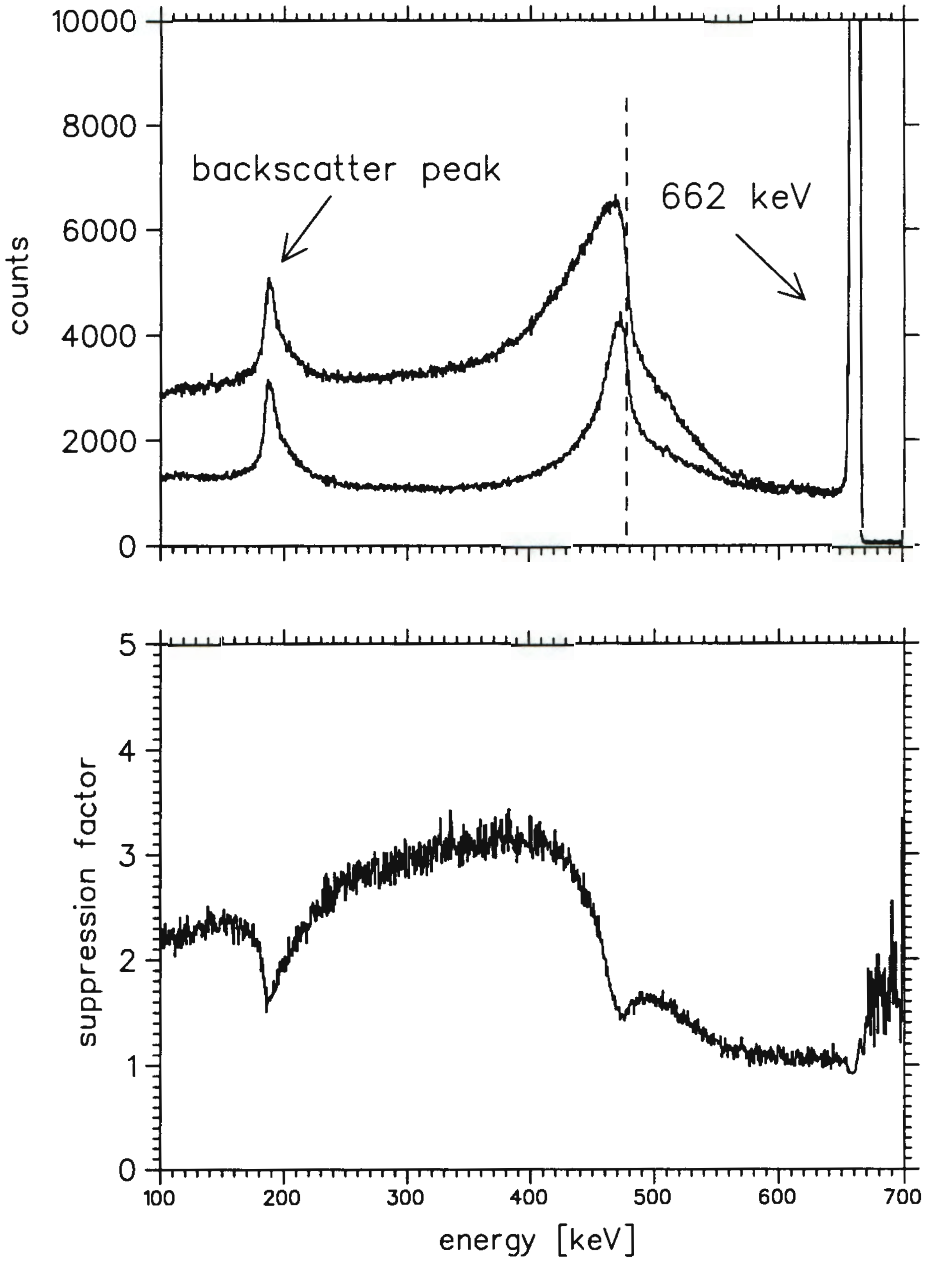

Figure 2.5: Top panel: suppressed and unsuppressed spectra measured by placing a ^{137}Cs source at the target position of AFŔODITE. The dashed line shows the location of the Compton edge. Bottom panel: suppression factors calculated from the data shown in the top panel [72].

[47, 49, 77] to measure the linear polarisation of γ–rays. This allows the magnetic or electric character of transitions to be determined (described in detail in Section 4.3.1), from which it is often possible to deduce the parities of nuclear states. The polarisation sensitivity of Clover detectors has been reported elsewhere, e.g. [77]. The Clover has also been used to determine lifetimes in the nanosecond range using the recoil shadow anisotropy method (RSAM) [11] (Section 4.5) in conjunction with thin-target in-beam experiments. RSAM relies on the unequal screening of detector elements, by the heavy-metal collimators, from γ-rays emitted during flight by a recoiling nucleus.

LEPS are planar [78] (10 mm thick, 60 mm diameter) detectors made from a single crystal of p-type HPGe electrically segmented into four quadrants. The signal from each quadrant is processed separately, as in the case of Clovers. One consequence of the planar geometry is that LEPS efficiency falls off much faster with increasing energy than that of Clovers, and that it is negligible above $\sim$ 400 keV (see Figure 2.6). Since low energy photons are less likely to Compton scatter out of the crystal, LEPS are thus neither BGO-suppressed nor operated with add-back. Some technical specifications for AFRODITE are listed in Table 2.3.

2.4.2 Auxiliary detectors

From AFRODITE's inception the intention was to develop a suite of auxiliary detectors to complement the existing Clovers and LEPS. These plans have only been partially realised, in part at least, for financial reasons. During recent years (1998-2000) the laboratory has been operating under duress on an austerity budget. Although auxiliary devices were not used in this work, they are given cursory mention here for completeness.

Figure 2.7 shows the mosaic of photovoltaic cells designed to fit inside the AFRODITE target chamber. This project was viable in part due to the low cost. In addition the AFRODITE frame may accomodate an array of eight 3" diameter NaI(Tl) detectors, mounted on the triangular faces (presently vacant), to serve as a multiplicity filter. The implementation of a neutron wall and a conversion-electron spectrometer has been discussed but not realised. Further development of the array is contingent upon funding.

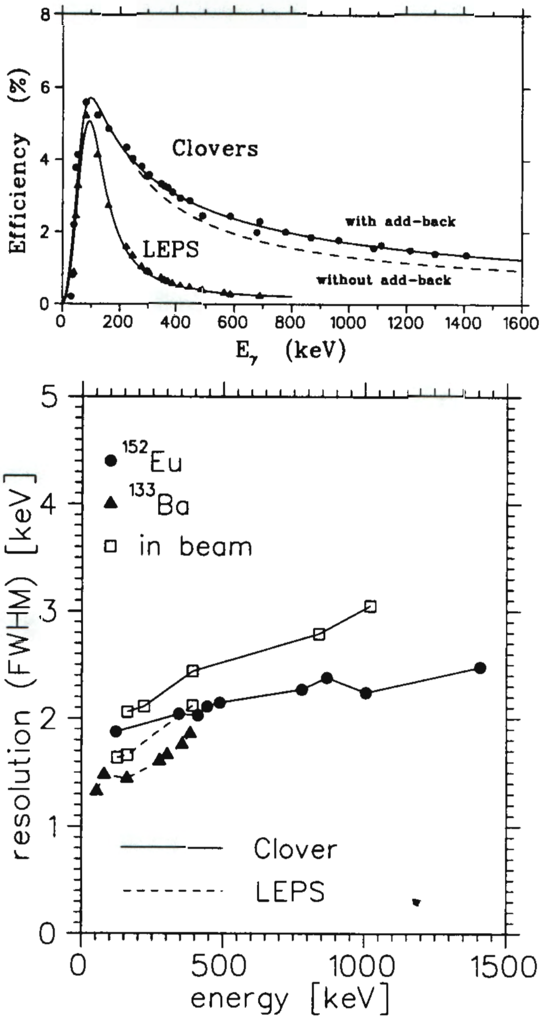

Figure 2.6: Upper panel: Total photopeak efficiencies for eight Clovers and seven LEPS detectors [72]. Lower panel: Typical single-element energy resolution for Clover and LEPS detectors in the AFRODITE array [72]

Table 2.3: Some technical specifications of AFRODITE [72]. R_{tc} denotes the distance from the target centre to the crystal surface.

	LEPS	Clover	BGO shield
number at NAC	8	8	8
supplier	Eurisys Mesures	Eurisys Mesures	Crismatec
entrance window	300 μm Be		
length	10 mm	71 mm	~26 cm
diameter	60 mm[a]	51 mm[b]	
R_{tc}	119 mm	196 mm[c]	
Ω per detect. (% of 4π)	1.38%	1.56%	
total Ω subt. (% of 4π)	12.5%	11%	

[a] Associated with the active area.

[b] Before shaping.

[c] For a 4 mm gap between target chamber and end-cap.

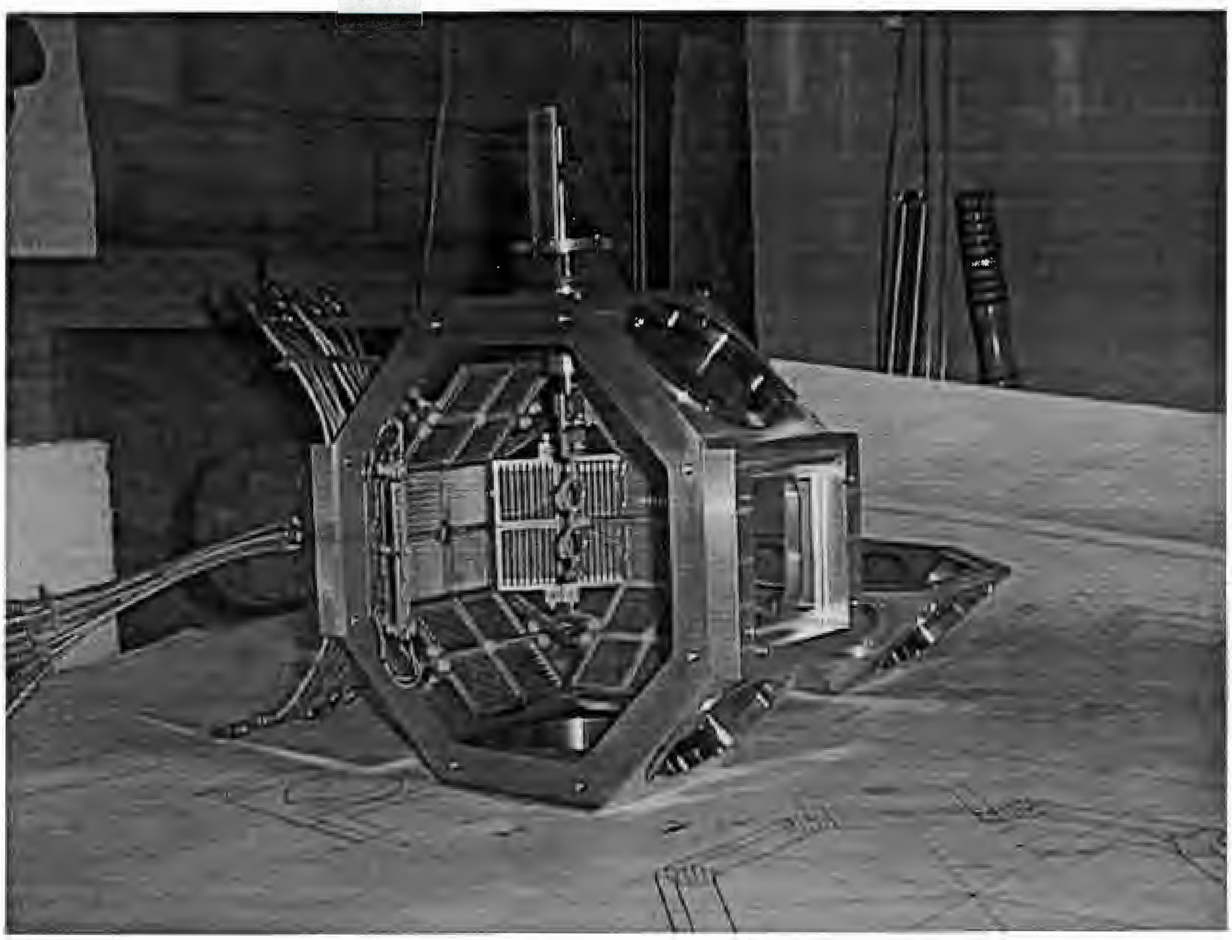

Figure 2.7: Solar cells mounted inside the target chamber. The target ladder is also visible.

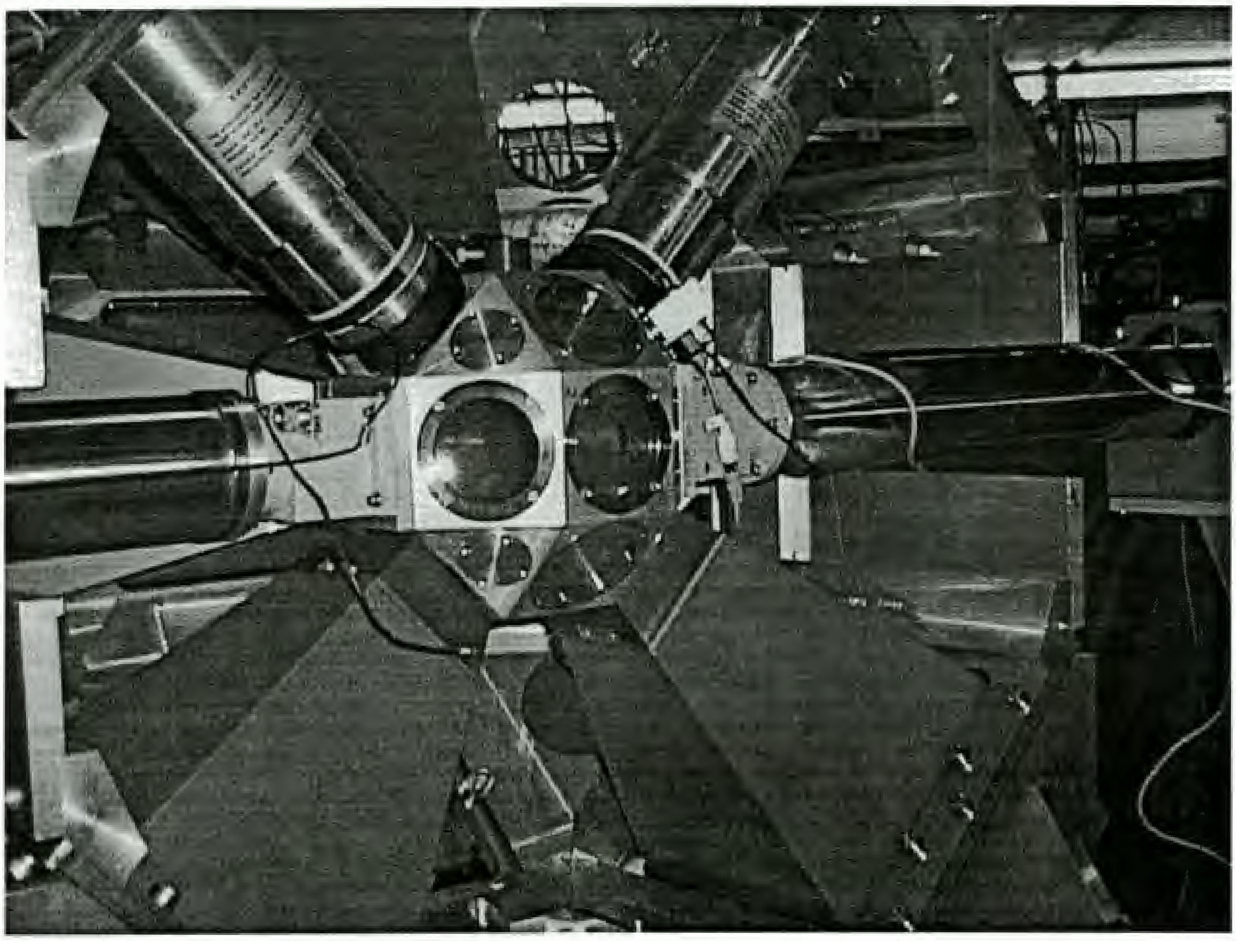

Figure 2.8: Target chamber, showing kapton windows. The closed circuit television camera (see text) is mounted on the top right-hand triangular facet.

2.4.3 Frame, target chamber and target ladder

The aluminium frame[9] supporting the 15 germanium detectors may be retracted from the beam line to allow access to the target chamber, as shown in Figure 2.9. The target chamber was designed to afford a direct view of the target ladder through 25 micron kapton windows, which are flexible, transparent to γ−rays and maintain good vacuum. The three frames of the target ladder usually support an aluminium oxide beam position monitor (top) and the target foil (bottom), while the middle frame is left empty for checking beam halo. A photograph of the target chamber with ladder in place is shown in Figure 2.8. Also visible are BGO shields of two of the Clovers (below beam line), two of the LEPS (above beam line), and a closed circuit television camera mounted on one of the triangular facets of the chamber to assist the cyclotron operators in positioning the beam.

Electronics and data acquisition system

AFRODITE requires instrumentation for up to 60 germanium channels. Signal processing is performed by standard NIM and CAMAC modules located in the experimental vault. The whole data acquisition system is directed from the data-taking room, via a workstation[10] running the VMS operating system and the XSYS[11] data acquisition package. One function of XSYS is to increment on-line spectra for immediate viewing from the control workstation. Signals from various points in the signal processing chain are patched through to the data room to allow the possibility of remote inspection, and the monitoring of event rates. Some of the adjustable parameters (e.g. amplifier gains, shaping times and pole zero settings) can be set from the data room although trouble-shooting the electronics is only possible from within the vault itself. This requires suspension of the beam (for safety reasons), a draw-back of the present setup.

The essential electronics for processing the signals from the 32 Clover and 28 LEPS elements are shown in Figure 2.10. The circuit may be subdivided into an energy and a timing circuit.

---

[9] Identical to EXOGAM frame, with 18 square and 8 triangular facets.

[10] VAXstation 4000-VLC.

[11] Developed at Indiana University Cyclotron Facility.

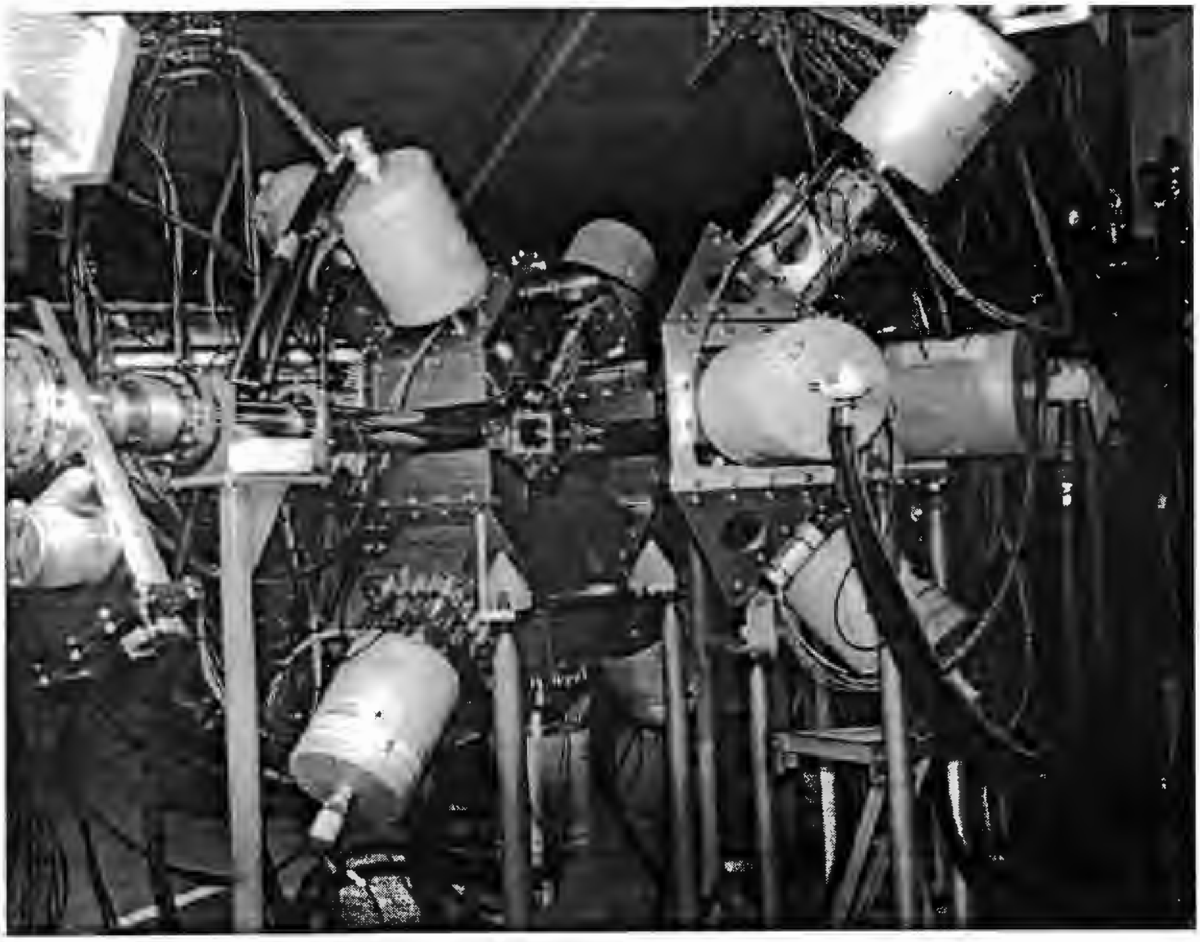

Figure 2.9: AFRODITE with part of the support frame retracted, exposing the target chamber.

Energy circuit The first element of the signal processing chain is the preamplifier housed in the detector cryostat. The preamplifier output pulse ($\approx$ 100 mV with a decay time of 50 μs), whose area is proportional to the gamma energy, is passed to the spectroscopy amplifier. Here the pulse is integrated and shaped (3 μs shaping time), giving a linear (energy) pulse ($\approx$1V - 10V) whose *height* is proportional to the gamma energy. The amplifier, in addition, outputs a fast (timing) signal which it feeds to a CFD where it is converted to a logic pulse required by the timing circuitry. The linear signal is sent directly to a 12-bit ADC (4096 channels) where it is digitised. Whether or not the ADC digitises the input signal is controlled by the ADC gate pulse. The ADC gate (width $\sim 4\mu s$) is open for a user-defined valid event and closed otherwise. The 'valid event' condition is set up in the timing circuit.

Timing circuit The timing circuit establishes all the coincidence relationships between signals from different hardware components for a specific experiment. It defines the event trigger used to filter out unwanted events, and controls the ADC gate, the TDC start and stop signals and the BGO veto. It links the detector elements, bit pattern registers, and CAMAC controller. The Clover, LEPS and BGO signals are processed somewhat differently. The 28 LEPS channels are treated identically to Clovers, the only difference being that there is no BGO veto.

A single BGO signal from the 16 series-connected PMs surrounding a Clover is used to veto the combined 4 elements of the associated Clover. After passing through a timing filter amplifier (TFA) the BGO pulse is fed to a CFD. Any BGO signal exceeding the threshold (typically $\approx$ 40 keV) is converted to a logic pulse (width 150 ns) which may veto the Clover signal.

After amplification the 32 Clover signals are fed to a CFD where each channel is split in two. The first branch goes to a bit pattern register while the second is bunched in groups of four (logical OR) giving one output channel per Clover. It is at this stage that a Clover signal may be vetoed. Appropriate delays are introduced to ensure that BGO and Clover signals from the same event are always in coincidence. The bit pattern register provides a record of which elements fired, a "fingerprint" of the event. Clover signals which were not vetoed may now be used to generate the event trigger, ADC gate, and TDC start and stop signals.

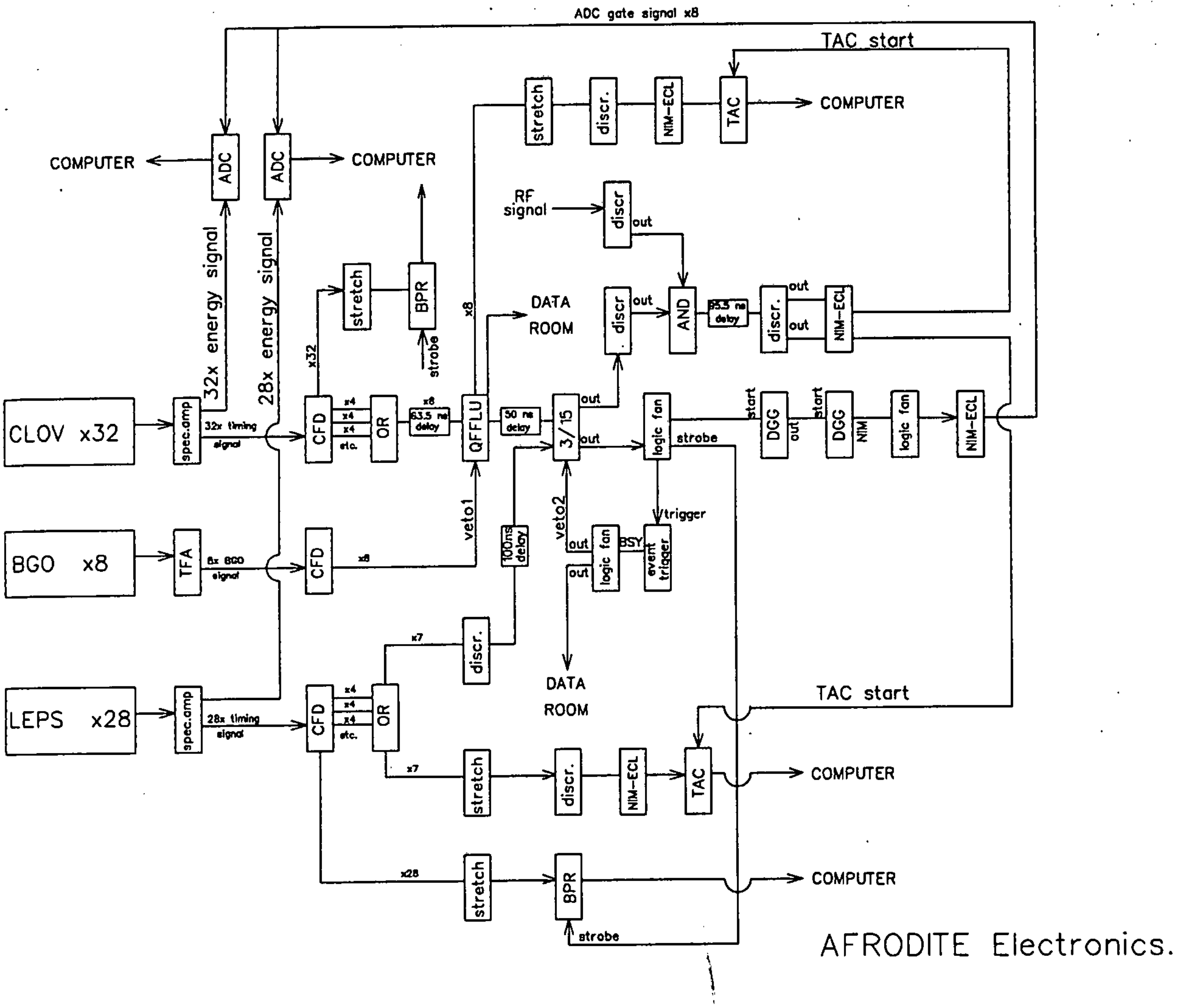

Figure 2.10: Electronics setup for experiment I.

Event trigger, ADC gate, TDC start and TDC stop The Clover signals are fed to the majority logic unit (MLU), a coincidence unit which accepts signals from all 15 detectors. Clover and LEPS signals are 50 *ns* wide giving a coincidence overlap time of 100 *ns*. The MLU generates the event trigger by requiring that an event of minimum fold f be present. In this work, for example, $f = 3$, meaning that MLU only has output when at least 3 detectors (Clover or LEPS) have fired. The simultaneous firing of *any* 3 detectors thus constitutes a valid event. The event trigger in turn is used to generate the ADC gate, the strobe for the bitpattern register, and the common start for all TDC channels.

The presence of a valid event alone satisfies the ADC gate condition. However, the common TDC start requires a coincidence between the event trigger and the first RF pulse after the beam burst. The TDC stop signal is provided by the first detector signal to arrive at the TDC (range 200 ns) after the TDC start pulse. The stop pulses are generated by individual detectors, and correspond to the first detector *element* to fire in the valid event. After a suitable delay for digitising the signal, the ADC and TDC may then be read out by CAMAC[12]/FERA[13].

Data readout During readout the event trigger module sends a busy signal to MLU, which prevents the recording of any further valid events for the duration of the signal. This prevents pile-up at the ADC. The resulting dead-time depends on the ADC conversion time as well as on the number of data words written per valid event, and is the main bottleneck in limiting the maximum achievable event rate. In an effort to enhance the maximum event rate readout was performed somewhat differently in the second experiment from the first (discussed in the following chapter). In the first experiment the data acquisition front-end module[14] read event data from the CAMAC instrumentation, while in the second the ADCs were read out by a front panel ECL data bus[15] and transferred to a Le Croy VME-based fast memory unit. This improved the maximum event rate from about 1 kHz for

---

[12] As in experiment I.

[13] As in experiment II.

[14] A 5-slot VME crate containing a Motorola 68040 processor module with an ethernet interface and a CBD 8210 CAMAC branch driver module from Creative Electronic Systems.

[15] FERA bus, a trademark of Le Croy. (Fast Encoding and Readout ADC module.)

the first experiment to about 2 kHz with FERA readout, at about 30% dead-time.

The data acquisition front-end module builds event buffers which it sends via the ethernet to the control workstation. An XSYS event-analysis task performs on-line sorting of the received buffers and stores the raw event buffers on tape. Each event is written as a group and contains energy and time information for each coincident γ−ray, and bit patterns recording which detector elements fired. The exact nature and format of the data words written to tape is specified in software by the user. This format must be exactly matched during off-line processing.

Chapter 3

The Experiments

The data presented in this work were taken in two independent fusion-evaporation experiments, using the AFRODITE array to measure $\gamma-\gamma$ and $x-\gamma$ coincidences. The heavy ion beams were provided by the K=200 separated sector cyclotron facility of NAC.

Preliminary calculations of reaction cross-sections using the Evapor code [79] predicted that both the ^{164}Ta and ^{165}Ta channels would be strongly populated in the first experiment. Consequently the $\gamma-$rays assigned to ^{164,165}Ta in this experiment, by gating on the Ta $x-$rays, could not be unambiguously identified with either ^{164}Ta or ^{165}Ta. The rationale for performing the second experiment, therefore, was to employ a reaction expected to strongly populate the ^{165}Ta channel while producing only insignificant amounts of ^{164}Ta. It was hoped that by comparing the production yields of Ta $\gamma-$rays in both experiments, it would be possible to unambiguously assign transitions to either ^{164}Ta or ^{165}Ta. The explicit identification of ^{164,165}Ta is deferred until the following chapter. The present chapter details the two experiments.

3.1 Experiment I

High-spin states in ^{164,165}Ta were produced in the reaction ^{142}Nd(^{27}Al,xn)^{164,165}Ta at an incident energy of 150 MeV. The target was a self-supporting metallic ^{142}Nd foil enriched to 98.7%, of thickness 750 μgcm^{-2}. The beam energy, based on calculations of relative production cross sections for all competing reaction channels using the code Evapor [79], was chosen to optimise the 4n and 5n reaction channels. Figure 3.1 (upper panel) shows these results for the strongest reaction channels around the bombarding energy. It also shows that at the beam energy of 150 MeV the dominant residual nucleus could be expected to be ^{164}Hf, with somewhat lower yields for ^{165}Hf, ^{164}Ta , ^{165}Ta and ^{162}Lu. The actual production yields were found to be ^{164}Hf (37%), ^{164}Ta (22%), ^{165}Hf (17%), ^{165}Ta (17%) and ^{162}Lu (8%).

Energy-loss calculations predicted that the beam energy would be degraded by about 4 MeV during its passage through the target. The target was sufficiently thin to permit the residuals to recoil into vacuum. It was therefore necessary to Doppler correct the measured energies of γ-rays emitted by the recoiling residual nuclei. An empirical value of $\beta \simeq 0.015$ was deduced for the recoiling nuclei using established ^{164}Hf lines of known energy. Doppler shifted, energy calibrated spectra from detectors at two extreme angles to the beam axis are shown in Figure 3.2. Because the residual nuclei were not stopped in the target, it was possible to use RSAM [11] (Section 4.5) to scan the data for nanosecond-range isomers.

The choice of the beam and target combination is subject to several practical constraints. First there is the limitation of which stable beams (ions and their energies) could be delivered by the cyclotron. A list of the available heavy-ion beams at NAC has already been given in Table 2.2. Second, the target element should not be difficult to handle or produce in an enriched form of high purity so that competing channels are reduced. The target used in this reaction is quick to react with atmospheric oxygen and cannot be stored for long periods (i.e. several weeks) except under high vacuum.

3.1.1 Data acquisition

The first experiment was performed over four weekends during July/August 1998, using the AFRODITE detector array with eight Clovers and seven of eight available LEPS. A deciding factor when determining the detector geometry was that it should optimise the number of coincident events between Clovers at 45°/135° relative to the beam direction and those at 90° to the beam. This is important, in order to maximise the number of Clover - Clover coincidences available for performing a DCO analysis (Section 4.3.1). Further details of the array configuration are given in Table 3.2.

The preparation for an experimental session starts weeks before the scheduled beam-

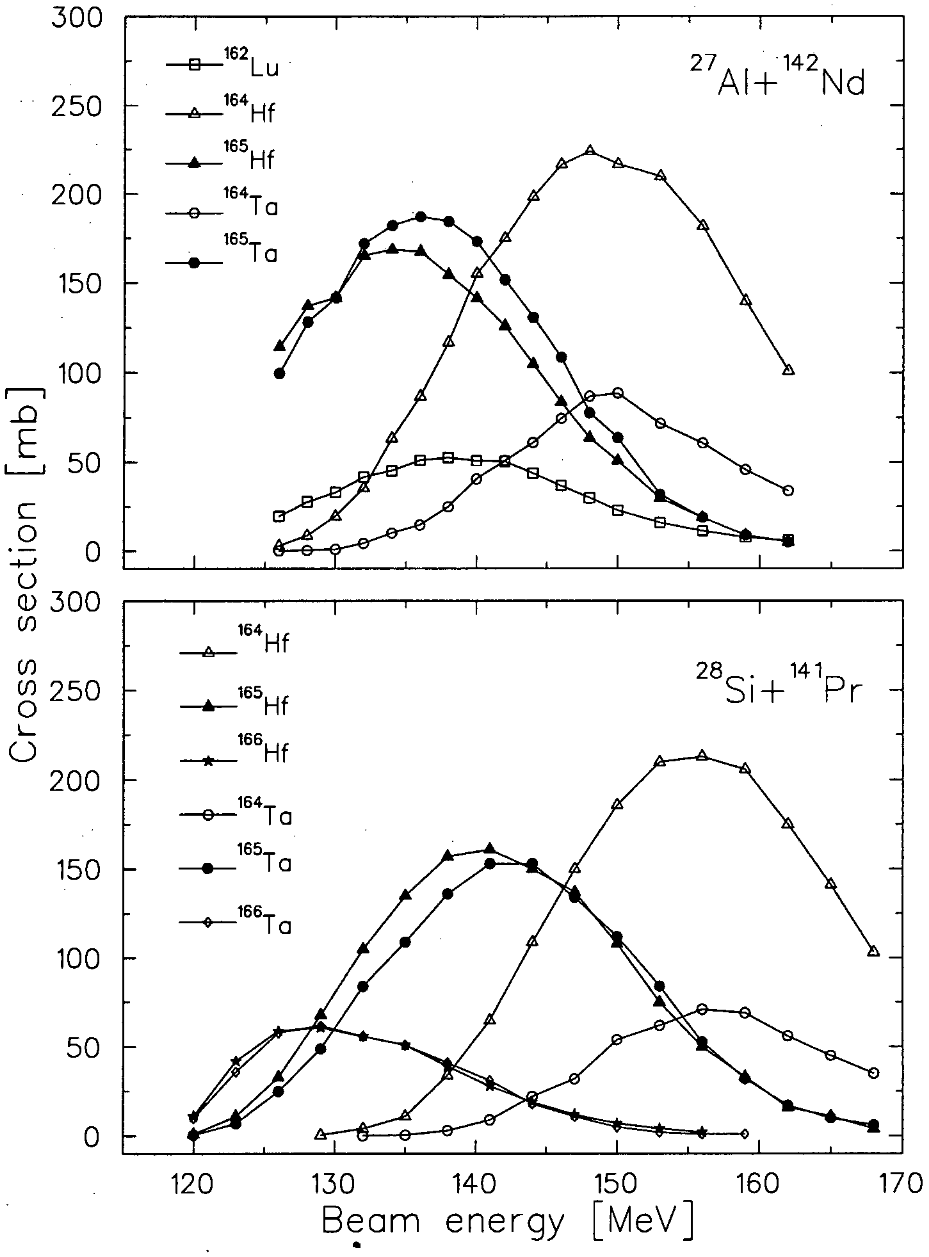

Figure 3.1: Results of EVAPOR code calculations for experiment I (upper panel) and experiment II (lower panel).

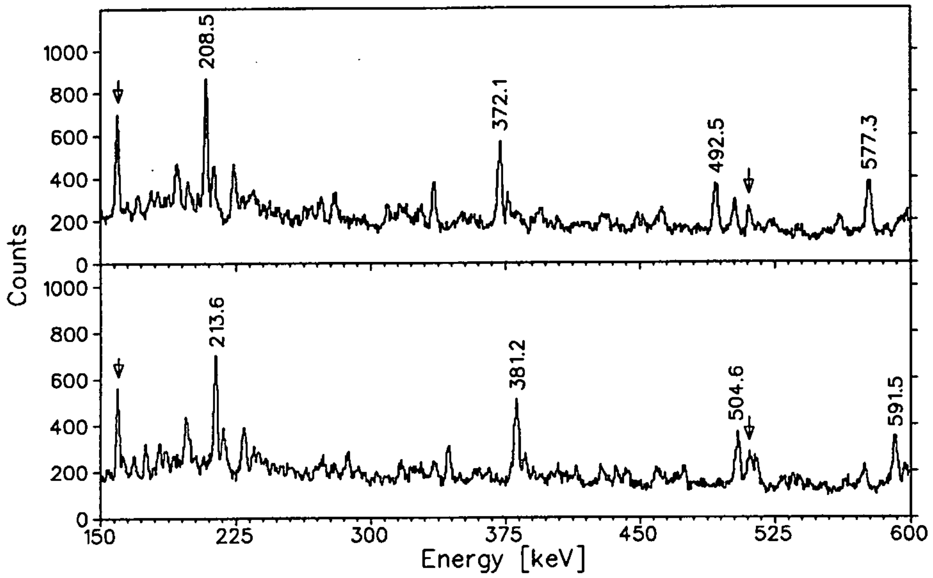

Figure 3.2: Energy calibrated, non-Doppler corrected singles spectra measured in Clover elements located at 141° (top panel) and 39° (lower panel) to the beam axis. In each spectrum the four strongest transitions in the yrast band of ^{164}Hf (210.8, 376.4, 498.2 and 583.7 keV) have been labelled with their respective Doppler shifted energies. The arrows indicate two unshifted peaks (160, 512 keV) due to non-recoiling contaminants.

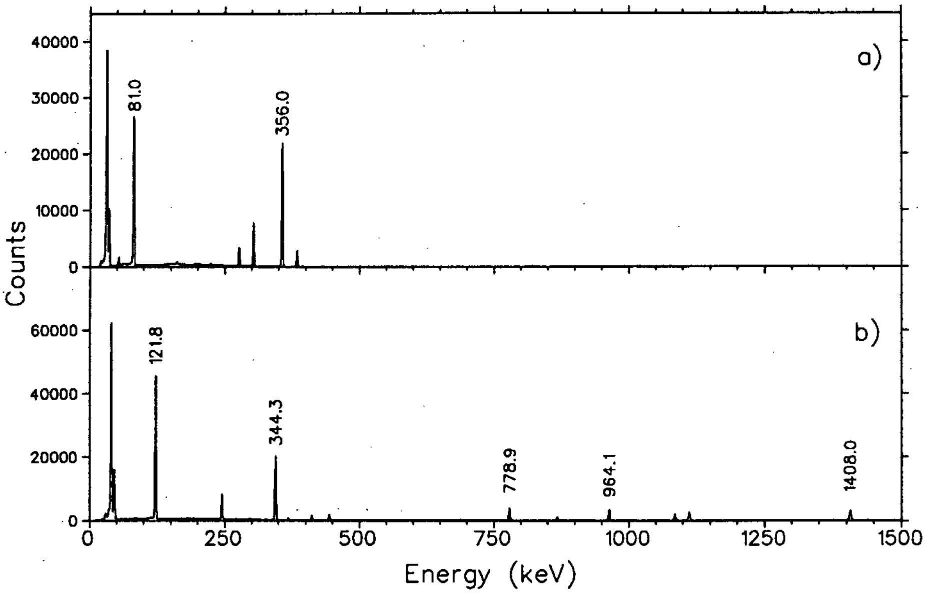

Figure 3.3: Standard ^{133}Ba (panel a) and ^{152}Eu (panel b) spectra measured by a single Clover element for the energy and efficiency calibrations in Experiment I.

time. Because there were no dedicated AFRODITE electronics, the timing circuit had to be built and debugged before the first weekend of data acquisition. Target foils were ordered from suppliers weeks in advance and stored under vacuum ($\sim 10^{-4}$ mbar). The detectors were mounted in the desired configuration, and the connections and performance of all detector elements were checked. All the detectors and electronics modules were correctly biased at least 48 hours before the start of the session to ensure performance stability. Immediately prior to each weekend a rough calibration of all 60 detector elements was performed. The amplifier gain for each of the 32 Clover elements was adjusted to about 0.5 keV/ch to provide a 2 MeV range for each 4096 channel ADC, and the LEPS dispersion was adjusted to about 0.2 keV/ch corresponding to a range of 0.8 MeV. All CFD lower thresholds were checked and set to about 30 keV using a ^{133}Ba source. The pole zero and integrating time constant for each amplifier channel were set, and remained fixed during the experiment. Finally, energy and efficiency calibration of all channels was performed in singles[1] mode, using standard ^{152}Eu and ^{133}Ba sources placed at the target position. This

---

[1] Coincidence level = 1.

was repeated immediately after acquisition had terminated at the end of each weekend. These calibrations provided a record of the performance of individual detector elements at the start and finish of the weekend for checking amplifier gain drifts. Typical ^{152}Eu and ^{133}Ba source spectra detected in a single Clover element are shown in Figure 3.3.

After completing the source calibrations, the ^{142}Nd target foil was removed from vacuum and attached to the target ladder under argon gas. Every precaution was taken to reduce exposure of the target to atmospheric oxygen. It was then transported to the cave, still under argon, and mounted in the target chamber, which had been previously flushed with nitrogen. Finally the target chamber and beam line were evacuated. The target remained in the evacuated target chamber from the first through third weekends but was replaced by a fresh foil for the final weekend.

The ^{27}Al^{7+} beam (prepared from 99.9% pure ^{27}Al) was extracted from the ECR ion source and fed to the SSC. The SSC delivered a pulsed beam with an energy of $\sim$ 150 MeV and 66 ns between beam bursts. With the target finally mounted and beam-line under vacuum, the alignment of beam and target was checked by reducing the current to about 5 nA and using closed circuit television to monitor the beam spot on an aluminium oxide viewer. This viewer had a 3 mm diameter hole at its centre. When perfectly aligned, the beam passed through this hole with no afterglow. Beam halo was reduced by tuning the beam in order to minimize the Clover count rate when using an empty target frame. In this manner it was possible to reduce the halo rate down to 10% of the count rate measured with the target in place.

Now that AFRODITE was ready for beam, the coincidence level on MLU was set to 3, and the ^{27}Al ion beam guided onto the ^{142}Nd target. Beam intensities on target fluctuated between 5 pnA and 7 pnA. This corresponded to an event rate of some 400 three-and-higher-fold coincidences per second. A higher event rate of about 800 sec^{-1} was measured during the fourth weekend as a consequence of using a fresh target foil[2]. An upper limit to the beam current was determined largely by the endurance of the fragile target to bombardment by the heavy-ion beam. Beam energies for the four respective weekends were 151.7, 149.9, 150.6 and 152.6 MeV.

The performance of all detectors and the data acquisition system was constantly mon-

---

[2] The previous target foil had become severely eroded by the beam during the first three weekends.

itored by regularly checking the on-line data rates, as well as the on-line spectra of all detector channels and the bit patterns. Some typical on-line spectra are shown in Figures 3.4, 3.5 and 3.6. Figure 3.4 shows raw pulse height spectra for a single Clover element and LEPS element, for a single run during experiment I. The dominant spectral lines have been labelled and are due to transitions in the ground state band of ^{164}Hf, shown in Figure 1.1. The figure also shows that the Hf and Ta $K_{\alpha 2}$ $x-$rays are resolved in the LEPS spectrum but not the Clover spectrum. Figure 3.5 shows the Clover and LEPS bit patterns for the same run. Deviations from a flat distribution, particularly for the LEPS, may be attributable to differences in CFD thresholds. Finally, Figure 3.6 shows the Clover, LEPS and total multiplicity spectra. It may be seen in the lower panel, for example, that the total fold peaks at 3 of any 15 detectors firing.

All the on-line spectra were written to disk at regular intervals, when acquisition would be temporarily halted. The raw coincidence event-by-event data were written directly to DLT tape in zero-suppressed mode, which produces a more compact data set. The data set of 29.2 Giga byte was divided into 86 run files. The segmentation of a large data set into discrete run files minimises the risk of data loss in the event of unexpected irregularities, such as ion source depletion, or the beam straying from target and hitting the target frame. It also ensures run files of manageable size for subsequent off-line analysis. The total data acquisition time amounted to about 206 hours or some 91% of the scheduled beam time. 538 million events of three-or-higher fold were recorded.

3.2 Experiment II

In the second experiment the reaction^{141}Pr(^{28}Si,4n)^{165}Ta at an incident energy of 142 MeV was used to populate high-spin states in ^{165}Ta. $\gamma-\gamma$ and $x-\gamma$ coincidences were measured with AFRODITE, comprising 7 Clovers and 8 LEPS. The target was a 17 mgcm^{-2} self-supporting ^{141}Pr foil. On the basis of energy loss calculations it was expected that both the beam and residuals would be stopped in the thick target. The choice beam energy was based on Evapor [79] code calculations, the results of which are shown in Figure 3.1. The energy was chosen to maximise the $4n$ exit channel from the ^{169}Ta compound system. Figure 3.1 shows that at the beam energy the dominant residual nuclei could be expected

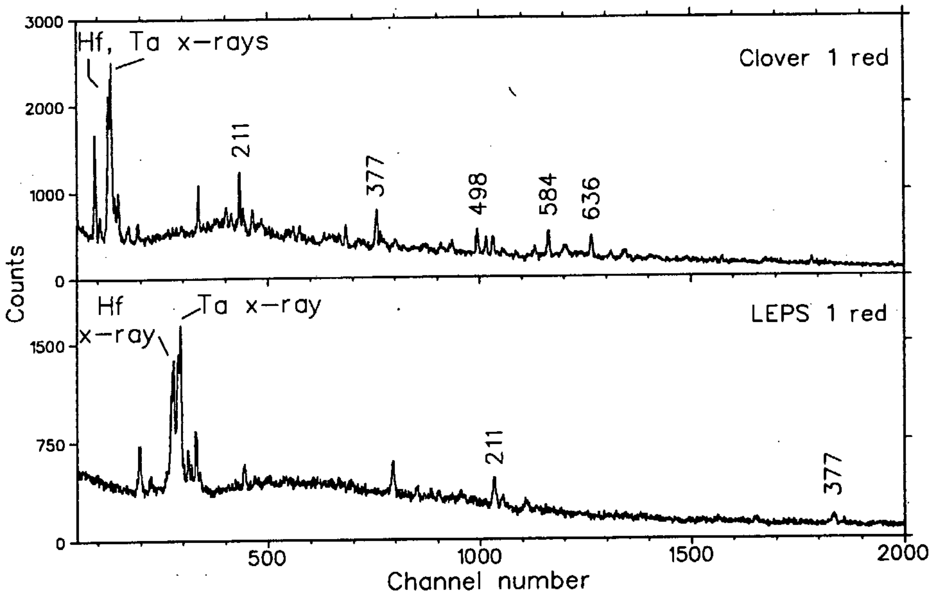

Figure 3.4: Raw pulse height spectra for a single Clover element (upper panel) and LEPS element (lower panel). The data are for a single run during experiment I. The dispersions are approximately 0.5 and 0.2 keV/channel, respectively. The strong γ−ray transitions in the ground-state band of ^{164}Hf are clearly visible (energies in keV).

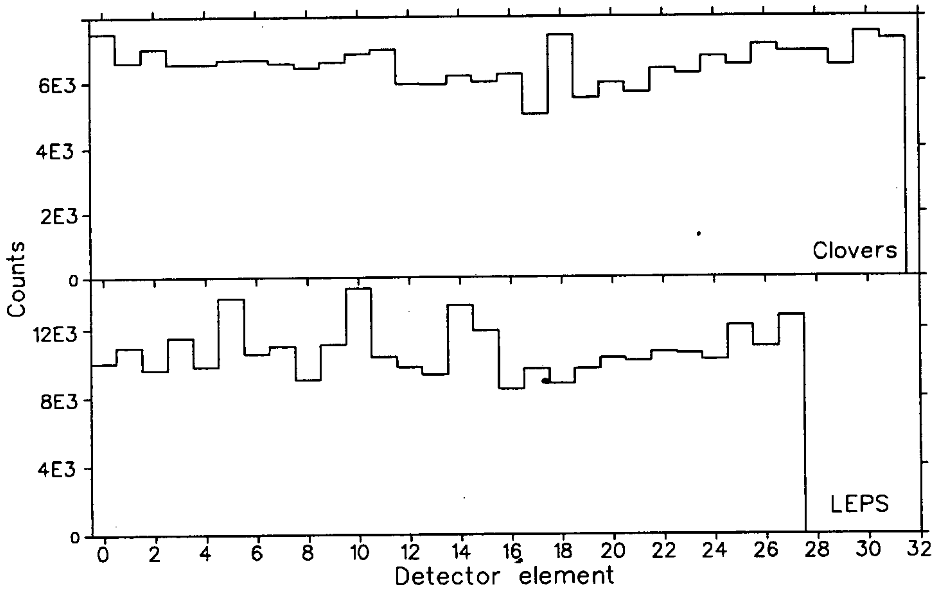

Figure 3.5: Clover and LEPS bit patterns for a single run during experiment I.

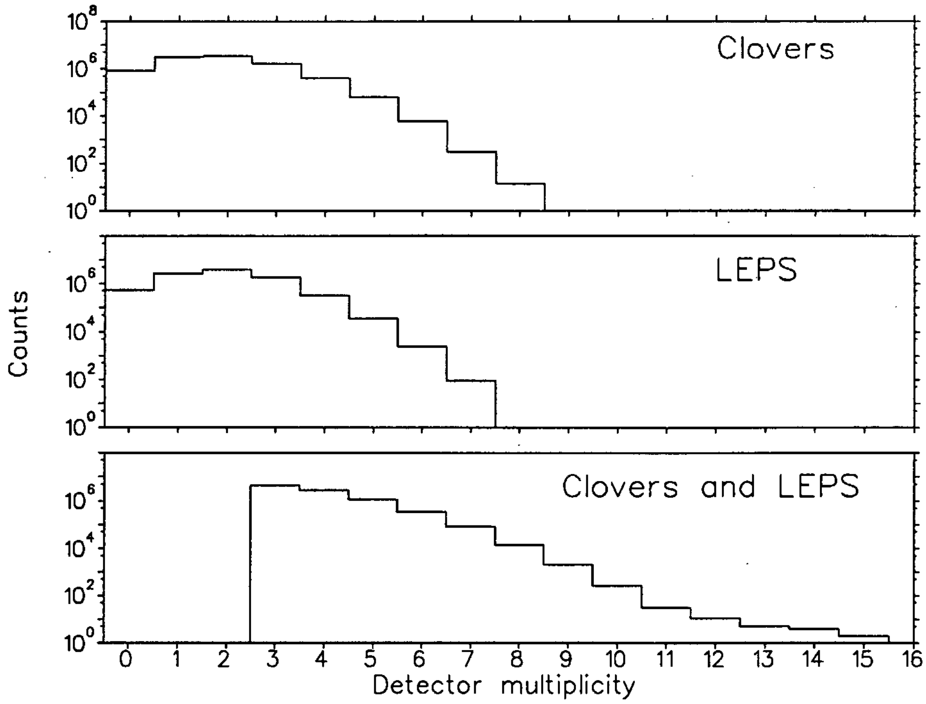

Figure 3.6: Detector multiplicity spectra for a single run during experiment I.

to be ^{165}Hf, ^{165}Ta and ^{166}Ta. It may also be seen that the expected yield for ^{164}Ta is negligible. The actual yields were determined to be approximately ^{166}Ta (41%), ^{166}Hf (23%), ^{165}Ta (19%), ^{165}Hf (14%) and ^{164}Hf (2%).

The overall setup for experiment II was the same as that in the first experiment. However, one difference is that one additional LEPS but one Clover detector less was mounted on the AFRODITE frame in the second experiment (the 8th Clover being unavailable). The second difference is that the integrating time constant for all amplifier channels was uniformly set to 3 μs (compared with 1 μs for the previous experiment). This resulted in a more complete charge collection and consequently better spectral resolution. Finally the ADCs were read out by FERA bus as discussed in Section 2.4.3. The detector geometry is given explicitly in Table 3.1. The event trigger condition required a three-or-higher fold coincidence between any of the 15 detectors, as for the first experiment.

	Experiment I	**Experiment II**
45° detectors	2 Clovers, 2 LEPS	2 Clovers, 2 LEPS
90° detectors	4 Clovers, 3 LEPS	3 Clovers, 4 LEPS
135° detectors	2 Clovers, 2 LEPS	2 Clovers, 2 LEPS
target	^{142}Nd foil, 750μgcm^{-2}	^{141}Pr foil, 17 mgcm^{-2}
beam	^{27}Al, pulsed	^{28}Si, pulsed
beam-burst separation	66 ns	70 ns
pulse selection	no	no
beam energy, week1	151.7 MeV	142.4 MeV
beam energy, week2	149.9 MeV	-
beam energy, week3	150.6 MeV	-
beam energy, week4	152.6 MeV	-
recoil velocity	0.0153c	0
compound system	^{169}Ta	^{169}Ta
dominant residuals	^{164}Hf(37%),^{164}Ta(22%), ^{165}Hf(17%),^{165}Ta(17%), ^{162}Lu(8%)	^{166}Ta(41%),^{166}Hf(23%), ^{165}Ta(19%),^{165}Hf(14%), ^{164}Hf(2%)
event trigger condition	$N \geq 3$	$N \geq 3$
number of events	538×10^6	106×10^6
amp. int. time const.	1μs	3μs
readout	CAMAC	FERA bus

Table 3.1: Experimental details.

3.2.1 Data acquisition

Experiment II was performed in October 1999. Coincidence data were taken during about 50 hours of beam time over a single weekend. A total of 4.5 Giga byte raw in-beam data consisting of 106 million three-and-higher fold coincidences, were written to magnetic tape in event-by-event, zero-suppressed mode. The 17 mgcm^{-2} thick target was more robust than that of the previous experiment, and could thus endure a higher beam current. The beam was prepared from NMR grade tetramethylsilane[3] injected directly into the ECR ion source, from which $^{28}Si^{5+}$ ions were extracted. Ths SSC delivered a pulsed beam with an energy of 142.4 MeV and a beam-burst separation of 70 ns. The beam intensity on target fluctuated between 10 pnA and 20 pnA. One consequence of using a thick target was the higher count rate. With the event trigger condition set to $N \geq 3$ the master event rate fluctuated between 500 - 1000 Hz.

---

[3] $Si(CH_3)_4$

Chapter 4

Data analysis and experimental results

Before the raw experimental data can be transformed into physically meaningful results they must be sorted into appropriate data structures. These may in principle be multi-dimensional, and should present the data in a manageable form for the off-line analysis. Since γ-ray energies are written to tape as raw pulse heights, they must be accurately calibrated, Doppler corrected if necessary, and gain-matched before data sorting may proceed. The calibration procedure and the different data structures used to perform the analysis are detailed in the present chapter. The final part of the chapter presents the level schemes, and discusses the assignment of an intrinsic configuration to the rotational bands.

4.1 Detector calibration

The first step in processing the data was to obtain a reliable set of calibration coefficients for all 60 detector channels, for each weekend. As discussed in the previous chapter, energy and efficiency calibrations were performed immediately before and after each experimental session. Standard ^{133}Ba and ^{152}Eu sources were placed at the target position in order to reproduce in-beam detector-target distances, and data were taken in singles mode. AUTOCAL, an automated peak-fitting routine on the VAX cluster, was used to determine centroids of the photopeaks of the calibration spectra. For both experiments the Ge detector elements were calibrated using the expression: $E_\gamma(x) = a + b \cdot x + c \cdot x^2$, where x represents the ADC channel number. The inclusion of terms such as $d \cdot x^3$ and $e \cdot \sqrt{x}$ in the above formula produced no significant improvements in the accuracy of the fit. The presence of the quadratic term, however, was important because detector response was found in several cases to be non-linear. Typical calibration curves for the four elements of a Clover are shown in Figure 4.1. The figure also shows, in addition to the residuals obtained for a quadratic fit, those obtained for a fit which included the cubic and square root terms. One set of calibration parameters was determined for each weekend of data acquisition.

The uncalibrated spectra for all detector elements were checked for possible gain drifts during each weekend. This was done by comparing the centroids of the intense 210.8 keV and 583.7 keV transitions in the ground-state band of ^{164}Hf, for each detector element, for a number of runs spanning the entire weekend. Clover elements whose gain had drifted by two ADC channels or more (i.e. a gain drift of $\geq$1 keV) during the course of a weekend were excluded from the data pocessing, as were LEPS elements showing a gain drift of four channels or more (i.e. a gain drift of $\geq$0.8 keV). The time evolution of the detector gain for selected elements is illustrated in Figure 4.1. Typically only two detector elements were excluded per weekend of acquisition due to either excessive gain drifts throughout the weekend or poor energy resolution.

Data from the first (thin target) experiment were Doppler corrected using an empirically determined β-value ($\beta \simeq 0.0153$). An average β-value was obtained by substituting into the standard Doppler formula the energy shift of the five most intense transitions (viz. 210.8, 376.4, 498.2, 583.7 and 635.6 keV) in the ^{164}Hf ground-state band (see Fig. 1.1), measured in detector elements located at 39° and 141° relative to the beam direction, respectively. For the second (thick target) experiment, no Doppler correction was necessary.

4.2 Data structures

The raw event data were sorted into one-, two- and three-dimensional spectra according to different selection criteria. The two-dimensional spectra are referred to as *matrices*

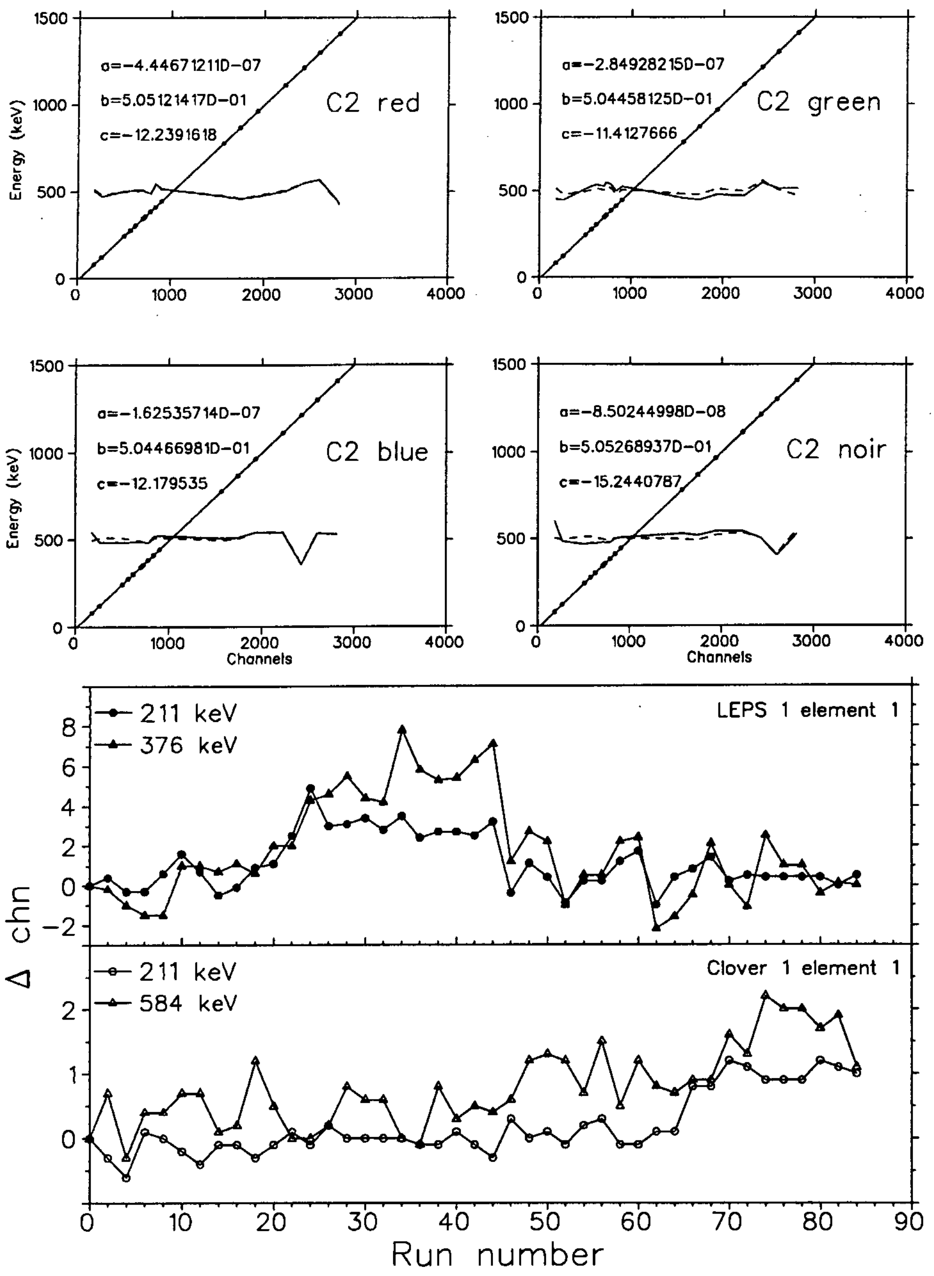

Figure 4.1: *Upper four panels:* Energy calibration of the four elements (labelled red, green, blue and noir) of a Clover detector, for the first weekend of experiment I, using a quadratic expression. The solid horizontal line shows the residuals, i.e. deviations from the calibrated value, $500\,[E_\gamma - (a \cdot x^2 + b \cdot x + c)] + 500$. The dashed horizontal line shows the residuals after the inclusion of cubic and square root terms. *Lower two panels:* Time evolution of the position of three selected γ-ray lines for a LEPS and a Clover element, for experiment I. The respective LEPS (Clover) dispersions were approximately 0.2 (0.5) keV/channel.

and the 3-D spectrum as a *cube*. The data structures used in the present analysis are summarised in Table 4.1 for convenience, and are described more fully below.

The raw event data were sorted using XSYS codes. While XSYS has the advantage of transparency and flexibility, particularly with regard to imposing selection criteria on the data, the codes are monolithic and execute painfully slowly. XSYS allows add-back or singles events to be selected on the basis of the bit pattern registers, and gates may be set in both the time and energy domains. It allows events to be selected on the basis of various detector combinations, or simply detector multiplicity. The code maps each germanium raw pulse height signal to a calibrated energy and performs the Doppler correction according to the detector angle relative to the beam direction. For the AFRODITE array the individual Clover elements are offset by ±6° relative to the angle subtended by the Clover midpoint and the beam direction. Therefore in cases where more than one element of a Clover fired, the respective energy contributions must be added *before* Doppler correction, using the average angle subtended by the elements which fired.

The calibrated, Doppler corrected energies can then be sorted into the desired data structures. A separate XSYS code was associated with each sorted data structure. Each was sorted directly from raw events with the exception of the cube. This was constructed by using the RADWARE code *incub8R* [81] in conjunction with a presorted tape (created using XSYS) containing calibrated Doppler corrected ADC data, TDC data, detector bit patterns and detector identification words. Several gated spectra were sorted by selecting only events in coincidence with the tantalum (or lutetium) x−rays detected in either LEPS or Clover detectors. Because the separation between the hafnium and tantalum $K_{\alpha 1}$ x−rays (see Table 4.2) is comparable with the Clover energy resolution, we needed to minimise the risk of contaminating the spectra gated on tantalum x−rays with γ−ray transitions in coincidence with hafnium x−rays. The tantalum x−ray gate (of width ~ 1 keV) was therefore somewhat offset from the centroid of the tantalum $K_{\alpha 1}$ x−ray.

The results presented in this thesis were obtained from an analysis of the first set of experimental data. This was the logical choice in view of the fact that it was the larger data set (538 M events). Data from the second experiment (106 M events) were used mainly to confirm the assignment of tantalum γ−rays to either ^{164}Ta or ^{165}Ta. The remainder of this chapter details the experimental results.

Experiment I		
Gate	**Data structure**	**Detectors**
none	cube	8 Clovers, 7 LEPS
none	matrix	8 Clovers
none	DCO matrix	4 Clovers @ 45°,135° vs. 4 Clovers @ 90°
none	DCO matrix	4 Clovers @ 45°,135° vs. 4Clovers @ 45°,135°
Ta $x-$ray	gated matrix	8 Clovers
Ta $x-$ray	1-D spectra, singles shadowed, unshadowed	4 Clovers @ 90°
Lu $x-$ray	1-D spectra, singles shadowed, unshadowed	4 Clovers @ 90°
Ta $x-$ray	1-D spectra, doubles in horiz. or vert. elements	4 Clovers @ 90°
Experiment II		
none	matrix	7 Clovers
Ta $x-$ray	gated matrix	7 Clovers

Table 4.1: Summary of data structures used in the analysis.

	$\mathbf{K}_{\alpha1}$	$\mathbf{K}_{\alpha2}$	$\mathbf{K}_{\beta1}$	$\mathbf{K}_{\beta2}$
$_{71}$**Lu**	54.070 (47.3)	52.965 (27.3)	61.290 (10.1)	62.929 (3.4)
$_{72}$**Hf**	55.790 (47.1)	54.611 (27.3)	63.243 (10.2)	64.942 (3.5)
$_{73}$**Ta**	57.535 (47.2)	56.280 (27.3)	65.222 (10.3)	66.982 (3.5)

Table 4.2: Energies (expressed in keV) of the strongest characteristic $x-$rays for Lu, Hf and Ta [80]. The relative intensities appear in parentheses.

4.3 Results for ^{165}Ta

4.3.1 Level Scheme

The level scheme for ^{165}Ta, shown in Figure 4.2, is based on the present work. Two distinct rotational decay sequences, band A and band B, have been associated with this nucleus. The relative placement of these bands in Figure 4.2 is arbitrary, since no interconnecting transitions could be firmly established from the data, and the possibility that there are highly converted low energy transitions to the ground state cannot be ruled out. Band A was the most strongly populated in this nucleus in both the reactions used and is therefore likely to be yrast. The arguments used to assign the γ−rays in bands A and B to ^{165}Ta, as well as the configurations of the two bands, will now be discussed.

Band A (yrast band) The yrast rotational decay sequence of ^{165}Ta was established up to spin 53/2 at an excitation energy of 6168 keV. Gamma-rays from ^{165}Ta had been previously identified by Clark *et al.* [6] but to the author's knowledge no definitive decay scheme has yet been constructed. Preliminary calculations of reaction cross sections using the EVAPOR code [79] predicted that both the ^{164}Ta and ^{165}Ta channels would be strongly populated in the first experiment, while the second experiment was expected to produce mainly ^{165}Ta and ^{166}Ta, but no ^{164}Ta. At the present time the decay scheme of ^{164}Ta is also unknown. Consequently the γ−rays assigned to ^{164,165}Ta in the first experiment, by gating on the Ta x−rays, could not be unambiguously identified with either ^{164}Ta or ^{165}Ta. The intensities of these γ−rays were therefore compared with those in the second experiment. Since the high-spin structure of ^{166}Ta is known [82], γ−rays present in both data sets, which are also in coincidence with the Ta x−rays, were assigned to ^{165}Ta.

For instance, the transition 134.5 keV was found to belong to a band sequence that is in coincidence with the Ta x−rays in both sets of experimental data. Figure 4.3(a) shows the spectrum obtained from the ^{142}Nd(^{27}Al,4n)^{165}Ta reaction data (first experiment) in coincidence with the 134.5 keV transition. This is to be compared with the spectrum obtained by setting a gate on the 134.5 keV γ−ray, but using the E_γ-E_γ matrix constructed from the ^{141}Pr(^{28}Si,4n)^{165}Ta reaction data (second experiment), in Figure 4.3(b). Since the γ-rays in this gate are not from ^{166}Ta [82], and since ^{164}Ta was not expected among

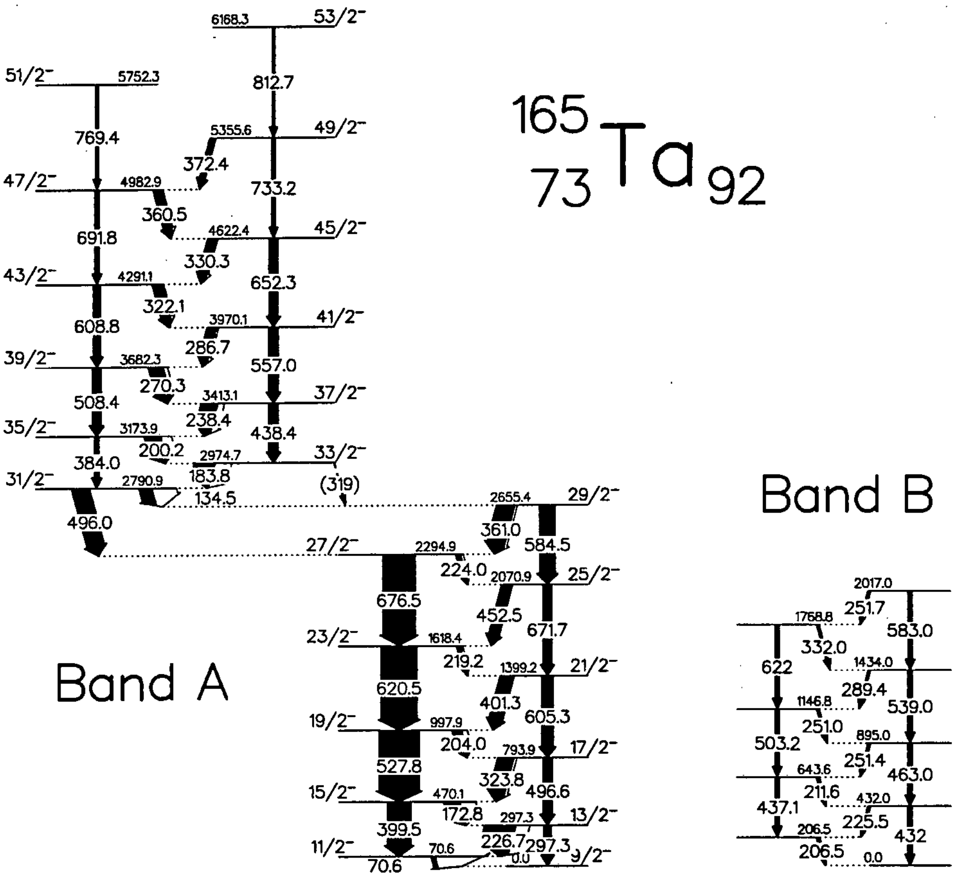

Figure 4.2: Partial level scheme of ^{165}Ta. In band A (yrast band) the arrow widths indicate the transition intensities, and excitation energies are relative to the $9/2^-$ level energy (assumed 0 keV). For band B they are relative to the lowest observed level of that band.

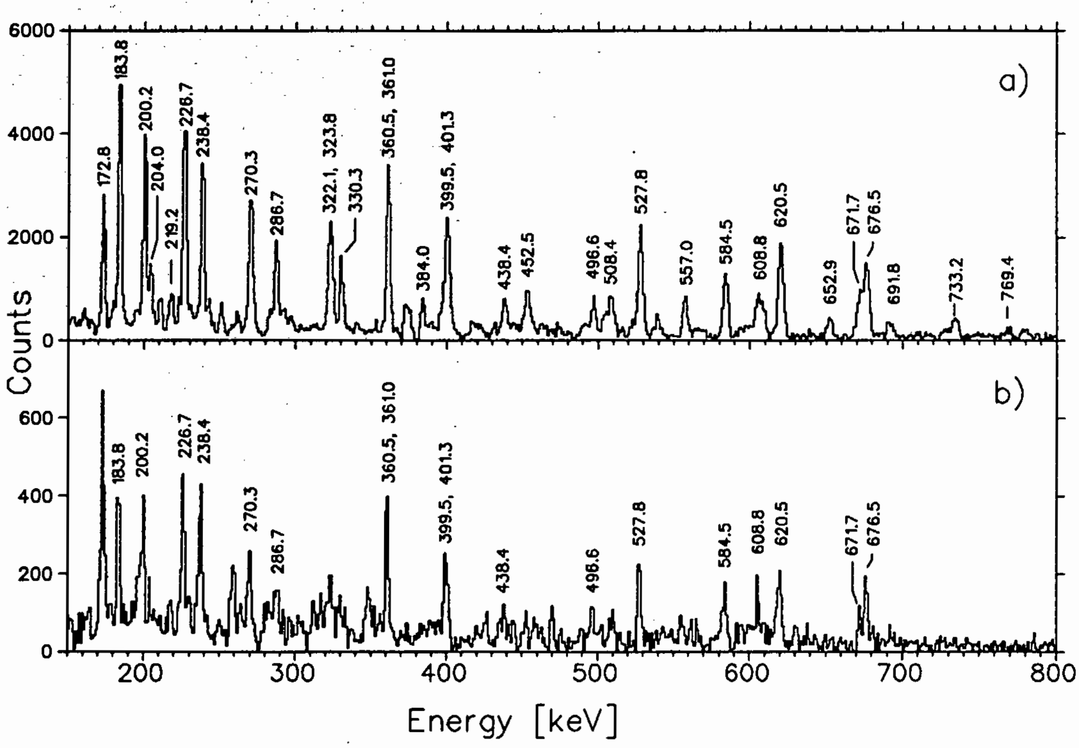

Figure 4.3: ^{165}**Ta, Band A:** Coincidence spectra gated on the 134.5 keV transition in Ta, measured in the reactions (a) ^{142}Nd(^{27}Al,4n)^{165}Ta and (b) ^{141}Pr(^{28}Si,4n)^{165}Ta.

the residuals in the second experiment, they were assigned to ^{165}Ta. This conclusion is supported by a previous identification of a number of these transitions with ^{165}Ta on the basis of mass 165 recoils [5, 83]. Indeed, some of the stronger transitions in this band are visible in the mass-gated spectrum shown in the upper panel of Figure 4.10. The level scheme was constructed on the basis of γ−ray coincidence relationships and intensities.

The analysis of triple coincidences obtained by setting double gates on the cube proved essential in resolving multiplets and placing them in the level scheme. For example, an unresolved doublet of about 400 keV occurs in the band. The spectrum in coincidence with the 399.5 keV transition and the Ta x−ray shows a strong line at 401.3 keV in addition to the other strong transitions in the band (Fig. 4.4(a)). The 401.3 keV transition is still visible in the spectrum double-gated on the 399.5 keV and 527.8 keV γ−rays, seen in Figure 4.4(b), but is absent from the spectrum double-gated on 399.5 and 620.5 keV presented in Figure 4.4(c). The 401.3 keV transition was therefore placed parallel to 620.5 keV. In a similar way the remaining doublets of 323, 361 and 496 keV could be placed

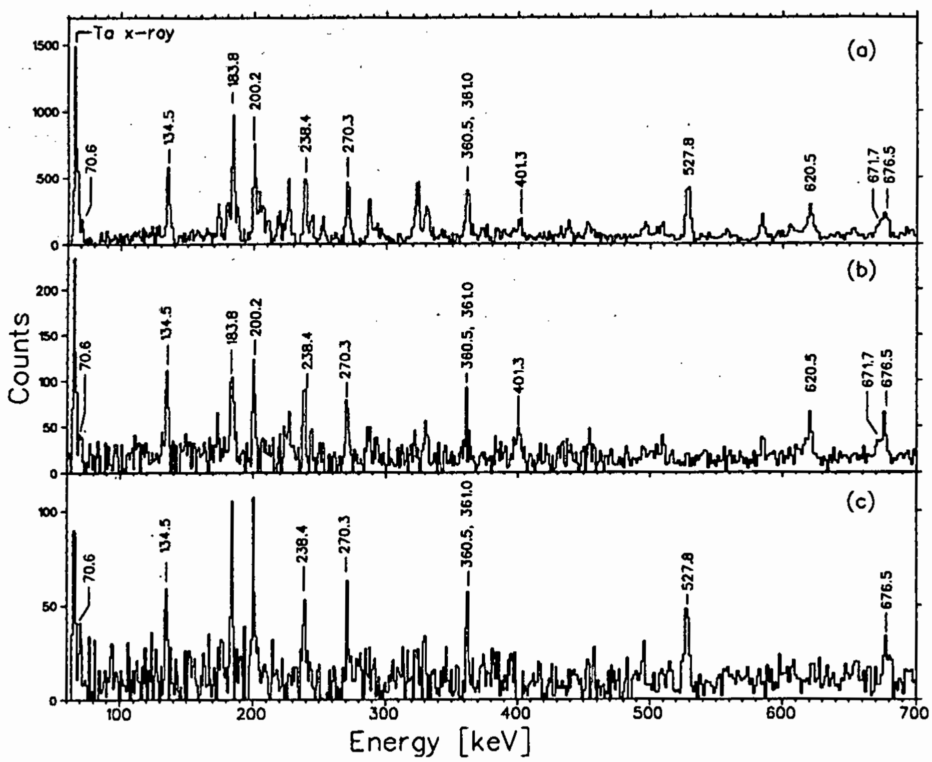

Figure 4.4: ^{165}**Ta, Band A:** Selected triple coincidence spectra. (a) Double gate on 399.5 keV and the Ta $x-$ray. (b) Double gate on 399.5 and 527.8 keV. (c) Double gate on 399.5 and 620.5 keV.

into the level scheme. Strong doublets were also seen at 173 and 226 keV. However an analysis of double-gated spectra revealed that these transitions are both singlets in this band, whereas they occur as doublets in a different band. The spectrum double gated on the 226 keV transitions (see Fig. 4.9), for example, shows some transitions (e.g. 207, 211 keV) which are in coincidence with band B. It was not possible to identify transitions depopulating the lowest lying levels of the yrast band. This can be due to the very low energy of the decaying transitions or long lifetimes.

It is known that the bands of odd nuclei in this mass region typically comprise two signature partner sequences, linked via cascade transitions. The level scheme for ^{165}Ta deduced in the present work is consistent with this trend. The directional correlation ratios (DCO-ratios $I_\gamma(45°)/I_\gamma(90°)$) for these cascade transitions in the yrast band are close to 0.8, while DCO ratios for the in-band cross-over transitions are close to 1.3.

These values are consistent with dipole and quadrupole transitions, respectively. The assignment of either electric or magnetic character to the twenty strongest transitions in the band is supported without exception by linear polarisation measurements performed using the Clovers as polarimeters as described in [77]. The experimental anisotropies A for transitions in the yrast band were calculated from the expression

$$A = \frac{N_V - \alpha N_H}{N_V + \alpha N_H} \tag{4.1}$$

with relative efficiency $\alpha = 0.994$, where N_V denotes the number of $\gamma-$rays which scattered in a plane perpendicular to the beam axis, and N_H the number which scattered in a plane parallel to the beam axis. The sign of A is positive for stretched electric transitions, and negative for stretched magnetic transitions. On the basis of the anisotropies and DCO measurements, most transitions could be assigned M1 or E2 character. The DCO ratio value for the 400 keV doublet is intermediate between the values for a dipole and a quadrupole transition, consistent with the placement of the 399.5 (E2) and 401.3 keV (M1) transitions in the level scheme. The difference spectrum corresponding to the numerator in the above expression, obtained by setting a gate on the Ta $x-$ray, is shown in Figure 4.5.

The $\gamma-$ray intensities for clean transitions were determined from the coincidence projection of a gate set on the Ta $x-$rays. It was verified that the relative intensities of these transitions to other transitions in the band were not skewed by gating on the $x-$ray. For the remaining transitions, the intensities were determined by using the $E_\gamma - E_\gamma - E_\gamma$ cube to generate double-gated spectra. In the upper part of the band, above the $29/2^-$ level, most of the intensity is carried by M1 transitions. Below the $27/2^-$ level however, most of the gamma intensity flows through the favoured $\alpha = -1/2$ sequence of E2 transitions. At the bottom of the band, the measured total intensity of the 70.6 KeV transition is markedly less than the summed total intensities of the 226.7 and 399.5 keV transitions. This discrepancy is most likely due to the fact that the array efficiency was obtained from radioactive sources in singles mode, whereas the efficiency for detecting low-energy $\gamma-$rays in coincidence mode will be considerably lower than that determined in singles.

In order to look for isomeric states (nanosecond range), the Recoil Shadow Anisotropy Method (RSAM) [11], that requires no additional device besides the AFRODITE array, was used. No evidence could be found for isomers in the nanosecond range in ^{165}Ta.

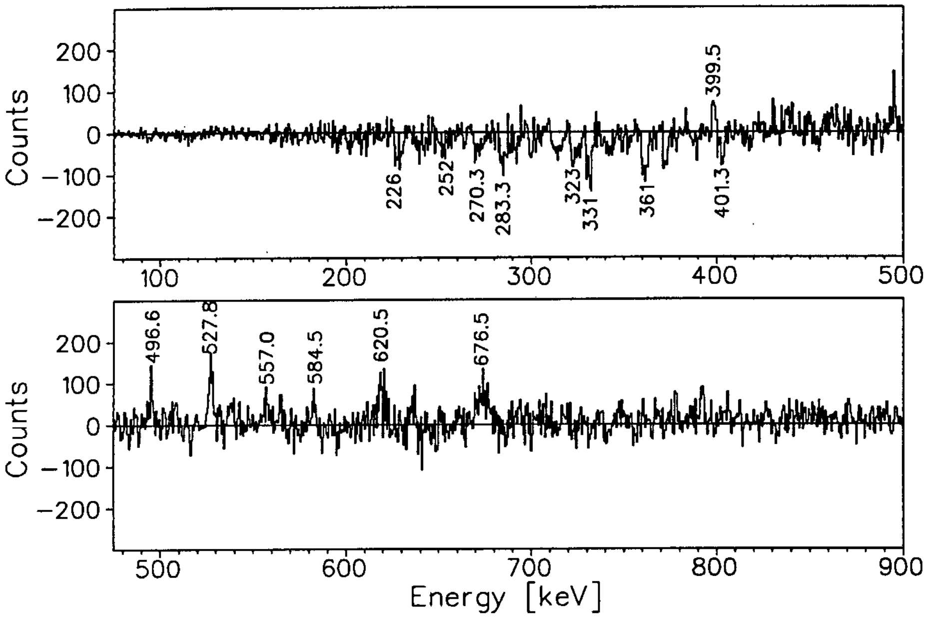

Figure 4.5: Difference spectrum, gated on the Ta x−ray, showing $N_V - 0.994N_H$. N_V (N_H) are the number of gamma rays which scattered perpendicular (parallel) to the beam axis. The data are taken from the first experiment.

From the present data it was not possible to firmly establish the existence of a 319 keV transition been the $33/2^-$ and $29/2^-$ levels. The placement of this transition in the level scheme is therefore tentative. An upper limit for the branching ratio of the decay out of the $33/2^-$ level was found to be $I_\gamma(319)/I_\gamma(183.8) \leq 0.04$. The level energies, γ−ray energies, intensities, spin assignments, DCO-ratios and anisotropies are summarised in Table 4.3.

Because no low-spin states in ^{165}Ta had been identified prior to this work, and because no transitions de-exciting the lowest-lying levels of the yrast band were observed, the spin and parity of the bandhead could not be measured experimentally. They were therefore assigned on the basis of systematics. This has been used for bands in several of the heavier odd-mass Ta isotopes [84, 85, 86, 87, 88, 89]. The lowest-lying level of the yrast band was assigned a spin and parity of $9/2^-$ and configuration $[514]9/2^-$ based on the following arguments:

(i) Excitation energies of the yrast states relative to the lowest-lying level observed in ^{165}Ta were compared with relative excitation energies in bands built on different intrinsic configurations for the heavier odd-mass $^{167-179}$Ta isotopes [84, 85, 86, 87, 88, 89, 90]. The present data follow the smooth trend of the level excitation energies only for bands assigned to the $[514]9/2^-$ orbital, and only if it is assumed that the spin and parity of the lowest-lying observed level is $9/2^-$ (see Figure 4.6).

(ii) A large signature splitting (69 keV at $\hbar\omega = 0.225$ MeV) of the yrast band below the backbend was measured. Since this is a characteristic feature only for bands built on the negative parity $\pi h_{11/2}$ orbital in the lighter odd-Z even-N rare earths with $N \leq 94$ (e.g. ^{159,161,163,165}Lu, see for example [91], ^{167}Ta [84]), the $\pi h_{11/2}$ orbital should be associated with this band.

(iii) Figure 4.7 shows the systematic variation of the energy staggering amplitude $E(I) - E(I-1)$ as a function of spin for the $\pi h_{11/2}$ $[514]9/2^-$ bands of the odd-A $^{165-179}$Ta isotopes. The ^{165}Ta yrast band follows the observed trend, with favoured states lying lower in energy than unfavoured states and a sudden decrease in the staggering amplitude at $I = 29/2$, only if spin $9/2$ is assigned to the lowest level of the yrast band.

(iv) Among the available negative parity, high-Ω proton orbitals for the odd-A isotopes $^{167-185}$Ta, the $\pi[514]9/2^-$ orbital was calculated to be the closest to the Fermi surface [7].

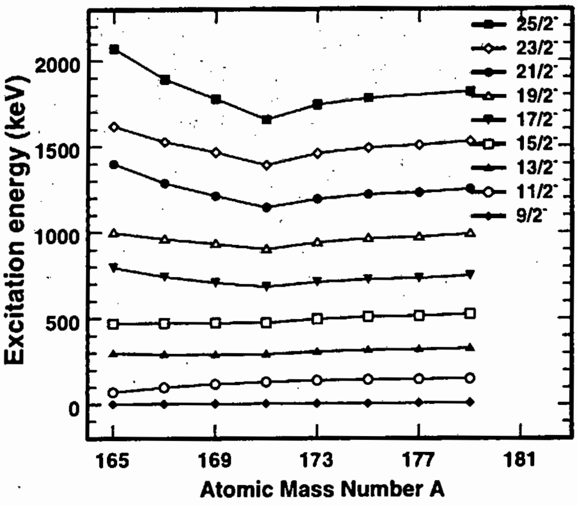

Figure 4.6: Excitation energies in the bands built on the [514]9/2$^-$ orbital, for the odd isotopes $^{165-179}$Ta, relative to the 9/2$^-$ level.

Our CSM calculations suggest that this will also be true for ^{165}Ta, (see Section 5.2.2). Indeed, the strongly coupled bands assigned to this configuration in the neighbouring odd-mass Ta isotopes have been found to lie at relatively low excitation energy, with the trend to become yrast for lighter isotopes (as it is for ^{167}Ta [84]).

(v) The measured $B(M1)/B(E2)$ ratios (Table 4.3) for the ^{165}Ta yrast band are consistent with the assignment of the [514]9/2$^-$ intrinsic configuration to this band.

Band B In addition to the yrast band in ^{165}Ta, it was possible to identify a different, less strongly populated structure, band B. A tentative decay scheme for band B is presented in Figure 4.2.

The reasoning used to assign this band to ^{165}Ta is similar to that used for the yrast band (band A). For example the 251 keV transition was found to be in anti-coincidence with band A. However it clearly belongs to a band sequence that is in coincidence with the tantalum x−rays in both sets of experimental data. For example, Figure 4.8 (upper panel) shows the triple coincidence spectrum obtained from the ^{142}Nd(^{27}Al,4n)^{165}Ta reaction data by double gating on the tantalum x−ray and the 251 keV γ−ray. From a comparision with the spectrum shown in Figure 4.8 (lower panel), obtained by setting a single gate

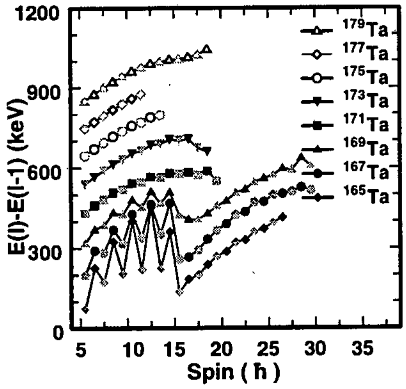

Figure 4.7: $E(I) - E(I-1)$ in the bands built on the [514]9/2^{-} orbital for the $^{165-179}$Ta nuclei. To avoid superposition of data corresponding to different isotopes, they are successively offset by 100 keV. The black (grey) symbols correspond to the favoured (unfavoured) signature of the [514]9/2^{-} orbital.

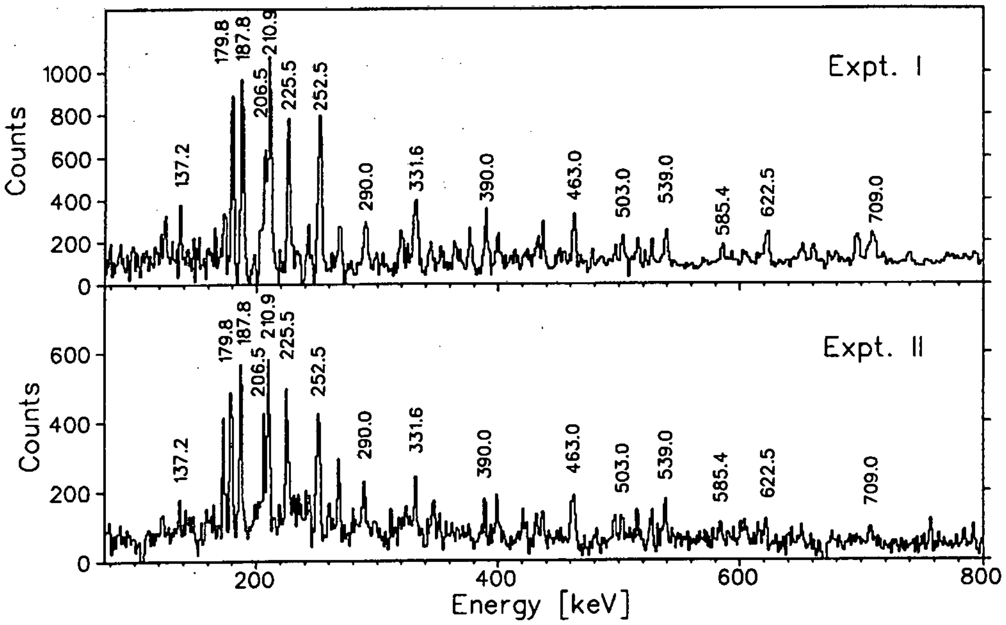

Figure 4.8: ^{165}**Ta, Band B:** *Upper panel*: triple coincidence spectrum gated on the tantalum x−ray and the 251 keV transition, using the ^{142}Nd(^{27}Al,4n)^{165}Ta reaction data. *Lower panel*: coincidence spectrum gated on the 251 keV transition, using the ^{141}Pr(^{28}Si,4n)^{165}Ta reaction data.

on the 251 keV transition but using the data from the ^{141}Pr(^{28}Si,4n)^{165}Ta reaction, it is obvious that the γ−rays in band B are present in both data sets. The transitions in this band were therefore assigned to ^{165}Ta. This conclusion is further supported by the presence of some of these transitions (211, 252 keV) in the mass-gated spectrum presented in the upper panel of Figure 4.10.

Many of the transitions coincident with band B could not be placed in a consistent level scheme on account of both the weakness of the band and the high incidence of energy multiplets. For the same reasons it was not possible to determine the γ−ray intensities for the transitions in this band. Particularly "troublesome" multiplets occur at about 173, 179, 187, 211, 226, 243, 251, 332 and 463 keV. Some of the stronger multiplets could be assigned to the level scheme by setting appropriate double gates. However this was not possible for the weaker ones (e.g. 173, 179, 187 and 243 keV) on account of poor statistics in the double-gated spectra. To give an indication of the problems involved in placing some of these transitions in the band, examples of triple coincidence spectra are presented in Figure 4.9. The upper panel shows the triple coincidence spectrum obtained by setting gates on both the 226 and 251 keV transitions. It shows some of the stronger transitions in the band (207, 211, 390, 463 keV), and also that additional 226 and 251 keV transitions occur in the same decay sequence. It would be interesting to know where in the level scheme the "second" member of each multiplet occurs. This question is addressed by setting double gates on both members of each multiplet as shown in the middle and lower panels of Figure 4.9. The middle panel shows the spectrum obtained by setting two gates on the 226 keV transition. While some of the transitions (viz. 207, 211 keV) in band B are visible in this spectrum, some others (viz. 251 keV) are no longer present. Further, a strong 243 keV transition is seen which is not in coincidence with the 226, 251 keV double gate (top panel). Evidently the 226 keV doublet sees a decay sequence which is in coincidence with only part of the band. The fact that the 243 keV transition is itself a multiplet complicates matters even further. Finally, the spectrum obtained by setting double gates on the 251 keV transition (lower panel) shows a spectral line at the same energy as the gates, indicating that there are at least *three* 251 keV transitions in coincidence in this decay sequence! A larger data set and possibly even a 4-D data structure would be necessary to place these transitions in a consistent level scheme. Let it be emphasised that the proposed structure for band B (Fig. 4.2) is tentative.

It was not possible to firmly establish whether a link exists between bands A and B. Due to the absence of definite linking transition of known multipolarity, it was not possible to make spin and parity assignments to the levels in band B. However wherever possible DCO ratios and anisotropies were established for transitions in this band. The $\gamma-$ray energies, DCO ratios and anisotropies for transitions in band B are listed in Table 4.5. The table also lists the transition energies of $\gamma-$rays which were observed to be in coincidence with band B, but could not be placed in a consistent band structure.

One-quasiparticle bands built on the $d_{5/2}[402]5/2^+$ configuration are observed systematically in this mass region, e.g. ^{167}Ta [84]. Moreover, the CSM calculations (Section 5.2.2, Fig. 5.22) performed for ^{165}Ta suggest that the $[402]5/2^+$ routhian is the second closest to the Fermi level. These considerations make the $[402]5/2^+$ configuration a good candidate for band B.

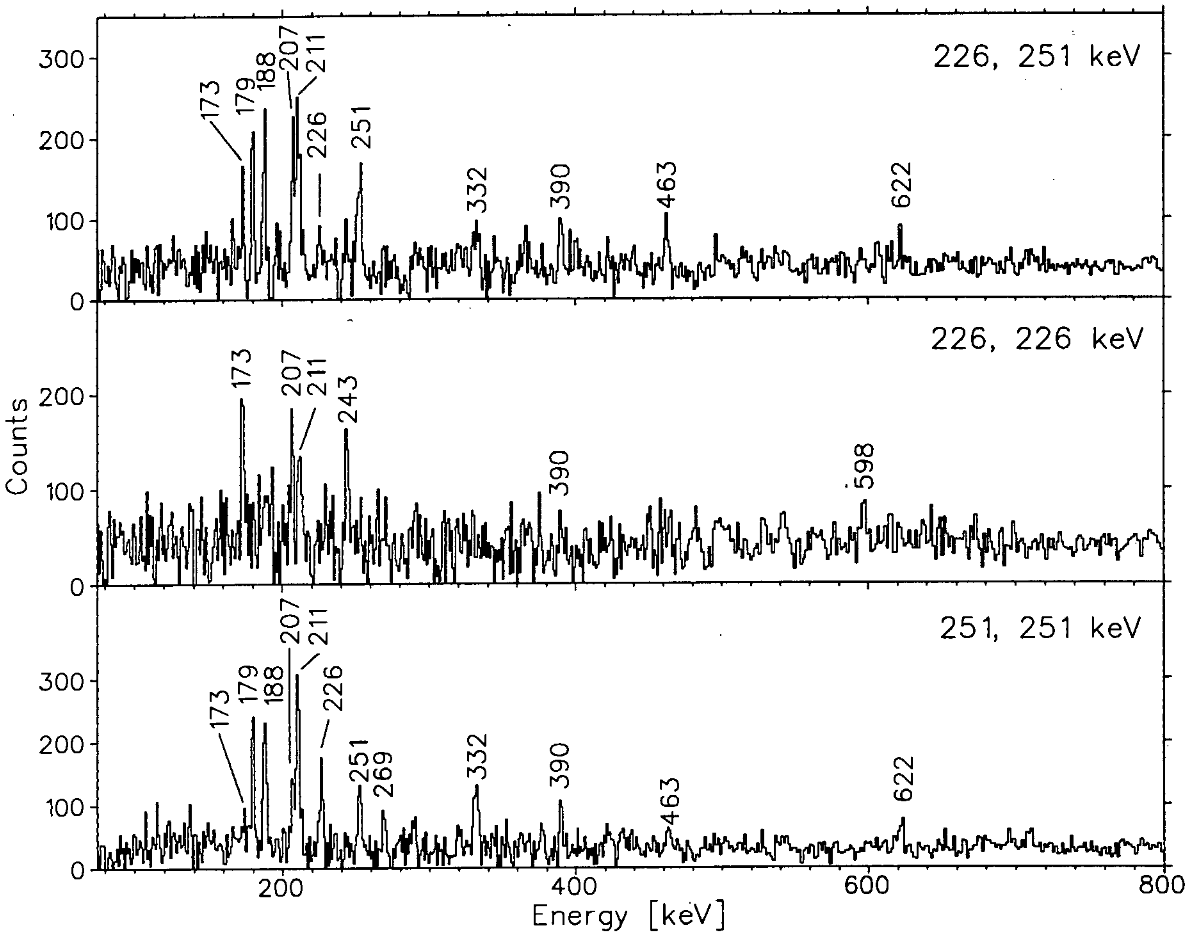

Figure 4.9: ^{165}**Ta, Band B:** Selected triple coincidence spectra. *Upper panel*: double gate on 226 and 251 keV. *Middle panel*: double gate on 226 keV. *Lower panel*: double gate on 251 keV.

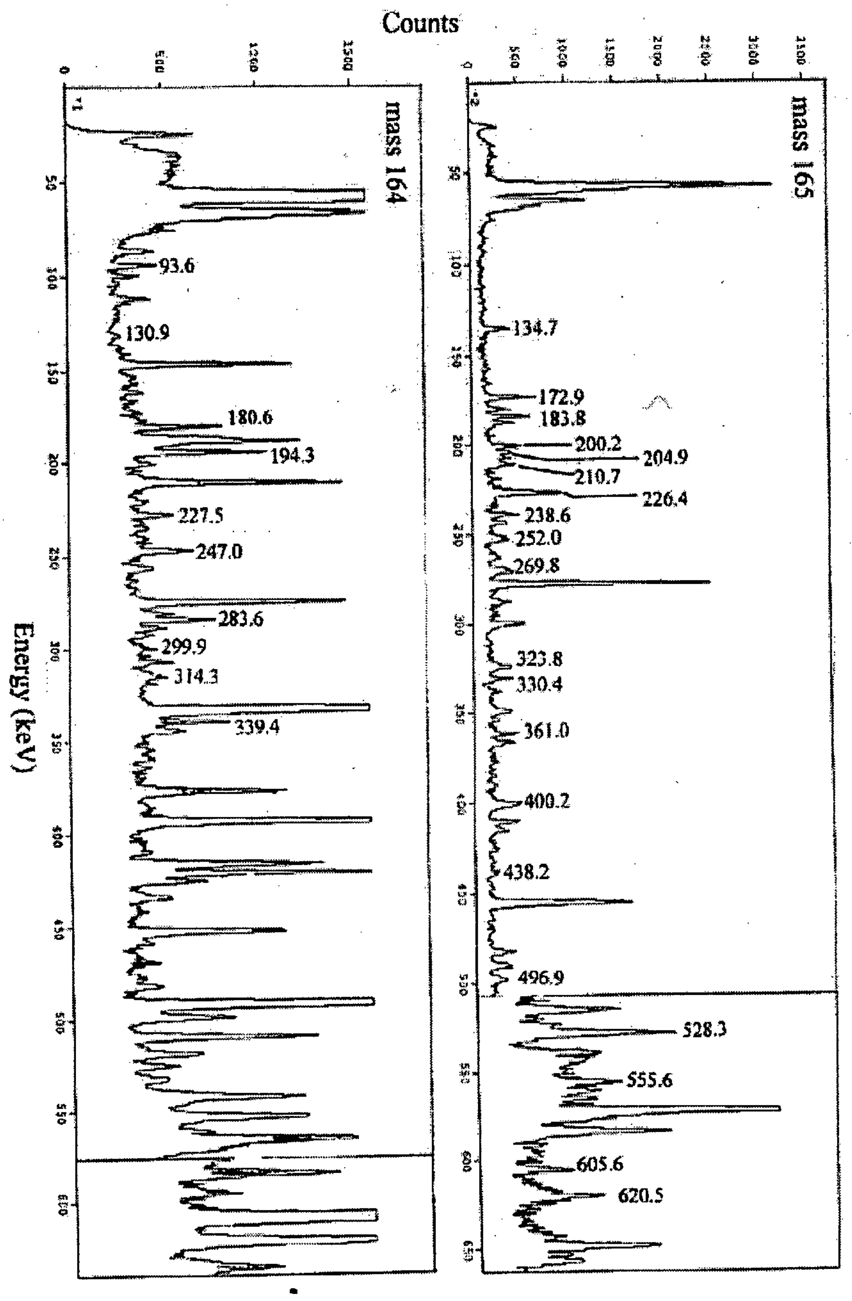

Figure 4.10: Spectrum gated on mass 165 (upper panel) and mass 164 (lower panel) recoils, using the ^{63}Cu + ^{104,106}Pd reaction reported in [83, 92]. Some of the γ−rays associated with ^{165}Ta and ^{164}Ta have been labelled. Most of the remaining strong spectral lines are associated with ^{165}W and ^{164}W.

4.4 Results for ^{164}Ta

4.4.1 Level Scheme

The two decay sequences (band A and band B) shown in Figure 4.11 were identified as belonging to ^{164}Ta, based on the present work. The relative placement of the bands is arbitrary since neither interband transitions nor transitions from these bands to the ground state could be found. Band A is the most intensely populated and carries a total intensity about four times that of band B. Although several gamma-rays from ^{164}Ta had been previously identified by Simpson *et al.* [92], no definitive decay scheme had been constructed at the time of writing.

The $\gamma-$rays in Figure 4.11 were associated with ^{164}Ta by comparing gated spectra from both sets of experimental data. As discussed in Section 4.3.1, the production yield of ^{164}Ta was expected to be considerable in the ^{142}Nd(^{27}Al,5n)^{164}Ta reaction but negligible in the ^{141}Pr(^{28}Si,5n)^{164}Ta reaction. Consequently $\gamma-$rays coincident with the Ta $x-$rays, and which were present in the first data set but not the second, could be associated with decays in ^{164}Ta.

The identification, construction and configuration of band A and band B will be discussed in the next few sections.

Band A (yrast band) The transitions 140.5 and 246.7 keV were found to be in coincidence with both the Ta $x-$rays and the transitions in band A in the first data set, but not in the second. This is illustrated in Figure 4.12, where the upper panel shows the sum of two triple coincidence spectra from the ^{142}Nd(^{27}Al,5n)^{164}Ta reaction data (first experiment), double gated on the Ta $x-$ray and the 140.5 keV transition, and the Ta $x-$ray and the 246.7 keV transition, respectively. This is to be compared with the spectrum shown in the lower panel of Figure 4.12, obtained by summing the 140.5 and 246.7 keV single gates but using the ^{141}Pr(^{28}Si,5n)^{164}Ta reaction data (second experiment). Single gates were chosen because the smaller data set obtained in the second experiment resulted in poor statistics in the triple coincidence spectra. The lower panel of Figure 4.12 shows several strong lines (marked with arrowheads) from contaminant nuclei, but it is obvious that the transitions in band A are not present in this spectrum. Band A was therefore

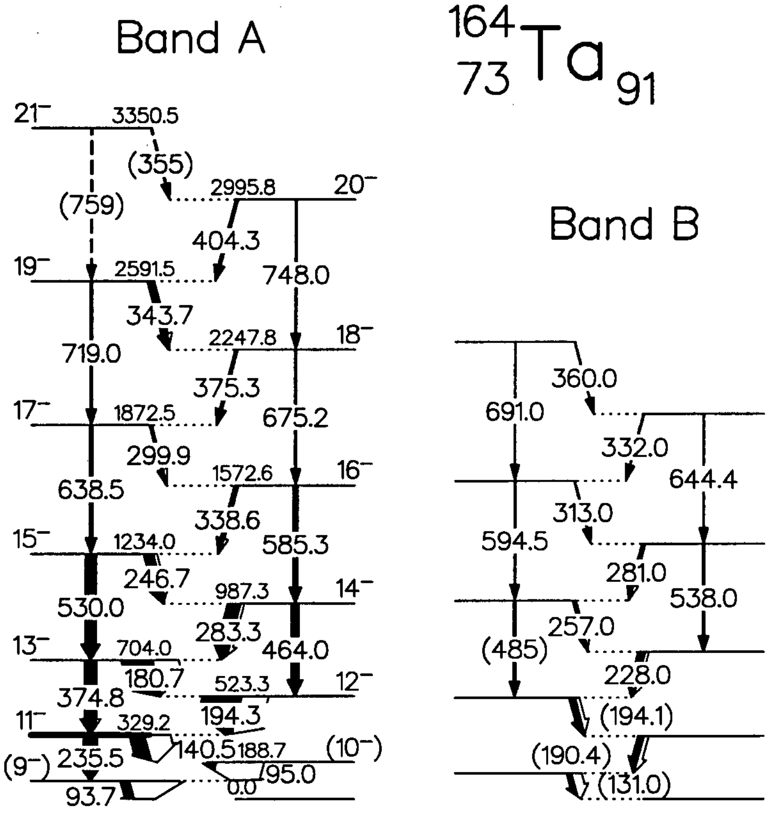

Figure 4.11: Partial level scheme of ^{164}Ta. The arrow widths reflect the transition intensities.

associated with ^{164}Ta. This conclusion is supported by an independent identification of some of these transitions with ^{164}Ta on the basis of mass 164 recoils [92, 5]. Indeed, the dominant transitions (for example at about 94, 181, 194 and 283 keV) in band A are evident in the spectrum [5] (see lower panel of Figure 4.10) obtained by gating on mass 164 residuals in the ^{63}Cu + ^{104}Pd reaction [92].

The DCO ratios for the cascade transitions in band A are close to 0.8, while DCO ratios for the in-band cross-over transitions are close to 1.3. These values are consistent with dipole and quadrupole transitions, respectively. The assignment of either stretched electric or stretched magnetic character to most of the transitions in this band is supported by linear polarisation measurements. The DCO ratios and anisotropies for the transitions (235.5, 140.5 and ~94 keV) below the level at 329 keV (subsequently assigned a spin and parity 11^-) were found to be perturbed. For example, a DCO ratio of 0.80(6) and an anisotropy of -0.03(1) was measured for the 235.5 keV transition, close to the values expected for a stretched magnetic dipole transition. However from a systematics point of view we expect the 235.5 keV γ-ray to be an E2 transition, while 140.5 keV and 95 keV are expected to have M1 character. Moreover the 235.5 keV transition is observed to be parallel to both the 140.5 and 95 keV transitions, which are mutually coincident. Therefore the nature of these transitions (and consequently also the I^π of the two lowest observed levels of band A) have been tentatively assigned from systematics considerations.

The transition intensities were determined using the method described above (Section 4.3.1) for ^{165}Ta. Below the 11^- level there is a marked reduction of the measured gamma intensity. The sum of the intensities of the 235.5 and 140.5 keV transitions depopulating the 11^- level is about 47% of that feeding the level.

We have found (see Section 4.5) that the 11^- level is isomeric. This is the first time that a nanosecond isomeric level has been found in the odd-odd tantalum or lutetium isotopes. The existence of an isomer can explain the "lost" gamma intensity below the 11^- level as well as the perturbation of the DCO ratios for the transitions depopulating the level. It is worth noting that a similar drastic reduction in gamma intensity has also been measured in neighbouring doubly-odd nuclei, and was considered as possibly due unseen low-energy transitions [93, 94]. For example the $N = 91$ isotone ^{162}Lu exhibits a loss of about 88% of the gamma intensity below the 11^- yrast level [93].

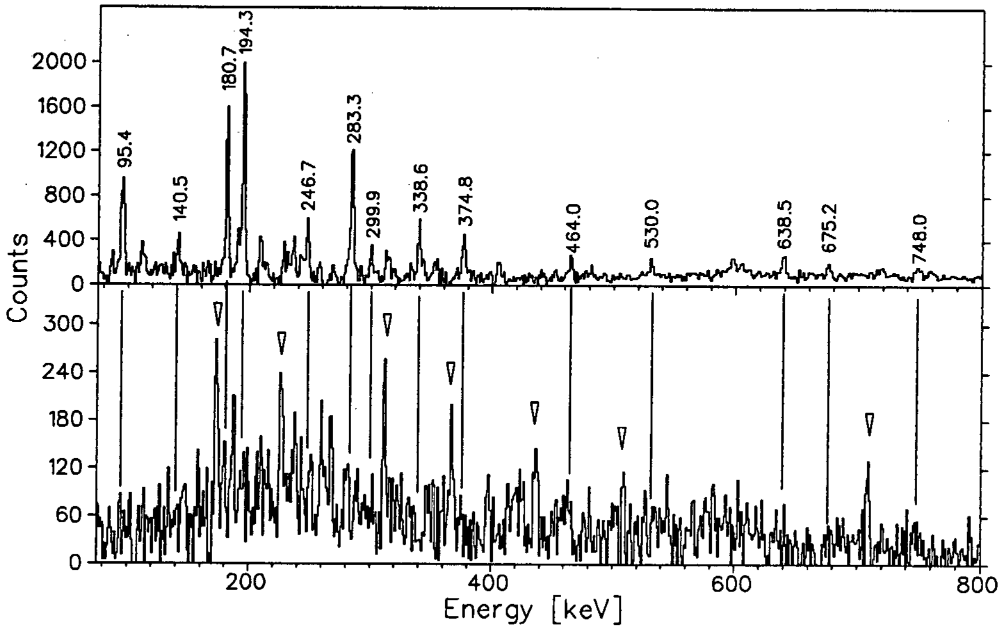

Figure 4.12: ^{164}**Ta, Band A:** *Upper panel:* Summed triple coincidence spectrum obtained from the ^{142}Nd(^{27}Al,5n)^{165}Ta reaction data by summing double gates on the Ta x−ray and 140.5 keV, and the Ta x−ray and the 246.7 keV transition, respectively. *Lower panel:* Sum of gates set at 140.5 and 246.7 keV, using the ^{141}Pr + ^{28}Si reaction data. Vertical lines show up the "missing" peaks in the lower spectrum.

Band A was assigned the configuration $\pi h_{11/2}[514]9/2^- \otimes \nu i_{13/2}$, and the 329 keV level a I^π value of 11^-, based on the following arguments:

(i) Since band A is the most intensely populated one, is likely to be yrast. The yrast bands of the neighbouring doubly odd light rare-earth nuclei, for example $^{156-162}$Ho, $^{158-166}$Tm, $^{160-166}$Lu [93] and $^{166-170}$Ta [82, 84, 95], are known to be built on the $\pi h_{11/2} \otimes \nu i_{13/2}$ configuration. It is therefore likely that the yrast band of ^{164}Ta is built on the same configuration.

(ii) In order to identify the possible Nilsson configuration for the yrast band in the odd-odd ^{164}Ta nucleus, the configuration of the participating proton (neutron) in the yrast bands of the neighbouring odd-Z (odd-N) nuclei is considered. The yrast bands of the odd-A isotopes ^{165,167}Ta$_{92,94}$ [12, 84] and ^{161,163}Lu$_{90,92}$ [96, 97] have been assigned to the configuration $\pi h_{11/2}[514]9/2^-$below the bandcrossing. On the other hand, the yrast band of ^{163}Hf$_{91}$[98] is known to be built on a highly aligned $\nu i_{13/2}$ orbital. Therefore the most likely scenario for ^{164}Ta is that the yrast band is built on a $h_{11/2}[514]9/2^-$ proton coupled with a low-Ω $i_{13/2}$ neutron.

(iii) As mentioned in Section 5.2.2, CSM calculations predict that the $\pi h_{11/2}[514]9/2^-$ routhian lies closest to the proton Fermi surface. Further, of the available highly aligned positive parity orbitals, $\nu i_{13/2}[660]1/2^+$ and $\nu i_{13/2}[651]3/2^+$ are expected to lie closest to the neutron Fermi surface, the former being closer. This may be seen in Figure 5.21. As a result the most probable configuration for band A must be $\pi h_{11/2}[514]9/2^- \otimes \nu i_{13/2}[660]1/2^+$. It should be remembered however that the above positive parity orbitals will become increasingly mixed at high rotational frequencies.

(iv) Because no low-spin states in ^{164}Ta were known, the spin and parity of the levels were assigned on the basis of systematics. It was assumed that the excitation energy of the levels with the same spin in the $\pi h_{11/2} \otimes \nu i_{13/2}$ yrast bands of a chain of odd-odd isotopes (isotones) varies smoothly with neutron (proton) number. Indeed such behaviour is observed for these bands of the neighbouring odd-odd $_{71}$Lu and $_{69}$Tm isotopes, as shown in Figure 4.14. Our data follow the smooth trend of the excitation energies of the odd-odd $_{73}$Ta isotopes and the odd-odd $N = 91$ isotones (Fig. 4.15) only if the spin and parity of the 329 keV level of the band are assumed to be 11^-. The γ−ray energies, intensities, spin assignments, DCO ratios and polarisation anisotropies for transitions in band A are

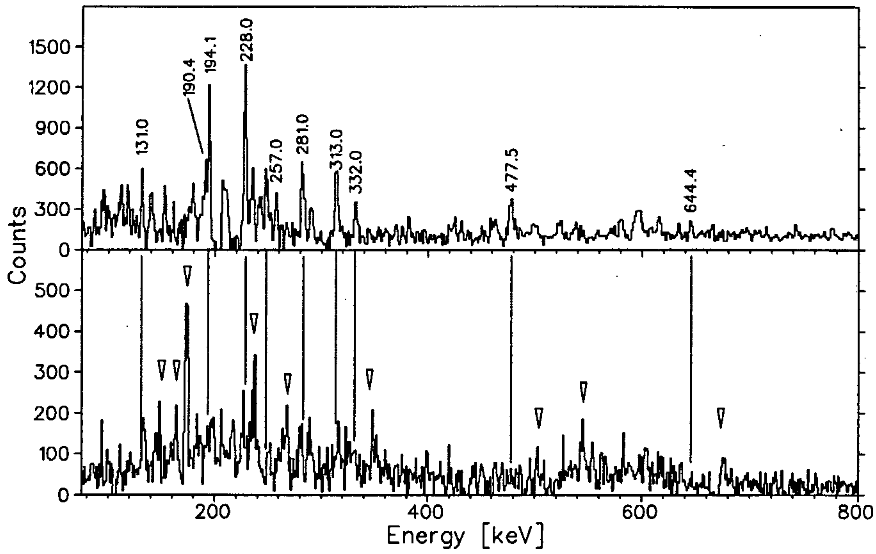

Figure 4.13: ^{164}**Ta, Band B:** *Upper panel*: triple coincidence spectrum obtained from the ^{142}Nd+^{27}Al reaction data by summing double gates set on the Ta $x-$ray and 190 keV, and the Ta $x-$ray and 257 keV, respectively. *Lower panel*: the spectrum obtained from the ^{141}Pr + ^{28}Si reaction data by summing gates at 190 and 257 keV. The spectral lines (labelled) associated with ^{164}Ta band B, in the upper panel, do not appear in the spectrum shown in the lower panel. The "missing" peaks are shown up by the vertical lines.

given in Table 4.5.

It should be noted however that the spin assignments in these nuclei are very controversial and should therefore be treated with caution. The spins of the levels of the $\pi h_{11/2} \otimes \nu i_{13/2}$ bands are frequently assigned on the basis of systematics and thus an initial incorrect spin assignment may be propagated along a chain of isotopes or isotones, undetected. A recent revision [99] of the spins of the $\pi h_{11/2} \otimes \nu i_{13/2}$ bands in the A $\sim$ 160 nuclei, for example, has reassigned the spins in ^{156}Tb and ^{158}Ho based on the assumption that the kinematic moment of inertia $J^{(1)}(I)$ is expected to increase smoothly with neutron number. An attempt was made in the present work to apply the same method

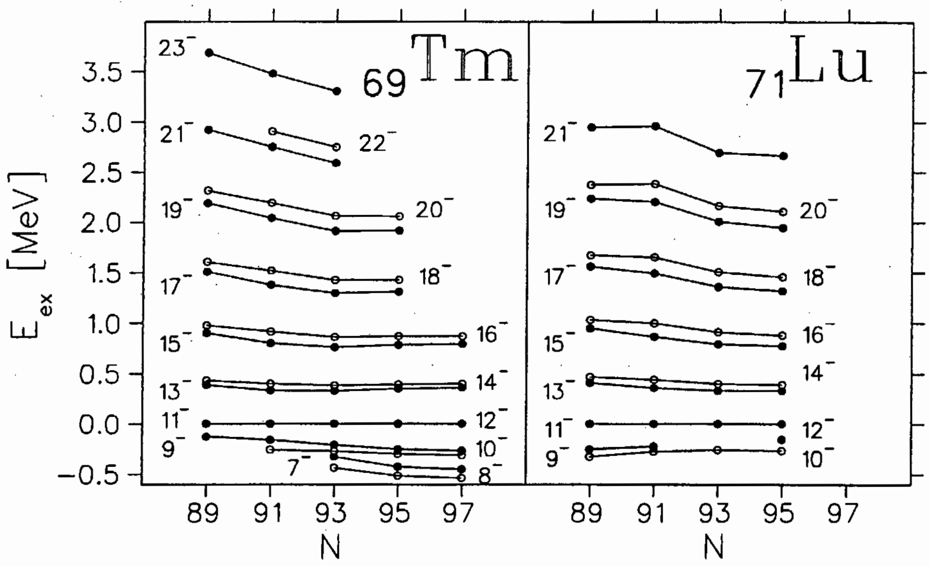

Figure 4.14: Excitation energy systematics of the $(h_{11/2})_p(i_{13/2})_n$ band in the $_{69}$Tm and $_{71}$Lu doubly odd isotopes.

to the doubly odd nuclei with $67 \leq Z \leq 73$ and $89 \leq N \leq 97$. However it was found that in each case $J^{(1)}(I)$ initially increased and then decreased with increasing neutron number, making it difficult to detect any smooth trend. The method therefore appears to be unsuited to the isotopes in this mass region.

Band B Band B was assigned to ^{164}Ta in much the same way as the yrast band, viz. by comparing summed spectra obtained by setting gates on some of the γ-rays in this band, in both sets of experimental data. The spectra obtained in this way are shown in Figure 4.13. The upper panel of Figure 4.13 shows the triple coincidence spectrum obtained from the ^{142}Nd + ^{27}Al reaction data (first experiment) by summing spectra double-gated on the Ta x−ray and 190 keV, and the Ta x−ray and 257 keV, respectively. In this spectrum the stronger transitions in band B have been labelled with their respective energies. The spectrum shown in the lower panel of Figure 4.13 was obtained from the ^{141}Pr + ^{28}Si reaction data (second experiment) by summing the 190 and 257 keV gates. Single gated spectra from the second data set were used on account of the poor statistics in the double gated spectra. It is obvious that the strong, labelled transitions visible in

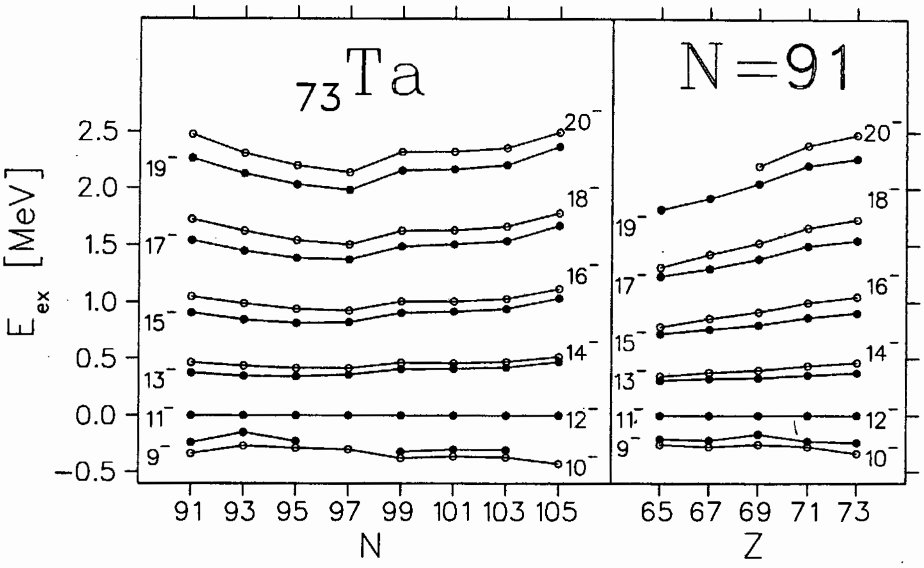

Figure 4.15: Excitation energy systematics of the $(h_{11/2})_p(i_{13/2})_n$ band in the $_{73}$Ta doubly odd isotopes and the doubly odd $N = 91$ isotones.

the upper panel do not occur in the lower panel, where the ”missing” peaks are shown up by the vertical lines. Since no ^{164}Ta was expected among the reaction products in the ^{141}Pr + ^{28}Si reaction, band B was assigned to ^{164}Ta. However only the 131 keV transition appears in the mass-gated spectrum shown in Figure 4.10, probably due to the weakness of this band. While it is certain that the 131.0, 190.4 and 194.1 keV transitions are in coincidence with band B, it was extremely difficult to place them correctly in the level scheme. The presence of ”parallel” E2 crossover transitions may have assisted in placing these transitions, but none was observed. The ordering of these γ−rays is therefore tentative. Two strong transitions of about 478 and 580 keV, as well as several weaker transitions, were also observed to belong to this decay sequence but could not be placed in a consistent level scheme. The γ−ray energies, intensities, spin assignments, DCO ratios and polarisation anisotropies for band B are listed in Table 4.6. It was not possible to establish a transition linking band B to either the yrast band, or the ground state. Consequently no reliable spin and parity assignments could be assigned to the levels in band B.

In order to speculate on a possible configuration of this band, it was compared with other non-yrast, semi-decoupled bands observed in the immediate doubly-odd neighbours. Two such bands, labelled band B and band C by Gupta *et al.* [93] were observed in the neighbouring $N = 91$ isotone ^{162}Lu. The $\gamma-$ray energies in band B of ^{164}Ta are strikingly similar to those of ^{162}Lu band B. A comparison of the staggering amplitude ΔE (defined in eq. 5.8) in band B of ^{164}Ta with that of bands B and C in ^{162}Lu respectively, emphasises the similarity between bands B in both these nuclei. Figure 4.16 shows the energy staggering of these three bands as a function of rotational frequency. It shows that the phase of the energy staggering in band B of both nuclei undergoes a change at about $\hbar\omega = 0.25$ MeV, unlike that of ^{162}Lu band C (upper panel), where there is no phase change at this frequency. Further, Figure 4.16 also shows that the staggering amplitude at $\hbar\omega = 0.25$ MeV is comparable in bands B of both nuclei (16 and 19 keV for ^{164}Ta and ^{162}Lu respectively), but that it is approximately only half that observed in ^{162}Lu band C at the same frequency.

The similarity between band B of ^{164}Ta and band B of ^{162}Lu also becomes apparent from a comparison of how the level excitation energies of these bands vary as a function of spin. Two quantities are defined for this purpose:

$$\Delta E_{BB}(I) = |E_{ex,{}^{164}Ta\,B}(I) - E_{ex,{}^{162}Lu\,B}(I)| \tag{4.2}$$

and

$$\Delta E_{BC}(I) = |E_{ex,{}^{164}Ta\,B}(I) - E_{ex,{}^{162}Lu\,C}(I)| \tag{4.3}$$

where $E_{ex,{}^{162}Lu\,B}(I)$, for example, represents the excitation energy relative to the 17^+ level in ^{162}Lu band B. For ^{164}Ta band B the level populated by the 131.0 keV transition was used as a reference. Figure 4.17 shows a plot of $\Delta E_{BB}(I)$ and $\Delta E_{BC}(I)$ as a function of spin. The smooth variation of $\Delta E_{BB}(I)$ (contrasted with the zig-zag variation of $\Delta E_{BC}(I)$) again points to the similarity between bands B in both these nuclei.

The above considerations suggest that ^{164}Ta band B may possibly be associated with the same intrinsic configuration as its analogue in ^{162}Lu. This band was associated with a four-quasiparticle structure involving the coupling of the odd neutron and proton with a pair of aligned quasiparticles ($i_{13/2}$ quasineutrons), and was assigned the configuration $\pi h_{11/2} \otimes \nu h_{9/2} \otimes (\nu i_{13/2})^2$ [93]. It is therefore possible that ^{164}Ta band B may also be of positive parity and have a similar four-quasiparticle structure.

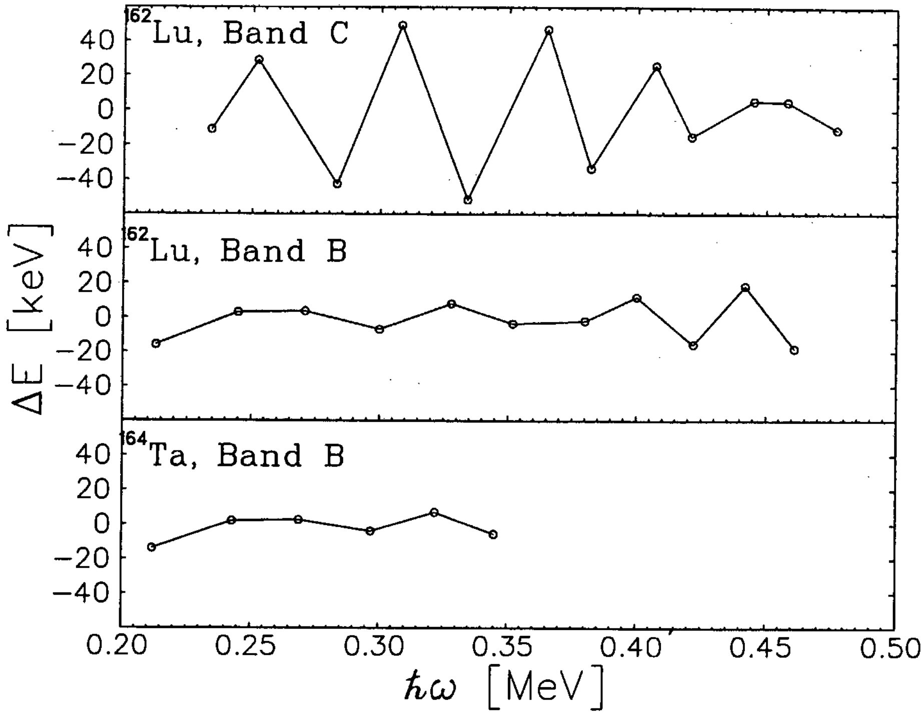

Figure 4.16: Energy staggering plots for ^{164}Ta band B, and ^{162}Lu bands B and C.

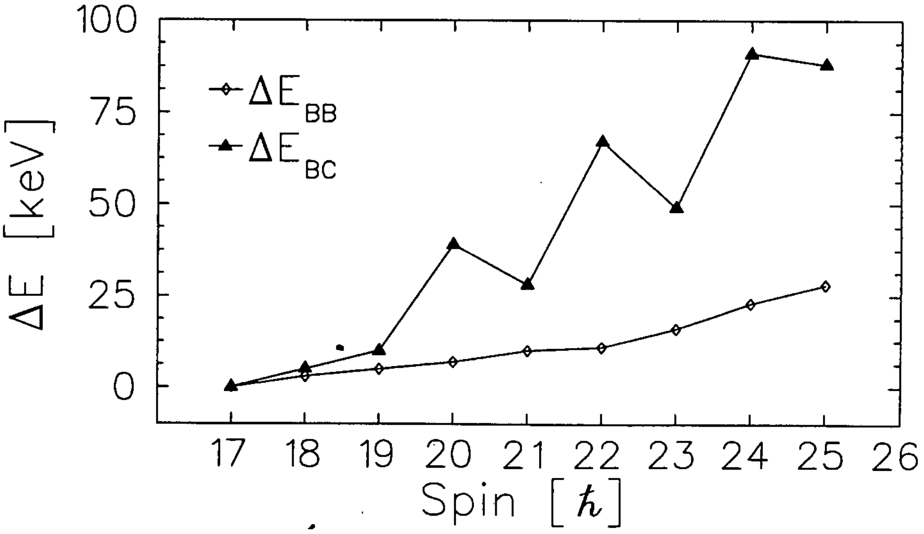

Figure 4.17: Plots of $\Delta E_{BB}(I)$ and $\Delta E_{BC}(I)$ as defined in eq. 4.2 and 4.3.

4.5 Lifetime measurements

No delayed transitions were found in the TDC data, meaning that if any isomers exist their lifetimes should be smaller than ~ 10 ns or longer than the 200 ns range of the TDC. RSAM as described in [11] was therefore used to search for nanosecond isomeric states in ^{164,165}Ta and ^{162}Lu. Two new isomeric states were discovered, in ^{164}Ta and ^{162}Lu. Only the data from the first (thin target) experiment were suitable for RSAM since the second experiment employed a target sufficiently thick to stop the residual nuclei. RSAM was performed by measuring spectra consisting of gamma rays, coincident with a gate set on the tantalum x−ray (lutetium x−ray), which had deposited their full photopeak energy in single Clover elements located at either 84° (shadowed spectra) or 96° (unshadowed spectra) to the beam axis. The experimental anisotropies A for transitions were calculated from the expression

$$A = \frac{N_U - \alpha N_S}{N_U + \alpha N_S} \tag{4.4}$$

with relative efficiency $\alpha = 0.845$, where N_U denotes the number of γ−rays detected in the unshadowed Clover elements, and N_S the number detected in the shadowed elements. The sum and difference spectra (corresponding to denominator and numerator of the above expression), gated on the tantalum and lutetium x−rays respectively, are shown in Figures 4.18 and 4.19. The measured anisotropies for selected transitions in ^{165}Ta, ^{164}Ta and ^{162}Lu are listed in Tables 4.7, 4.8 and 4.9, placed at the end of this chapter. At the time of writing, the calibration of AFRODITE to extract lifetimes from the anisotropy measurements was not yet complete.

No isomeric states were observed in ^{165}Ta. The anisotropies for all transitions in ^{165}Ta listed in Table 4.7 are less than ~ 4%. However, the lower panel of Figure 4.18, showing the difference spectrum obtained by gating on the tantalum x−ray, clearly shows that the 95, 140.5 and 235.5 keV transitions in ^{164}Ta are substantially delayed. The respective anisotropies for these transitions are 16.7(7)%, 36.7(39)% and 26.7(7)%, while the anisotropies for the remaining transitions in band A are less than ~ 3%, as may be seen in Table 4.8. Because the delayed transitions are all located below the 11^- yrast level of ^{164}Ta, and because all transitions above this level are prompt, this is an indication that the 11^- level is isomeric. The anisotropy is greatest for the transitions directly depopulating the 11^- level viz. 140.5 and 235.5 keV, while that for 95.0 keV is somehow

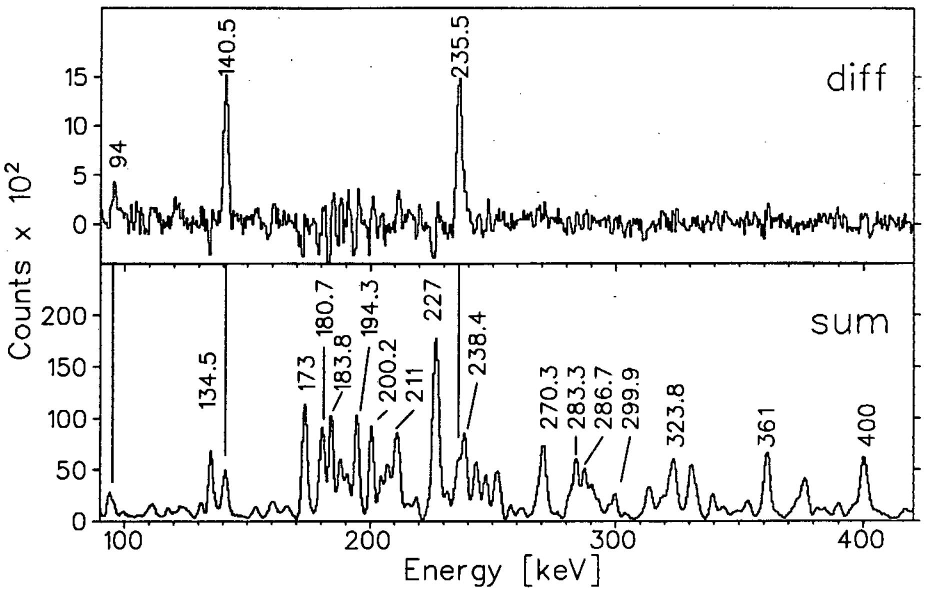

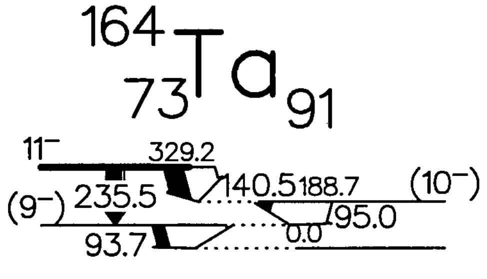

Figure 4.18: Above: summed (upper panel) and difference (lower panel) spectra, gated on the Ta x−ray. The vertical lines indicate delayed transitions below the 11^- state in ^{164}Ta *viz.* 140.5, 235.5 and ~94 keV.

smaller, probably on account of side-feeding. The low-lying yrast states of ^{164}Ta have also been included in Figure 4.18 so that the placement of the delayed transitions may easily be seen.

A similar situation exists in the $N = 91$ isotone, ^{162}Lu. The lower panel of Figure 4.19 shows the difference spectrum obtained by gating on the lutetium $x-$ray. It is obvious from this spectrum that several transitions are considerably delayed viz. 97, 143.6, 108.0, 164.4 and 268.3 keV. The respective anisotropies are 37.7(17)%, 37.6(15)%, 18.5(11)%, 25.8(46)%, and 12.9(3)%. All of these transitions have been associated with decays in the yrast band of ^{162}Lu. Although there is no consensus on the exact placement of these transitions in the band, they were all consistently placed below the 11^- level by different authors (see for example references [93, 100, 101, 102]). This may be seen in the lower part of Figure 4.19, which shows some of the low-lying yrast states of ^{162}Lu observed to be consistent with our own experimental data. The exact ordering of the multiple parallel transitions below the 11^- level is very difficult on account of energy multiplets. Tentatively placed transitions have been placed in parentheses. In contrast, the transitions occuring above the 11^- level do not appear to be delayed. The anisotropies for these transitions, listed in Table 4.9, are less than $\sim 6\%$, i.e. considerably smaller than those for the delayed transitions. This indicates that the 11^- yrast level of ^{162}Lu is also isomeric.

It should be noted that the anisotropies discussed above were obtained by gating on the respective $x-$rays, and not on the transition directly feeding the isomeric states. It is natural to ask why this was not done, as it would have allowed the anisotropies to be measured while excluding side-feeding. However in both ^{164}Ta and ^{162}Lu the strong transitions (194.3 and 195.6 keV respectively) populating the 11^- yrast states were energy doublets in their respective bands. They were therefore unsuitable for gating. A further attempt to perform RSAM, by setting double gates on one of the above transitions and the respective $x-$ray, was unsuccessful on account of the low counts in the double gated spectra.

The presence of the 11^- isomeric state raises the question about the position of the bandhead. Because a similar isomer had never been observed in any of the neighbouring nuclei, the band was considered to continue down to lower spins. Measurements of the transition probabilities of the delayed $\gamma-$rays is therefore essential in order to determine if

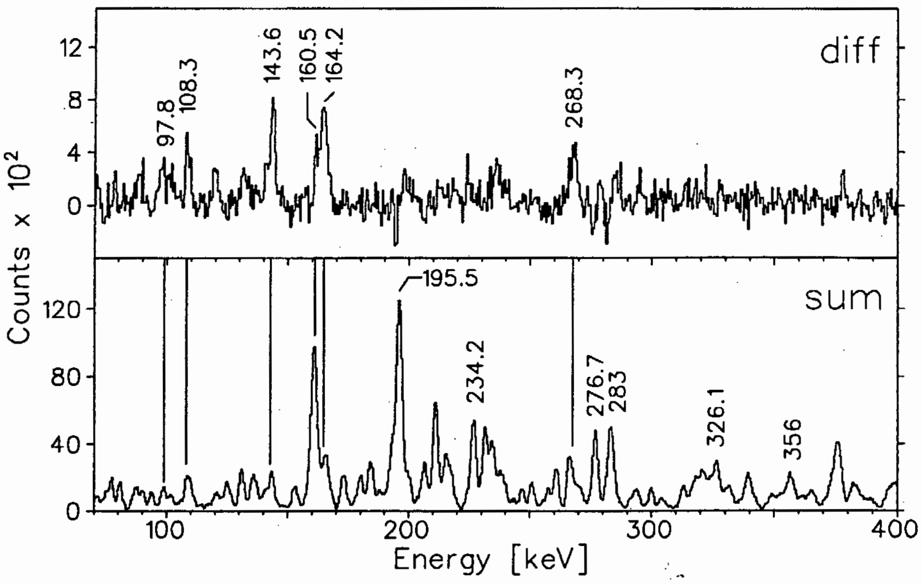

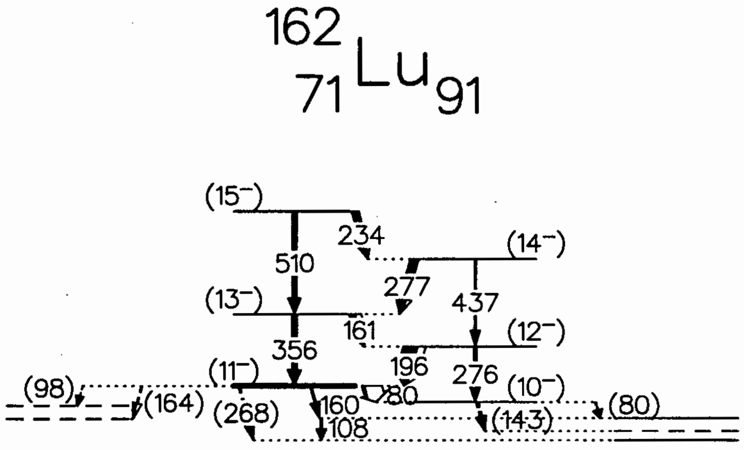

Figure 4.19: Above: summed (upper panel) and difference (lower panel) spectra, gated on the Lu x−ray. The vertical lines indicate delayed transitions below the 11^- state in ^{162}Lu. These are also shown in lower portion of the yrast band, below.

the 11^- level can be considered to be the bandhead. A determination of the bandhead spin would supply important information on the mode of coupling of the two quasiparticles, $\nu i_{13/2}$ and $\pi h_{11/2}$. Further, a study of the decay of the yrast band below the isomeric level, down to the $I^\pi = 3^+$ ground state, is needed to firmly establish the spins of the band.

Table 4.3: Level energies, spin assignments, γ-ray transition energies, intensities, branching ratios, $B(M1)/B(E2)$ ratios, DCO ratios and the anisotropy in the yrast band (band A) of ^{165}Ta.

E_{ex} (keV)^a)	Initial $\rightarrow$ final spin	E_γ (keV)^b)	I_γ ^{c})	Branching Ratio ^{d})	$B(M1)/B(E2)^e$	DCO ratio $\frac{I_\gamma(45^\circ)}{I_\gamma(90^\circ)}$	A $\frac{N_V-\alpha N_H}{N_V+\alpha N_H}$ ^{h})
70.6	$\frac{11}{2}^- \rightarrow \frac{9}{2}^-$	70.6	206(43)			1.01(20)	^{f})
297.3	$\frac{13}{2}^- \rightarrow \frac{9}{2}^-$	297.3	181(80)	0.12(06)	1.16(54)	^{f})	^{f})
	$\frac{13}{2}^- \rightarrow \frac{11}{2}^-$	226.7	1506(211)			1.06(15)^g)	-0.08(1)
470.1	$\frac{15}{2}^- \rightarrow \frac{11}{2}^-$	399.5	1133(226)	1.43(40)	0.96(26)	1.02(14)^g)	+0.07(1)
	$\frac{15}{2}^- \rightarrow \frac{13}{2}^-$	172.8	790(150)			0.90(13)	-0.14(2)
793.9	$\frac{17}{2}^- \rightarrow \frac{13}{2}^-$	496.6	456(46)	0.58(15)	1.07(28)	1.54(30)^g)	+0.06(1)^g)
	$\frac{17}{2}^- \rightarrow \frac{15}{2}^-$	323.8	787(189)			0.80(15)^g)	-0.10(1)
997.9	$\frac{19}{2}^- \rightarrow \frac{15}{2}^-$	527.8	1978(59)	4.33(62)	0.78(11)	1.16(19)	+0.07(1)
	$\frac{19}{2}^- \rightarrow \frac{17}{2}^-$	204.0	457(64)			0.68(19)	^{f})
1399.2	$\frac{21}{2}^- \rightarrow \frac{17}{2}^-$	605.3	572(132)	0.91(29)	0.96(31)	^{f})	^{f})
	$\frac{21}{2}^- \rightarrow \frac{19}{2}^-$	401.3	626(138)			1.02(14)^g)	-0.07(1)
1618.4	$\frac{23}{2}^- \rightarrow \frac{19}{2}^-$	620.5	1790(54)	8.91(93)	0.68(07)	1.28(20)	+0.07(1)
	$\frac{23}{2}^- \rightarrow \frac{21}{2}^-$	219.2	201(20)			0.62(10)	^{f})
2070.9	$\frac{25}{2}^- \rightarrow \frac{21}{2}^-$	671.7	437(136)	0.88(30)	1.18(40)	^{f})	^{f})
	$\frac{25}{2}^- \rightarrow \frac{23}{2}^-$	452.5	499(65)			0.84(17)	-0.05(1)
2294.9	$\frac{27}{2}^- \rightarrow \frac{23}{2}^-$	676.5	1606(209)	6.35(101)	1.38(22)	1.25(17)	+0.06(1)
	$\frac{27}{2}^- \rightarrow \frac{25}{2}^-$	224.0	253(23)			^{f})	^{f})
2655.4	$\frac{29}{2}^- \rightarrow \frac{25}{2}^-$	584.5	775(109)	0.87(24)	1.16(32)	1.49(30)	+0.03(1)
	$\frac{29}{2}^- \rightarrow \frac{27}{2}^-$	361.0	890(214)			0.84(12) ^{g})	-0.11(1)
2790.9	$\frac{31}{2}^- \rightarrow \frac{27}{2}^-$	496.0	862(78)	1.39(17)	6.18(75)	1.54(30)^g)	+0.06(1)
	$\frac{31}{2}^- \rightarrow \frac{29}{2}^-$	134.5	619(50)			0.85(12)	^{f})
2974.7	$\frac{33}{2}^- \rightarrow \frac{29}{2}^-$	(319)	$\leq$40	$\leq$0.04	$\geq$12.1	^{f})	^{f})
	$\frac{33}{2}^- \rightarrow \frac{31}{2}^-$	183.8	1000(80)			0.78(11)	-0.15(3)
3173.9	$\frac{35}{2}^- \rightarrow \frac{31}{2}^-$	384.0	229(41)	0.29(06)	2.54(50)	^{f})	^{f})
	$\frac{35}{2}^- \rightarrow \frac{33}{2}^-$	200.2	801(64)			0.83(12)	-0.22(3)

E_{ex} (keV)a)	Initial → final spin	E_γ (keV)b)	I_γ c)	Branching Ratio d)	$B(M1)/B(E2)$e	DCO ratio $\frac{I_\gamma(45^\circ)}{I_\gamma(90^\circ)}$	A $\frac{N_V-\alpha N_H}{N_V+\alpha N_H}$ h)
3413.1	$\frac{37}{2}^- \to \frac{33}{2}^-$	438.4	449(86)	0.55(11)	1.51(29)	f)	+0.11(1)
	$\frac{37}{2}^- \to \frac{35}{2}^-$	238.4	813(24)			0.89(12)	-0.09(1)
3682.3	$\frac{39}{2}^- \to \frac{35}{2}^-$	508.4	452(162)	0.62(23)	1.93(70)	f)	+0.08(1)
	$\frac{39}{2}^- \to \frac{37}{2}^-$	270.3	727(51)			0.78(11)	-0.09(1)
3970.1	$\frac{41}{2}^- \to \frac{37}{2}^-$	557.0	454(64)	0.82(12)	1.93(28)	0.93(38)	+0.18(1)
	$\frac{41}{2}^- \to \frac{39}{2}^-$	286.7	551(220)			0.81(11)	-0.08(1)
4291.1	$\frac{43}{2}^- \to \frac{39}{2}^-$	608.8	338(68)	0.71(21)	2.45(72)	f)	f)
	$\frac{43}{2}^- \to \frac{41}{2}^-$	322.1	475(101)			0.80(15)g)	-0.10(1)
4622.4	$\frac{45}{2}^- \to \frac{41}{2}^-$	652.3	421(59)	1.01(15)	2.27(35)	1.25(25)	+0.11(2)
	$\frac{45}{2}^- \to \frac{43}{2}^-$	330.3	418(25)			0.78(12)	-0.18(1)
4982.9	$\frac{47}{2}^- \to \frac{43}{2}^-$	691.8	228(93)	0.53(24)	4.45(202)	f)	+0.07(1)
	$\frac{47}{2}^- \to \frac{45}{2}^-$	360.5	430(86)			0.84(12)g)	-0.11(1)
5355.6	$\frac{49}{2}^- \to \frac{45}{2}^-$	733.2	167(43)	0.64(18)	4.47(123)	1.50(30)	f)
	$\frac{49}{2}^- \to \frac{47}{2}^-$	372.4	261(25)			f)	f)
5752.3	$\frac{51}{2}^- \to \frac{47}{2}^-$	769.4	122(20)			f)	f)
6168.3	$\frac{53}{2}^- \to \frac{49}{2}^-$	812.7	129(30)			f)	f)

a)Relative to the $\frac{9}{2}^-$ level.

b)Uncertainties: 0.3 keV, but up to 1.0 keV for weak transitions and multiple lines.

c)Normalised to the 183.8 keV $\frac{33}{2}^- \to \frac{31}{2}^-$ transition. Uncertainties: 5-10% for weak transitions, and up to 50% for multiple lines.

d)$\lambda = I_\gamma(I \to I-2)/I_\gamma(I \to I-1)$.

e)Determined assuming $\delta^2 = 0$.

f)Could not be determined due to poor statistics.

g)Unresolved doublet. DCO ratio is for total peak.

h)$\alpha = 0.994$.

Table 4.4: A list of the γ−ray transition energies in coincidence with band B of ^{165}Ta. Many of these transitions could not be placed in the level scheme. The DCO ratios and polarisation anisotropy are given where possible.

E_γ	DCO ratio	A
(keV)^{a})	$\frac{I_\gamma(45°)}{I_\gamma(90°)}$	$\frac{N_V-\alpha N_H}{N_V+\alpha N_H}$ ^{b})
123.5	^{d})	^{d})
137	^{d})	^{d})
173^{c})	0.82(12)	-0.14(2)
180^{c})	0.81(8)	-0.05(2)
187^{c})	0.66(6)	^{d})
206.5	1.02(13)	^{d})
210^{c})	0.97(6)	^{d})
226^{c})	1.08(7)	-0.08(1)
243^{c})	^{d})	-0.08(2)
251^{c})	0.85(6)	-0.18(2)
268	^{d})	^{d})
289.4	^{d})	^{d})
332^{c})	^{d})	-0.18(2)
376	^{d})	-0.02(1)
389.4	^{d})	^{d})
398^{c})	^{d})	^{d})
432^{c})	^{d})	^{d})
437.1	^{d})	^{d})
462^{c})	1.59(16)	+0.07(1)
497	^{d})	+0.06(1)
503.2	1.37(25)	+0.06(1)

E_γ (keV)[a]	DCO ratio $\frac{I_\gamma(45^\circ)}{I_\gamma(90^\circ)}$	A $\frac{N_V-\alpha N_H}{N_V+\alpha N_H}$ [b]
511	[d]	[d]
515	[d]	[d]
539.0	[d]	+0.13(1)
584	1.19(14)	+0.03(1)
597	[d]	-0.05(1)
605	[d]	[d]
616	[d]	[d]
622	[d]	[d]
676	[d]	+0.06(1)
696	[d]	[d]
709	[d]	+0.11(2)
785	[d]	[d]
792	[d]	[d]

[a] Uncertainties: 0.3 keV, but up to 1.0 keV for weak transitions and multiple lines.

[b] $\alpha = 0.994$

[c] Unresolved multiplet. Energy, DCO ratio and/or anisotropy is for total peak.

[d] Could not be determined due to poor statistics.

Table 4.5: Level energies, spin assignments, γ-ray transition energies, intensities, branching ratios, B(M1)/B(E2) ratios, DCO ratios and the anisotropy for the yrast band (band A) in ^{164}Ta.

E_{ex} (keV)^{a})	Initial → final spin	E_γ (keV)^{b})	I_γ ^{c})	Branching Ratio ^{d})	$B(M1)/B(E2)^{e}$)	DCO ratio $\frac{I_\gamma(45°)}{I_\gamma(90°)}$	A $\frac{N_V-\alpha N_H}{N_V+\alpha N_H}$ ^{h})
93.7	$9^- \rightarrow$	93.7				0.91(7)^{g})	^{f})
188.7	$10^- \rightarrow 9^-$	95.0				0.91(7)^{g})	^{f})
329.2	$11^- \rightarrow (9^-)$	235.5	437(16)	1.75(8)	0.10(1)	0.80(6)	-0.03(1)
	$11^- \rightarrow (10^-)$	140.5	250(5)			0.97(5)	^{f})
523.3	$12^- \rightarrow 11^-$	194.3	1000(230)			0.84(6)^{g})	-0.13(2)^{g})
704.0	$13^- \rightarrow 11^-$	374.8	477(103)	0.65(20)	1.34(40)	^{f})	-0.02(1)^{g})
	$13^- \rightarrow 12^-$	180.7	731(148)			0.75(4)^{g})	-0.05(2)^{g})
987.3	$14^- \rightarrow 12^-$	464.0	289(58)	0.64(13)	1.03(21)	1.15(22)	+0.07(1)
	$14^- \rightarrow 13^-$	283.8	455(12)			0.85(7)	-0.11(1)
1234.0	$15^- \rightarrow 13^-$	530.0	430(40)	1.47(15)	1.33(14)	1.07(20)	^{f})
	$15^- \rightarrow 14^-$	246.7	299(14)			0.93(11)	+0.02(1)
1572.6	$16^- \rightarrow 14^-$	585.3	181(29)	1.37(27)	0.89(18)	1.32(20)^{g})	+0.03(1)^{g})
	$16^- \rightarrow 15^-$	338.6	132(15)			0.76(6)	^{f})
1872.5	$17^- \rightarrow 15^-$	638.5	127(10)	1.76(36)	1.57(32)	1.30(42)	+0.09(1)
	$17^- \rightarrow 16^-$	299.9	72(14)			0.74(10)	-0.15(2)
2247.8	$18^- \rightarrow 16^-$	675.2	62(15)	0.68(29)	2.72(116)	^{f})	+0.06(1)^{g})
	$18^- \rightarrow 17^-$	375.3	91(33)			^{f})	-0.02(1)^{g})
2591.5	$19^- \rightarrow 17^-$	719.0	83(37)	0.94(43)	3.55(164)	1.67(26)	+0.13(2)
	$19^- \rightarrow 18^-$	343.7	88(12)			0.64(13)	^{f})

E$_{ex}$ (keV)[a])	Initial → final spin	E$_\gamma$ (keV)[b])	I_γ [c])	Branching Ratio [d])	$B(M1)/B(E2)$[e])	DCO ratio $\frac{I_\gamma(45^\circ)}{I_\gamma(90^\circ)}$	A $\frac{N_V-\alpha N_H}{N_V+\alpha N_H}$ [h])
2995.8	$20^- \to 18^-$	748.0	60(8)	0.54(8)	4.54(64)	1.10(16)	[f])
	$20^- \to 19^-$	404.3	110(3)			0.85(12)	[f])
3350.5	$21^- \to 19^-$	(759)				[f])	[f])
	$21^- \to 20^-$	(355)				[f])	[f])

[a]) Relative to the lowest observed level in the decay sequence.

[b]) Uncertainties: 0.3 keV, but up to 1.0 keV for weak transitions and multiple lines.

[c]) Normalised to the 194.3 keV $12^- \to 11^-$ transition. Uncertainties: 5-10% for weak transitions, and up to 50% for multiple lines.

[d]) $\lambda = I_\gamma(I \to I-2)/I_\gamma(I \to I-1)$.

[e]) Determined assuming $\delta^2 = 0$.

[f]) Could not be determined due to poor statistics.

[g]) Unresolved doublet. DCO ratio and/or anisotropy is for total peak.

[h]) $\alpha = 0.994$.

Table 4.6: Level energies, spin assignments, γ-ray transition energies, intensities, branching ratios, $B(M1)/B(E2)$ ratios, DCO ratios and the anisotropy in ^{164}Ta band B.

E_{ex} (keV)^{a})	E_γ (keV)^{b})	I_γ ^{c})	Branching Ratio ^{d})	$B(M1)/$ $B(E2)^{e}$)	DCO ratio $\frac{I_\gamma(45°)}{I_\gamma(90°)}$	A $\frac{N_V-\alpha N_H}{N_V+\alpha N_H}$ ^{h})
131.0	131.0	67(5)			1.10(28)	^{f})
321.0	190.4	^{f})			0.65(12)	^{f})
515.0	194.1	587(278)			0.97(14)	-0.13(2)^{g})
743.0	228.0	219(76)			0.90(9)	-0.08(1)^{g})
1000.0	(485)	86(20)	1.03(31)	1.07(32)	^{f})	^{f})
1000.0	257.0	84(15)			0.71(9)	^{f})
1281.0	538.0	85(41)	0.89(66)	1.59(118)	1.69(39)	+0.13(2)
1281.0	281.0	96(54)			^{f})	^{f})
1594.0	594.5	56(33)	1.76(160)	0.95(86)	1.30(39)	-0.05(1)
1594.0	313.0	32(22)			0.99(16)	-0.18(2)
1925.0	644.4	97(18)			^{f})	^{f})
1925.0	332.0	^{f})			1.00(16)	-0.18(2)^{g})
2285.0	691.0	^{f})			1.22(28)	+0.07(2)
2285.0	360.0	^{f})			^{f})	^{f})

^{a}) Relative to the lowest observed level in Band B.

^{b}) Uncertainties: 0.3 keV, but up to 1.0 keV for weak transitions and multiple lines.

^{c}) Normalised to the 194.3 keV $12^- \rightarrow 11^-$ transition. Uncertainties: 5-10% for weak transitions, and up to 50% for multiple lines.

^{d}) $\lambda = I_\gamma(I \rightarrow I-2)/I_\gamma(I \rightarrow I-1)$.

^{e}) Determined assuming $\delta^2 = 0$.

^{f}) Could not be determined due to poor statistics.

^{g}) Unresolved doublet. DCO ratio and/or anisotropy is for total peak.

^{h}) $\alpha = 0.994$.

Table 4.7: Anisotropies determined using RSAM, expressed as percentages, for selected transitions in ^{165}Ta. Transitions energies have been listed in order of increasing spin of the depopulating level.

E_γ (keV)	Initial level I^π	Anisotropy A ($\times 100$) $A = \frac{N_U - N_S \alpha}{N_U + N_S}$ a)
227	$13/2^-$	+0.3(1) b)
173	$15/2^-$	-0.2(1) b)
400	$15/2^-$	+1.0(1) b)
323.8	$17/2^-$	+2.3(2)
527.8	$19/2^-$	+1.0(1)
620.5	$23/2^-$	+0.5(1)
452.5	$25/2^-$	+1.6(2)
676.5	$27/2^-$	+1.2(1)
361	$29/2^-$	+2.1(1) b)
134.5	$31/2^-$	+0.5(1)
496	$31/2^-$	+3.0(2) b)
183.4	$33/2^-$	+1.5(2)
200.2	$35/2^-$	+2.2(2)
238.4	$37/2^-$	+1.3(2)
438.4	$37/2^-$	+2.1(3)
270.3	$39/2^-$	+3.8(2)
286.7	$41/2^-$	+3.4(4)
557.0	$41/2^-$	+1.0(2)
206.5	c)	+0.4(1)
211.6	c)	+4.1(2)
251	c)	+1.9(1) b)

a) $\alpha = 0.845$.

b) Unresolved multiplet. Anisotropy is for total peak.

c) Band B; spins unknown.

Table 4.8: Anisotropies determined using RSAM, expressed as percentages, for selected transitions in ^{164}Ta. Transitions energies have been listed in order of increasing spin of the depopulating level.

E_γ (keV)	Initial level I^π	Anisotropy A ($\times 100$) $A = \frac{N_U - N_S}{N_U + N_S}$ [a]
95	$<11^-$	+16.7(7) [b]
140.5	11^-	+36.7(39)
235.5	11^-	+26.7(7)
194	12^-	+1.3(1) [b]
180.7	13^-	+2.3(2)
283.3	14^-	+1.4(1)
464.0	14^-	+1.1(2)
246.7	15^-	+2.9(3)
300.0	17^-	+0.8(2)
638.5	17^-	+2.1(4)
131.0	[c]	+7.3(9)
257.0	[c]	+2.0(3)
313.0	[c]	-0.6(1)

[a] $\alpha = 0.845$.

[b] Unresolved multiplet. Anisotropy is for total peak.

[c] Band B; spins unknown.

Table 4.9: Anisotropies determined using RSAM, expressed as percentages, for selected transitions in ^{162}Lu. Transitions energies have been listed in order of increasing spin of the depopulating level.

E_γ (keV)	Initial level I^π	Anisotropy A ($\times$100) $A = \frac{N_U - N_S \alpha}{N_U + N_S}$ [a]
143.6	10^-	+37.6(15)
108.0	$< 11^-$	+18.5(11)
80	11^-	+2.9(3) [b]
97	11^-	+37.7(17)
164	11^-	+25.8(46) [b]
268.3	11^-	+12.9(3)
195.5	12^-	-0.2(2) [b]
160.5	13^-	+4.4(1) [b]
355.9	13^-	+4.2(5)
276.7	14^-	+1.3(7)
234.2	15^-	+6.3(3)
192.7	(18^+)	-1.5(2)
231.0	(20^+)	+1.8(1)
260.6	(21^+)	-0.2(2)
282.8	(22^+)	+1.3(2)
317.8	(23^+)	+6.6(13)

[a] $\alpha = 0.845$.

[b] Unresolved multiplet. Anisotropy is for total peak.

Chapter 5

Discussion

The present chapter details the interpretation of the experimental data in relation to the theoretical predictions of Total Routhian Surface (TRS), Cranked Shell Model (CSM) and Tilted Axis Cranking (TAC) calculations. The discussion of the ^{165}Ta yrast band has recently been published [12].

Section 5.1 deals with the transformation of the experimental observables - such as excitation energies and spins - into the rotating frame. As already discussed in Section 1.6.4, such a transformation is necessary in order to compare the experimental results with theory. The following section (5.2) presents the predicted theoretical values for some of the above observables, and discusses some discrepancies between the theoretical predictions and experimental results. The possibility that the light tantalum isotopes may deviate from axial shapes is considered in Section 5.3. Finally, Section 5.4 discusses the signature inversion phenomenon in doubly-odd rare-earth nuclei.

5.1 Experimental quantities in the rotating frame

In order to extract the alignments and routhians, a core reference corresponding to the ground-state band of the doubly-even nucleus ^{164}Hf, with $J_0 = 21\,\hbar^2$ MeV^{-1} and $J_1 = 63\,\hbar^4$ MeV^{-3} [98], was used for both ^{165}Ta and ^{164}Ta nuclei. The same reference was used when comparing the alignments of the above nuclei with those of neighbouring nuclei.

5.1.1 Experimental bandcrossings and alignments

^{165}Ta The experimental bandcrossing frequencies ($\hbar\omega_c$) can be measured from the plot of experimentally determined routhians (Fig. 5.2, upper panel) and alignments (Fig. 5.1, upper panel) for both signatures of the yrast band. The crossing frequencies are $\hbar\omega_c = 0.26$ MeV for the negative signature sequence and $\hbar\omega_c = 0.25$ MeV for the positive signature sequence, with an alignment gain of $\approx 10\ \hbar$. These bandcrossing frequencies are close to those observed in the neighbouring nuclei, and follow the trend for $\hbar\omega_c$ to first decrease and then to increase sharply with decreasing N (see Figure 5.13).

The first bandcrossing in the odd Ta isotopes is known to correspond to the alignment of a pair of $i_{13/2}$ neutrons. This is also called an AB crossing in accordance with the CSM labels. The naming convention for these labels is given in Table 5.3.

^{164}Ta CSM calculations (Section 5.2.2, see Fig. 5.21) predict a BC bandcrossing to occur at about $\hbar\omega = 0.34$ MeV for the yrast band. However the present data set does not extend to sufficiently high spins for it to be observed. The upper panel of Figure 5.1 shows the alignments of the yrast bands of ^{164}Ta, ^{165}Ta and ^{163}Hf plotted as a function of the rotational frequency. It is apparent from Figure 5.1 that the AB neutron band crossing, which occurs at $\hbar\omega \simeq 0.26$ MeV for the neighbouring ^{165}Ta, is definitely absent in the case of ^{164}Ta. This is consistent with the AB crossing in ^{164}Ta being blocked by the odd neutron, the next available crossing being BC. BC bandcrossings have been observed in some of the heavier odd-odd tantalum isotopes e.g. ^{168}Ta [84]. The i_x plot for ^{164}Ta (e.g. upper panel of Figure 5.1) suggests the onset of a sharp increase in the alignment at $\hbar\omega \simeq 0.37$ MeV. This figure also shows that this value is very close to the bandcrossing frequency $\hbar\omega = 0.36$ MeV associated with the $i_{13/2}$ neutron BC crossing in the positive-parity yrast band of ^{163}Hf [98]. It is therefore likely that the observed onset in the alignment gain of the ^{164}Ta yrast band is due to the BC crossing. The proton crossing ef is similarly blocked by the odd proton.

Also evident from the upper panel of Figure 5.1 is that the alignment of the ^{164}Ta yrast band ($i_x = 7.5\,\hbar$) at $\hbar\omega = 0.25$ MeV is approximately equal to the sum of the alignments of the yrast proton and neutron configurations of its odd-N and odd-Z neighbours at the same rotational frequency, ^{163}Hf ($i_x = 4.9\,\hbar$) and ^{165}Ta ($i_x = 2.4\,\hbar$), consistent with the

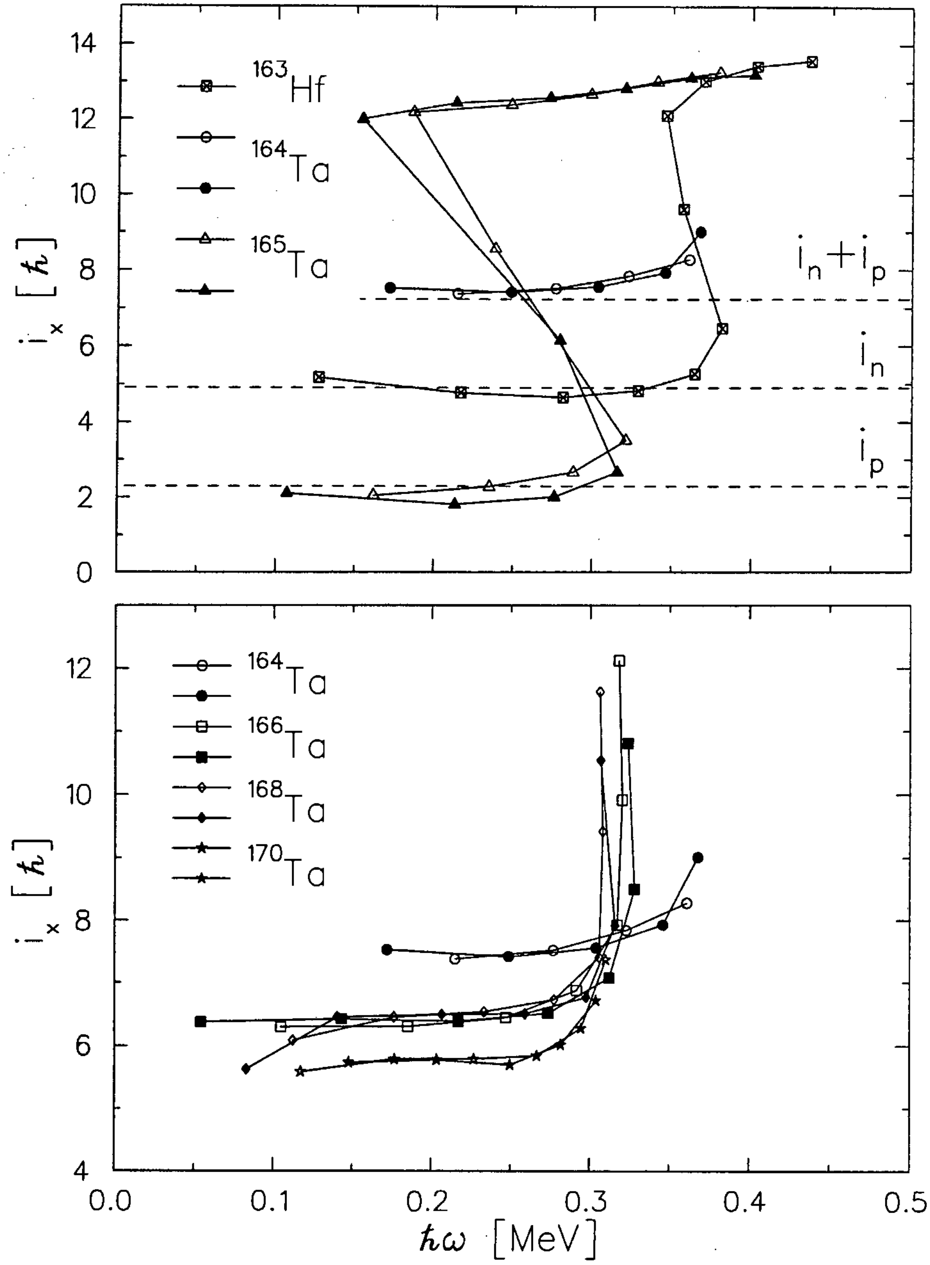

Figure 5.1: *Upper panel:* Plots of the aligned angular momentum of ^{164}Ta and its odd-A neighbours, as a function of the rotational frequency. The contributions of the odd proton (neutron) are labelled i_p and i_n. *Lower panel:* Plots of the aligned angular momentum of ^{164}Ta and the neighbouring doubly-odd Ta isotopes, as a function of the rotational frequency. The open (filled) symbols correspond to the favoured (unfavoured) signature.

assignment of the $\pi h_{11/2}[514]9/2^- \otimes \nu i_{13/2}$ configuration to this band. The contributions to the total alignment of the odd proton and odd neutron are indicated in Figure 5.1 by the dashed horizontal lines. The additivity of the alignments has also been reported for bands built on the $\pi h_{11/2} \otimes \nu i_{13/2}$ configuration in other $A \sim 160$ nuclei (e.g. $^{158-166}$Tm [103]).

The lower panel of Figure 5.1 shows the alignment as a function of rotational frequency for the $\pi h_{11/2} \otimes \nu i_{13/2}$ yrast bands of the doubly-odd isotopes $^{164-170}$Ta. The figure shows that, below the BC crossing, there is a tendency for the alignment to decrease as neutrons are added. This may be understood in terms of the neutron Fermi level rising to higher Ω-orbitals in the $\nu i_{13/2}$ shell (i.e. orbitals less aligned). In each of the above isotopes the AB (ef) crossings are blocked by the odd neutron (proton). It is also evident from this figure that the BC bandcrossing appears to be considerably delayed in the case of ^{164}Ta. However it is not clear from our data whether the onset of the gain in alignment in ^{164}Ta corresponds to an upbend or a backbend. An extension of the present ^{164}Ta level scheme to higher spin values would be necessary before a realistic comparison with the heavier odd-odd isotopes can be made.

5.1.2 Routhians and signature splitting

^{165}Ta The experimental quasiparticle energies in the rotating frame (routhians) for the yrast band of ^{165}Ta as a function of the rotational frequency are shown in the upper panel of Figure 5.2. It was determined from this diagram that the experimental signature splitting is $\Delta e' = +69$ keV at $\hbar\omega = 0.225$ MeV. However, above the bandcrossing the signature splitting reverses sign (becomes inverted) and is of considerably smaller magnitude. The behaviour of the signature splitting follows the known trend, shown in the lower panel of Figure 5.13, for $\Delta e'$ to increase with decreasing N in the $A \sim 160$ nuclei. However the splitting magnitude could not be reproduced by our CSM calculations assuming an axial nuclear shape (Section 5.2.2).

^{164}Ta The lower panel of Figure 5.2 shows the routhians for the yrast band of ^{164}Ta as a function of the rotational frequency. The slopes of the favoured and unfavoured routhians in Figure 5.2 are both $\simeq -7.5$ at $\hbar\omega = 0.25$ MeV. This is consistent with the alignment

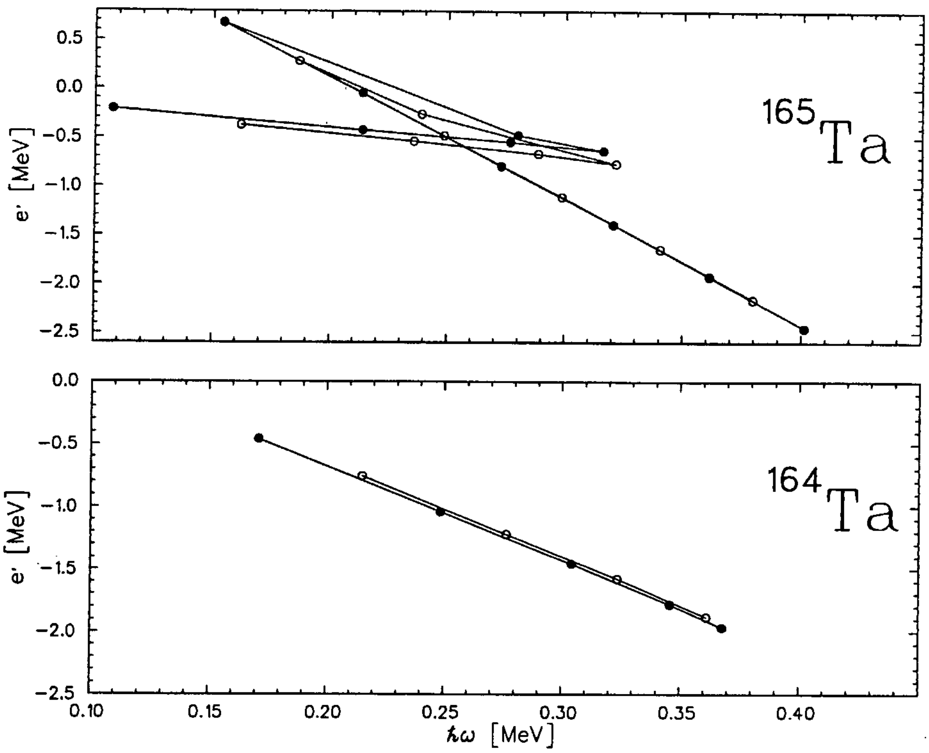

Figure 5.2: Experimental routhians extracted from the yrast band of ^{165}Ta and ^{164}Ta. A core reference with $J_0 = 21\,\hbar^2\,MeV^{-1}$ and $J_1 = 63\,\hbar^4\,MeV^{-3}$ was subtracted from the data set. The open (filled) symbols correspond to the favoured (unfavoured) signature.

$i_x \simeq 7.5\,\hbar$ shown in Figure 5.1.

A small anomalous signature splitting of the routhians is evident. The fact that the energy splitting is inverted and considerably reduced ($\Delta e' = -28$ keV at $\hbar\omega = 0.225$ MeV) with respect to that below the first band crossing of the $\pi h_{11/2}$ configuration of the nearest odd-A system ^{165}Ta is in agreement with the known systematic trend.

The systematics of signature splitting of the yrast bands of the doubly-odd neighbouring nuclei have been plotted in Figure 5.3. Evidently the general trend is for the splitting magnitude to increase (i.e. the splitting becomes increasingly negative) with decreasing N, as shown for the doubly-odd Tm, Lu and Ta isotopes in Figure 5.3 (right panel). However, one also notices that the splitting in ^{164}Ta and ^{166}Ta have roughly the same magnitude ($\Delta e' \approx -28$ keV at $\hbar\omega = 0.225$ MeV), contrary to the above trend. It should be noted that the routhians are extracted using a different fixed K value for each respective nucleus. However K is not a constant of the motion, and the splitting may be

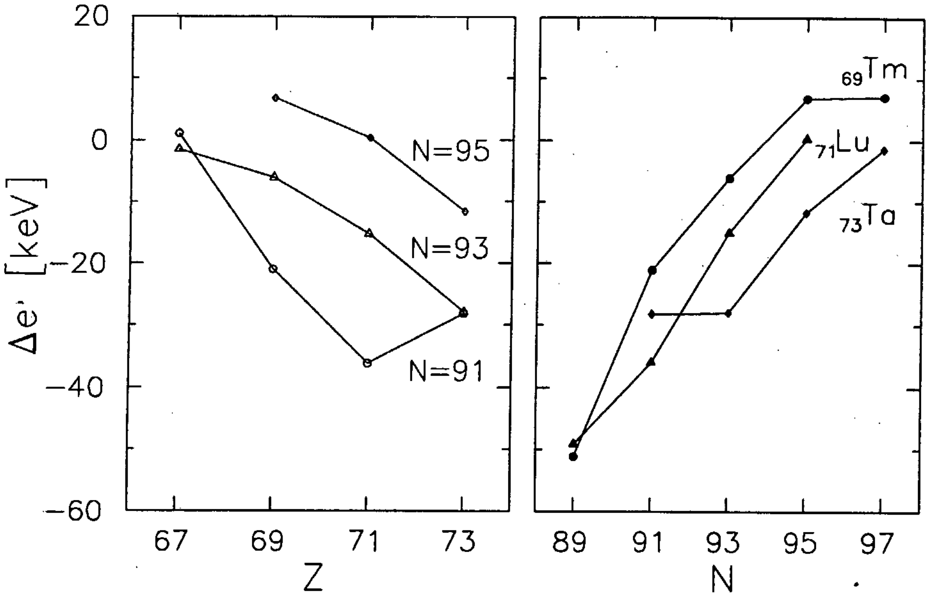

Figure 5.3: Systematic behaviour of the signature splitting of the routhians, $\Delta e'$, of the $\pi h_{11/2} \otimes \nu i_{13/2}$ yrast systems in the doubly-odd rare-earth nuclei. $\Delta e'$ is defined in the text. For each nucleus $\Delta e'$ was evaluated at 0.225 MeV.

somewhat K-dependent. On the other hand the systematics of the K-independent *staggering amplitude* ΔE (Section 5.4) does show increasing $\mid \Delta E \mid$ values with decreasing N for these nuclei (see Figure 5.16).

A crossing of the routhians is not observed, although they are expected to cross one another on the basis of systematics. The inversion frequency $\hbar\omega_i$ is expected to increase with decreasing N. This is observed for doubly-odd $^{158-166}$Tm [103] and $^{160-166}$Lu [104, 100, 105] (see Figure 5.17). The heavier tantalum isotopes ^{170}Ta [106], ^{168}Ta [84] and ^{166}Ta [82] exhibit inversion frequencies of 0.248 MeV, 0.311 MeV and $\geq$ 0.320 MeV respectively. The tentative lower limit of $\hbar\omega_i$ = 0.38 MeV for ^{164}Ta is therefore consistent with this trend. The inversion frequencies for the above nuclei were extracted from the level schemes presented in the respective references.

5.1.3 Moments of inertia

^{165}Ta Figure 5.4 shows the variation of the level energies of both signatures of the yrast band as a function of $I(I+1)$. Since the slope of each curve is proportional to $\hbar^2/2J$, the steeper slope below the backbend reflects a smaller value for the moment of inertia

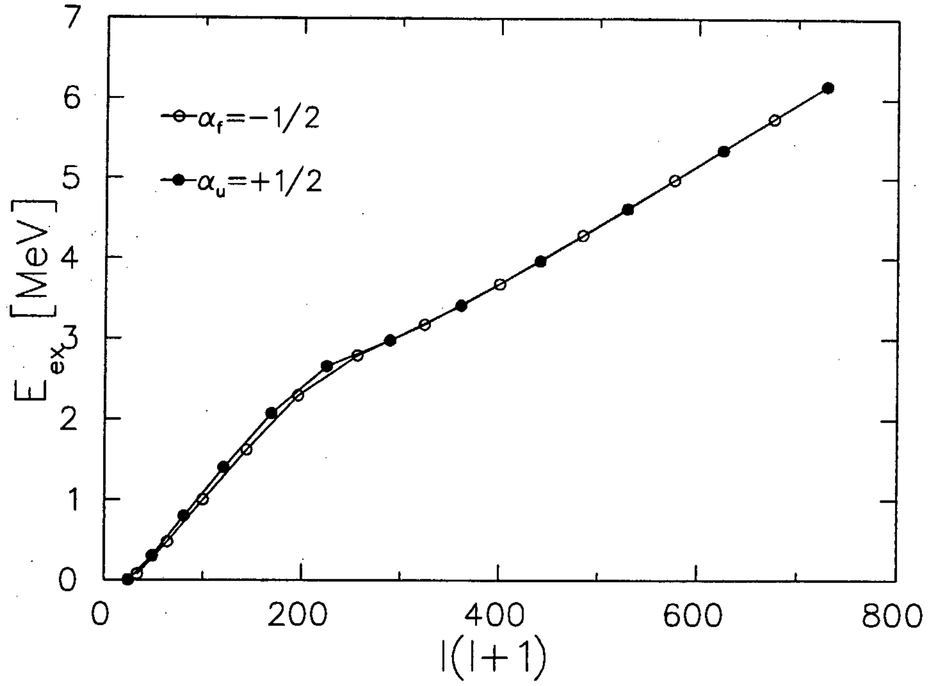

Figure 5.4: Excitation energies of the yrast band of ^{165}Ta as a function of $I(I+1)$. The open (filled) symbols correspond to the favoured (unfavoured) signature.

J. The $\nu i_{13/2}$ alignment is characterised by a rapid reduction in the slope, meaning that J increases around the backbend. This larger J value could reflect different deformation parameters and/or the quenching of pairing.

^{164}Ta The dynamic moments of inertia $J^{(2)}$ of the yrast bands of the doubly-odd isotopes $^{164-170}$Ta are compared in Figure 5.5, as a function of the rotational frequency. Below the BC bandcrossing they all exhibit a smooth increase at low rotational frequencies, which may be attributed to a gradual reduction of the strength of pairing correlations with increasing rotational frequency. On the other hand at $\hbar\omega \sim 0.3$ MeV the $J^{(2)}$ values of ^{166,168,170}Ta increase rather sharply with rotational frequency. This most likely corresponds to the onset of the alignment of the $i_{13/2}$ neutrons associated with the first available (BC) bandcrossing.

As mentioned above, the alignment plot (Fig. 5.1, lower panel) indicates that the BC crossing occurs close to 0.37 MeV for ^{164}Ta. The onset of a sharp increase in $J^{(2)}$ for ^{164}Ta

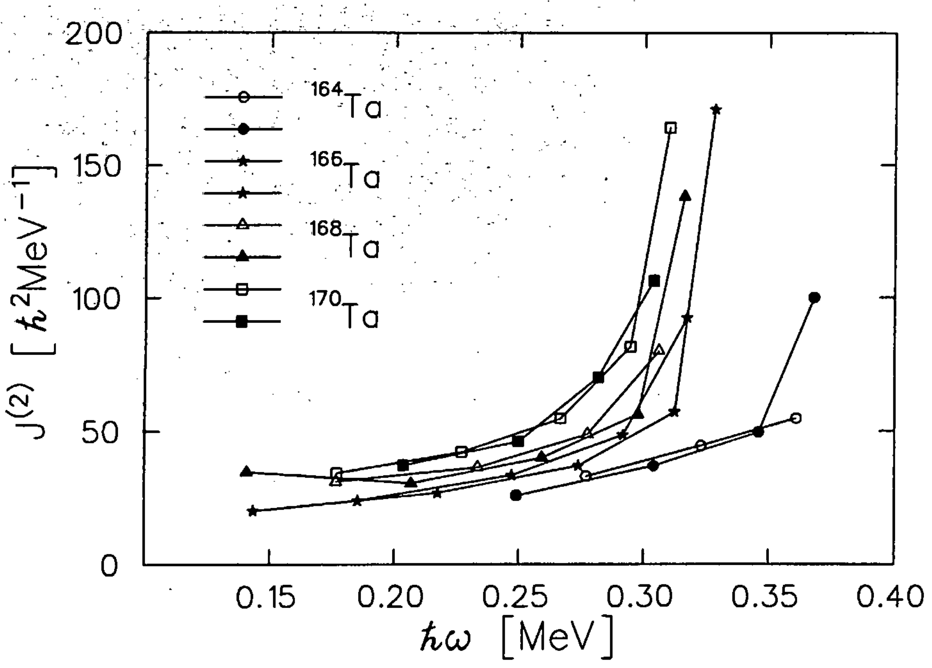

Figure 5.5: Plots of the kinematic moment of inertia $J^{(2)}$ as a function of the rotational frequency for doubly-odd ^{164,166,168,170}Ta. The open (filled) symbols correspond to the favoured (unfavoured) signature.

(Fig. 5.5) at the same rotational frequency is consistent with this suggestion.

5.1.4 Electromagnetic transition probabilities

The ratios of the reduced transition probabilities can be determined from the experimental data using the expression (e.g. [97]):

$$\frac{B(M1, I \to I-1)}{B(E2, I \to I-2)} = 0.697 \cdot \frac{E_\gamma^5(E2)}{E_\gamma^3(M1)} \cdot \frac{1}{\lambda(1+\delta^2)} \quad [\mu^2/e^2b^2] \qquad (5.1)$$

The branching ratios $\lambda = \frac{I_\gamma(E2)}{I_\gamma(M1)}$ and the γ−ray intensities for ^{165}Ta and ^{164}Ta have been listed in Tables 4.3 and 4.5. The mixing ratios $\delta^2 = I_\gamma(E2, I \to I-1)/I_\gamma(M1, I \to I-1)$ could not be evaluated in our case (lack of angular correlation data). The δ^2 values estimated from a rotational formula (e.g. ref. [107]) were found to be small. Therefore we have assumed $\delta = 0$ in this analysis. The error introduced by this assumption is negligible compared with the errors in λ.

The experimentally determined $B(M1)/B(E2)$ ratios for both ^{165}Ta and ^{164}Ta are also listed in Tables 4.3 and 4.5. Figure 5.9 shows the $B(M1)/B(E2)$ ratios as a function of spin. At low spins the ratio shows a signature dependence for both nuclei. An increase in the $B(M1)/B(E2)$ ratios is observed at the $\nu i_{13/2}$ crossing, signalling a change in the nature of the wave functions.

5.2 Calculations

5.2.1 Total Routhian Surface calculations

^{165}Ta Calculations of TR surfaces were performed for a number of low lying one-quasiproton configurations. Since at high rotational frequencies signature α ($I = \alpha \bmod 2$) and parity π are the only two good quantum numbers, the quasiparticle configurations were labelled using the convention described in Table 5.3. One should keep in mind that the Nilsson labels, showing the orbitals with the most important contribution to the wave functions, are strictly valid only at $\hbar\omega = 0$ MeV. On the other hand the shell model labels are approximately valid only at small quadrupole deformations. The TRS minima for the lowest negative parity one-quasiproton configurations e and f are given in Table 5.1. It is worthwhile repeating that each TR surface has a well defined parity and signature but no other conserved quantum numbers.

Selected examples of TR surfaces for the lowest-lying $(\pi, \alpha) = (-, -1/2)$ configuration before and after the neutron alignment are presented in Figure 5.7. The calculated surface of this negative parity configuration is γ-soft at low rotational frequencies: the lowest energy contour line, corresponding to an energy difference of 100 keV, includes γ-values varying from $-20°$ to $+20°$, with potential energy minimum at prolate deformation with $\beta_2 \sim 0.18$ (left panel in Figure 5.7). After the first bandcrossing no significant changes are predicted for the nuclear shape, it is still γ-soft with the energy minimum at about the same quadrupole deformation with small γ-deformation (middle panel in the same figure). At still higher rotational frequencies, in addition to the minimum at "normal" deformation, other potential energy minima appear corresponding to much larger quadrupole deformation. This is not unexpected, since in the neighboring ^{163}Lu and ^{165}Lu nuclei such highly deformed shapes were both theoretically predicted and experimentally observed [97, 108]. In ^{165}Ta however, although such shape coexistence is predicted already at $\hbar\omega \sim 0.40$ MeV and $I \simeq 24\hbar$ (see the right panel in Figure 5.7), it has not been

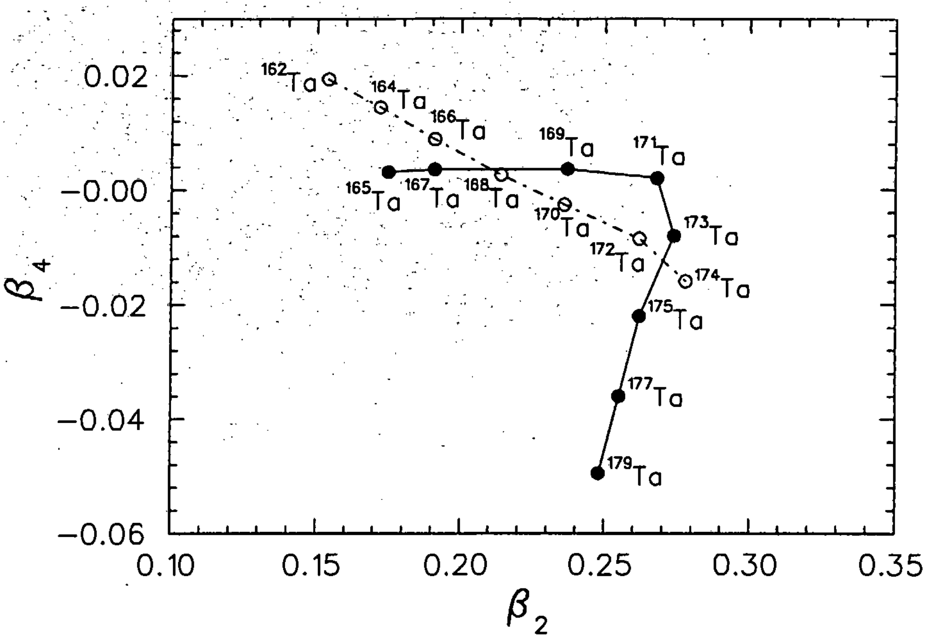

Figure 5.6: The filled symbols indicate the β_2 and β_4 deformation parameters for the $^{165-179}$Ta nuclei, calculated by the TRS for the lowest $(-,-1/2)_p$ configuration at $\hbar\omega = 0.131$ MeV. The open symbols correspond to the same deformation parameters calculated for the lowest $(-,-1/2)_p \otimes (+,+1/2)_n$ configuration for the doubly-odd $^{162-174}$Ta isotopes.

observed in our data.

Table 5.1: Equilibrium deformations of the lowest one-quasiproton configuration, corresponding to $Z = 73$, $N = 92$, obtained from the TRS calculations at $\hbar\omega = 0.150$ MeV.

$(\pi,\alpha)_p$	Label	β_2	γ	β_4
$(-,+\frac{1}{2})$	f	0.176	-0.2	0.006
$(-,-\frac{1}{2})$	e	0.177	-0.8	0.006

^{164}Ta Selected examples of the TR surfaces for the favoured two-quasiparticle configuration of ^{164}Ta are shown in Figure 5.8. The figure shows that at low rotational frequencies (e.g. $\hbar\omega = 0.151$ MeV, upper left panel) the nuclear shape is γ-soft with minimum at $\beta_2 = 0.171$, $\gamma = +6.2°$, $\beta_4 = 0.013$. No significant shape changes are predicted for this configuration, apart from a gradual reduction in the γ-softness towards higher rotational

Table 5.2: Equilibrium deformations of the lowest two-quasiparticle configuration, corresponding to $Z = 73$, $N = 91$, obtained from TRS calculations at $\hbar\omega = 0.150$ MeV.

$(\pi, \alpha)_n \otimes (\pi, \alpha)_p$	Label	β_2	γ	β_4
$(+, +\frac{1}{2})_n \otimes (-, +\frac{1}{2})_p$	Af	0.171	+6.5	0.013
$(+, +\frac{1}{2})_n \otimes (-, -\frac{1}{2})_p$	Ae	0.171	+6.2	0.013

frequencies (e.g. at $\hbar\omega = 0.403$ MeV, lower right panel). TR surfaces were also calculated for ^{164}Ta with the proton (neutron) occupying the unfavoured (favoured) orbital. These were essentially identical to the TR surfaces shown in Figure 5.8 and are therefore not shown. The TRS minima for the two lowest negative parity two-quasiproton configurations Ae and Af are given in Table 5.2. The calculations did not predict signature splitting of the experimentally observed yrast band ($\hbar\omega < 0.4$ MeV).

TRS calculations were performed for the favoured two-quasiparticle configuration $(-, -1/2)_p \otimes$ $(+, +1/2)_n$ of the doubly-odd $^{162-174}$Ta nuclei, as well as for the favoured one-quasiparticle configuration $(-, -1/2)_p$ of the odd-A $^{165-179}$Ta nuclei. Figure 5.6 shows the predicted trend of the shape parameters (β_2, β_4) for the favoured configurations of each of the above nuclei. The trend for β_2 to decrease with decreasing N is apparent. Small β_2 values are associated with greater γ-softness.

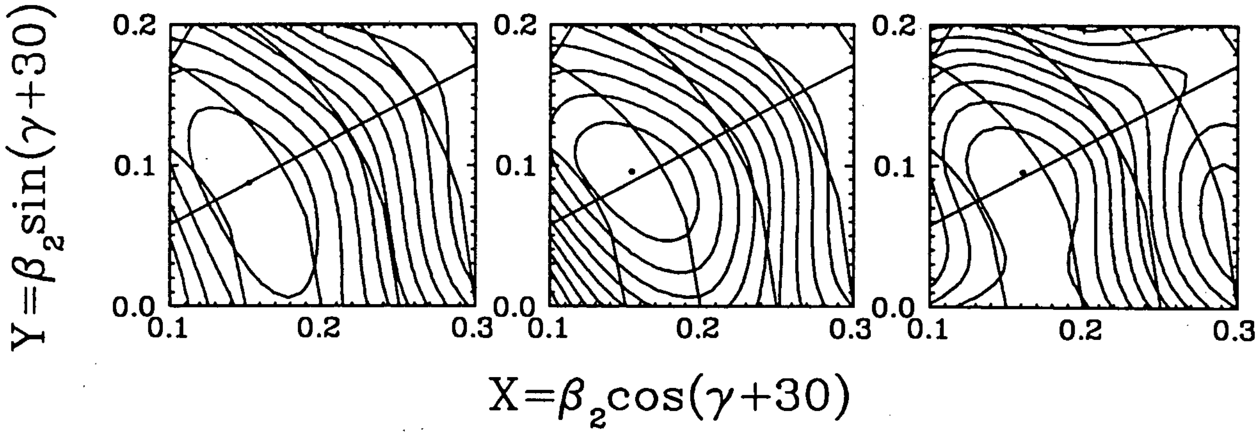

Figure 5.7: Total routhian surfaces for ^{165}Ta, calculated for configuration $(\pi,\alpha) = (-,-1/2)$ before and after the $\nu i_{13/2}$ alignment. The left figure corresponds to $\hbar\omega = 0.15$ MeV (minimum at $I = 4.6\hbar$, $\beta_2 = 0.177$, $\gamma = -0.8$, $\beta_4 = 0.006$), the middle figure to $\hbar\omega = 0.25$ MeV (minimum at $I = 17.6\hbar$, $\beta_2 = 0.180$, $\gamma = 1.0$, $\beta_4 = 0.017$) , while the right figure corresponds to $\hbar\omega = 0.40$ MeV (minimum at $I = 25.1\hbar$, $\beta_2 = 0.185$, $\gamma = +0.2$, $\beta_4 = 0.015$).

5.2.2 Single-particle energies and Cranking Shell Model calculations

^{165}Ta The single-particle proton and neutron levels calculated with a Woods-Saxon potential[1] for $Z = 73$ and $N = 92$, are presented in Figure 5.18. For the predicted nuclear deformation of $\beta_2 \sim 0.18$, the single particle orbitals lying close to the $Z = 73$ Fermi level are [404]7/2$^+$, [402]5/2$^+$, [523]7/2$^-$, and [514]9/2$^-$ (as shown in Figure 5.18).

The quasiparticle routhians for neutrons and protons are plotted in Figure 5.22 as a function of the rotational frequency for deformation parameters obtained from the minimum in the TR surface ($\beta_2 = 0.177$, $\beta_4 = 0.006$, $\gamma = -0.8^\circ$). The lowest lying proton orbital, as shown in Figure 5.22, is predicted to be [514]9/2$^-$, which was one of the arguments used for the assignment of this configuration to the yrast band of ^{165}Ta. However, the predicted signature splitting between the e and f routhians is $\sim$ 11 keV at $\hbar\omega \sim 0.225$ MeV, much smaller than the experimentally measured value of 69 keV. Since the odd proton occupies the e level, the crossing at $\hbar\omega \sim 0.42$ MeV is blocked and the first proton alignment is predicted at $\hbar\omega \sim 0.51$ MeV. For neutrons, at $\hbar\omega \sim 0.20$ MeV the vacuum is crossed by the AB configuration and a change in the aligned angular momentum $\Delta i \simeq 11\hbar$ is predicted. The next change in the aligned angular momentum occurs at $\hbar\omega \sim 0.32$ MeV. A comparison with the experimentally measured bandcrossing frequency and gain in alignment in the yrast band suggests that the first bandcrossing involves the alignment of an $i_{13/2}$ neutron pair. This suggestion is supported by the systematics, as such a neutron bandcrossing is systematically observed in all the nuclei in the rare-earth mass region. However, the bandcrossing frequency $\hbar\omega_c \sim 0.20$ MeV predicted by CSM for the yrast band of ^{165}Ta is rather low in comparison with the experimentally measured $\hbar\omega_c \sim 0.26$ MeV.

For completeness the neutron and proton single-particle routhians for this nucleus are also shown, in Figure 5.20.

The experimental routhians (Fig. 5.2, upper panel) for the [514]9/2$^-$ band indicate

---

[1] The mean field was described by "universal" parameters determined by the Warsaw group [43]. A detailed comparison between the modified harmonic oscillator (Nilsson) potential and the Woods-Saxon potentials is provided in [109]. Note that there are some differences, [110], compared to the standard modified harmonic oscillator Nilsson diagrams, in particular, the re-ordering of the $1g_{\frac{7}{2}}$ and $2d_{\frac{5}{2}}$ shells.

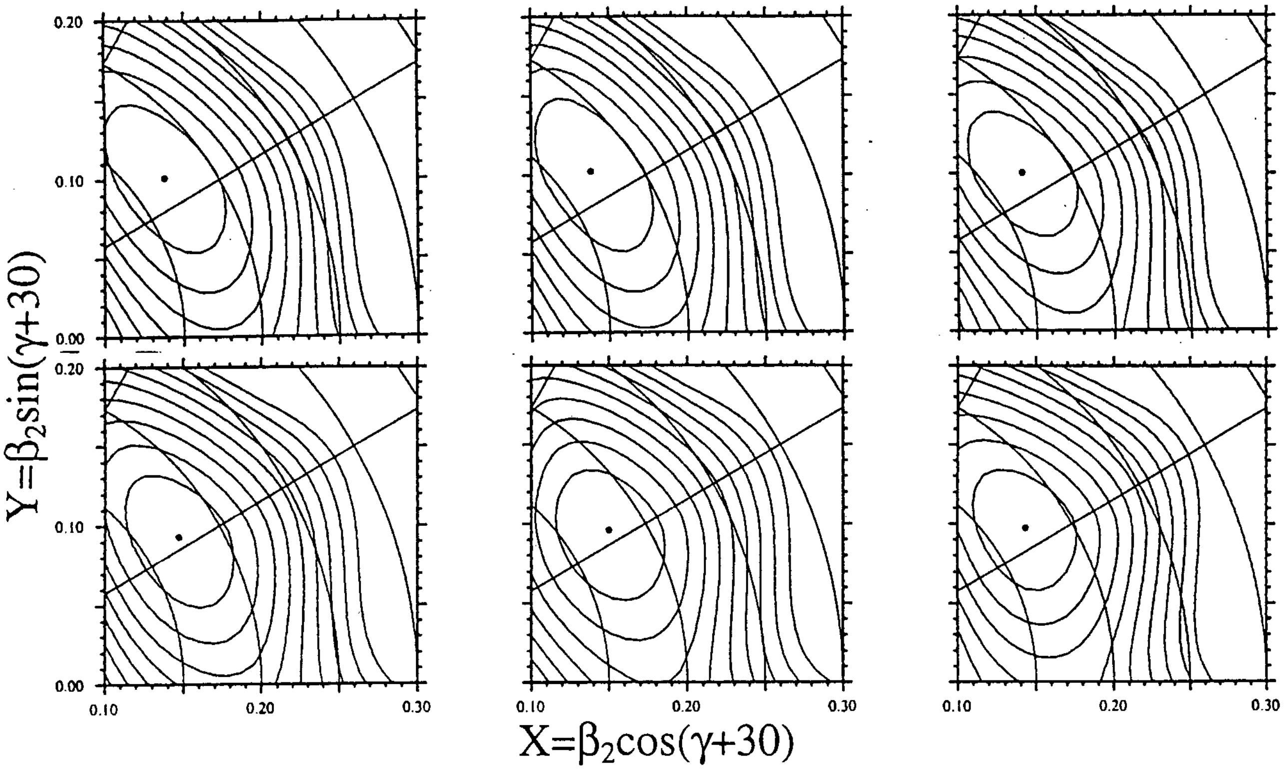

Figure 5.8: Total routhian surfaces for ^{164}Ta, calculated for favoured configuration $\pi h_{11/2} \otimes \nu i_{13/2}$. The rotational frequencies are, from left to right, *top row*: $\hbar\omega = 0.15,\ 0.20,\ 0.25$ MeV; *bottom row*: $\hbar\omega = 0.30,\ 0.35,\ 0.40$ MeV.

that the interaction strength between the one-quasiparticle and three-quasiparticle bands is $|V| \sim 100$ keV. This is consistent with the results of CSM calculations (see upper panel of Figure 5.22).

Table 5.3: Convention for labelling the orbitals described by different parity and signature quantum numbers. The neutron (proton) configurations are described by uppercase (lowercase) letters.

Shell model label	Nilsson label	(π,α)	addopted label
$\pi h_{11/2}$	[514]9/2$^-$	$(-,-\frac{1}{2})$	e
$\pi h_{11/2}$	[514]9/2$^-$	$(-,+\frac{1}{2})$	f
$\nu i_{13/2}$	[660]1/2$^+$	$(+,+\frac{1}{2})$	A
$\nu i_{13/2}$	[660]1/2$^+$	$(+,-\frac{1}{2})$	B
$\nu i_{13/2}$	[651]3/2$^+$	$(+,+\frac{1}{2})$	C
$\nu i_{13/2}$	[651]3/2$^+$	$(+,-\frac{1}{2})$	D

^{164}Ta The single-particle levels for protons and neutrons as a function of β_2 deformation using a Woods-Saxon potential for $Z = 73$ and $N = 91$ are shown in Figure 5.18. The proton single-particle levels lying close to the $Z = 73$ Fermi level are [404]7/2$^+$, [402]5/2$^+$, [523]7/2$^-$ and [514]9/2$^-$, as for ^{165}Ta. On the other hand for the neutron system, single-particle levels [660]1/2$^+$, [651]3/2$^+$, [521]3/2$^-$ and [523]5/2$^-$ are closest to the $N = 91$ Fermi level.

The quasiparticle routhians for neutrons and protons are plotted in Figure 5.21 as a function of the rotational frequency for deformation parameters obtained from the minimum in the TR surface ($\beta_2 = 0.172$, $\beta_4 = 0.0144$, $\gamma = 6.4°$, $\Delta_n = 1.06$ MeV and $\Delta_p = 1.11$ MeV). The lowest-lying proton orbital, as shown in Figure 5.21, is predicted to be [514]9/2$^-$. The same figure shows that the lowest-lying neutron orbital is expected to be [660]1/2$^+$.

Since the odd proton occupies the e level, the first proton crossing at $\hbar\omega \sim 0.4$ MeV is blocked and the first proton alignment is predicted at $\hbar\omega \sim 0.5$ MeV. The AB neutron crossing at $\hbar\omega \sim 0.22$ MeV is similarly blocked by the occupation of the A level by the odd neutron, the next available neutron crossing (BC) being at $\hbar\omega \sim 0.35$ MeV. It has already been suggested (Section 5.1.1) that the onset of the rapid gain in alignment at $\hbar\omega \sim 0.37$ MeV shown in Figure 5.1 reflects the BC alignment of a pair of $i_{13/2}$ neutrons. This interpretation is supported by CSM calculations (Fig. 5.21) and also by the fact that the BC $\nu i_{13/2}$ alignment is observed at about the same frequency ($\hbar\omega \sim 0.36$ MeV) in the odd-N neighbour ^{163}Hf (Fig. 5.1, upper panel). This crossing frequency should be contrasted with that associated with the AB crossing in ^{165}Ta ($\hbar\omega \sim 0.26$ MeV) and doubly-even ^{164}Hf ($\hbar\omega \sim 0.25$ MeV) [98] where there is no neutron blocking effect.

For completeness the neutron and proton single-particle routhians for this nucleus are also shown, in Figure 5.19.

CSM predicted normal splitting between the routhians, but anomalous splitting is observed experimentally. Anomalous splitting at low spins has also been reported for many other doubly-odd $A \sim 160$ nuclei (Section 5.4). The reader will recall that normal splitting is attributed to the Coriolis mixing of $\Omega = 1/2$ components into the wavefunction (Section 1.9). However, the cause of anomalous splitting is not well understood and currently the focus of an on-going debate (Section 5.4.2).

5.2.3 B(M1)/B(E2) ratios

^{165}Ta Some discrepancies were observed when comparing experimental $B(M1)/B(E2)$ ratios with theoretical predictions, obtained by using a semi-classical approximation based on the cranking approach (e.g. [111]):

$$\frac{B(M1, I \to I-1)}{B(E2, I \to I-2)} = \frac{12}{5Q_o^2 \cos^2(30^\circ + \gamma)}(1 - \frac{K^2}{(I-\frac{1}{2})^2})^{-2} \cdot K^2 \tag{5.2}$$

$$\times[(g_p - g_R)(\sqrt{1 - \frac{K^2}{I^2}} - \frac{i_p}{I} \pm \frac{\Delta e'}{\hbar\omega}) - (g_n - g_R)\frac{i_n}{I}]^2 \tag{5.3}$$

where g_R is the g-factor of the collective rotation and g_p (g_n) the intrinsic g-factor of the quasiproton (quasineutron). The proton and neutron aligned angular momenta are denoted by i_p and i_n, and $\Delta e'$ represents the experimental signature splitting. The formula is valid only for axially symmetric nuclei but can be expected to give a reasonable description for ^{165}Ta if only a small deviation from axial symmetry is assumed.

A quadrupole moment of $Q_o = 4.9$ eb (calculated as in ref. [112]) and $\gamma = 0°$, reflecting the minimum in the TR surface, were used. In order to obtain the average values of the $B(M1)/B(E2)$ ratio the signature splitting was neglected. The gyromagnetic factor g_R was chosen to be 0.4 [113] below the bandcrossing. Unsatisfactory agreement between the experimental and the theoretical (dash-dotted curve in Fig. 5.9) values was obtained if $g_p = 1.3$ was used - values between 1.24 and 1.34 were previously used for the g-factor of the proton [514]9/2$^-$ orbital in ^{167,169}Ta and ^{163,165,167}Lu isotopes [84, 85, 97, 114, 115, 116].

The signature splitting in the $B(M1)/B(E2)$ ratios below the backbend has been calculated (the dotted curve on Fig. 5.9) using the experimentally measured signature splitting $\Delta e'$. In order to obtain a good average overlap with the experimental data a value of $g_p = 1.1$ was used. It can be seen that the theoretical curve strongly overestimates the splitting amplitude.

The experimental $B(M1)/B(E2)$ ratios show a sudden increase above the bandcrossing at $\hbar\omega = 0.26$ MeV. This is mainly a result of the increase in the $B(M1)$ values, due to the alignment of the $i_{13/2}$ neutrons, and may also reflect a change in the nuclear deformation induced by this quasiparticle alignment. The theoretical $B(M1)/B(E2)$ ratios above the backbend (dashed line in Fig. 5.9) were calculated using the values for the aligned angular momenta obtained from the experiment (Fig. 5.1), the value $g_n = -0.2$ (which is characteristic for $i_{13/2}$ neutrons [117]), and $g_R = 0.3$ (which takes into account the increased neutron contribution to the moment of inertia). Again unsatisfactory agreement with the experimental ratios was obtained.

The experimental $B(M1)/B(E2)$ data appear to increase smoothly with angular momentum at higher spins. This may reflect a decrease in the $B(E2)$ rates, since the $B(M1)$ rates are not expected to increase (there is no indication of another quasiparticle alignment). For the nuclei ^{156}Dy$_{90}$, ^{160}Yb$_{90}$ and ^{161}Yb$_{91}$ lifetime measurements [118, 119, 120] have revealed a decrease in collectivity of the ground band at the $\nu i_{13/2}$ bandcrossing, which was explained as a result of the decreased nuclear deformation induced by the aligning neutrons. For the more stable ^{166}Yb$_{96}$ lifetime measurements [121] have also shown a loss of collectivity, but at higher spins. In the Lu and Ta isotopes no lifetime measurements have been performed, but in the light ^{161,163,165}Lu isotopes a similar increase in the $B(M1)/B(E2)$ ratio was observed at higher spins [115] and a possible decrease in the nuclear quadrupole deformation was suggested. In the ^{167,169}Ta isotopes no evidence for such increase in the $B(M1)/B(E2)$ has been found [84, 85]. Therefore, although it is likely that a decrease in nuclear quadrupole deformation causes the observed increase in the $B(M1)/B(E2)$ ratios at higher spins, lifetime measurements are needed to confirm such a suggestion.

^{164}Ta For doubly-odd nuclei, a theoretical estimate of the B(M1)/B(E2) ratio can be obtained from the semi-classical formula developed by Dönau and Frauendorf [122]. The following expressions were used:

$$B(M1) = \frac{3}{8\pi}[(g_p - g_R)(\Omega_p\sqrt{1 - \frac{K^2}{I^2}} - i_p\frac{K}{I}) + (g_n - g_R)(\Omega_n\sqrt{1 - \frac{K^2}{I^2}} - i_n\frac{K}{I})]^2 \ \mu_N^2 \quad (5.4)$$

and

$$B(E2) = \frac{5}{16\pi}\langle IK20|I-2K\rangle^2 Q_0^2 \ e^2b^2 \quad (5.5)$$

The calculated values have been plotted in Figure 5.9 (lower panel) together with the experimental ones. The parameters used for the calculations are: $g_p = 1.3$, $g_n = -0.25$, $g_R = 0.4$, $i_p = 2.4$, $i_n = 5.0$, $\Omega_p = 4.5$, $\Omega_n = 0.0$, $Q_0 = 4.6eb$, and $K = \Omega_p + \Omega_n$ following the Gallagher-Moszkowski rule [123]. Figure 5.9 shows that the experimental $B(M1)/B(E2)$ values are not well reproduced at low spins.

The experimental $B(M1)/B(E2)$ values show a parabola-like increase at higher spins. This has also been observed in neighbouring doubly-odd $\pi h_{11/2} \otimes \nu i_{13/2}$ yrast systems, for example ^{160}Ho [124, 125], ^{166}Tm [126] and ^{162,164}Lu [100]. Salicio *et al.* [125] suggested that the increase of the $B(M1)/B(E2)$ ratios at higher spins could be due to a gradual change of the coupling scheme between the region $I < (j_p + j_n)$ and the region $I \gg (j_p + j_n)$. Part of the increase is due to a small admixture in the wavefunctions of components from the band which is expected to cross the two-quasiparticle configuration. The transition matrix elements can be very sensitive to small changes in the wavefunctions.

5.2.4 Tilted Axis Cranking (TAC) calculations

The rotational model for both the strongly coupled band in ^{165}Ta, and the semi-decoupled band in ^{164}Ta corresponds to a tilted rotational axis, since in both cases the total spin vector **I** has non-zero projections onto the 1−axis as well as the 3−axis.

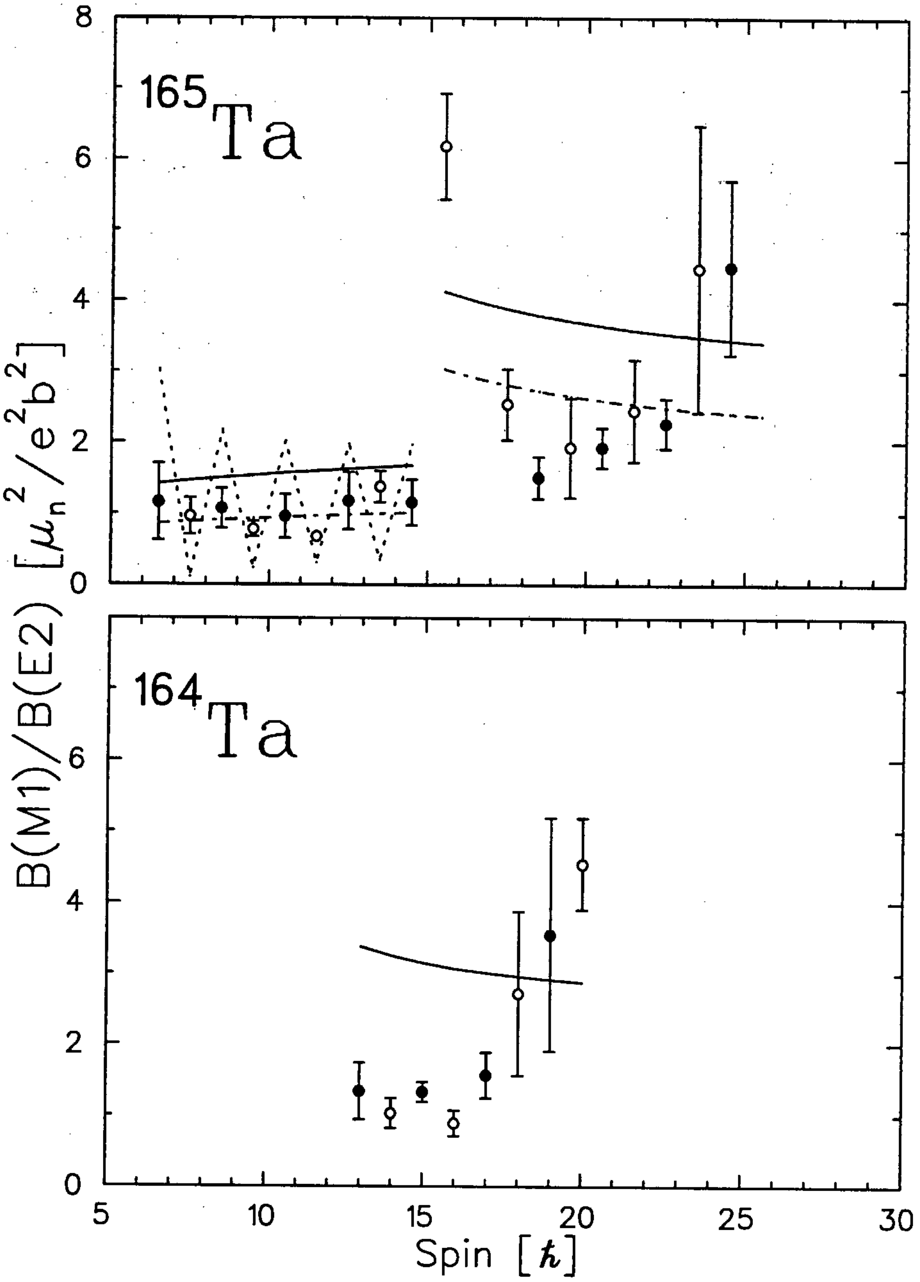

Figure 5.9: *Upper panel:* Experimental and predicted $B(M1)/B(E2)$ ratios for the yrast band of ^{165}Ta. The solid (dash-dotted) curve represents the theoretical calculation corresponding to $g_p = 1.3$ ($g_p = 1.1$), neglecting the signature splitting. The dotted curve represents the theoretical calculation corresponding to $g_p = 1.1$, with the experimental signature splitting taken into account (see text for details). *Lower panel:* Experimental and predicted $B(M1)/B(E2)$ ratios for the ^{164}Ta yrast band. The solid curve shows the predicted values corresponding to $g_p = 1.3$. The open (filled) symbols correspond to the favoured (unfavoured) signature.

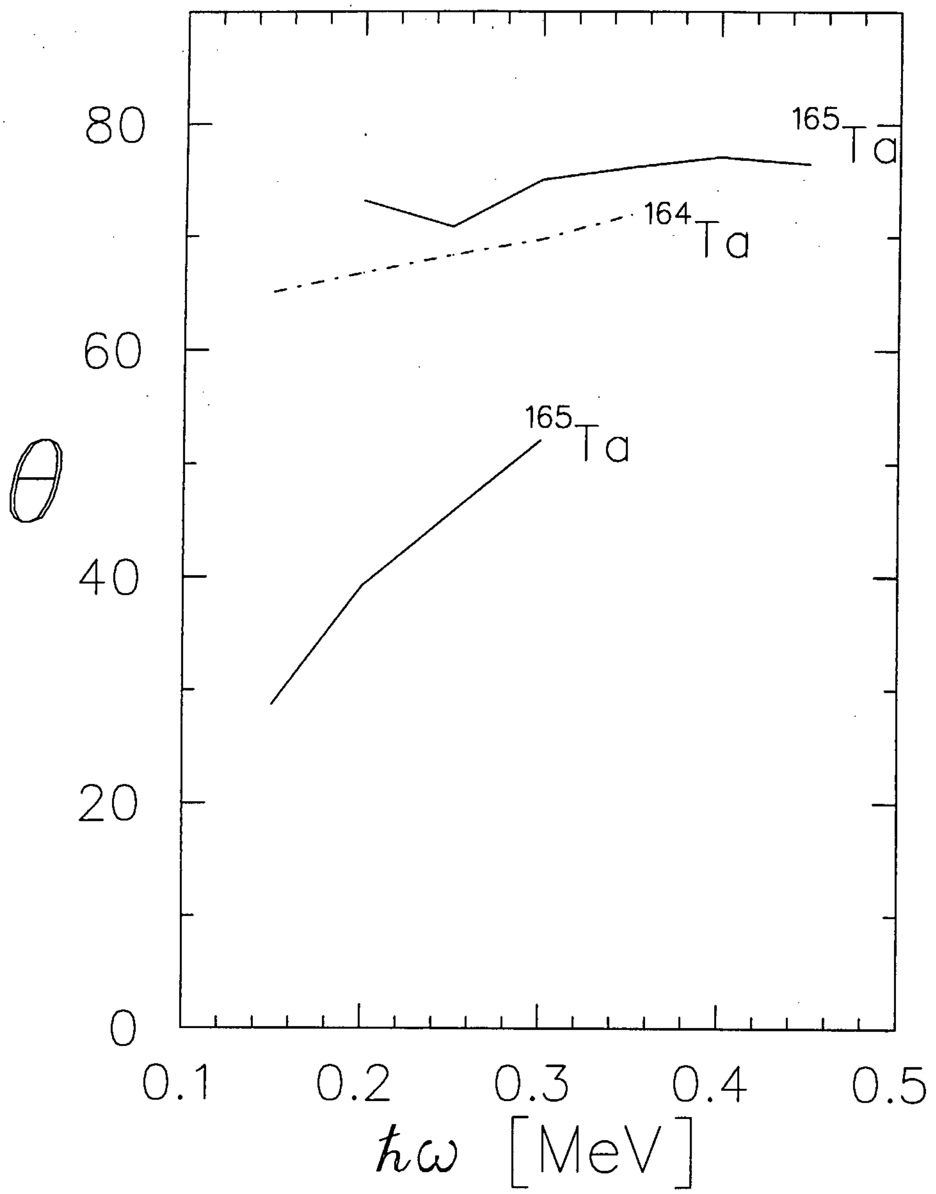

Figure 5.10: Tilt angle θ plotted as a function of rotational frequency for the yrast bands of ^{165}Ta below the backbend (lower solid curve), above the backbend (upper solid curve), and ^{164}Ta (dot-dashed curve).

TAC calculations [27, 26] were performed for both ^{164,165}Ta. The quasiparticles in the rotating potential are found by diagonalising the TAC routhian

$$h^{\omega} = h(\varepsilon_2, \varepsilon_4) - \Delta(P^{+} + P) - \lambda N - \hbar\omega(\sin\theta j_1 + \cos\theta j_3), \tag{5.6}$$

where $h(\varepsilon_2, \varepsilon_4)$ represents the Nilsson Hamiltonian, and $P^{+}(P)$ the pair creation (annihilation) operator. This was done by stepping through 13 values of rotational frequency ω (in steps of $\hbar\omega = 0.05$ MeV), and minimising the total routhian with respect to the tilt angle θ, in steps of $\theta = 10°$ for fixed ω. The calculations were done with a fixed quadrupole deformation of $\varepsilon_2 = 0.168$ for ^{165}Ta, and $\varepsilon_2 = 0.160$ for ^{164}Ta. For both nuclei the parameters $\varepsilon_4 = 0$, $\gamma = 0$, $\Delta_n = 1.06$ MeV and $\Delta_p = 1.11$ MeV were used. The code computes the tilt angle θ corresponding to stable uniform rotation, for each value of ω, as well as the projections of single-particle angular momenta on the principal axes, and B(M1)/B(E2) ratios.

Figure 5.10 shows the variation of θ with rotational frequency for ^{165}Ta above and below the backbend (solid lines) and for ^{164}Ta (dot-dashed line). The three curves show a clear trend for the tilt angle of the rotation axis to approach 90° (i.e. collective rotation) at high rotational frequencies. This behaviour may be qualitatively understood by considering the coupling of the relevant quasiparticles and the collective rotation vector **R**. The decomposition of the total angular momentum vector **I** into its quasiparticle components is shown in Figure 5.11.

For ^{165}Ta, the lowest quasiparticle state is $\pi[514]9/2^{-}$, with $j_p = 11/2$. The quasiproton angular momentum vector $\mathbf{j_p}$ is expected to be oriented at about $\theta_p \simeq \cos^{-1}(K/j_p) = 35°$ relative to the symmetry axis at zero rotational frequency. This is shown by the upper left diagram in Figure 5.11. The lower diagram of the same figure shows the coupling of three quasiparticles (two $i_{13/2}$ neutrons and an $h_{11/2}$ proton) above the $\nu i_{13/2}$ alignment in the yrast band of ^{165}Ta. The two aligned $i_{13/2}$ quasineutrons are expected to have an alignment of $\simeq 12\hbar$ and projection onto the symmetry axis of close to zero. Simple vector addition then suggests that the total spin vector **I**, obtained by coupling the angular momentum vector for the total neutron spin with that of the quasiprotons, should be oriented at about $\theta = 74°$ relative to the symmetry axis and have magnitude $\sim 16\hbar$ in the absence of rotation. Finally, the upper right diagram in Figure 5.11 shows the situation for ^{164}Ta, where the ground state is a two-quasiparticle excitation, $\pi h_{11/2} \otimes \nu i_{13/2}$. The

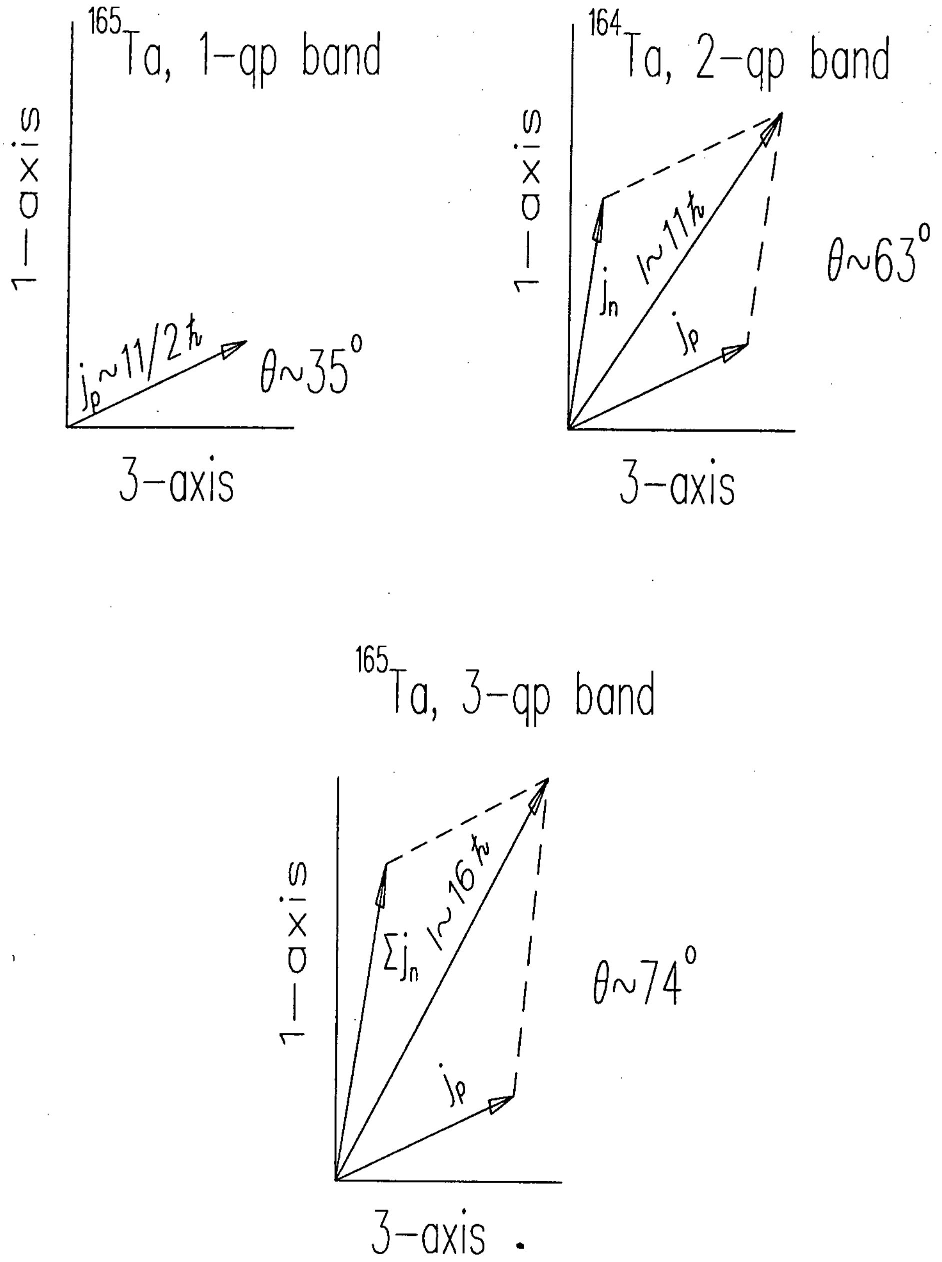

Figure 5.11: Decomposition of the total spin vector **I** into single-particle components, at zero rotational frequency: for ^{165}Ta below (upper left) and above (bottom) the backbend, and for ^{164}Ta (upper right).

resultant of coupling the vectors $\mathbf{j_p}$ and $\mathbf{j_n}$ is expected to have a tilt angle of about 63° and magnitude $\sim 11\hbar$, as shown in the diagram.

We may use this simple classical picture to speculate on the origin of some features of Figure 5.10. Firstly, it is evident from this figure that at low rotational frequencies, $\theta \simeq 30°(73°)$ for ^{165}Ta below (above) the backbend, and $\theta \simeq 63°$ for ^{164}Ta. Thus the axis of uniform rotation is expected to be considerably titled away from the principal axes in each case. This is in close agreement with the predictions of the simple geometrical picture (Fig. 5.11) described above. Secondly, the rather strong dependence of θ on ω in the case of the ^{165}Ta yrast band before the alignment may be described. As the nucleus rotates faster, there is increased contribution to $\mathbf{I}$ from the collective rotation $\mathbf{R}$. The component R_1 will effect a greater change in the tilt angle when the magnitude I of the spin vector is small. Therefore the lower solid curve slopes steeply upward ($I_{\omega=0} \simeq 5.5\hbar$), while the $\omega-$dependence of the upper solid curve (^{165}Ta yrast band above the alignment, $I_{\omega=0} \simeq 16\hbar$) and also the dot-dashed curve (^{164}Ta yrast band, $I_{\omega=0} \simeq 11\hbar$), is relatively weak.

Figure 5.12 compares the $B(M1)/B(E2)$ ratios predicted by TAC with the experimental values, plotted as a function of the rotational frequency. For ^{165}Ta below the backbend the experimental values are fairly well reproduced, although above the backbend the predictions do not agree well with the observed trend to increase with ω. However, TAC is performed using a fixed set of deformation parameters. Therefore if the increased $B(M1)/B(E2)$ ratios at higher spins result from a decrease in the quadrupole deformation, such a discrepancy is not unexpected. For ^{164}Ta the agreement between theory and experiment is poor and the parabola-like increase in the $B(M1)/B(E2)$ ratios is not reproduced.

5.2.5 Discrepancies between theory and experiment in ^{165}Ta

Although the assignment of the [514]9/2$^-$ quasiparticle configuration to the ^{165}Ta yrast band can be considered unambiguous, the bandcrossing frequency, the signature splitting of the routhians and the splitting of the $B(M1)/B(E2)$ ratios, in particular below the backbending, could not be reproduced satisfactorily by the CSM calculations. Indeed, these calculations were made assuming that the nucleus has a rigid deformation described

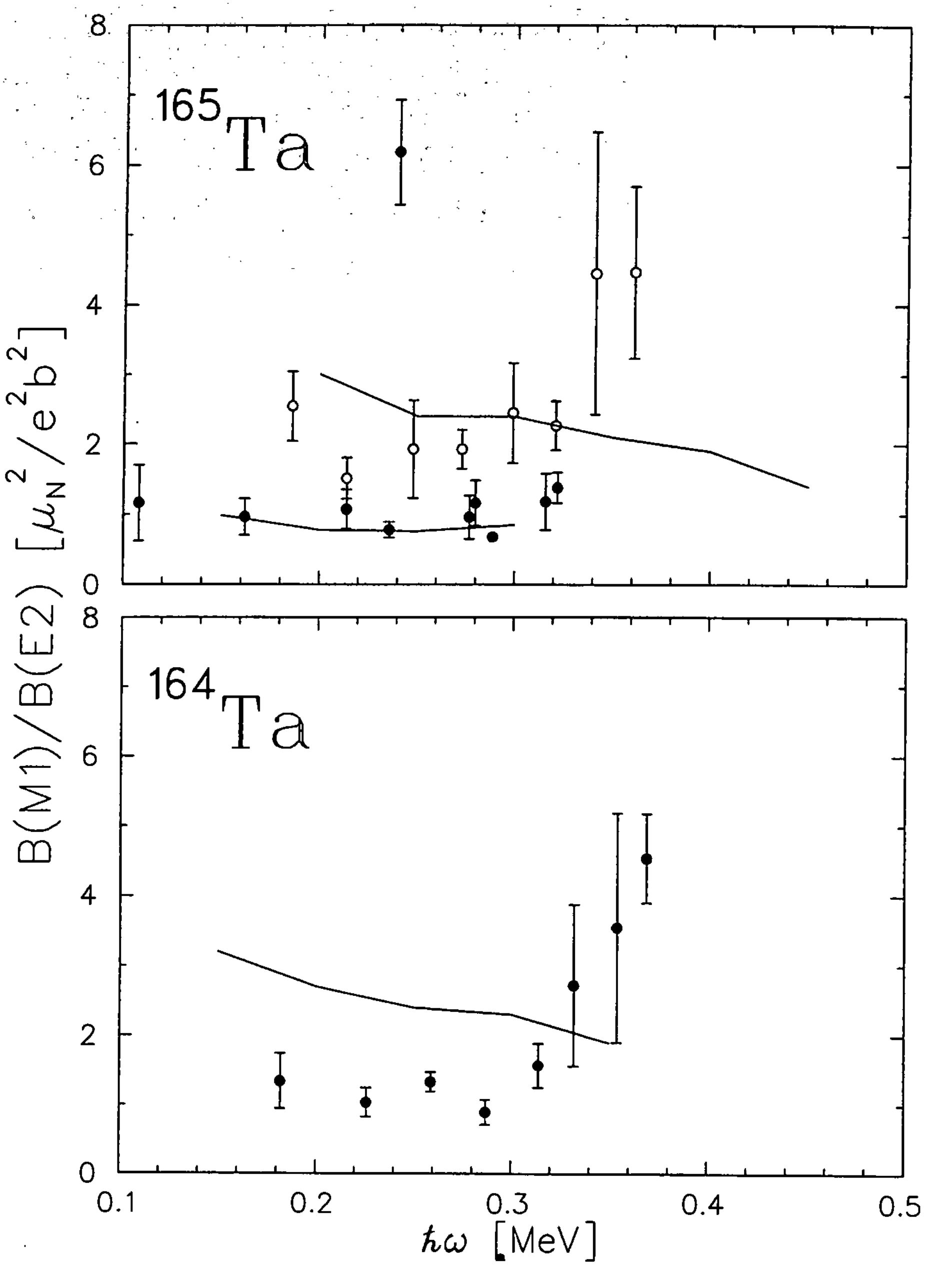

Figure 5.12: Comparison of experimental B(M1)/B(E2) values and theoretical predictions of TAC, plotted as a function of the rotational frequency. The open (filled) symbols correspond to the part of the yrast band above (below) the neutron alignment.

by the parameters at the potential energy minimum of the TR surface, while in fact a γ-soft shape was predicted (see Figure 5.7).

Similar discrepancies between the experimental quantities and the theoretical CSM predictions were previously found in the neighbouring odd-A Ta and Lu nuclei with $N \geq 90$, and were considered as a possible indication of a triaxial and/or γ-soft nuclear deformation [84, 91, 96, 97, 114, 115, 116, 127]. On the other hand Bengtsson *et al.* [10] considered that only the rare-earth nuclei with $N \sim 90$ and $62 < Z < 70$ would be sufficiently γ-soft for the odd quasiparticle to drive the nuclear shape toward sizeable γ-deformation. Therefore the question about γ-deviations from axial symmetry for the light Lu and in particular Ta isotopes remains open.

5.3 Are the light Ta isotopes non-axially symmetric?

It is difficult to find conclusive experimental evidence [128, 129] for the existence of a γ-deformed shape. However, a number of indications, concerning the odd-Ta isotopes in particular, lead to such a suggestion.

Increased backbending frequency for N$\sim$90. The upper part of Figure 5.13 shows the bandcrossing frequency $\hbar\omega_c$ of the AB (neutron $i_{13/2}$) alignment for the ground bands in the even-even $_{70}$Yb, $_{72}$Hf and $_{74}$W isotopes, as well as for the $\pi h_{11/2}$ bands in the odd $_{71}$Lu and $_{73}$Ta isotopes and the $\pi[402]5/2^+$ bands in the odd $_{73}$Ta isotopes, as a function of the neutron number N. The data used in plotting the figures are from ref. [84, 85, 86, 91, 96, 130, 131, 132, 133, 134, 135, 136, 137]. The main trend of the measured bandcrossing frequency for the isotopic chains in even-even nuclei is to decrease slowly with decreasing N and then to again increase for the lightest isotopes. It has been suggested [92, 114] that the relative position of the neutron Fermi level with respect to the $\Omega = 1/2$ orbitals of the $i_{13/2}$ shell, as well as the decrease of the monopole pairing energy with increasing N, play a crucial role in explaining this trend. Although this suggestion can qualitatively describe the observed trends, the calculated $\hbar\omega_c$ values lie much lower than the experimental ones for the lightest even-even isotopes [92]. Thus, changes in the deformation parameters [92], and in particular deviations from axial symmetry for the $N \geq 88$ isotopes [114], have been proposed.

The AB bandcrossing frequency in the odd-Z nuclei is similar to that of their even-even neighbours (see Fig. 5.13). The slightly lower $\hbar\omega_c$ values for the odd-mass isotones have been explained [114] as due to a small decrease in the quadrupole deformation of the nucleus, induced by the odd quasiproton (the positive slopes of the $\pi[514]9/2^-$ and the $\pi[402]5/2^+$ orbitals vs deformation can be seen in Figure 5.18). Since for these nuclei the valence protons and neutrons occupy different major shells, the proton-neutron interactions are negligible, and therefore the odd proton is not expected to influence the bandcrossing frequency [138]. This similarity is therefore an indication that the observed trend in the odd-Z isotopes is mainly due to the properties of the even-even core and will reflect the nuclear shape.

Thus, the higher experimental value of $\hbar\omega_c = 0.26$ MeV in $^{165}\mathrm{Ta}_{92}$ when compared with the theoretical prediction of 0.20 MeV is very likely a consequence of increased γ-softness of the core for this light Ta isotope.

Enhanced signature splitting. The experimentally observed signature splitting in the $9/2^-$ bands in the odd-even rare-earth nuclei is unexpectedly large for the light isotopes, increasing rapidly with decreasing neutron number when approaching the nuclei with $N \sim 90$. The CSM calculations have not been able to reproduce it.

Signature splitting appears as a consequence of the mixing into the wavefunctions of orbitals with $\Omega = 1/2$, due to the Coriolis interaction. However, since the proton Fermi level lies high in the $h_{11/2}$ shell the mixing of the $\Omega = 1/2$ components into the wave functions is small for an axially symmetric nuclear shape. Decreasing nuclear quadrupole deformation leads to an increased signature splitting since in the lowest order $\Delta e'$ is proportional to $\beta_2^{-2\Omega+1}$ if pairing is neglected [139]. Although an increase in signature splitting is expected with increasing Z and decreasing N (since the quadrupole deformation decreases, see Figure 5.6 and ref. [7]), the predicted magnitude of the splitting is nevertheless much less than observed [96]. Thus, in order to reproduce the large signature splitting of high-Ω orbitals, a mechanism leading to enhanced mixing with an $\Omega = 1/2$ orbital is needed. It seems that for the light odd-mass Ta and Lu isotopes only non-axially symmetric shapes can cause such an effect.

The enhanced signature splitting in the high-Ω $\pi h_{11/2}$ orbitals observed in the odd-A rare-earth isotopes, has been attributed [9] to deviations from an axially symmetric nuclear

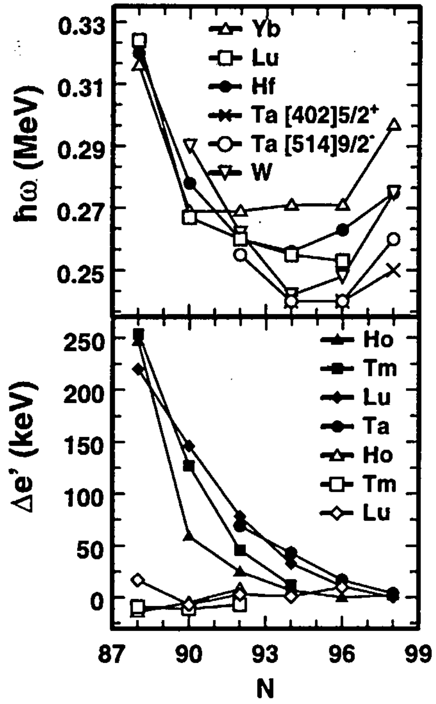

Figure 5.13: *Upper panel*: bandcrossing frequencies for the $\nu i_{13/2}$ alignment in the ground bands of even-even Yb, Hf and W isotopes and in the $\pi h_{11/2}$ and $\pi d_{5/2}$ bands in odd Lu and Ta isotopes. *Lower panel*: signature splitting of the high-Ω $\pi h_{11/2}$ routhians in the odd rare-earth isotopes with $Z \sim 70$. Filled symbols correspond to the signature splitting below the bandcrossing measured at $\hbar\omega$ =0.225 MeV, and open symbols to the signature splitting above the bandcrossing at $\hbar\omega$ =0.350 MeV.

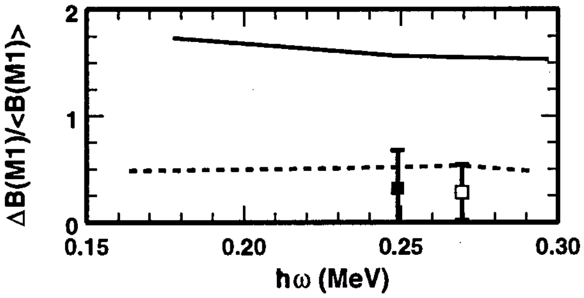

Figure 5.14: $\Delta B(M1)/ < B(M1) >$ ratios shown as a function of rotational frequency for the [514]9/2$^-$ bands. The solid (dotted) line represents the theoretical values in ^{165}Ta (^{167}Ta). Also shown are the experimental values for ^{165}Ta (filled square) and ^{167}Ta (open square) at rotational frequencies of 0.25 MeV and 0.27 MeV respectively.

indicate a considerable negative γ-deformation for ^{165}Ta.

It is therefore very likely that sizeable deviations from axial symmetry cause the observed discrepancies between the experimental data, and theoretical calculations which assume an axially symmetric nuclear shape. Since CSM cannot properly treat nuclear γ-softness, we performed such calculations with a fixed value of γ, representing the "mean" deviations from axial symmetry. A negative deformation with $\gamma = -18°$ not only raised the calculated crossing frequency to $\hbar\omega \sim 0.26$ with $\Delta i = 10.2\hbar$, (see the inset of upper part of Figure 5.22), but also gave a very good agreement between the experimental signature splitting (69 keV at $\hbar\omega = 0.225$ MeV) and the theoretical value (67.1 keV, see the inset of the lower part of Figure 5.22). Further, when theoretical $B(M1)/B(E2)$ ratios were calculated using $\gamma = -18°$ (neglecting the signature splitting), the values lay on a curve mid-way between the solid ($g_p = 1.3$) and dot-dashed ($g_p = 1.1$) curves (not shown in Figure 5.9). Although according to ref. [128] the CSM is not quantitatively reliable when describing the low frequencies in triaxially deformed nuclei, the above results indicate that it is quite likely that a considerable triaxial nuclear deformation and/or increased γ-softness plays a crucial role in the $\pi[514]9/2^-$ yrast band of ^{165}Ta.

5.4 Signature inversion in doubly-odd nuclei

The yrast bands of doubly-odd neutron-deficient rare-earth nuclei have the configuration $\pi h_{11/2} \otimes \nu i_{13/2}$. This two-quasiparticle band decouples into two sequences with favoured and unfavoured signatures respectively. In the neighbouring odd-proton (-neutron) nuclei the $\alpha = -1/2$ $(+1/2)$ is favoured, so that the signature $\alpha = 0$ (1) is expected to be favoured (unfavoured) in the doubly-odd $A \sim 160$ nuclei. However, in many cases the $\alpha = 0$ band is found to be raised above the $\alpha = 1$ band. This has been observed to occur systematically (but not exclusively) in bands of high-j parentage in the doubly-odd neutron-deficient rare-earth nuclei. The effect has been previously reported in the $\pi h_{11/2} \otimes \nu i_{13/2}$ structures of ^{152}Eu, ^{154,156}Tb, $^{156-160}$Ho, $^{158-166}$Tm, $^{160-166}$Lu, and ^{166,168}Ta [106]. Signature inversion is specific to doubly-odd systems, since for odd-A nuclei anomalous splitting has never been observed below the first $(\nu i_{13/2})^2$ alignment.

5.4.1 Experimental trends

An analysis of systematic trends of the energy signature dependence and the inversion frequency has been performed for the odd-odd nuclei with $89 \leq N \leq 97$ and $67 \leq Z \leq 73$ in a spin-independent way by plotting the *staggering amplitude* ΔE as a function of $\hbar\omega$:

$$\Delta E(I) = E(I) - E(I-1) - \frac{1}{2}[E(I+1) - E(I) + E(I-1) - E(I-2)] \qquad (5.8)$$

The results of this analysis are presented in Figures 5.15, 5.16 and 5.17. (i) Figure 5.15 shows plots of ΔE vs $\hbar\omega$ for the above nuclei. The inversion point marked by the arrow corresponds to the crossing of the curves $\Delta E_{favoured}$ and $\Delta E_{unfavoured}$. (ii) Figure 5.16 shows the systematic behaviour as functions of Z (left panel) and N (right panel) of the "maximum staggering amplitude" $\Delta E'_{\text{max}}$ below the inversion point, i.e. the *maximum* vertical displacement between the two curves:

$$\Delta E'_{\text{max}} = \Delta E_{unfavoured} - \Delta E_{favoured} \qquad (5.9)$$

(iii) Finally, Figure 5.17 shows the systematics if the inversion point $\hbar\omega_i$ as a function of Z (left panel) and N (right panel). In fact Figures 5.16 and 5.17 give alternative representations of the systematic trends which are already apparent from Figure 5.15. The findings are summarised as follows:

1. For a given chain of isotopes $|\Delta E'_{\text{max}}|$ decreases smoothly with increasing N, as illustrated in the right-hand panel of Figure 5.16 for the doubly-odd $Z = 67, 69, 71$ and 73 isotopes. The ^{164}Ta yrast band is consistent with this trend.

2. For the $N = 89$, 91 chains of isotones, $|\Delta E'_{\text{max}}|$ first increases and then decreases again with increasing Z, as illustrated in the left-hand panel of Figure 5.16. For the $N = 93$, 95 chains of isotones however, $|\Delta E'_{\text{max}}|$ simply increases with increasing Z.

3. The well-known tendency of the inversion frequency to decrease with increasing N along an isotope chain is evident from Figures 5.15 and 5.17 (right panel). Although the present data restrict our view of the ^{164}Ta yrast band to the region below the inversion point, a tentative lower limit of $\hbar\omega_i \sim 0.38$ MeV can be inferred from Figure 5.15, in agreement with the systematic trend. Tentative lower limits of $\hbar\omega_i \sim 0.36$ and $\hbar\omega_i \sim 0.38$ MeV can similarly be inferred for ^{160}Lu and ^{158}Tm.

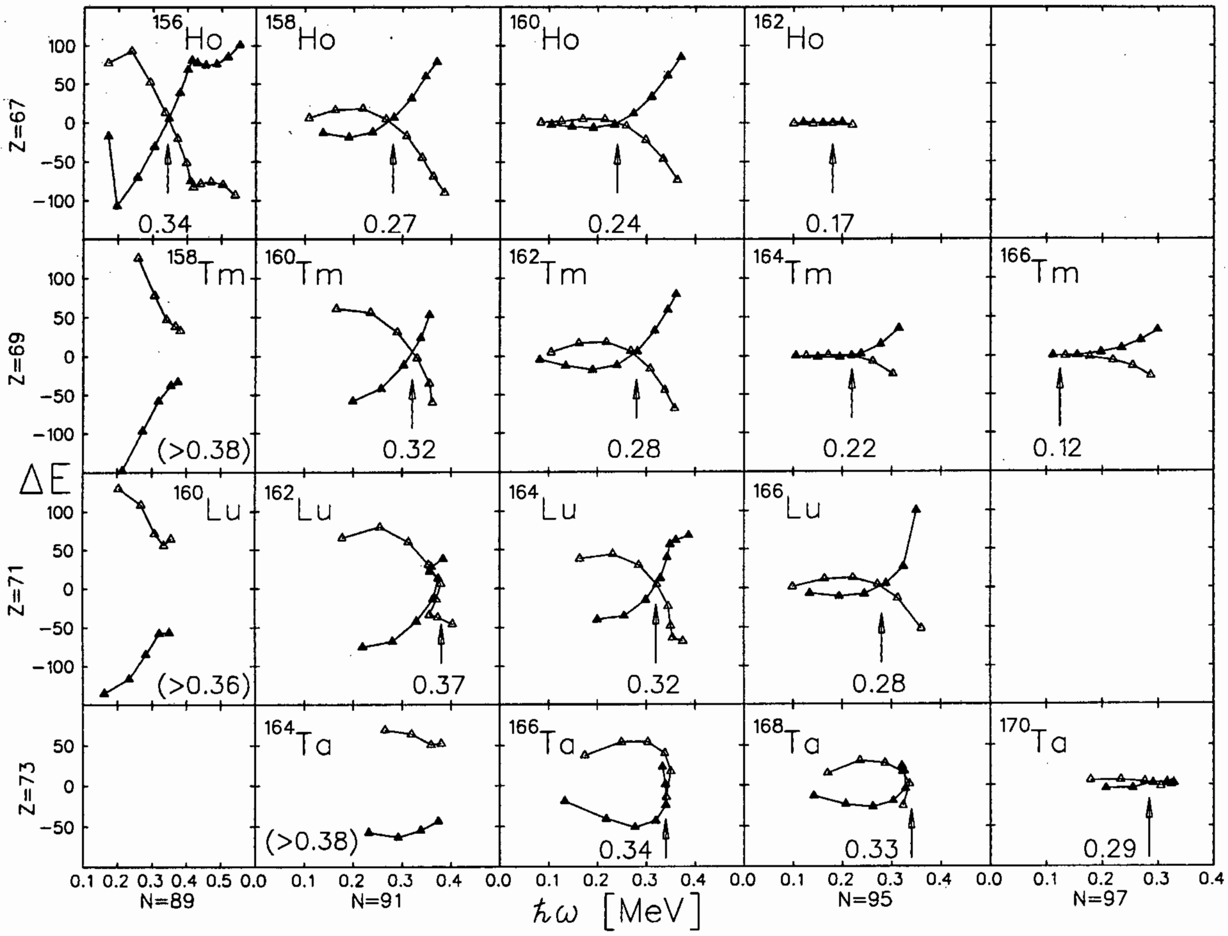

Figure 5.15: Plots of the energy staggering amplitude ΔE (in keV) as a function of the rotational frequency for the yrast systems of some doubly-odd rare-earth nuclei. The filled (open) symbols correspond to unfavoured (favoured) signatures. Where possible, the inversion frequency $\hbar\omega_i$ (marked by the arrow) is given. In the cases where the curves do not cross, a tentative lower limit for $\hbar\omega_i$ is given in parentheses.

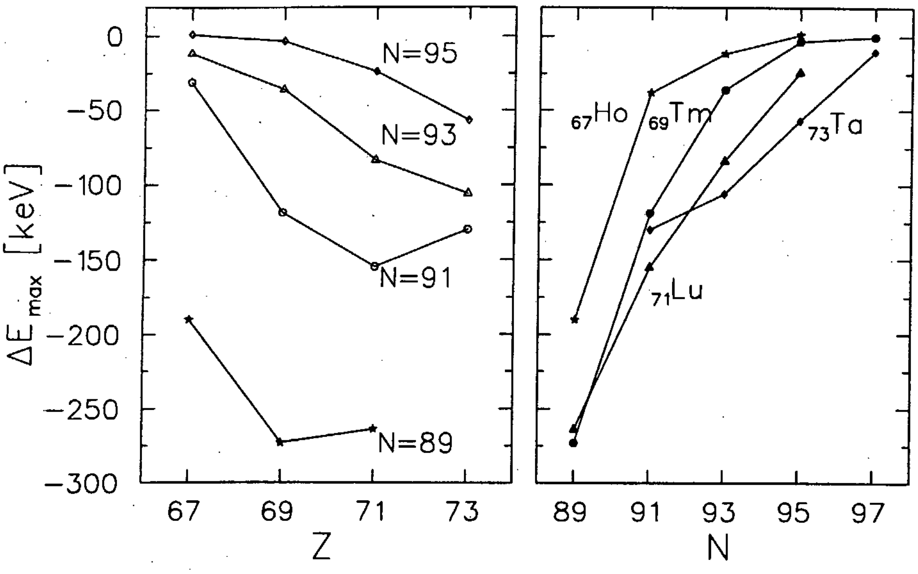

Figure 5.16: Systematic behaviour of the maximum staggering amplitude $\Delta E'_{\mathrm{max}}$ below the backbend for the yrast systems of some doubly-odd rare earth nuclei.

4. Along a chain of isotones, the inversion frequency increases with increasing Z as illustrated in Figures 5.15 and 5.17 (left panel) for the $N = 89-97$ isotones. Again, the behaviour of the ^{164}Ta yrast band conforms with this trend if $\hbar\omega_i \sim 0.38$ MeV is taken as the lower limit.

5. For nuclei with a constant $(N-Z)$ difference, the inversion frequency remains almost constant. This is valid for nuclei with $N - Z = 22, 24, 26$ and 28. The inversion frequency decreases with increasing $(N - Z)$ values. These trends are illustrated in Figure 5.15. It is evident that the behaviour of ^{164}Ta is again consistent with the systematic trend.

6. Our data are consistent with previous observations (for example reference [124]) that signature inversion is not only present for nuclei with $62 < Z < 70$ and N close to 90 as considered by Bengtsson *et al.* [10], but also for those with $Z = 71$ and 73, and N up to 97.

Observations (2) and (4) show the proton dependence. CSM calculations have shown [10] that, for fixed N, γ-deformation increases and β_2 decreases with increasing Z. There is thus a strong correlation between these systematic trends and changes in the nuclear

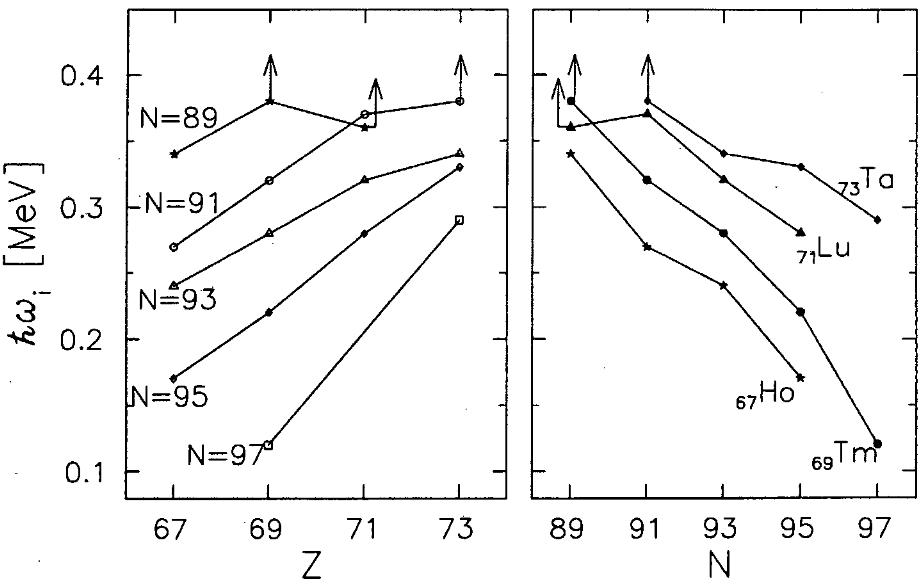

Figure 5.17: Systematic behaviour of the inversion frequency $\hbar\omega_i$ for the yrast systems of some doubly-odd rare earth nuclei. The arrows indicate data points representing lower limits.

shape.

A similar remark applies for the neutron dependence shown by points (1) and (3) above. This follows from the well-known trend for γ-deformation to increase and β_2 to decrease with decreasing N, for fixed Z.

Observation (5) shows that the inversion frequency remains nearly constant for nuclei with masses $A(Z+2n, N+2n)$ $n = 0, 1, 2...$ Evidently the addition of a multiple of α-particles to the core does not strongly affect the inversion frequency, whereas the addition of a *pair* of like nucleons (which also changes the deformation of the core) does have a marked effect. This may be understood if the effect of adding a proton pair is "cancelled" by adding a neutron pair, and underscores the existence of a correlation between the shape of the core and its response to the polarising effects of the odd particle.

5.4.2 Mechanisms for signature inversion in doubly-odd nuclei

The essential underlying mechanism for low-spin signature inversion in doubly odd rare-earth nuclei remains unresolved. More explicitly, the question of whether non-axiality of the core is necessary to induce the signature inversion, and to what extent the residual two-body interaction may be involved, has been the focus of an on-going polemic. The phenomenon has been previously studied through several theoretical approaches, such as the Cranked Shell Model (CSM) [10, 145], the Particle Rotor Model (PRM) [146, 147, 148], the Interacting Boson-Fermion Model (IBFM) [149], the Angular Momentum Projection Method [150], and most recently, in terms of the mean-field contribution of the $(\lambda\mu) = (22)$ component of the quadrupole pairing interaction [99]. None of the above approaches has been able to satisfactorily reproduce all the observed features of the signature inversion. An overview of some of these attempts to interpret the problem will now be given.

At high frequencies ($I \gg j_p + j_n$) signature inversion was explained by Bengtsson *et al.* [10], in the framework of CSM, as a consequence of a triaxial ($\gamma > 0$) nuclear shape. It was argued that observation (1) above could be understood by considering changes of the core deformation associated with the filling of the $\nu i_{13/2}$ shell. Taking the tantalum isotopes as examples and starting with the isotope ^{164}Ta$_{91}$, we consider the changes in the position of the neutron Fermi surface as more neutrons are added. The ^{164}Ta$_{91}$ *proton* Fermi surface lies close to the strongly coupled $\Omega = 9/2$ level of the $h_{11/2}$ shell. Such a high-Ω configuration drives the odd-A nuclei such as ^{165}Ta towards a negative γ-deformation, as discussed earlier. For the odd neutron on the other hand, $N = 91$ corresponds to the start of filling the $i_{13/2}$ shell. This neutron therefore occupies a low-Ω ($\Omega = 1/2$, $\alpha = +1/2$) orbital which is completely aligned, and may therefore be viewed as orbiting the nucleus in the equatorial plane. It polarises the core as a consequence of the short range of the nuclear interaction preferring maximal overlap of wavefunctions. The odd neutron thus drives the core towards a *positive* γ-deformation. Since the driving force of the odd neutron is stronger than that of the odd proton, a combination of the two effects results in a net positive γ-deformation.

As additional neutrons are added the Fermi surface shifts within the $i_{13/2}$ shell to higher-Ω (less aligned) orbitals. Consequently the polarisation effect, and by corollary the γ-deformation, is reduced. The fact that the signature splitting varies monotonically with increasing N strongly suggests that shape degrees of freedom must be responsible. CSM calculations reported in reference [9] showed that signature splitting exhibits no definite dependence on the quadrupole deformation parameter ϵ_2. It is therefore likely that the γ degree of freedom plays an important role, and that the trend of decreased splitting amplitude with increasing N reflects a diminishing triaxial deformation. So, for example, the signature inversion in $^{156}\mathrm{Ho}_{89}$ and $^{160}\mathrm{Ho}_{93}$ (see Fig. 5.16) was associated with respective γ-values of $\sim 20^\circ$ and 5° [10].

There are however several indications that the presence of triaxiality alone may not always be sufficient to explain the phenomenon. For example, in some cases signature inversion is observed although PES calculations predict almost axial shapes [99]. It is moreover impossible to directly determine γ-values experimentally. Further, inversion is observed at low frequencies ($\hbar\omega \leq 0.2$ MeV) for well-deformed nuclei where the presence of triaxiality is unlikely [124]. These considerations seem to call for an alternative or supplementary mechanism.

Alternative explanations have been provided within the framework of the Particle Rotor Model (PRM) by properly taking into account the coupling of the core and odd-particle angular momenta. Such attempts have either included [151] or excluded [152] the residual proton-neutron (pn) interaction. For example, Hamamoto [152] demonstrated that the experimentally observed signature inversion in the well-deformed nucleus $^{156}\mathrm{Tb}$ could be reproduced in terms of PRM without invoking triaxiality. However it should be noted that this conclusion was deduced from an analysis of the experimental data of a single nucleus, and all the theoretical studies involving a systematic calculation for a series of isotopes or isotones indicate the necessity of incorporating triaxiality into the models [102]. It has also been possible within the framework of PRM to accurately reproduce, *inter alia*, some $\pi h_{11/2} \otimes \nu i_{13/2}$ bands in rare-earth nuclei without invoking triaxiality [153, 154] by including a residual pn contact force with spin-spin interaction $V_{pn}\delta(\mathbf{r_p} - \mathbf{r_n})(\mathbf{u_0} + \mathbf{u_1}\sigma_\mathbf{n} \cdot \sigma_\mathbf{p})$ as suggested by Semmes and Ragnarsson [151].

While CSM can qualitatively explain the signature crossing in axially symmetric doubly-odd nuclei at high rotational frequencies, the experimental splitting was not well reproduced [155], even after calculations were improved [145] by considering the residual pn interaction.

According to Hara and Sun [150] signature inversion is also predicted in the $A \sim 160$ region by the angular momentum projection method at axially symmetric shapes, due to the crossing of two bands with opposite signature dependence. However, the expectation that the staggering amplitude would increase with proton number (predicted by this mechanism) was not fulfilled for doubly odd nuclei with $N = 91$ and $Z = 65, 67, 69$ [155].

Recently Xu *et al.* [99] demonstrated that it was possible to accurately reproduce signature inversion in the $A \sim 160$ region (and the $A \sim 130$ region) without invoking the *pn* interaction. They used an extended TRS model which includes quadrupole pairing correlations (QQ-pairing). Their calculations predicted that the $\Gamma^{(\lambda\mu)} = \Gamma^{(22)}$ component of the quadrupole pairing interaction would create signature inversion of the order of a few tens of keV already at fixed *axial* shapes. The extent to which it favours the unfavoured signature depends on the position of the Fermi level. The contribution of the $\Gamma^{(22)}$ potential is strongest when the Fermi energy is near the middle of a shell. In this case it competes with the Coriolis force which is usually diminished at low rotational frequencies, and therefore favours the inversion. When the calculations were repeated for a fixed *triaxial* shape ($\gamma = 15°$) the anomalous splitting was found to increase further. Thus at low frequencies where the Coriolis mixing is weak the anomalous splitting is accounted for by triaxiality combined with the contribution of the $(\lambda\mu) = (22)$ component of the quadrupole pairing interaction [99]. At higher rotational frequencies the Coriolis interaction dominates, and the sign of the splitting is restored to normal. It is worth noting that this model does not account for anomalous splitting in γ-soft nuclei.

Although it is unlikely that a single mechanism can account for the anomalous splitting across the entire range of inversion frequencies ($0.14 \leq \hbar\omega_i \leq 0.38$ MeV), it is very likely that non-axial shapes play an important role in these nuclei.

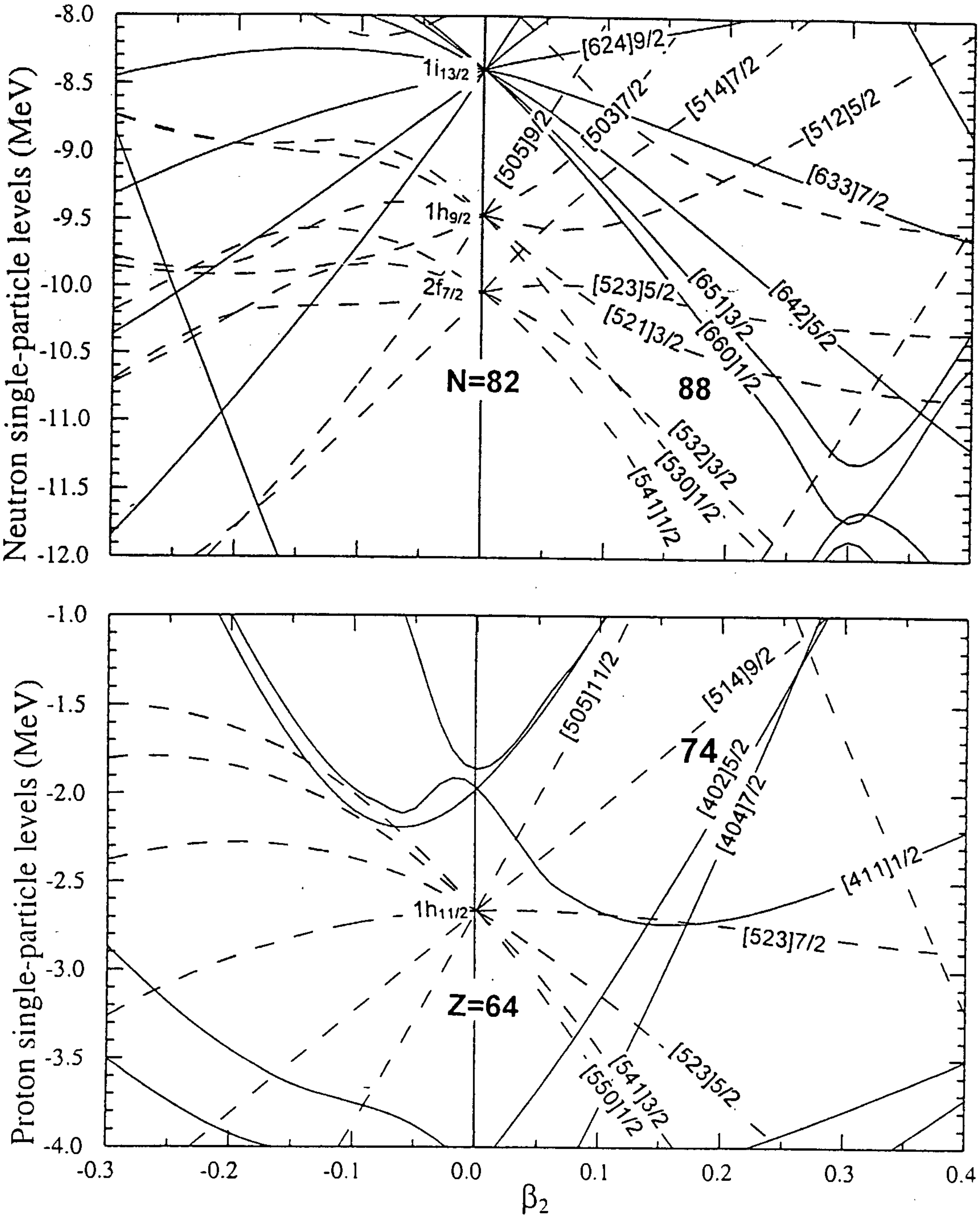

Figure 5.18: Single-particle levels calculated using a Woods-Saxon potential, for neutrons (upper panel) and protons (lower panel). Orbitals are labelled with Nilsson asymptotic quantum numbers. Solid (dashed) lines denote orbitals of positive (negative) parity.

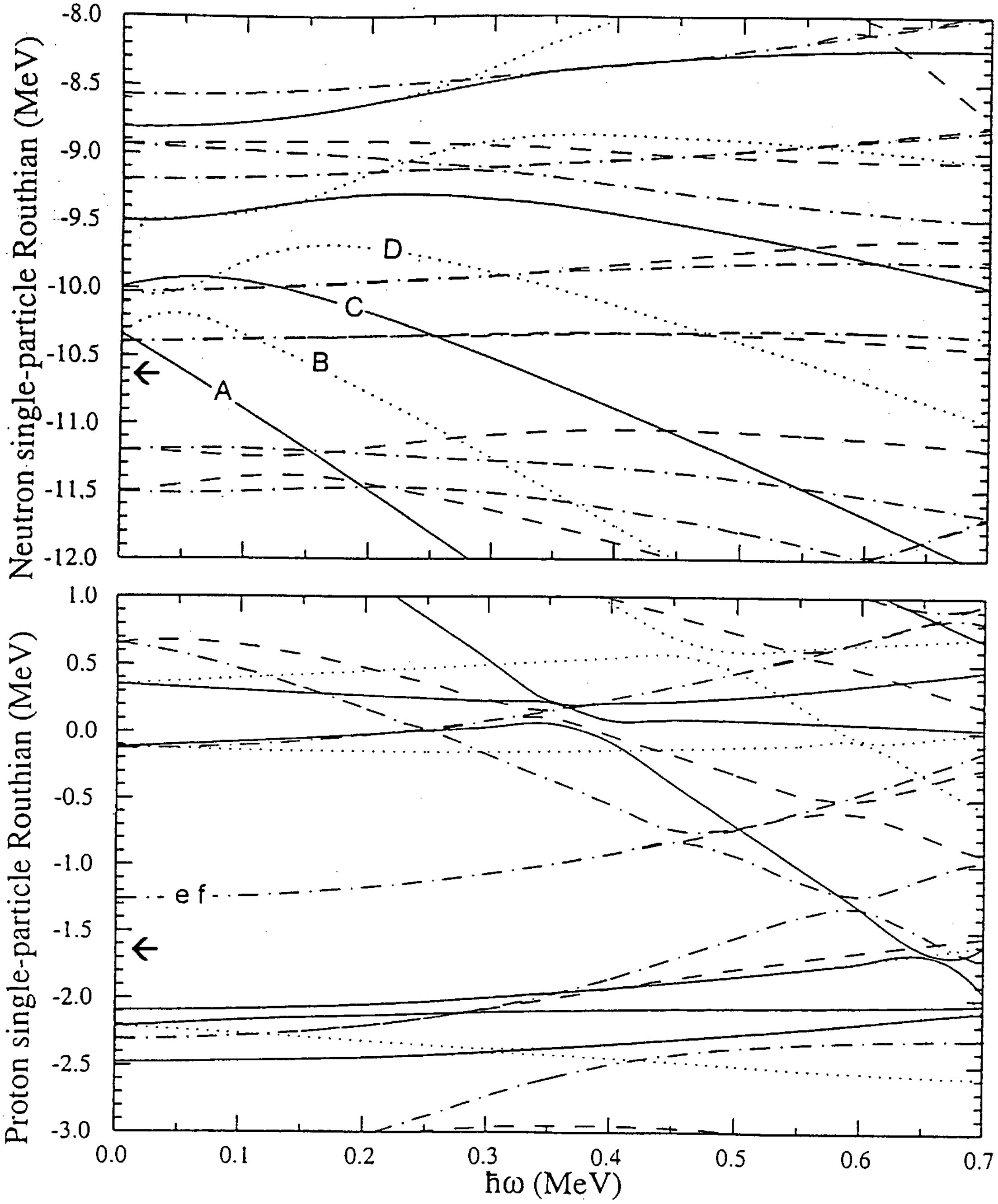

Figure 5.19: Single-particle routhians for neutrons (upper panel) and for protons (lower panel) plotted as a function of rotational frequency for ^{164}Ta. The calculations were done using $\beta_2 = 0.172$, $\gamma = 6.4°$, $\beta_4 = 0.014$. The parity and signature (π, α) of the routhians are represented as follows: $(+, +1/2)$ solid lines, $(+, -1/2)$ dotted lines $(-, +1/2)$ dash-dotted lines and $(-, -1/2)$ dashed lines. Arrows denote the position of the Fermi level.

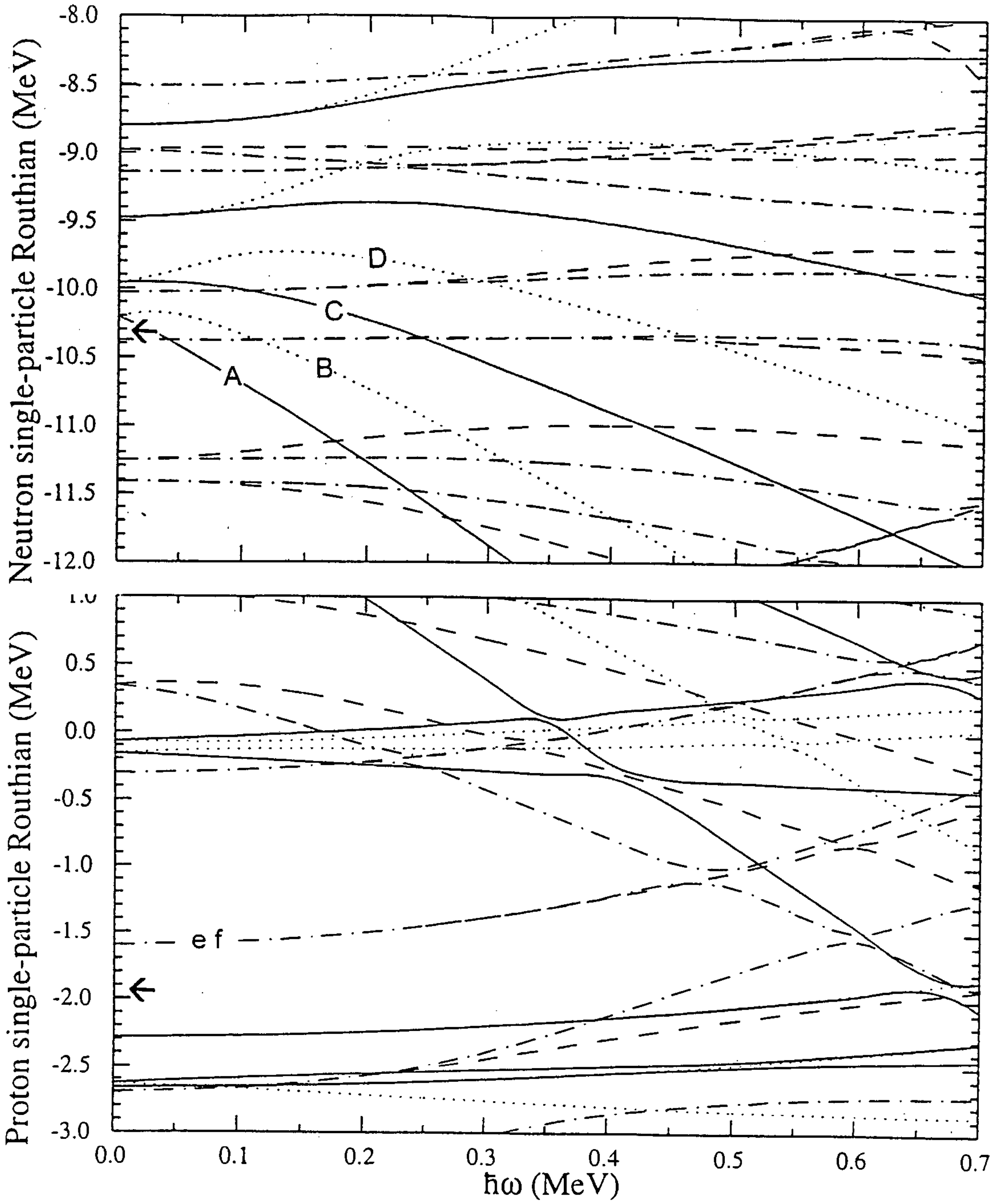

Figure 5.20: Single-particle routhians for neutrons (upper panel) and for protons (lower panel) plotted as a function of rotational frequency for ^{165}Ta. The calculations were done using $\beta_2 = 0.177$, $\gamma = -0.8°$, $\beta_4 = 0.006$. The parity and signature (π, α) of the routhians are represented as follows: $(+, +1/2)$ solid lines, $(+, -1/2)$ dotted lines $(-, +1/2)$ dash-dotted lines and $(-, -1/2)$ dashed lines. Arrows denote the position of the Fermi level.

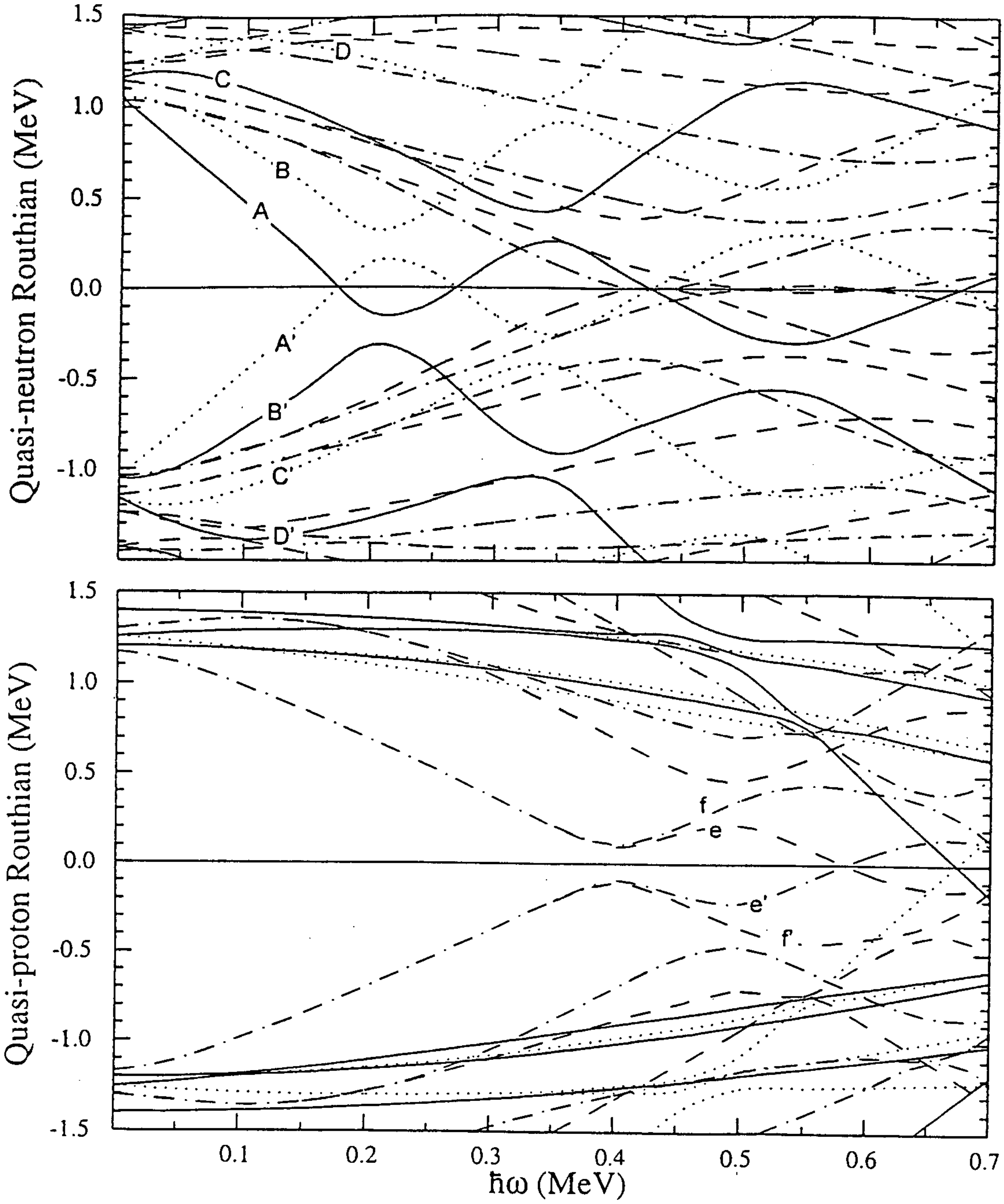

Figure 5.21: Quasiparticle routhians for neutrons (upper panel) and for protons (lower panel) plotted as a function of rotational frequency for ^{164}Ta. The calculations were done using $\beta_2 = 0.172$, $\gamma = 6.4°$, $\beta_4 = 0.014$. The parity and signature (π, α) of the routhians are represented as follows: $(+,+1/2)$ solid lines, $(+,-1/2)$ dotted lines $(-,+1/2)$ dash-dotted lines and $(-,-1/2)$ dashed lines.

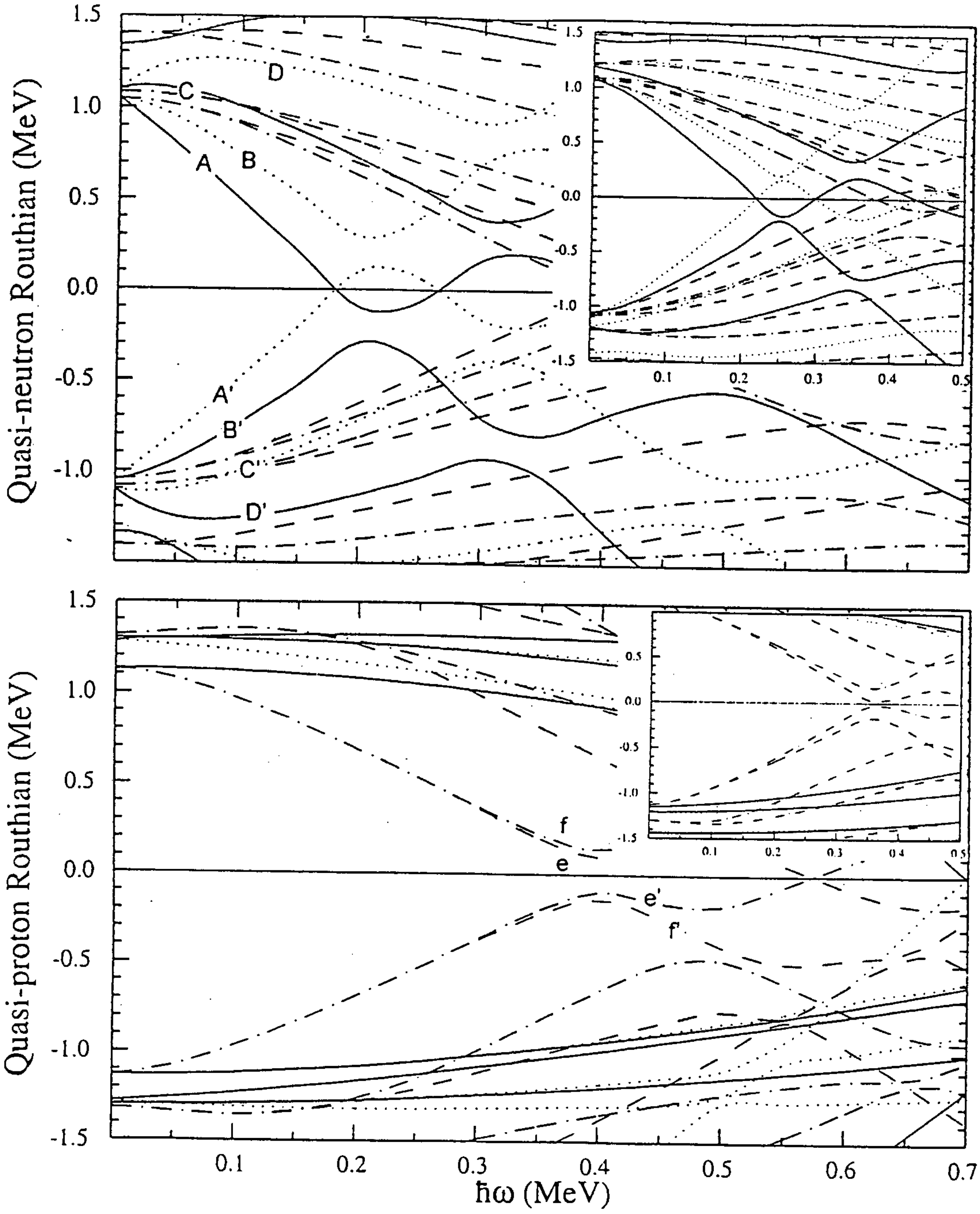

Figure 5.22: Quasiparticle routhians for neutrons (upper panel) and for protons (lower panel) plotted as a function of rotational frequency for ^{165}Ta. The calculations were done using $\beta_2 = 0.177$, $\gamma = -0.8°$, $\beta_4 = 0.006$. The insets correspond to calculations using the same parameters, but $\gamma = -18°$. The parity and signature (π, α) of the routhians are represented as follows: $(+, +1/2)$ solid lines, $(+, -1/2)$ dotted lines $(-, +1/2)$ dash-dotted lines and $(-, -1/2)$ dashed lines.

Chapter 6

Summary

This work is based on coincidence data acquired in two of the first experiments performed using the AFRODITE spectrometer array. It comprises a spectroscopic investigation of high-spin states in the nuclei ^{164}Ta and ^{165}Ta, currently the lightest tantalum isotopes to have been studied at high spin.

The identification of ^{164,165}Ta was based on (i) coincidence relationships between the $\gamma-$rays and the tantalum K $x-$rays and (ii) a comparison of the intensities of $\gamma-$rays measured in two separate fusion-evaporation reactions.

The yrast band of ^{165}Ta, comprising two signature-partner sequences linked by M1 cascade transitions, was identified up to $I^{\pi} = 53/2^{-}$ and excitation energy 6168 keV for the first time. The configuration $\pi[514]9/2^{-}$ was assigned to this band, and $I^{\pi} = 9/2^{-}$ assigned to the bandhead. A less intense excited band was also identified, and tentatively assigned the configuration $\pi[402]5/2^{+}$. The ordering of the $\gamma-$ray transitions in the excited band is tentative. A larger, high-fold data set is needed to fix this band. Although the present data set (from the first experiment) is large (~538 million three-and-higher-fold events), it must be remembered that only $\sim$ 10% of these were triples in Clovers. This limited the usefulness of some of the double-gated spectra, essential for placing energy multiplets in the band.

For the yrast band, a number of discrepancies were observed between the experimental data and CSM predictions. These include exaggerated signature splitting below the AB bandcrossing, delayed AB bandcrossing frequency, and overestimated signature splitting in the B(M1)/B(E2) ratios below the $\nu i_{13/2}$ alignment. It is argued that these discrepancies are consistent with a non-axial nuclear shape in the yrast band. The latter is expected to be γ−soft on the basis of TRS calculations, which also predict shape co-existence at higher rotational frequencies.

The ^{164}Ta yrast band, found to consist of two signature partner sequences linked by M1 transitions, was identified up to $I^{\pi} = 21^{-}$ for the first time and assigned the configuration $\pi[514]9/2^{-} \otimes \nu[660]1/2^{+}$. A weaker excited band, tentatively associated with a four-quasiparticle configuration, could also be identified.

Two new isomers were identified. The 11^{-} yrast levels of ^{164}Ta$_{91}$ and ^{162}Lu$_{91}$ (a by-product of the first experiment) were found to be isomeric. This is the first time that nanosecond-range isomers have been observed in the light tantalum or lutetium isotopes. The presence of these isomers raises the question of the bandhead spin, which would be interesting to determine in order to shed light on the coupling mode of the odd proton and odd neutron. However the γ−rays from transitions below the 11^{-} level are probably highly converted. A proposal is therefore being drafted to study low-lying states in the light tantalum and lutetium isotopes using the electron spectrometer at CSNSM, Orsay. It is intended to measure the half-life of the isomer from the time-distribution of the delayed transitions detected in the electron spectrometer. Observation of the decay of the yrast band down to the $I^{\pi} = 3^{+}$ ground state would also allow confirmation of the spin assignments to this band, which have hitherto been based on systematics.

Low-spin signature inversion was observed in the ^{164}Ta yrast band. Several attempts to explain this phenomenon in the $\pi h_{11/2} \otimes \nu i_{13/2}$ yrast bands of the doubly-odd rare-earth nuclei are reviewed in Chapter 5. In summary it may be said that (i) no single mechanism could thus far reproduce all the observed features of the inversion, and (ii) it is likely that non-axiality needs to be included in the models. The question of the ultimate mechanism behind signature inversion remains open.

Bibliography

[1] C.F.Liang and P.Paris, Z. Phys. **A309**, 185 (1982).

[2] U.J.Schrewe *et al.*, Z. Phys. **A310**, 295 (1983).

[3] T.Hild *et al.*, Nucl. Phys. **A492**, 237 (1989).

[4] E.Hagberg *et al.*, Phys. Rev. C **45**, 1609 (1992).

[5] J.Simpson, (2000), private communication.

[6] R.M.Clark *et al.*, App. to Daresbury Ann. Rep. **37**, 37 (1990/1991).

[7] W.Nazarewicz *et al.*, Nucl. Phys. **A512**, 61 (1990).

[8] Y.Liu *et al.*, Phys. Rev. C **52**, 2514 (1995).

[9] S.Frauendorf and F.R.May, Phys. Lett. B **125**, 245 (1983).

[10] R.Bengtsson *et al.*, Nucl. Phys. **A415**, 189 (1984).

[11] E.Gueorguieva *et al.*, Physica Scripta **T88**, 135 (2000).

[12] D.G.Roux *et al.*, Phys. Rev. C **63**, 024303 (2001).

[13] A.Bohr and B.Mottleson, *Nuclear Structure, Vol. II* (Benjamin, Reading, MA, 1975).

[14] G.Andersson *et al.*, Nucl. Phys **A268**, 205 (1976).

[15] K.E.G.Löbner *et al.*, Nucl. Data Tables **7**, 495 (1970).

[16] S.M.Harris, Phys. Rev. B **138**, 509 (1965).

[17] P.Ring and P.Schuck, *The Nuclear Many-Body Problem* (Springer-Verlag, New York, 1980).

[18] H.Toki and H.L.Yadav, Phys. Lett. B **66**, 310 (1977).

[19] H.Toki *et al.*, Z. Phys. **A292**, 79 (1979).

[20] J.Bardeen *et al.*, Phys. Rev. **108**, 1175 (1957).

[21] D.R.Inglis, Phys. Rev. **96**, 1059 (1954).

[22] D.R.Inglis, Phys. Rev. **103**, 1786 (1956).

[23] D.R.Inglis, Phys. Rev. **97**, 701 (1955).

[24] S.G.Nilsson and I.Ragnarsson, *Shapes and Shells in Nuclear Structure* (Cambridge University Press, Cambridge, 1995).

[25] B.R.Mottleson and J.G.Valatin, Phys. Rev. Lett. **5**, 511 (1960).

[26] S.Frauendorf, in press (unpublished).

[27] F.Dönau, Balkan Phys. Lett. **Special Issue**, 123 (1998).

[28] A.Brockstedt *et al.*, Nucl. Phys. **A571**, 337 (1994).

[29] W.Reviol *et al.*, Phys. Rev. C **59**, 1351 (1999).

[30] J.R.B.Oliveira *et al.*, Phys. Rev. C **50**, 1360 (1994).

[31] C.J.Pearson, Phys. Rev. Lett. **79**, 605 (1997).

[32] R.M.Lieder, Nucl. Phys. **A645**, 465 (1999).

[33] T.Horibata and N.Onishi, Phys. Lett **325**, 283 (1994).

[34] T.Horibata and N.Onishi, Nucl. Phys. **A596**, 251 (1994).

[35] H.Frisk and R.Bengtsson, Phys. Lett. B **196**, 14 (1987).

[36] C. Weizsäcker, Z. Phys. **96**, 431 (1935).

[37] H.A.Bethe and R.F.Bacher, Rev. Mod. Phys. **8**, 82 (1936).

[38] V.M.Strutinsky, Nucl. Phys. **A95**, 420 (1967).

[39] V.M.Strutinsky, Nucl. Phys. **A122**, 1 (1968).

[40] R.A.Wyss, *Alignment, Shape and Pairing Effects in Atomic Nuclei in the Mass = 120-140 Region* (KTH, Stokholm, 1990).

[41] W.D.Myers and W.Swiatecki, Ark. Fys. **36**, 343 (1967).

[42] W.Nazarewicz *et al.*, Nucl. Phys. **A435**, 397 (1985).

[43] J.Dudek *et al.*, Phys. Rev. C **23**, 920 (1981).

[44] F.S.Stephens, Rev. Mod. Phys. **47**, 43 (1975).

[45] J.O.Newton, Contemporary Physics **30**, 277 (1989).

[46] F.A.Beck, Prog. Part. Nucl. Phys. **28**, 443 (1992).

[47] C.W.Beausang and J.Simpson, J. Phys. G: Nucl. Part. Phys. **22**, 527 (1996).

[48] I.Lee, Prog. Part. Nucl. Phys. **28**, 473 (1992).

[49] R.M.Lieder, *Experimental Techniques in Nuclear Physics* (Walter de Gruyter, Berlin, 1995), p. 137.

[50] J.Simpson, Z. Phys. **A358**, 139 (1997).

[51] J.F.Sharpey-Schafer and J.Simpson *et al.*, Prog. Part. Nucl. Phys. **21**, 293 (1988).

[52] H. A.Johnson and J.Sztarkier, Phys. Lett. B **34**, 605 (1971).

[53] P.J.Nolan *et al.*, Nucl. Instr. Meth. A **236**, 95 (1985).

[54] F.A.Beck, in *Proceedings of the Conference on Instrumentation for Heavy Ion Nuclear Research, pg. 129*, Vol. 7 of *Nuclear Science Research Conferences*, edited by D.Shapira (Harwood, New York, 1984).

[55] R.M.Lieder *et al.*, Nucl. Instr. Meth. A **220**, 363 (1984).

[56] B.Herskind *et al.*, Nucl. Phys. **A447**, 353c (1985).

[57] R.M.Diamond and F.S.Stephens, in *Proceedings of the Conference on Instrumentation for Heavy Ion Nuclear Research, pg. 259*, Vol. 7 of *Nuclear Science Research Conferences*, edited by D.Shapira (Harwood, New York, 1984).

[58] J.P.Martin *et al.*, Nucl. Instr. Meth. A **257**, 301 (1983).

[59] P.J.Twin *et al.*, Phys. Rev. Lett. **57**, 811 (1986).

[60] G.Baldsiefen *et al.*, Phys. Rev. C **54**, 1106 (1996).

[61] R.M.Clark *et al.*, Phys. Rev. Lett **78**, 1868 (1997).

[62] H.Schnare *et al.*, Phys. Rev. C **54**, 1598 (1996).

[63] R.Wadsworth *et al.*, Phys. Rev. C **53**, 2763 (1996).

[64] K.Vetter *et al.*, Nucl. Instr. Meth. A **452**, 105 (2000).

[65] M.A.Deleplanque *et al.*, Nucl. Instr. Meth. A **430**, 292 (1999).

[66] G.J.Schmid *et al.*, Nucl. Instr. Meth. A **430**, 69 (1999).

[67] K.Vetter *et al.*, Nucl. Instr. Meth. A **452**, 223 (2000).

[68] K.S.Krane, *Introductory Nuclear Physics* (John Wiley and Sons, New York, 1988), p. 235.

[69] W.Kutschera, Phys. Rev. C **5**, 1658 (1972).

[70] D.Schwalm *et al.*, Nucl. Phys. **A293**, 425 (1977).

[71] B.R.S.Babu *et al.*, Dept. of Atomic Energy, Govt. of India, Ann. Nuc. Phys. Symp. **40 B**, 416 (1997).

[72] R.T.Newman *et al.*, Balkan Phys. Lett. **Special Issue**, 182 (1998).

[73] F.A.Beck *et al.*, in *Proceedings of the Conference on Physics from Large Gamma-ray Detector Arrays, pg. 154* (LBL 35687, Berkeley, 1994).

[74] P.J.Nolan *et al.*, Ann. Rev. of Nucl. and Part. Sci. **45**, 561 (1994).

[75] J.Gerl and R.M.Lieder, GSI Darmstadt Report (1992).

[76] P.K.Joshi *et al.*, Nucl. Instr. and Meth. in Phys. Res. A **399**, 51 (1997).

[77] P.M.Jones *et al.*, Nucl. Instr. and Meth. A **362**, 556 (1995).

[78] G.F.Knoll, *Radiation Detection and Measurement*, 2nd ed. (John Wylie and Sons, New York, 1989), p. 489.

[79] N.G.Nicolis *et al.* (unpublished).

[80] F.Yang and J.H.Hamilton, *Modern Atomic and Nuclear Physics* (McGraw-Hill Inc., New York, 1996), p. 764.

[81] D.C.Radford, Nucl. Instr. and Meth. A **361**, 297 (1995).

[82] H.Zheng *et al.*, J. Phys. G: Nucl. Part. Phys **23**, 723 (1997).

[83] J.Simpson *et al.*, J. Phys. G: Nucl. Part. Phys **18**, 1207 (1992).

[84] K.Theine *et al.*, Nucl. Phys. **A536**, 418 (1992).

[85] S.G.Li *et al.*, Nucl. Phys. **A555**, 435 (1993).

[86] J.C.Baclear *et al.*, Nucl. Phys. **A442**, 547 (1985).

[87] F.G.Kondev *et al.*, Nucl. Phys. **A601**, 195 (1996).

[88] D.E.Archer *et al.*, Phys. Rev. C **52**, 1326 (1995).

[89] F.G.Kondev *et al.*, Nucl. Phys. **A617**, 91 (1997).

[90] R.B.Firestone, *Table of Isotopes, Evaluated Nuclear Structure Data Files*, eighth ed. (National Nuclear Data Center, Brookhaven National Laboratory, www.nndc.bnl.gov, 1996).

[91] Y.Ma *et al.*, J. Phys. G: Nucl. Part. Phys **21**, 937 (1995).

[92] J.Simpson *et al.*, J. Phys. G: Nucl. Part. Phys **17**, 511 (1991).

[93] S.L.Gupta *et al.*, Phys. Rev. C **56**, 1281 (1997).

[94] P.Juneja *et al.*, Phys. Rev. C **53**, 1221 (1996).

[95] Y.H.Zhang *et al.*, Eur. Phys. J. A **1**, 119 (1998).

[96] C.-H.Yu *et al.*, Nucl. Phys. **A489**, 477 (1988).

[97] W.Schmitz *et al.*, Nucl. Phys. **A539**, 112 (1992).

[98] K.P.Blume *et al.*, Nucl. Phys. **A464**, 445 (1987).

[99] F.R.Xu *et al.*, Nucl. Phys. **A669**, 119 (2000).

[100] M.A.Cardona *et al.*, Phys. Rev. C **56**, 707 (1997).

[101] Y.H.Zhang *et al.*, Z. Phys. **A355**, 335 (1996).

[102] S-G.Zhou *et al.*, J. Phys. G: Nucl. Part. Phys. **22**, 415 (1996).

[103] S.Drissi *et al.*, Nucl. Phys. **A543**, 495 (1986).

[104] H.Sun *et al.*, Z. Phys. **A351**, 241 (1995).

[105] D.Hojman *et al.*, Phys. Rev. C **45**, 90 (1992).

[106] Y.H.Zhang *et al.*, Phys. Rev. C **60**, 044311 (1999).

[107] R.A.Bark *et al.*, Nucl. Phys. **A501**, 157 (1989).

[108] H.Schnack-Petersen *et al.*, Nucl. Phys. **A594**, 175 (1995).

[109] R.Bengtsson *et al.*, Phys. Scr. **39**, 1996 (1989).

[110] T.Bengtsson and I.Ragnarsson, Nucl. Phys. **A436**, 14 (1985).

[111] F.Dönau, Nucl. Phys. **A451**, 313 (1987).

[112] K.Alder *et al.*, Rev. Mod. Phys. **28**, 432 (1956).

[113] F. O.Prior and S.G.Nilsson, Nucl. Phys. **A110**, 257 (1968).

[114] C.-H.Yu *et al.*, Nucl. Phys. **A511**, 157 (1990).

[115] P.Frandsen *et al.*, Nucl. Phys. **A489**, 508 (1988).

[116] S.Jonsson *et al.*, Nucl. Phys. **A422**, 397 (1984).

[117] S.Frauendorf, Phys. Lett. B **100**, 219 (1981).

[118] H.Emling *et al.*, Nucl. Phys. **A419**, 187 (1984).

[119] M.Fewell *et al.*, Phys. Rev. C **31**, 1057 (1985).

[120] M.Fewell *et al.*, Phys. Rev. C **37**, 101 (1988).

[121] J.C.Bacelar *et al.*, Phys. Rev. Lett. **57**, 3019 (1986).

[122] F.Dönau and S.Frauendorf, in *Proceedings of the Conference on High Angular Momentum Properties of Nuclei, Oak Ridge, Tennessee, pg. 143*, edited by N.Johnson (Harwood Academic, Chur, Switzerland, 1982).

[123] C.J.Gallagher and S.A.Moszkowski, Phys. Rev. **111**, 1282 (1958).

[124] S.Drissi *et al.*, Nucl. Phys. **A600**, 63 (1996).

[125] J.L.Salicio *et al.*, Nucl. Phys. **A512**, 109 (1990).

[126] S.J.Mannanal *et al.*, Nucl. Phys. **A582**, 141 (1995).

[127] P.Frandsen *et al.*, Phys. Lett B **177**, 287 (1986).

[128] G.B.Hagemann and I.Hamamoto, Phys. Rev. C **40**, 2862 (1989).

[129] I.Hamamoto, Proceedings of the Workshop on Microscopic Models in Nuclear Structure Physics, Oak Ridge, World Scientific, Singapore 173 (1988).

[130] C.Foin *et al.*, Nucl. Phys. **A199**, 129 (1973).

[131] S.Jónsson *et al.*, Nucl. Phys. **A449**, 537 (1986).

[132] Y-J.Ma *et al.*, J. Phys. G **26**, 43 (2000).

[133] R.A.Bark *et al.*, Nucl. Phys. **A644**, 29 (1998).

[134] L.Funke *et al.*, Nucl. Phys. **A170**, 593 (1971).

[135] D.C.Radford *et al.*, in *Proc. Conf. on Nucl. Structure at the Limits* (Argonne, Illinois, 1996).

[136] A.G.Smith *et al.*, Nucl. Phys. **A587**, 150 (1995).

[137] H.J.Jensen *et al.*, Z. Phys. **A340**, 351 (1991).

[138] J.D.Garrett *et al.*, Phys. Rev. Lett. **47**, 75 (1981).

[139] W.F.Mueller *et al.*, Phys. Rev. C **50**, 1901 (1994).

[140] G.B.Hagemann *et al.*, Phys. Rev. C **25**, 3224 (1982).

[141] G.B.Hagemann *et al.*, Nucl. Phys. **A424**, 365 (1984).

[142] A.J.Larabee and J.C.Waddington, Phys. Rev. C **24**, 2367 (1981).

[143] I.Hamamoto and B.R.Mottelson, Phys. Lett. B **132**, 7 (1983).

[144] J.Gascon *et al.*, Nucl. Phys. **A467**, 539 (1987).

[145] M.Matsuzaki, Phys. Lett. B **269**, 23 (1991).

[146] I.Hamamoto, Phys. Lett. B **235**, 221 (1990).

[147] A.K.Jain and A.Goel, Phys. Lett. B **277**, 233 (1992).

[148] R.R.Zheng *et al.*, Phys. Rev. C **56**, 175 (1997).

[149] H. N.Yoshida and J.Otsuka, Nucl. Phys. **A567**, 17 (1994).

[150] K.Hara and Y.Sun, Nucl. Phys. **A531**, 221 (1991).

[151] P.B.Semmes and I.Ragnarsson, in *Proc. of Int. Conf. on High-Spin Physics and Gamma-Soft Nuclei, Pittsburgh, 1990* (World Scientific, Singapore, 1991), p. 500.

[152] I.Hamamoto, Nucl. Phys. **A520**, 297c (1990).

[153] B.Cederwall *et al.*, Nucl. Phys. A **542**, 454 (1992).

[154] N.Tajima, Nucl. Phys. A **572**, 365 (1994).

[155] S.Drissi *et al.*, Nucl. Phys. **A543**, 495 (1992).